

Optical MEMS Sensors for Wall-Shear Stress Measurements



by

NIMA EBRAHIMZADE

THESIS SUBMITTED TO THE FACULTY OF
SCIENCE, AGRICULTURE AND ENGINEERING
IN PARTIAL FULFILLMENT OF THE REQUIREMENTS
FOR THE DEGREE OF
DOCTOR OF PHILOSOPHY

SCHOOL OF ENGINEERING
NEWCASTLE UNIVERSITY
UNITED KINGDOM

July 2021

Abstract

This research reports on the development and experimental characterisation of optical sensors based on Micro-Electro-Mechanical-Systems (MEMS) technologies for wall-shear stress quantification in turbulent boundary-layer flows. The MEMS sensors are developed to measure the instantaneous wall-shear stress directly via a miniature flush-mounted floating element, which is on the order of hundreds of microns square. The floating element is suspended flush to the wall by up to four specially designed micro-springs. As the flow passes over the wall, the sensor's floating element moves, allowing direct measurement of the local forces exerted by the flow on the wall. A new optical transduction scheme based on the Moiré fringe pattern is developed alongside with an optical pathway to measure the instantaneous wall-shear stress using a single photodetector. Using this new optical technique consists of a lens array and fibre optics that provides the ability to detect the wall-shear stress using different sensing element sizes, leads to miniaturisation of sensors. Utilising the lens array, the focused light spot size is controlled, providing the opportunity of scanning the Moiré fringe pattern area on the sensors with different sensing element sizes.

The microfabrication process of the devices are carried out by using a four mask bulk Silicon-on-Insulator (SOI) process and a BF33 wafer, where each device is placed at the center of a 5 mm × 5mm chip. Two generations of sensor packaging are developed to accommodate the sensors' dies as well as the sensors' optoelectronics, whilst the floating element is flush-mounted to the surface. The MEMS sensors calibration is carried out in a laminar flow rig over a wall-shear stress range of 0 to 5.32 Pa, where the results indicate a sensitivity range of 38 to 740 nm/Pa, an accuracy range of 1.4 to 2.36% and a repeatability range of 0.68 to 1.96%. The value of the of minimum detectable wall-shear stress for the developed MEMS wall-shear stress sensors varies in a range of 17 to 593 μ Pa, resulting in a minimum and maximum dynamic range value of 79 dB and 109 dB, respectively. The results from the dynamic characterisation indicate a

resonant frequency range of 1 to 8.3 kHz. In a series of wind tunnel experiments over a range of $Re_\tau = 560$ to 1320, the instantaneous wall-shear stress within the turbulent boundary-layer flow is measured simultaneously by the MEMS sensors and an by either hot-wire anemometry or laser Doppler velocimetry using the near-wall velocity gradient technique. Excellent agreement is observed in the time series and statistics across these three independant measurement techniques.

The Moving Finger writes; and, having writ,

Moves on: nor all thy Piety nor Wit

Shall lure it back to cancel half a Line,

Nor all thy Tears wash out a Word of it.

"Khayyam"

To Homeland, to Iran...

Declaration

I hereby declare that except where specific reference is made to the work of others, the contents of this dissertation are original and have not been submitted in whole or in part for consideration for any other degree or qualification in this, or any other university. This dissertation is my own work and contains nothing which is the outcome of work done in collaboration with others, except as specified in the text and acknowledgements.

Nima Ebrahimzade

July 2021

Acknowledgements

I would like to acknowledge the Faculty of Science, Agriculture and Engineering (SAGe) and the Newcastle University for funding this research project, without which this work would not have been possible.

I would like to express my sincere gratitude to my supervisor Dr Richard Whalley for his support and for giving me the opportunity to study the interesting realm of micro-systems. This provided me with the chance to learn more about the world from a micro-scale up to a global scale by meeting all the interesting people, across the globe, during the course of my Ph.D. study in Newcastle. I continue to learn from him.

I would also like to thank professor Peter Cumpson, Dr John Hedley and Dr Jose Portoles for their valuable help, support and guidance during the course of this study.

Thanks must go to my colleagues within the Fluid dynamics laboratory. To Jodi Reeve for being a good partner in crime, and for all the laughter and unconditional support during the final year of my studies. You are the best Persian language learner that I have ever seen (Tou khayli bahooshi). Special thanks to Aryan Moody who redefined the meaning of the "friendship" to me. Thank you for being there and for all the supports during the wind tunnel experiments.

To my colleagues and friends in Stephenson building who made the Ph.D journey a unique experience. I have been enlightened by learning more about their cultures. To Ricardo Ribeiro, Priscila Melo, Nilly Hojat, Joe Barrow and Fadoo Unom, for the shared fun memories and for being there.

I would like to extend my thanks to all the staff and technicians who helped me with one thing or the other: Michael Foster, Stuart Baker, Brian Stoker, Stephen Charlton, Paul Scott, Paul Harrison, Paul Watson, and Frank Atkinson.

I would like to thank Dr Sheida Hosseinian for her eternal support during my Ph.D. study. I hope her the best in life.

Finally and most importantly, I owe an enormous debt of gratitude to my parents, Habib and Hoorah, as well as my sisters, Maryam and Kimia. Without their unwavering support the completion of my Ph.D. would have not been possible.

Table of Contents

List of Figures	xv
List of Tables	xxxi
Nomenclature	xxxiii
1 Wall-shear stress and its importance	1
1.1 What is wall-shear stress?	3
1.2 Turbulent boundary-layer	5
1.3 Sensors' requirements for turbulence measurements	7
1.4 What is MEMS?	8
1.5 Research Aim and Objectives	9
1.6 Thesis outline	10
2 A Review on Wall-Shear Stress Measurement Methods	13
2.1 Readily-available methods	14
2.2 MEMS-based measurement methods	16
2.2.1 Indirect measurements	17
2.2.1.1 Thermal sensors	17
2.2.1.2 Surface fences and micro-pillars	28
2.2.1.3 Indirect optical methods	34
2.2.2 Direct measurements	36
2.2.2.1 Sensors with capacitive transduction	37
2.2.2.2 Sensors with Piezoresistive transduction	44
2.2.2.3 Sensors with optical transduction	47
2.3 Summary	53

3	MEMS Wall-Shear Stress Sensors Modelling and Development	59
3.1	Sensors Mechanical Modelling	59
3.1.1	Clamped-clamped micro-spring model	61
3.1.2	Serpentine micro-spring	64
3.1.3	Dynamic modelling of MEMS wall-shear stress sensors	68
3.1.4	Pressure gradient effects	70
3.1.4.1	Computational Fluid Dynamics Modelling	71
3.1.5	Finite Element Analysis	75
3.2	MEMS sensors optoelectronics	79
3.2.1	Moiré fringe pattern optical transduction	80
3.2.2	Moiré fringe pattern detection technique	86
3.2.3	LED drive circuit	87
3.2.4	Photo-detector transimpedance amplifier circuit	90
3.2.5	Lens array system	92
3.2.6	Material optical effects	95
3.2.7	Lens array test-bed	96
3.3	Moiré fringe pattern detection test-beds	100
3.3.1	Moiré Fringe pattern image processing test-bed	100
3.3.2	Moiré fringe pattern detection using rippling LEDs optoelectronics	102
3.4	Summary	104
4	Microfabrication and sensors packaging	105
4.1	Microfabrication process steps	105
4.1.1	Microfabrication process flow	106
4.1.2	Trench Etch	107
4.1.3	Gold deposition	107
4.1.4	Structure etch	107
4.1.5	BF33 optical gratings	110
4.1.6	Anodic bonding	111
4.1.7	Sensors release	111
4.2	Inspection and metrology	113
4.3	Sensors Packaging	117

4.3.1	Angle sensor packaging - First generation	117
4.3.2	Direct illumination sensor packaging - Second generation	122
4.4	Sensor control unit electronics	125
4.5	Summary	127
5	Experimental Setup	129
5.1	Laminar flow cell development	129
5.1.1	Sensors' calibration experimental setup	134
5.2	Dynamic Characterisation Experimental Setup	134
5.3	Wind Tunnel	137
5.4	Hot-wire Anemometry	139
5.4.1	Hot-wire probe calibration	141
5.4.2	Traverse System	143
5.4.3	Data Acquisition	145
5.4.4	Near-Wall Measurements	145
5.5	Laser Doppler Velocimetry	147
5.6	Summary	150
6	MEMS wall-shear stress sensors' characterisation	151
6.1	MEMS devices static characterisation	151
6.1.1	Sensors' calibration data processing procedure	152
6.1.2	Static calibration result	155
6.1.2.1	Repeatability error	161
6.1.2.2	Accuracy	162
6.1.3	Noise floor	163
6.2	Dynamic characterisation	165
6.2.1	Image Processing Algorithm	167
6.2.2	Dynamic Characterisation Results	168
6.3	Summary	173
7	Turbulent boundary-layer measurements	175
7.1	MEMS and Hot-Wire Anemometry	175
7.1.1	Canonical Turbulent Boundary-layer	175

Table of Contents

7.1.2	Wall-Shear Stress Measurement Result- MEMS and Hot-wire . . .	181
7.2	MEMS and LDV	184
7.2.1	LDV Canonical Turbulent boundary-layer Measurements	184
7.2.2	Wall-shear stress measurement-MEMS and LDV	188
7.3	Summary	199
8	Conclusion and Future Recommendations	201
8.1	Conclusion	201
8.2	Research contributions	203
8.3	Future Recommendations	204
8.3.1	Sensor development	204
8.3.2	Microfabrication	205
8.3.3	Sensor packaging and sensor control unit	206
8.3.4	Sensor characterisation	206
	References	207

List of Figures

1.1	An schematics of the turbulent flow over the fuselage of a commercial aircraft. The turbulent flow generates skin-friction drag (shown by red arrows). Wall-shear stress sensors can be implemented as a part of a drag reduction unit to provide feedback to the drag reduction device. The image of the sensors and the drag reduction unit is not to scale.	2
1.2	Boundary-layer transition from a laminar state into a turbulent state. . .	4
1.3	Turbulent boundary-layer velocity profile regions.	6
2.1	Wall-shear stress measurement methods classification. Taken from (Löfdahl and Gad-el Hak, 1999a)	14
2.2	Development of an oil film under the flow during a time period. The flow direction is from bottom to top a Taken from (Örlü and Vinuesa, 2020) .	16
2.3	A schematics of a hot-wire thermal sensor. The sensing element forms one arm of the Wheatstone bridge. From (Fingerson and Freymuth, 1977)	18
2.4	A schematic of a thermal wall-shear stress sensor. The heating of the sensing element produces a thermal boundary layer, δ_T , inside the velocity boundary layer of the flow, δ . From (Naughton and Sheplak, 2002) .	18
2.5	(a) Schematic of a MEMS thermal shear stress sensor developed by Lin et al. (2004), (b) Schematics view of the sensor developed by Xu et al. (2002), (c) The sensor developed by Liu et al. (1999)	20
2.6	(a) 3D view of the thermal sensor developed by Ou et al. (2016). (b) An image of a wall-shear stress sensor developed by Breuer et al. (1999). The coloured circle is the silicon-nitride membrane over the vacuum cavity.	21

List of Figures

2.7	(a) An image of a wall-shear stress sensor developed by Haneef et al. (2007). The aluminium sensing element is located at the center of a silicon oxide membrane. (b) An image of MEMS wall double hot-wire developed by Buder et al. (2008).	22
2.8	(a) SEM image of the hot-wire sensor suspended by a silicon oxide bridges. Taken from (Ghouila-Houri et al., 2016). (b) SEM image of the hot-wire micro sensor fabricated by Ghouila-Houri et al. (2020).	22
2.9	(a) A SEM image of two five-wire micro-sensors developed by Löfdahl et al. (2003). (b) SEM images of the nano-wire based thermal wall-shear stress sensor developed by Bailey et al. (2010).	23
2.10	(a) A SEM image of two five-wire micro-sensors developed by Löfdahl et al. (2003). (b) Top view of the tip of a multi-array micro hot-film sensor. Taken from (Borisenkov et al., 2015)	24
2.11	A SEM image of the sensor with suspended hot-film and CNT fins presented by Ito et al. (2010).	24
2.12	(a) An image of the calometric thermal wall-shear stress sensor, (b) A photo of the device wire bonded and mounted on a CPGA package. Taken from (De Luca et al., 2015).	25
2.13	SEM images of the calometric thermal sensor developed by Weiss et al. (2017). (a) The beams are suspended over a cavity. (b) Three beams configuration where the central beam is the heater and the beams on its sides are the detectors.	26
2.14	(a) A schematic drawing of a classical surface fence featuring a rigid blade with pressure tappings implemented on both side of it; (b) The MEMS-based surface fence using piezoresistors; (c) A close-up image of a surface fence device. Taken form (Von Papen et al., 2002).	29
2.15	Images of micro surface fences with trapezoidal cantilevers. (a) An image of the device developed by Schiffer et al. (2006), (b) Image of the device developed by Ma and Ma (2016).	30
2.16	SU-8 based sensory hair with capacitive read out. (a) A schematics of the sensor structure with SU-8 hair; (b) The SEM image of array of sensory hairs. Adopted from (Dijkstra et al., 2005).	32

2.17 (a) The SEM image of a single micro-pillar; (b) An image of a micro-pillar array. Taken from (Große and Schröder, 2007)	33
2.18 An image of a test setup for a micro-pillar wall-shear stress sensor. As it can be seen, the system requires bulky optics and optical access in the test rig. Taken from (Gnanamanickam et al., 2013)	34
2.19 (a) Schematics of the indirect optical MEMS wall-shear stress sensor. (b) 3D schematics of the optical sensor based on LDA. Taken from (Modarress et al., 2000).	35
2.20 A schematic view of floating-element wall-shear stress sensors.	36
2.21 A schematic cross section view of floating-element wall-shear stress sensors with differential capacitance readout. Taken from (Schmidt et al., 1988)	37
2.22 (a) Top view of the floating element with comb fingers (b) A SEM image of the MEMS wall-shear stress using comb fingers. The sensor displacement is measured via the differential capacitance from the comb finger electrodes. Adapted from Pan et al. (1999).	38
2.23 (a) The schematic view of the top surface of the sensor developed by Zhe et al. (2005). (b) A photo from the top surface of the device showing the floating element and the long cantilever beam. Taken from (Zhe et al., 2005).	39
2.24 (a) The schematic view of the differential capacitive sensor developed by Chandrasekharan et al. (2011). (b) The SEM image of the capacitive sensor developed by Sells et al. (2011). Images are taken from (Sells et al., 2010) and (Sells et al., 2011).	40
2.25 An image of the differential capacitive wall-shear stress sensor using TSVs technology. Taken from (Barnard, Meloy and Sheplak, 2016).	42
2.26 A SEM image of the differential MEMS wall-shear stress sensor developed by Ding et al. (2018).	43
2.27 A schematics of the differential capacitive MEMS wall-shear stress sensor by Mills et al. (2017).	43

2.28 A Schematic view of the floating element sensor with piezoresistive readout. The micro-springs are formed in line with the flow, so that the deflection is normal to the micro-spring direction to generate axial strain in the piezoresistors. Taken from Schmidt et al. (1988) 45

2.29 Schematics of the piezoresistive MEMS wall-shear stress sensor with top and side-wall implementation developed by Barlian et al. (2007). Taken from (Barlian et al., 2007). 45

2.30 Schematics of the MEMS wall-shear stress sensor with side-implemented piezoresistors. Taken from (Li et al., 2008). 46

2.31 (a) The Schematic view of the detection principle for the sensor with integrated photodiode. (b) A Schematics of the optical sensor with split diode configuration. Taken from (Padmanabhan et al., 1996) and (Padmanabhan et al., 1997). 47

2.32 (a) A schematic cross section view of the sensor using the micro-Fabry–Perot interferometry. (b) A SEM image of the fabricated optical sensor with the micro mirror (floating element) is shown at the middle of the picture. Taken from (Tseng and Lin, 2003). 48

2.33 Illustration on using an laboratory microscope to observe the MEMS sensor displacement. Taken from (Chen, 2012). 49

2.34 The schematic view of the WGM based sensor. Taken from (Ayaz et al., 2011). 50

2.35 A schematics of the optical test bed developed to mimic the Moiré fringe pattern and to check the ability of the fibre optics bundle approach for Moiré fringe pattern displacement quantification. Taken from (Chen et al., 2010). 51

2.36 Sapphire wall-shear stress sensor with Moiré fringe transduction and four fibre optics for high temperature applications. Image is taken from (Mills et al., 2016). 52

3.1	MEMS wall-shear stress sensor structures. Devices with clamped-clamped and serpentine micro-springs are designed for wall-shear stress measurements. As the air flows over the MEMS device, the floating element is free to move, courtesy of the micro-spring arrangements, in the direction of the fluid flow, whilst remaining parallel to the aerodynamic surface. . .	60
3.2	Mechanical modelling of MEMS devices with clamped-clamped micro-springs. (a) Half plane model, (b) Mechanical model of clamped-clamped micro-spring.	61
3.3	Free body diagram of the clamped-clamped micro-spring.	63
3.4	Mechanical Model of a MEMS wall-shear stress device with serpentine micro-spring	65
3.5	Free body diagram of the serpentine micro-spring	66
3.6	Lumped element models for the MEMS devices where 1D sensors are modelled as a SDOF system.	69
3.7	Slide-film damping between the sensor floating element and the fixed substrate. τ_{gap} is the shear stress that is applied to the lower surface of the floating element due to the fluid flow through the gaps in the sensor.	70
3.8	Illustration of the pressure gradient acting on the sides of the floating element and the additional wall-shear stress term on the bottom face of the floating element.	71
3.9	2D geometry of the calibration rig with the floating element placed at the center of it. The flow boundary conditions are a fully developed laminar flow velocity inlet and a atmospheric pressure outlet.	72
3.10	(a) A contour plot showing the pressure gradient in the rig across the sensor. (b) A contour map showing the velocity profile in the rig. It can be noticed from the velocity contour that the flow is fully-developed when it enters the model.	74
3.11	Wall-shear stress values on the top and bottom surface of the floating element obtained by CFD modelling .Blue circles represent the wall-shear stress values on the bottom surface of the floating element, τ_g , and red squares represent the wall-shear stress on the top surface of the floating element, τ_w	74

3.12 MEMS wall-shear stress sensors deflection model using FEA. (a) sensor with clamped clamped micro-spring. Sensor's specifications in this model are $W_e = 1000\mu m$, $L_e = 1000\mu m$, $L_t = 1000\mu m$, $W_t = 7\mu m$, and $T = 20\mu m$, (b) sensor with serpentine micro-spring. Sensor's specifications in this model are $W_e = 800\mu m$, $L_e = 800\mu m$, $L_t = 800\mu m$, $W_t = 7\mu m$, $T = 20\mu m$, and $n = 4$. 76

3.13 MEMS wall-shear stress sensor displacement. (a) Device with clamped-clamped micro-spring, (b) Device with serpentine micro-spring. Dashed lines (- - -) and black circles (●) represent the analytical model and FEA for devices with $W_e = 500\mu m$, $L_e = 500\mu m$, $L_t = 500\mu m$ respectively, dashed-dot line (-·-·-) and black triangles (▲) represent analytical model and FEA for devices with $W_e = 800\mu m$, $L_e = 800\mu m$, $L_t = 800\mu m$ respectively, and solid line (—) and black squares (■) represent analytical model and FEA for devices with $W_e = 1000\mu m$, $L_e = 1000\mu m$, $L_t = 1000\mu m$ respectively. Devices thickness and micro-spring width considered to be fixed and equal to $20\mu m$ and $7\mu m$ 76

3.14 Clamped-clamped micro-spring geometry effects. (a) Effect of micro-spring width and length on mechanical stiffness, (b) Effect of micro-spring width and length on resonant frequency. Solid line (—) represent the analytical model for L_t effect, dashed line (- - -) represent the analytical model for W_t effect, and black squares (■) represent the FEA results. . . 78

3.15 Serpentine micro-spring geometry effects. (a) Effect of micro-spring width and length on mechanical stiffness and resonant frequency, (b) Effect of number of foldings on mechanical stiffness and resonant frequency. all the lines are analytical models and black squares (■) represent the FEA results. 78

3.16 schematics of Moiré fringe pattern generated on the sensor. 80

3.17 schematics of Moiré fringe pattern generated on the sensor. 80

3.18 Binary square-wave representation of the Moiré fringe pattern gratings. The width of the grating is considered to be half the spatial pitch of the grating set. 83

3.19 Moiré fringe pattern formation and shift based on transmittance function of grating's sets. 84

3.20 Schematics of the phase shift tracking sensor transduction. Applied wall-shear stress results in the phase shift in the corresponding sinusoidal function of the pattern.	87
3.21 Phase shift tracking of the Moiré fringe pattern. The black dots represent the scanning light spots on the pattern. the phase shift and Moiré fringe pattern shift are shown on the sine curves.	88
3.22 Schematics of LEDs drive circuit. "TP"s are terminal ports for each LED, where the output of the micro-controller are connected to them. The number of LEDs depend on the size of the Moiré fringe pattern.	89
3.23 Schematics of the photodiode transimpedance amplifier circuit.	91
3.24 Magnitude against frequency for the open-loop gain of the amplifier and closed-loop gains for two stages of the non-inverting amplifications. . .	92
3.25 Schematics of the lens system for light spots projection.	94
3.26 Schematic of the light transmittance and reflectivity in different mediums of the wall-shear stress sensor.	96
3.27 Lens array test-bed.	97
3.28 Lenses array test-bed results. (a) Intensity profile a projected light spot over an area and its intensity profile curve, $1/e^2$ method is used to measure the light spot size, (b) Model validation result for the lenses array test-bed for three different distances between the lenses.	99
3.29 Intensity function curves of eight $20\ \mu\text{m}$ light spots across an area. The light spot size is obtained using $1/e^2$ definition.	100
3.30 Test-bed for Moiré fringe pattern detection using image processing. . . .	101
3.31 Moiré fringe pattern displacement tracking test-bed results using image processing method, (a) Generated pattern as a result of supposition of gratings sets on film slides, (b) Intensity profile across the Moiré fringe pattern area where solid black line (—) presents the average intensity profile (c) Sinusoidal curves of the initial and displaced Moiré fringe pattern, (d) Sinusoidal curve phase shift against stage displacement. . .	102
3.32 Rippling LEDs test-bed. (a) A photo of the test-bed, (b) Phase difference against displacement for the rippling LEDs method test-bed.	103

List of Figures

4.1	Microfabrication process flow of the MEMS wall-shear stress sensors.	106
4.2	Details of the MEMS wall-shear stress sensors microfabrication process.	109
4.3	Optical images of the patterned sensors' structures as well as gold optical gratings. (a) sensor with clamped-clamped micro-spring, (b) sensor with serpentine micro-spring.	110
4.4	Image of the sensor devices on the bonded wafers.	112
4.5	Images of fabricated MEMS wall-shear stress sensors with clamped-clamped and serpentine micro-springs. The mechanical structure of the MEMS sensors were fabricated at the center of 5 mm × 5mm. MEMS sensors dies placed alongside a coin for comparison purpose. (a) SEM image of a clamped-clamped MEMS sensor,)b) SEM image of a MEMS sensor with serpentine micro-spring.	114
4.6	(a) Schematics of white light interferometry, (b) MEMS sensors surface profiling under Zygo interferometer.	115
4.7	(a) Surface profile contour of MEMS DEV SER27, (b) corresponding surface profiles across the lines of scan in streamwise and spanwise directions.	116
4.8	Schematics views of the sensor packaging.	118
4.9	Sensor plug, (a) CAD modelling of the sensor plug, (b) Top view of a 3D printed sensor plug.	118
4.10	Schematics of the sensor die holder with the recess at the center. The MEMS sensor is placed into the recess and epoxied to be fixed.	119
4.11	Explosive map of components inside the optical tube. The spacers are designed to fix the lenses and fibre optics groove in place and also to provide the gap between the components in the optical system. All these components are fixed inside an enclosure and then are assembled into the main sensor plug.	120

4.12 The process flow for the fibre optics micro-groove fabrication.(a) Two parts are fabricated using 3D printing technology, (b) The fibre optics are placed and retained in the grooves, (c) UV curable epoxy is applied to the first part and on top of the fibre optics, (d) Second part is assembled to the first part using the alignment pillars and holes , (e) Fibre optics are fixed inside the micro-grooves. 121

4.13 A prototype of the sensor packaging. The MEMS wall-shear stress sensor can be seen at the center of the sensor die holder. 121

4.14 CAD modelling of the second generation sensor packaging. (a) schematics of the overall sensor packaging, (b) cross section view of the sensor packaging with one lens, (c) cross section view of the sensor packaging with two lenses, (d) the optical tube (spacer) with the female MTP connector plugged into it and. The lens can be seen at the top of the optical tube. 123

4.15 An image of a prototyped sensor packaging, with the MEMS sensor dies placed at the center of it. on end of the fibre optics array with a male MTP connector can be seen in the image, whilst the other end is plugged into the sensor packaging. 125

4.16 Electronics of the sensor control unit including the LEDs drive circuit's PCB, photodiode transimpedance amplifier circuit's PCB, and the Arduino DUE microprocessor. A bundle of 12 OM4 fibre optics were used to transfer the lights from the LEDs into the sensor packaging via a female to male MTP connection. 126

5.1 A schematics of the calibration rig. The high aspect ratio of the duct ensures that the flow is laminar and fully-developed inside the rig during the sensors' calibration. 130

5.2 (a) Half section view of the calibration rig duct. Pressure tapings are placed on either sides of the sensor to measure the pressure gradient across the channel. (b) End plate sealing attachment. 131

5.3 Validation profiles of the calibration rig. (a) Pressure drop across the calibration rig versus the flow rate for various pressure tapings' distances. (b) Friction factor versus Reynolds number for laminar flow in the calibration rig. The black solid line is $ff = 24/Re$ 133

5.4 Experimental setup for the MEMS wall-shear stress sensors calibration. (a) A schematic view of the experimental setup; (b) an image of the calibration rig with the sensor plugged into it. The Betz manometer and a plugged sensor are shown in the insets. 135

5.5 Experimental setup for the dynamic characterisation of the MEMS wall-shear stress sensors. (a) Shows the schematics of the setup and (b) shows the actual setup. The MEMS devices are mounted on the top surface of a 2D piezoelectric shear stack, which actuate the devices. . . 136

5.6 Wind tunnel facility at the Fluid Dynamics laboratory. 138

5.7 A picture of the wind tunnel test section , showing (1) the elliptical leading edge and (2) the turbulence trip. 138

5.8 DANTEC Dynamics streamLine pro with 91C10 CTA modules. 140

5.9 (a) 55P15 boundary-layer hot-wire probe, (b) 55P11 Free-stream hot-wire probe, (c) 55H22 1D right-angle probe support. Courtesy of DANTEC Dynamics. 140

5.10 Optimum square-wave response of a Hot-wire probe. Taken from (Bruun, 1996). 141

5.11 An image illustrating the diagnostic tools that are used for Hot-wire calibration and wind tunnel testings, showing (1) FlowMatser probe, (2) RTD probe, (3) boundary-layer hot-wire probe on the traverse system, (4) Free-stream hot-wire probe 142

5.12 Hot-wire calibration curves over a temperature range. (a) Traversing boundary-layer hot-wire probe and (b) Free stream hot-wire probe. . . 143

5.13 Hot-wire probes traverse system. Three stepper motors provide the movement of the hot-wire probe in three directions independently. . . . 144

5.14 Boundary layer probe positioning. a) probe not tilted, b) probe not tilted and traversed into the wall, and c) probe tilted to allow prong tips to touch the wall. Taken from (Hutchins and Choi, 2002). 146

5.15	Near wall velocity profile showing the heat transfer region below $y^+ = 3$. Taken from (Hutchins and Choi, 2002).	146
5.16	Schematics the LDV setup. Genesis MX series lasers STM/SLM providing two laser beams with a wavelength of 514 nm and 488 nm. These laser beams then are transferred in to the LDV probe, where they are projected and focused inside the wind tunnel test-section. The LDV receiver with a focal length of 300mm detect the signal and transfer it to the FSA3500 signal processor via fibre optics.	148
6.1	Algorithm to determine the location and diameter of the light spots on the sensor and to retrieve the Moiré fringe pattern profile. Image processing is performed on the images of the projected light spots and the SEM image of the Moiré fringe pattern.	152
6.2	Procedure of determining the location and diameter of the projected light spot on the sensor. (a) A USB microscope is used to take the picture of the light spots on the sensor. (b) Normalised intensity profile contour across the sensor. The inset shows the 2D contour of the light intensity on the sensor surface.	153
6.3	Retrieving the Moiré fringe pattern profile by image processing. (a) SEM image of the Moiré fringe pattern on a sensor. Black circles represent the location of the light spots across the pattern. This is for the device with the first generation of the packaging and seven fibre optics. (b) The resulting intensity profile of the Moiré fringe pattern with the corresponding sinusoidal curve. Black sine curve is the corresponding sinusoidal profile of the pattern obtained by applying a low-pass filtering on the image. Black squares are the photodiode voltage response of each light spot, that are in good agreement with the profile.	154

6.4 Static calibration procedure result for device number 20. (a) Shows the SEM image of the Moiré fringe pattern with the blue line presents the line of scan and black circles represent the location of the projected light spots on the pattern; (b) Shows the fitted sine curve to the photodiode output data. The inset illustrates the residuals of the photodiode output data to the sine curve; (c) Sensor’s time signal at different wall-shear stress values. 157

6.5 An example of the MEMS wall-shear stress sensor response with and without pressure gradient correction. It can be seen that the calibration curve shifts noticeably. 158

6.6 Calibration curve for device number 20. One of the insets show the the data points residuals to the linear curve fitting and the second inset show the temperature reading during the calibration for two test runs. The shaded area around the calibration curve demonstrates the $\pm 95\%$ prediction bounds in the least square curve fitting. 159

6.7 Relative uncertainty in wall-shear stress measurement. 161

6.8 Illustration of the repeatability error quantification from the sensors calibration tests. 162

6.9 Power spectral density (PSD) of the phase shift noise. The dashed black line presents the Noise floor of the signal. 163

6.10 Calibration curves of the MEMS wall-shear stress sensors. 165

6.11 An example of a MEMS wall-shear stress sensor at its resonant frequency. It is seen that when the sensor is actuated with the external frequencies near its resonant frequency, its image becomes blurry due to a low exposure time on the image sensor. 165

6.12 Illustration of a clamped-clamped sensor displacement at its resonant frequency using the phase delay method with (a) 0° phase delay, (b) 90° phase delay, (c) 180° phase delay. The dashed line is added to the images as a reference for the device displacement at each phase delay. It should be noticed that the images are taken at one corner of the device. 166

6.13	Illustration of the sensors' displacement at their resonant frequencies, using the Frequency delay method. (a) and (b) represent the displacement of a clamped-clamped device, (c) and (d) Show the displacement of a serpentine device. Dashed lines are imposed on the images as a reference to show the displacement.	167
6.14	An illustration of the intensity profile across a serpentine sensor displacement frame. (a) A 20X image of a serpentine device. The red line is line of scan for the intensity profile. (b) Corresponding intensity profile of the image.	168
6.15	Frequency response of the MEMS wall-shear stress devices. (a) MEMS DEV CC13; (b) MEMS DEV SER69; (c) MEMS DEV SER68; (d) MEMS DEV CC23; (e) MEMS DEV CC25; (f) MEMS DEV CC20; (g) MEMS DEV CC30; (h) MEMS SEV SER27; (i) MEMS DEV SER26. The insets present the displacement time response of the sensors as well as the voltage input to the piezoelectric actuators. Thick black line represents the experimental results and the dashed blue line is derived from the analytical solution.	172
6.16	An illustration of the time delay between the actuator signal and the sensor's response.	173
7.1	Hot-wire and MEMS measurements. (a) Schematics of the hot-wire probe and MEMS sensor in the wind-tunnel flat plate, (b)An image of the hot-wire probe traversed into the wall on the spanwise direction of the MEMS sensor.	176
7.2	Integral time calculation for the fluctuating velocity at the location with the maximum turbulence intensity ($y^+ = 14$). The insets show the velocity fluctuations and the turbulence energy spectra at this location.	178
7.3	Mean value of the near-wall velocity within the turbulent boundary-layer. The points in the wall-effect region are excluded in the least squares fitting to avoid inaccurate measurements of the friction velocity.	179

7.4 Turbulent boundary-layer canonical data measured by hot-wire. (a) Mean streamwise velocity profile, (b) turbulence intensity profile of the streamwise velocity, (c) averaged skewness profile of the streamwise velocity, and (d) averaged kurtosis of the streamwise velocity. 180

7.5 PDFs of fluctuating wall-shear stress measured by the hot-wire probe (black line with the stars) and the MEMS sensor DEV CC20 (blue line) at $Re_\tau = 560$. The inset shows the normalised PDFs of the wall-shear stress fluctuations. 183

7.6 An illustration of MEMS and LDV experiments. (a) A schematics of the MEMS an LDV test. Three MEMS wall-shear stress sensors are placed across the span of the flat plate to measure the flow statistics. LDV laser beams are focused over the floating element of the central MEMS sensor, while the two other MEMS sensors are taking data across the span. (b) An image of the MEMS and LDV experiments. 186

7.7 Turbulent boundary-layer canonical data measured by LDV at $z = 0$ for a Reynolds number range of $Re_\tau = 600$ to 1320. (a) Mean streamwise velocity profiles, (b) turbulence intensity profiles of the both streamwise and spanwise velocities. Due to the surface reflection issues the spanwise direction velocity component measurement, started at $y^+ = 25$, (c) skewness profiles of the streamwise velocity, (d) kurtosis profiles of the streamwise velocity, and (e) Reynolds stress profiles, where insets show the fluctuating velocity components in streamwise, u' , and spanwise, v' , and the negative product of these components, $-u'v'$ 190

7.8 Turbulent boundary-layer canonical data measured by LDV at $z = 75\text{mm}$. 191

7.9 Wall-shear stress time signals captured by MEMS sensors and the LDV. (a) DEV CC20 and LDV τ_w time signals with a correlation of 66%, (b) DEV SER27-1 and LDV τ_w time signals with a correlation of 81%, (c) DEV SER26 and LDV τ_w time signals with a correlation of 72%, and (d) DEV SER27-2 and LDV τ_w time signals with a correlation of 70%. 196

- 7.10 Fluctuation magnitude of the wall-shear stress, $\tau_{w,RMS}^+ = \tau_{w,RMS}' / \overline{\tau_w}$, as a function of Re_τ . Red triangles show the data captured by LDV and blue circles represent the data captured by MEMS DEV SER27. Inset shows the effect of sensor sizes, L^+ and W^+ , on $\tau_{w,RMS}^+$ at $Re_\tau = 600$. Black square represent the LDV data, south pointing triangle show the MEMS SER27-1, diamond shows the data for MEMS CC20, and black cross represents the data for DEV CC13. 197
- 7.11 PDFs of fluctuating wall-shear stress measured by LDV and the MEMS sensors at $Re_\tau = 600$ (black lines), $Re_\tau = 910$ (red lines), $Re_\tau = 1060$ (blue lines), and $Re_\tau = 1320$ (orange lines). LDV data captured at the location of the central MEMS sensor for each Re_τ . The inset shows the normalised PDFs of the wall-shear stress fluctuations. 198

List of Tables

2.1	Summary of the specifications of the MEMS wall-shear stress sensors.	57
3.1	Mechanical properties of Silicon used for model verification.	75
3.2	Sensors resonant frequency validation results.	77
4.1	Specifications of the microfabricated MEMS wall-shear stress sensors. .	113
4.2	Surface profile height measurements of the MEMS wall-shear stress sensors.	116
4.3	Required length of spacers for MEMS sensor packaging	124
6.1	Calibration results of the MEMS wall-shear stress sensors.	164
6.2	Dynamic specifications of the devices.	169
7.1	Turbulent flow wall-shear stress parameter measured by a MEMS sensor and the Hot-wire anemometry.	182
7.2	Canonical turbulent boundary-layer parameters.	187
7.3	Turbulent flow wall-shear stress parameter measured by MEMS sensors and LDV.	192

Nomenclature

Roman Symbols

\hat{u} True value of the mean velocity in streamwise direction

\hat{I} Predicted Moiré fringe pattern response value

$\overline{U_b}$ Flow's bulk velocity (m/s)

\bar{u} Mean component of the stream-wise velocity (m/s)

$\tilde{I} = \frac{LCI_L}{I_{Lc}}$ Length factor (m)

A_0 DC gain

A_n Amplitude of Moiré fringe pattern sinusoidal curves

b Channel and test section width (m)

C Constant

C_e Sensor's equivalent damping (N.s/m)

D Diameter of Pitot tube

d_i image distance from the lens (m)

d_o Object distance from the lens (m)

d_{spot} Projected light diameter (m)

DH Hydraulic diameter (m)

E Young's modulus (Pa)

e Euler's number = 2.7182

Nomenclature

F	Force (N)
f	Frequency (Hz)
f_0	Resonant frequency (Hz)
F_e	Floating element force (N)
f_l	Focal length of the lens (m)
f_t	Unity-gain bandwidth
F_{drag}	Drag force (N)
f_{L1}	First lens focal length(m)
f_{L2}	second lens focal length(m)
f_{Min}	Minimum sensor frequency requirement (Hz)
f_{PC}	Calibration function of the Pitot tube
f_{res}	Resonant frequency (Hz)
ff	Friction factor
G	Moiré fringe pattern spatial period (m)
g	Gap size (m)
G_1 and G_2	Operational amplifier gains
g_1 and g_2	Spatial pitch of the grating sets (m)
G_T	Total gain
h	Channel half height (m)
h_i	Image height (m)
h_o	Object height (m)
h_{gap}	Height of the gap between the floating element and the fixed substrate underneath it (m)

I	Cross section moment of inertia (m^4)
I_0	Peak light intensity
I_G	Gaussian light intensity profile
I_{Lc}	Cross section moment of inertia for the connector beams (N.m)
I_{Lt}	Cross section moment of inertia for the span beams (N.m)
K_e	Sensor's equivalent stiffness (N/m)
K_{x_s}	Serpentine micro-spring stiffness in x_s direction (N/m)
K_{z_s}	Serpentine micro-spring stiffness in z_s direction (N/m)
K_{CC}	Clamped-clamped micro-spring stiffness (N/m)
l	Characteristic length (m)
L_C	Meander length in serpentine micro-spring (m)
L_e	Floating element length (m)
L_t	Micro-spring length (m)
$L_{entrance}$	Entrance length (m)
L_{Max}	Maximum sensing element size requirement (m)
M	Moment (N.m)
M_e	Sensor's equivalent mass (kg)
M_{Lc}	Moment in the connector beam of serpentine micro-spring (N.m)
M_{Lt}	Moment in the span beam of serpentine micro-spring (N.m)
$m_{lensarray}$	Lens system magnification
m_{lens}	Lens magnification
N	Number of independent samples

Nomenclature

n	Number of serpentine foldings
n_0	Air refractive index
n_{BF33}	BF33 substrate refractive index
OG	Open-loop gain
PD	Photodiode output data
Q	Flow rate (m^3/s), <i>QualityFactor</i>
q	Distributed shear force per unit area (N/m)
R	Resistance (Ω)
R_r	Reference resistance (Ω)
r_{spot}	Projected light radius (m)
R_{uu}	Auto-correlation function for the streamwise velocity fluctuations
$Re = \frac{Ul}{\nu}$	Reynolds number based on the characteristic length
$Re_x = \frac{Ux}{\nu}$	Reynolds number based on stream-wise distance
$Re_\tau = \frac{u_\tau \delta}{\nu}$	Reynolds number based on friction velocity
$Re_\theta = \frac{u_\tau \theta}{\nu}$	Reynolds number based on momentum thickness
$Re_{DH} = \frac{2Q\rho}{b\mu}$	Reynolds number based on the hydraulic diameter
SD_u	Streamwise velocity component standard deviation
SD_v	Spanwise velocity component standard deviation
T	Device thickness (m)
T	Time Period
T_d	Talbot distance (m)
T_i	Integral time

T_s	Sampling time (s)
T_s	Sensing element constant temperature
$t_{3\%}$	Time taken for the signal to drop to 3% of the maximum value
T_∞	Fluid flow Temperature
t_{gi}	Weight time
t_{Max}	Maximum sensor period requirement (s)
TU	Turbulence intensity
U	Flow speed (m/s)
U	Total strain energy (N.m)
u	Stream-wise velocity component (m/s)
u'	Fluctuating component of the stream-wise velocity (m/s)
U_∞	Free stream velocity (m/s)
$u_\tau = \sqrt{\tau_w/\rho}$	Friction velocity (m/s)
U_{fe}	Floating element velocity (m/s)
u_{RMS}	streamwise velocity root mean square
V_i	Input voltage (v)
V_o	Output voltage (v)
w_0	Initial light radius (m)
W_e	Floating element width (m)
W_i	Weight function based on the weight time
W_t	Micro-spring width (m)
X_i	Independent variables

Nomenclature

x_i x value of the data point i

Y A measured quantity

y Wall normal distance (m)

y_i y value of the data point i

Greek Symbols

α Temperature coefficient

Δr Maximum difference between the output signals of a sensor in two separate run cycle

κ Constant

Δ Moiré fringe pattern displacement)

$\Delta\Phi$ Phase difference (rad)

δ^* Displacement thickness

δ Boundary layer thickness (m)

δ_{τ_w} Sensor's maximum displacement (m)

ΔP Pressure differential (Pa)

Δt Sampling intervals (s)

δ_{x_s} Serpentine micro-spring displacements in x_s direction (m)

δ_{z_s} Serpentine micro-spring displacements in z_s direction (m)

ε Error

ε_r Repeatability error

λ_n Period of additional Moiré fringe pattern sinusoidal curves

τ_{Max} Maximum wall-shear stress value

μ Dynamic viscosity (N.s/m²)

ν	Kinematic viscosity (m^2/s)
ω	Angular frequency (rad/s)
ω_b	Break frequency
∂	Differential derivation
Φ_0	Initial phase (rad)
Φ_n	Phase of additional sinusoidal curves
$\Delta\Phi_{RMS}$	Phase difference root mean square
Ψ_0	Micro-spring rotation
ρ	Density (kg/m^3)
$\rho_{uu}(\tau)$	Auto-correlation coefficient
σ	standard deviation
τ_w	Wall-shear stress (Pa)
λ	Light wavelength
τ	Time lag
$\overline{\tau_w}$	Mean component of the wall-shear stress (Pa)
F_{drag}	Drag force shear stress (Pa)
τ_{eff}	Effective wall-shear stress (Pa)
τ_{gap}	Wall-shear stress in the gap between the floating element and the fixed substrate (Pa)
τ_w^I	Fluctuating component of the wall-shear stress (Pa)
$\tau_{w, MEMS}^*$	Complex conjugate
θ_{glass}	Acceptance angle of BF33 glass
θ	Momentum thickness (m)

Nomenclature

θ_{air} Acceptance angle of air

$\tau_{w,LDV}$ Wall-shear stress time measured by LDV

$\tau_{w,MEMS}$ Wall-shear stress time measured by MEMS sensors

Superscripts

$+$ indicates viscous scaling or inner scaling of viscous time, length and velocity,

$$y^+ = \frac{yu_\tau}{\nu}, U^+ = \frac{u}{u_\tau}, t^+ = \frac{tu_\tau^2}{\nu}$$

' Fluctuating component of the quantity

Subscripts

RMS Root mean square value

Other Symbols

§ Symbol for sections

Acronyms / Abbreviations

BJT Bipolar Junction Transistors

BW Bandwidth

CFD Computational Fluid Dynamics

DNS Direct Numerical simulation

DR Dynamic range

FS Measurement full scale

FTBA Front To Back Alignment

LDV Laser Doppler Velocimetry

LED Light Emitting Diode

MDSS Minimum detectable wall-shear stress

MEMS Micro-Electro-Mechanical-Systems

PDF Probability Density Function

PSD Power Spectral Density

RTD Resistance-based Temperature Detector

SEM Scanning Electron Microscope

SNR Signal to Noise Ratio

SSR Sum of squares of the regression

SST Total sum of squares

WLI white Light Interferometry

Chapter 1

Wall-shear stress and its importance

The instantaneous measurement of wall-shear stresses is vital for various applications. The measurements of the wall-shear stress provides valuable information about the fluid flow structure and the different flow phenomena such as transition to turbulence and turbulence eddies. Turbulence can be explained as the random and chaotic motion of the fluid that contains numerous space and time scales (Bailly and Comte-Bellot, 2015). Study of the turbulence provides the core requirement for various science and engineering disciplines. Underpinning the characterisation, development and exploitation of these turbulent boundary-layers is the measurement of instantaneous wall-shear stress (Naughton and Sheplak, 2002). To explain the importance of this in the field of aerodynamics, as the air flows over the fuselage of an aircraft or high speed trains, a layer of turbulence is formed near to the body of the vehicle. The formed turbulence is responsible for the generation of a resistive force that is known as the skin-friction drag; schematically shown by red arrows in Figure 1.1. Skin-friction drag produces the wall-shear stress across the body of the vehicle. It is known that the skin-friction drag accounts towards $\approx 50\%$ of the total drag on a commercial aircraft, which means half of the energy consumption is used to overcome this resistive force (Bushnell and Hefner, 1990). Therefore, the quantification of the wall-shear stress is the key toward the evolution of the active drag reduction technologies, which in turn reduced the energy consumption and consequently, benefits the society by reducing the effects of the global warming. To put this in context, a 3% reduction in the skin-friction drag on a commercial aircraft would reduce the carbon dioxide (CO₂) emissions into the atmosphere by 3,000 tonnes per year (Bushnell and Hefner, 1990).

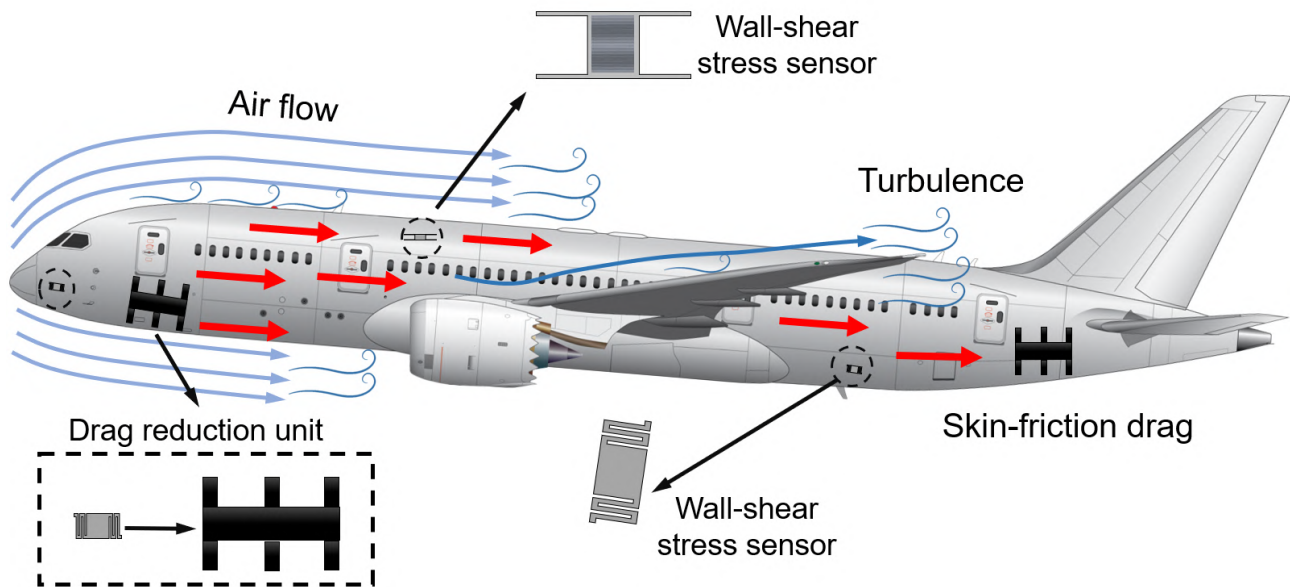


Figure 1.1 A schematic of the turbulent flow over the fuselage of a commercial aircraft. The turbulent flow generates skin-friction drag (shown by red arrows). Wall-shear stress sensors can be implemented as a part of a drag reduction unit to provide feedback to the drag reduction device. The image of the sensors and the drag reduction unit is not to scale.

In addition to the environmental benefit, commercial benefit can be achieved by saving an estimated value of £1.2m in jet fuel per year for each aircraft. Today, there are nearly 23,600 active aircraft in the world (Bushnell and Hefner, 1990). Considering a 3% reduction in the skin-friction drag, results in an estimated 70.8 million tonnes reduction in the CO₂ emissions annually.

Accurate measurements of the fluctuating wall-shear stress, however, can be particularly challenging in air flows, since the value of the wall-shear stress is normally small. For an aircraft cruising at 420 km/h, this value is around 2 Pa (Gerhart et al., 2016), which means a highly sensitive device is required to evaluate the value of this small force per unit area.

Measurement of the wall-shear stress is also vital in other industrial flow applications. This is important for fluid flow controlling and manufacturing purposes. An example of this is the measurement of the fluid properties in extrusion processes. Biomedical society can also benefit from the shear stress measurement in such application as tissue engineering. To put this in context, an study on the effectiveness of hydrodynamic forces on the vascular endothelial structure and cellular function in blood flow has been carried out utilising a flow chamber, which can produce a controlled wall-shear stress (Li et al., 2005).

Despite the recent developments on wall-shear stress sensors, most of the existing sensors are limited by lacking of sufficient sensitivity and accuracy to detect the low values of the wall-shear stress and to resolve the small fluctuations in the turbulent flow. Furthermore, while the existing optical MEMS wall-shear stress sensors show a good performance under calibration environments, there is no report showing the optical MEMS sensors being tested in turbulent flow environment.

Present work reports the development of floating element based MEMS wall-shear stress sensors using an optical transduction technique. Here the idea of optical Moiré fringe pattern is used to track the displacement of the MEMS sensors structures. Moreover, in this research a novel optoelectronics is used to overcome the limits associated with the accuracy in previous sensors, as well as eliminating errors related to cross-talk. In addition to a new optoelectronics, serpentine micro-spring is used in the micro-sensors structure to enhance the mechanical sensitivity, alongside with the classical clamped-clamped micro-spring configuration.

1.1 What is wall-shear stress?

When a viscous fluid flows over a rigid wall the velocity of flow is not equal at all points above the surface. The flow's velocity is the highest at the free stream and it drops at points toward the surface, generating a velocity gradient. This velocity gradient is due to the frictional forces that are exerted between the adjacent layers. The engine behind the generation of these frictional forces is the fluid's viscosity. Moreover, the viscous fluid flow exerts force on the boundary surfaces. This force can be decomposed into normal and tangential forces. The normal component of force per unit area is pressure and the tangential component of force per unit area is known as wall shear stress (White, 2016). The magnitude of the wall-shear stress is proportional to the velocity gradient near the wall, which is how fast the velocity changes moving from the wall to an adjacent point in the wall-normal direction. Hence, low values of wall-shear stress are linked to low local velocities and long residence time of fluid in the near wall-region (Katritsis et al., 2007). The near-wall region velocity gradient also is known as the wall-shear rate. According to Newton's law of friction, wall-shear stress, τ_w , for Newtonian fluid is expressed as

Wall-shear stress and its importance

(White, 2016)

$$\tau_w = \mu \left(\frac{\partial u}{\partial y} \right) \quad (1.1)$$

where μ is the fluid's dynamic viscosity, u is the flow velocity parallel to the wall, y is the wall-normal distance, and index w indicates the value at the wall. The stream-wise velocity of the flow cannot jump from zero at the wall to the free stream velocity, U_∞ . Rather, the transition in the velocity happens in a thin layer, with a thickness of δ , near to the wall which is called the boundary-layer (Schlichting and Gersten, 2016). Here, the velocity increases with increasing distance normal to the surface, y , until it reaches 99% of the free stream velocity. Beyond the boundary-layer the velocity is constant in both the stream-wise and span-wise directions, and as a result of this, the pressure is impressed into the boundary-layer and it remains constant throughout the boundary-layer.

The development of the boundary-layer is due to the inherent viscosity of the fluid and its formation depends on the characteristic length, l , the flow speed, U , and the viscosity. All of these parameters can be expressed as the Reynolds number

$$Re = \frac{Ul}{\nu} = \frac{\rho Ul}{\mu} \quad (1.2)$$

where ν is the kinematic viscosity of the fluid and ρ is the fluid density.

Depending on the Reynolds number the boundary-layer develops from a laminar state, in which the stream-wise velocity changes uniformly and the local pressure stays constant, into a turbulent state, in which the stream-wise velocity is characterised by unsteady swirling flow and substantial velocity and pressure fluctuations (White and Corfield, 2006); see Figure 1.2.

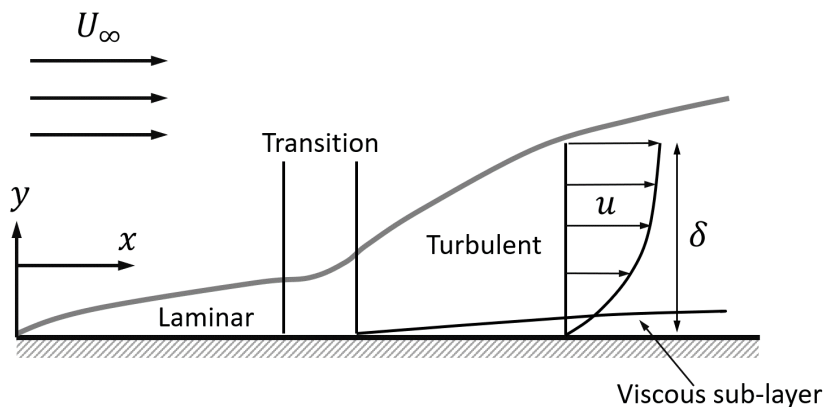


Figure 1.2 Boundary-layer transition from a laminar state into a turbulent state.

1.2 Turbulent boundary-layer

Transition from the laminar to turbulent boundary-layer happens at a certain point in flow downstream at Reynolds number of $Re_x \approx 3.2 \times 10^5$. At this point, a greater rate of mixing of fluid occurs across the boundary, transporting mass and momentum, and the velocity and pressure measurements of the fluid become irregular with higher fluctuations. In other words, the turbulent boundary-layer is characterised by the velocity and pressure fluctuations, where the kinetic energy of the free stream is transmitted based on the Reynolds stresses (Schlichting and Gersten, 2016). This effectively generates a much greater velocity gradient near the wall and additional shearing force due to the Reynolds stress. As a result of the fluctuations, the velocity vector can be decomposed into the mean, \bar{u} , and the fluctuating, u' , components as

$$u = \bar{u} + u' \quad (1.3)$$

As a result of this, the wall-shear stress vector in the turbulent boundary-layer is consisted of both the mean, $\bar{\tau}_w$, and fluctuating, τ_w' , values that can be written as

$$\tau_w = \bar{\tau}_w + \tau_w' \quad (1.4)$$

The mean value of the wall-shear stress is indicative of the overall state of the flow, whilst the fluctuating wall-shear stress provides information on individual processes in the flow that lead to the momentum transfer to the wall. The stream-wise velocity measurements at different locations in the wall normal direction indicates that the turbulent boundary-layer is composed of four regions of viscous sublayer, buffer layer, logarithmic region, and the wake region (Davidson, 2015). These regions are depicted in Figure 1.3. The Friction velocity, u_τ , which relates the wall-shear stress to the velocity close to the wall, is used to to make the stream-wise velocity and the wall-normal distance non-dimensional, which are denoted as U^+ and y^+ , respectively.

$$u_\tau = \sqrt{\frac{\bar{\tau}_w}{\rho}} \quad (1.5)$$

$$U^+ = \frac{U}{u_\tau} \quad (1.6)$$

Wall-shear stress and its importance

$$y^+ = \frac{u_\tau y}{\nu} \quad (1.7)$$

These dimensionless parameters are used to define the turbulent boundary-layer regions. Within the turbulent boundary-layer, the viscosity effect is limited to a layer adjacent to the wall, $y^+ < 5$, that is called the viscous sublayer (Schlichting and Gersten, 2016). In this region the streamwise velocity follows a linear relation with the wall normal distance as (Kline et al., 1967)

$$U^+ = y^+ \quad (1.8)$$

Within the viscous sub-layer, the fluid mixing phenomena does not take place to the extent as in the above regions and as a result of this the fluctuations become negligible and the Reynolds shear stresses diminish. As the wall normal distance increases, the inertial forces dominate over the viscous stresses. Between $60 < y^+ < 200$ is the log-law region in which the stream-wise velocity profile follows a logarithmic relationship. This relationship is termed the law of the wall or Newtonian log-law and it is expressed as (Kline et al., 1967)

$$U^+ = \frac{1}{\kappa} \ln(y^+) + C \quad (1.9)$$

κ and C are the constant that are found to be dependant upon the Reynolds number

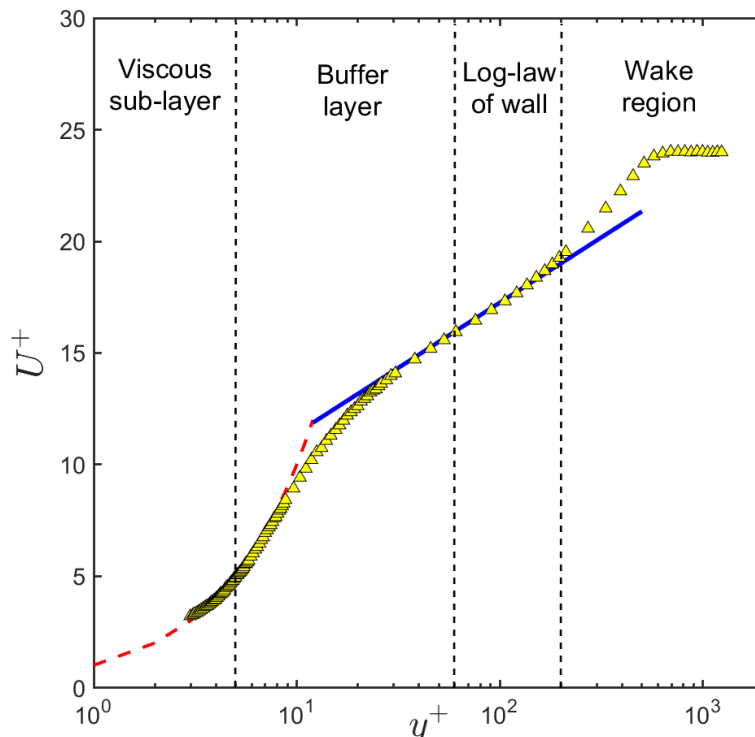


Figure 1.3 Turbulent boundary-layer velocity profile regions.

of the flow. Buffer region forms in between the viscous sub-layer and the log-law region, $5 < y^+ < 60$. Beyond $y^+ > 200$ is defined as the wake region where the large scale flow structures interact with the outer flow.

1.3 Sensors' requirements for turbulence measurements

In order to accurately capture the fluctuations of the turbulent flow and the turbulence spectra, the wall-shear stress sensor should be designed so that it posses adequate spatial and temporal resolution. Hutchins et al. (2009) carried out experimental investigations on hot-wire probes across a large range of Reynolds numbers and with the careful matching of the viscous scale length of the hot-wire, to consider the issue of spatial resolution in the turbulent boundary-layer. This study provided an insight into the scaling requirements for wall-shear stress sensors for turbulence measurement. Based on this empirical study, sensor's length scale, L^+ and time scale, t^+ , are defined for turbulence measurements as

$$L^+ = \frac{Lu_\tau}{\nu} \quad (1.10)$$

and

$$t^+ = \frac{tu_\tau^2}{\nu} \quad (1.11)$$

To obtain reliable measurements within the turbulent boundary-layer, it was empirically determined for the sensors to have a length scale of $L^+ \leq 20$ and a time scale of $t^+ \leq 3$ (Hutchins et al., 2009). Considering these limits and by using Eq 1.10 and Eq 1.11, the length and frequency scales requirements for the wall-shear stress sensors can be expressed as

$$L_{Max} \leq 20 \left(\frac{\nu}{u_\tau} \right) \quad (1.12)$$

and

$$f_{Min} = \frac{1}{t_{Max}} \geq \left(\frac{u_\tau^2}{3\nu} \right) \quad (1.13)$$

To put this in context, for a flow with a friction velocity of $u_\tau = 0.4$ m/s ($U_\infty \approx 10$ m/s) and $\nu = 1.51 \times 10^{-5}$ m²/s the suggested maximum sensing element length would be $L_{Max} \leq 750$ μ m, and the required sensor frequency would be $f_{Min} \geq 3.5$ kHz.

In addition to adequate spatial and temporal resolutions, the wall-shear stress sensors are required to possess other qualities. The sensors must possess high sensitivity to the wall-shear stress to be able to resolve small wall-shear stress values, whilst at the same time their pressure (out of plane) sensitivity should be significantly smaller than their wall-shear stress sensitivity. Moreover, it is required for the sensors to have an appropriate range of operation to provide the opportunity for the flow measurements within a range of Reynolds numbers. Minimal intrusiveness is another requirement for the wall-shear stress sensors. For the sensors to be hydraulically smooth, the structures of the sensors should lay within the viscous sub-layer and hence, the height of the elements on the sensor, such as the sensing element, micro-springs, and electronics, should be smaller than the thickness of the viscous sub-layer, $y^+ = 5$; (Tennekes and Lumley, 2018). The sensors should provide high signal to noise ratio (SNR) and the effect of the environmental parameters such as temperature drifts, humidity and Electro-Magnetic-Interference (EMI) on their performance should be minimal. Additionally, the sensors should be able to measure the directional wall-shear stress, which is important for reversal flows detection.

1.4 What is MEMS?

Micro-Electro-Mechanical-Systems (MEMS) fabrication technologies enable the miniaturisation of wall-shear stress sensors. The word "Micro" in the MEMS means that the size of these devices are normally in the order of 1-1000 μm . The word "Electro" means that these devices have electronic parts. "Mechanical" suggests that these devices normally have moving parts. MEMS technology has been developing rapidly since the 1960's and it has been used to fabricate different types of micro-systems such as micro-sensors, micro-actuators, and micro-structures (Gad-el Hak, 2005). MEMS devices are normally fabricated from silicon, metals, polymers, or a combination of them. However, the physical and chemical properties of silicon, make it the most commonly used material in the MEMS devices fabrication processes.

The micro-scale size and the favourable scaling of the sensors that are fabricated using the MEMS technologies make them suitable for turbulence measurements by

offering the necessary small length scale and high frequency and by satisfying the spatial and temporal resolutions requirement. To compare this with the macro-scale devices, consider two sensors one macro-scale and one micro-scale. If we consider the sensing element length of the macro-scale sensor to be 30 mm and the sensing element length of the micro-scale device to be 30 μm , in this case the characteristic length scale of the micro-scale sensor is 10^{-3} of the macro-scale sensor. Moreover, since the devices can be fabricated using the bulk micro-machining processes, any misalignment on the sensors would be minimal. In addition, the miniaturised size of the gaps around the sensor's structure, alongside with the small height of the elements ensure that the devices are hydraulically smooth. Developing wall-shear stress sensors using the MEMS technologies require very little material for fabrication. This results in using less resources and hence, make them less expensive compared to the macro-scale wall-shear stress sensors. Furthermore, most of the MEMS devices are fabricated using batch processes, where large number of devices are manufactured using a single operation, which further reduces the total cost (Adams and Layton, 2014).

1.5 Research Aim and Objectives

The aim of this study is to design, develop, and characterise a range of sensitive optical floating element-based wall-shear stress sensors using MEMS technologies that provides the capability of direct, time-resolved measurements of turbulent boundary-layer flows.

The objectives of this research are

- To design sensitive optical MEMS sensors for instantaneous wall-shear stress measurements using different micro-spring types.
- To design and develop the optical transduction alongside with the opto-electronics for the sensor control unit.
- To design the micro-fabrication process for the MEMS sensors fabrication and characterise the fabricated devices.

- To design and develop the sensor packaging with the aim to provide the potential for the sensors to be flush-mounted on the wall.
- To develop test rigs for characterisation of the MEMS sensors.
- To calibrate the MEMS wall-shear stress sensors and characterise their dynamic performance.
- Deploy and install the MEMS sensors to wall-bounded turbulent flow within a wind tunnel for the turbulence measurements.
- Conduct LDV and hot-wire anemometry fluid flow measurements alongside with the MEMS wall-shear stress sensors to verify and compare their performances within the turbulent flow.

1.6 Thesis outline

Chapter 2 provides a review on the wall-shear stress measurement methods. The categories of these measurement techniques are discussed based on their size and transduction. § 2.1 introduces the conventional measurements methods including Pitot tubes, Preston tubes, Stanton tubes, and thin-oil-film interferometry. § 2.2 introduces the MEMS-based measurement methods. In § 2.2.1 MEMS-based indirect measurements are discussed. This includes thermal sensors, surface fences, micro-pillars, and indirect optical methods. This is followed by an introduction on the MEMS-based direct measurements methods in § 2.2.2. Here, the sensors based on the floating element method are discussed and an overview on their transduction methods such as capacitive, piezoresistive, and optical methods are provided. A summary on the merits and drawbacks of all these methods are presented in § 2.3.

Chapter 3 provides the details on the MEMS devices modelling and development. In § 3.1 mechanical design and modelling of the sensors' structure is provided. Details on the design of two micro-spring types and their stiffness/sensitivity governing equations are provided in § 3.1.1 and § 3.1.2. Finite Element Analysis is performed to verify the analytical models. The result of the mechanical designs using both analytical and Finite Element Analysis are presented in § 3.1.5. Details of the MEMS sensors optoelectronics

are outlined in § 3.2. This includes the theory behind the Moiré fringe pattern design in § 3.2.1, followed the details of the sensor's detection technique in § 3.2.2. § 3.2.3 and § 3.2.4 outline the details of the electronics circuit design of the sensor's control unit. Design of the optical part of the sensor control unit is presented in § 3.2.5 and § 3.2.6. Test-beds are developed as a proof of concept for the sensor's transduction. The test-beds details and the preliminary results from the proof of concept experiments are discussed in § 3.2.7 to § 3.3.2.

Chapter 4 outlines the microfabrication and packaging of the MEMS wall-shear stress sensors. § 4.1 discussed the microfabrication process steps that are involved in the devices' development. § 4.2 provides the details of the inspection and meteorology of the fabricated devices. In § 4.3, the sensors' packaging are discussed. In Chapter 5 the experimental setup used for the sensors characterisation are outlined. In § 5.1 the detail of the laminar flow cell, which is used for the sensors' calibration is presented, followed by the details of the sensors' calibration experimental setup in § 5.1.1. § 5.2 discusses the dynamic characterisation experimental setup to quantify the resonant frequency of the sensors. The details of the wind tunnel setup, hot-wire anemometry setup, and the laser Doppler velocimetry setup are provided in § 5.3, § 5.4, and § 5.5, respectively.

In chapter 6, the characterisation of the MEMS sensors are presented. The devices' calibration and the corresponding results are presented in § 6.1. Here the calibration data processing procedure, calibration curves, and the uncertainty analysis are provided. The discussion on the dynamic performance characterisation and the corresponding results are presented in § 6.2.

The details of the turbulent boundary-layer measurements using the MEMS wall-shear stress sensors are presented in Chapter 7. The canonical turbulent boundary-layer data measurements using the hot-wire anemometry and LDV are discussed in § 7.1 and 7.2, respectively. The details and discussion of the instantaneous wall-shear stress within the turbulent boundary-layer flow that is measured simultaneously by the MEMS sensors and by either the hot-wire anemometry are presented in § 7.1.2 and § 7.2.2.

In chapter 8, the conclusions that have been documented throughout the thesis are presented, along with the recommendations for future investigations.

Chapter 2

A Review on Wall-Shear Stress

Measurement Methods

This chapter provides an overview of the wall-shear stress measurement methods with the focus on the MEMS based wall-shear stress sensors. Different measurement methods and sensor transduction techniques are introduced and their limitations, novelities, and performances are discussed. Importance of the quantitative and qualitative measurement of the skin-friction drag, has motivated many researchers to develop significant methods and different types of sensors to quantify the wall-shear stress. Most of this research was focused on miniaturizing the wall-shear stress sensors and detecting the fluctuating wall-shear stress (Naughton and Sheplak, 2002).

Haritonidis, Joseph II. (1988) classified the available techniques for the wall-shear stress measurements as shown in Figure 2.1. Depending upon whether the sensor infers the wall-shear stress from other flow properties or quantifies it directly, the wall-shear stress measurement methods are classified into indirect and direct categories (Haritonidis, Joseph II. , 1988; Löfdahl and Gad-el Hak, 1999*b*). From the size of the sensing element point of view, existing wall-shear stress measurement devices can be classified as either macro-scale (conventional), where the sensing element size is normally $> 1000 \mu\text{m}$ or micro-machined sensors, in which the sensing element size is $< 1000 \mu\text{m}$.

Since mid-1950s, the development of the skin-friction measurement methods were directed toward using smaller sensors, leading to an enhanced accuracy and resolution (Löfdahl and Gad-el Hak, 1999*a*), which is discussed in the following sections

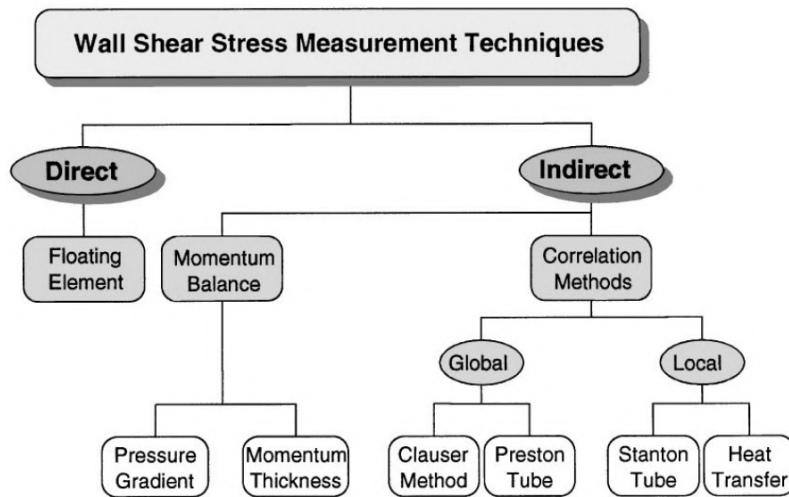


Figure 2.1 Wall-shear stress measurement methods classification. Taken from (Löfdahl and Gad-el Hak, 1999a)

2.1 Readily-available methods

A comprehensive review on the conventional techniques presented by Haritonidis (Haritonidis, Joseph II. , 1988; Löfdahl and Gad-el Hak, 1999b) and Winter (1979). The main problem with the conventional macro-scale sensors is the limit on the minimum achievable size using conventional macro-machining techniques. From the experimental fluid dynamics point of view, smaller sensing elements are required for the higher spatial and temporal resolution measurements. Due to the larger area, macro-scale sensors can measure small forces. However the spatial resolution of these devices is not sufficient to satisfy the turbulence measurement requirements. This is a tradeoff between the sensor's spatial resolution and the minimum detectable force (Winter, 1979). Moreover, the larger size of these devices results in measurement errors that are associated with misalignment and larger size of the gaps in the devices. The effect of pressure gradient and measurement errors associated with it is also not negligible. In addition, the cross-axis sensitivity to acceleration, vibration, and thermal expansion effects, affect the performance of the devices. The main examples for the conventional macro-scale methods include the Pitot tube, Preston tubes, Stanton tubes, and oil film interferometry.

Pitot tubes are facing the fluid flow and the wall-shear stress, τ_w , is then quantified by the dynamic pressure, ΔP , measurements by the tube as (Winter, 1979):

$$\frac{\Delta P}{\tau_w} = f_{PC} \left(\frac{U_\infty D}{\nu} \right) \quad (2.1)$$

Here f_{PC} , U_∞ , D , and ν are the calibration function, free-stream velocity, the diameter of the Pitot tube, and the kinematic viscosity respectively. Although the Pitot tubes are easy to implement, the head of the tubes protrude into the fluid flow and hence, they cause flow disruption. Moreover, any variation of the flow can potentially result in producing different calibration results, making the Pitot tubes to be reliable method only in smooth boundaries. Furthermore, there are challenges due to the spatial and time-averaged measurement due to the temporal resolutions and errors due to misalignment. Both Preston and Stanton tubes developed based on the Pitot tube. Preston tube is based on a simple Pitot tube that is implemented on the wall and measure the flow's velocity at a known distance from the wall (Ackerman et al., 1994; Preston, 1954). The velocity profile for the Preston tube extends into the logarithmic region of the boundary layer and therefore can cause flow disturbances. The Stanton tube was developed to investigate the laminar sub-layer of the turbulent flow (Stanton et al., 1920).

Another conventional technique of wall-shear stress measurement which became widespread after 1980's is the use of thin-oil-film interferometry (Driver, 2003; Monson, 1983; Tanner and Blows, 1976). This technique is based on the behaviour of a thin-oil-film under applied shear stress that arises from the flow over the oil film (Naughton et al., 2003). The thinning rate in the oil film is a function of the magnitude of the applied shear stress. The motion of the thin-oil-film is sensitive to the shear stress, gravity, surface curvature of the oil film, and the pressure gradient. However, in most cases the shear stress is the dominant factor (Tanner and Blows, 1976). Here, the surface is covered with a thin-oil-film and then exposed to the flow. As flow passes over the surface, the oil-film thickness reduces. The oil-film thickness is then measured via interferometry to measure the thinning rate of the oil. Measuring the oil-film thickness over time provides the local skin-friction values using the thin-oil-film equation (Squire, 1961). Some other implementation of the thin-oil-film technique, which were developed upon the the method developed by Tanner et al (Tanner and Blows, 1976; Tanner, 1977; Tanner and Kulkarni, 1976), are laser interferometry skin-friction (LISF), expanded laser beam interferometry skin-friction technique, fringe imaging skin-friction (FISF), global

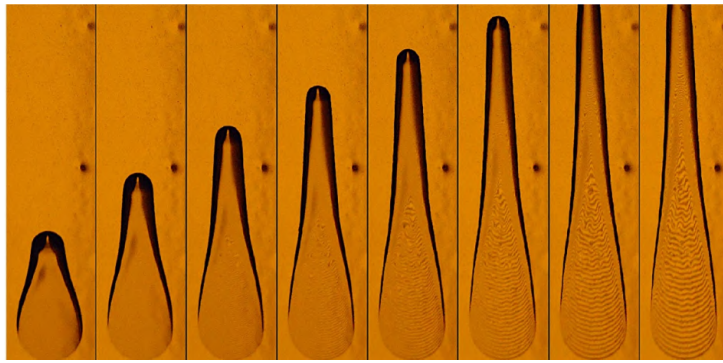


Figure 2.2 Development of an oil film under the flow during a time period. The flow direction is from bottom to top a Taken from (Örlü and Vinuesa, 2020)

imaging skin-friction (GISF), and surface imaging skin-friction (SISF) techniques (Driver, 1998; Settles, 1986; Zilliac, 1996).

Thin-oil-film techniques provide a broad two or three dimensional region of the skin friction with an improved spatial resolution, however to use these techniques, the model surface must be reflective, and hence these techniques are not applicable to rough surfaces. For many applications, the optical access and the setup is a challenge. Moreover, the temporal resolution for this techniques are poor, as thin-oil-film techniques demand an amount of time to capture the data and process the data. The model should be photographed over a longer period of time and after a time consuming data processing, only the mean value of the wall-shear stress is obtained.

Among the conventional macro-scale measurement technologies, none can be considered accurate. This can be observed in techniques such as oil-film interferometry and wall pulsed wires (Castro and Dianat, 1990), where the uncertainties in the mean wall-shear stress measurement reported to be at least 4% for incompressible flows (Fernholz et al., 1996).

2.2 MEMS-based measurement methods

Advancements in super-miniature engineering using MEMS technologies provides the potential to develop devices and sensors having performance that sufficiently exceeds conventional measurements techniques. The miniature size of these systems provide the potential to overcome the limits associated with macro-scale devices, and offers a favorable spatial and temporal resolutions for turbulence measurements. During the past

two decades many techniques have emerged using MEMS technologies for wall-shear stress measurements. MEMS wall-shear stress measurement methods are generally classified into two distinct categories of indirect and direct techniques. The former measures other flow quantities, to extract the value of the wall-shear stress, whereas direct MEMS wall-shear stress sensors respond to the momentum transfer at the wall and measure the displacement of a flush-mounted movable floating element structure due to the applied wall-shear stress (Naughton and Sheplak, 2002).

An overview of the developed MEMS-based sensors using both indirect and direct techniques, their advantages and drawbacks are presented in the following sections.

2.2.1 Indirect measurements

As mentioned above, indirect sensors measure other quantities of the flow such as heat transfer, pressure drop, and velocity profile, to infer the value of the wall-shear stress via empirical correlations. The empirical correlation is typically valid for specific conditions and a prior knowledge of the testing environment (such as Doppler shift for optical sensors and Joulean heating rate for thermal sensors) and hence, extra measurements are required (Sheplak et al., 2004). Various MEMS-based sensors with indirect transduction schemes, such as heat transfer, surface micro-fences, and near-wall velocity gradients were developed in the recent years, which are described in the following section.

2.2.1.1 Thermal sensors

The working principle of the thermal sensors is based on various mechanisms of heat transfer between the sensor and the flow. Elwenspoek (1999) and Kuo et al. (2012) classified the thermal sensors into three categories: (a) anemometric sensors, (b) calorimetric sensors, (c) time of flight sensors.

The operating principle of the anemometric thermal wall-shear stress sensors such as Hot-wire sensors (Chew et al., 1998; Comte-Bellot, 1976; Khoo et al., 1998) and Hot-film sensors (Bellhouse and Schultz, 1968; Brison et al., 1979) is based on the converting convective heat transfer rate inside the flow into a voltage output. These types of sensors consist of a small sensing element (a resistive wire sensor element

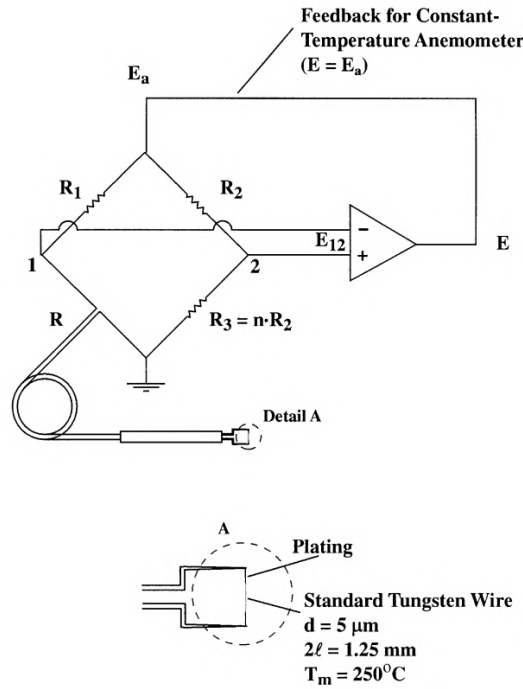


Figure 2.3 A schematics of a hot-wire thermal sensor. The sensing element forms one arm of the Wheatstone bridge. From (Fingerson and Freymuth, 1977)

for hot-wire probes and a thin film resistive sensor for hot-film probes) with desirable temperature resistance characteristics. This small sensing element forms one arm in a associated Wheatstone bridge (Fingerson and Freymuth, 1977) as depicted in Figure 2.3. The sensing element is heated up to a constant temperature, T_s , greater than the fluid flow’s temperature, T_∞ , as a result of a constant current that passes through the sensing element. The heating of the sensing element produces a thermal boundary layer inside the velocity boundary layer of the flow; see Figure 2.4. The increase in the heat transfer rate from the sensing element to the flow results in the sensor cooling, and hence decrease the sensor’s resistance, R .

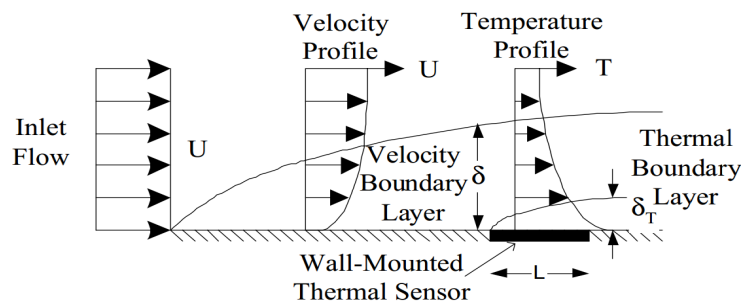


Figure 2.4 A schematic of a thermal wall-shear stress sensor. The heating of the sensing element produces a thermal boundary layer, δ_T , inside the velocity boundary layer of the flow, δ . From (Naughton and Sheplak, 2002)

The resistance change with temperature can be expressed as (Perry, 1982)

$$R = R_r [1 + \alpha(T_s - T_r)] \quad (2.2)$$

where R_r is the resistance at the reference temperature T_r , and α is the temperature coefficient of resistance.

Although conventional Hot-wire and Hot-film probes were used earlier than the MEMS technologies development, utilising the MEMS technologies to develop miniature thermal sensors increases the measurements accuracy and reduces flow disruptions (Van Oudheusden, 1992).

A two component hot-film sensor was developed by Sumer et al. (1993) to measure the instantaneous wall-shear stress in time-dependant flows where the flow reversals occur in a periodic manner. Two components of the sensor were two hot-film elements that were designed to be at 90° to each other, enabling the wall-shear stress vector measurements. Development and applications of a surface hot-wire were presented by Sturzebecher et al. (2001). This sensor was a flush-mounted thermal resistive wire with as small slot underneath.

Many of the MEMS thermal wall-shear stress sensors emerged based on the sensor design that was developed by Huang et al. (1995) and Huang et al. (1996) for gaseous flow measurements. Here the sensing element is patterned on a diaphragm (normally silicon-nitride) that is formed at the top of a vacuum cavity. Utilising the vacuum cavity in this configuration, minimises the heat conduction from the diaphragm to the substrate and provides an effective thermal isolation between the sensing element and the substrate. Liu et al. (1999) and Xu et al. (2005) developed a micro hot-film shear stress sensor using surface micromachining as a continuation of a work by Huang et al. (1996). The sensor consisted of a suspended silicon-nitride diaphragm patterned at the top of a vacuum-sealed cavity. The sensing element of this sensor was 20 to 200 μm long, 2 and 0.45 μm thick and was made of phosphorous-doped poly-silicon material.

Using the vacuum-cavity insulation, Xu et al. (2002) developed a micro-machined, thermal shear stress sensor with the focus on underwater applications, by means of a 2 μm Chemical vapor deposited Parylene waterproof coating.

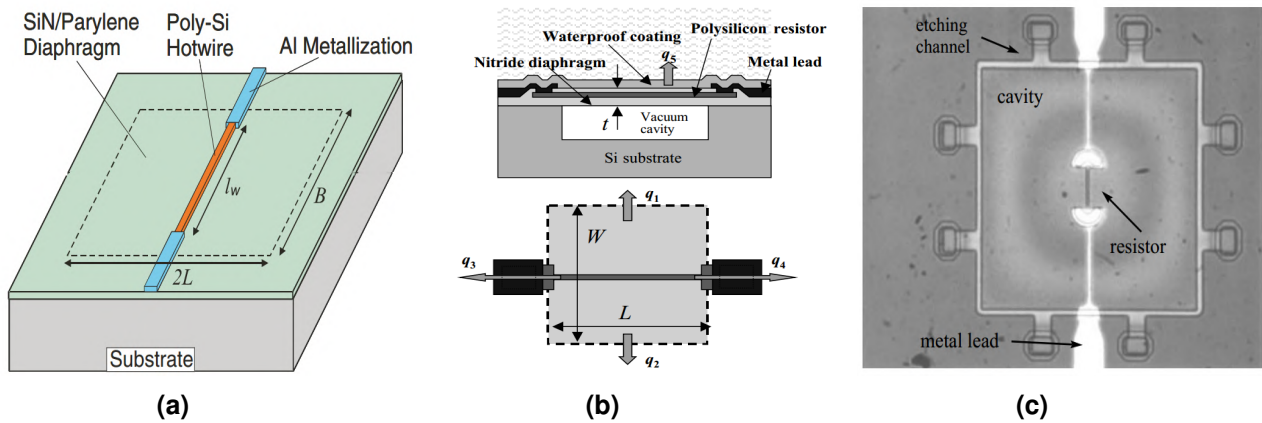


Figure 2.5 (a) Schematic of a MEMS thermal shear stress sensor developed by Lin et al. (2004), (b) Schematics view of the sensor developed by Xu et al. (2002), (c) The sensor developed by Liu et al. (1999)

Diaphragms with various width were fabricated to compare the performance of the sensor and effect of its width on the sensor performance. It was reported that the sensor with larger diaphragm has higher sensitivity and the average shear stress sensitivity were reported to be between 0.31 V/Pa and 1.1 V/Pa.

Lin et al. (2004) carried out an experimental investigation on the thermal MEMS wall-shear stress sensors with a focus on the sensor with a similar structure as the sensors developed by Huang et al. (1996) and Liu et al. (1999). The experimental results revealed that classical theories that are developed for conventional hot-wire and hot-film probes, which states that the net power of the hot-wire probe is proportional to the 1/3-power of shear stress are not valid for the MEMS thermal wall-shear stress sensors due to the lack of a thin thermal boundary layer at their surfaces. Instead, this study predicted that the net power of the MEMS hot-wire is proportional to the 0.67th and 0.85th powers of the wall-shear stress for two types of sensing elements with different materials. Considering this, Ou et al. (2016) developed a MEMS thermal wall-shear stress sensor by combining the substrate free structures with a glass substrate using anodic bonding technology. Here, the Silicon substrate was removed using an isotropic wet etching process to provide the cavity between the silicon substrate and the glass substrate, as depicted in Figure 2.6a. The increased depth of the vacuum cavity in this sensor results in an improved sensitivity compared with the sensors developed based on a sacrificial layer technique. The 525 μm deep vacuum cavity in this sensor resulted in a sensitivity of 184.5 mV/Pa. This study also demonstrated that the power is proportional

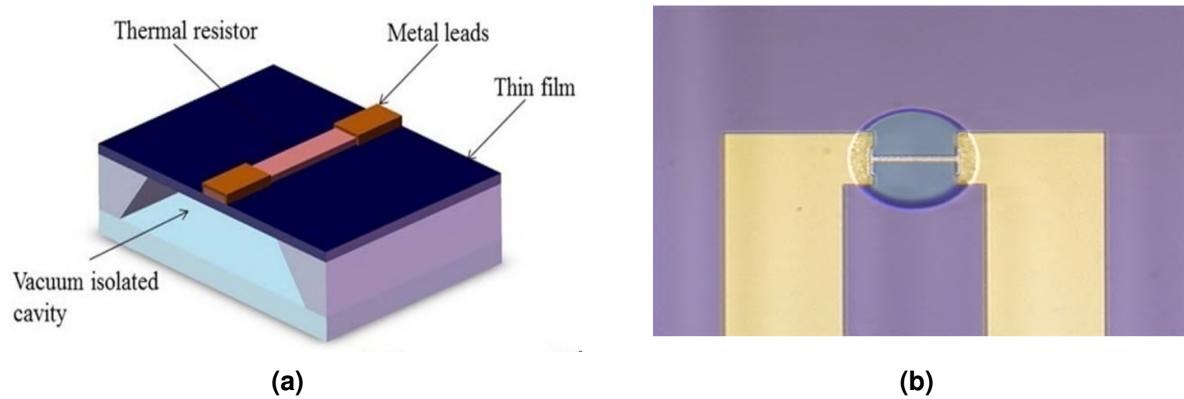


Figure 2.6 (a) 3D view of the thermal sensor developed by Ou et al. (2016). (b) An image of a wall-shear stress sensor developed by Breuer et al. (1999). The coloured circle is the silicon-nitride membrane over the vacuum cavity.

to the 1/3-power of the applied wall-shear stress as in case of the conventional thermal sensors, which is in a contradiction to the results provided by Lin et al. (2004).

An extensive characterisation of an uncompensated, silicon micro-machined thermal wall-shear stress sensor, was carried out by Sheplak et al. (2002). The sensor design and fabrication was similar to the sensors developed by Breuer et al. (1999) and Breuer (2000) as illustrated in Figure 2.6b. The sensing element of the sensor was fabricated by patterning a thin-film platinum at the top of a silicon-nitride membrane, and a vacuum cavity was fabricated for thermal isolation purposes. The sensor characterisation reported a sensitivity of 11 mV/Pa and a minimum detectable wall-shear stress of 9 μ Pa. This investigation also addressed the sensor sensitivity to ambient temperature variations.

Haneef et al. (2007) developed a silicon on insulator (SOI) complementary metal oxide semiconductor (CMOS) thermal MEMS wall-shear stress sensor. The CMOS-based aluminum metallization was utilised to fabricate the sensing element with an active area of 130 μ m \times 130 μ m located at the center of a 500 μ m \times 500 μ m silicon oxide membrane for thermal isolation as shown in Figure 2.7a. Using aluminium as the sensing element material reduces the piezoresistivity induced pressure sensitivity of the device. The characterisation result of this sensor showed a sensor sensitivity of 22 mV/Pa in a wall-shear stress range of 0-1.5 Pa. Buder et al. (2008) developed a polyimide-based MEMS double hot-wire sensor with two resistors in a close proximity of 200 μ m; see Figure 2.7b. The experimental investigations in this study showed this type of sensor is capable of the wall-shear stress measurement as well as flow direction

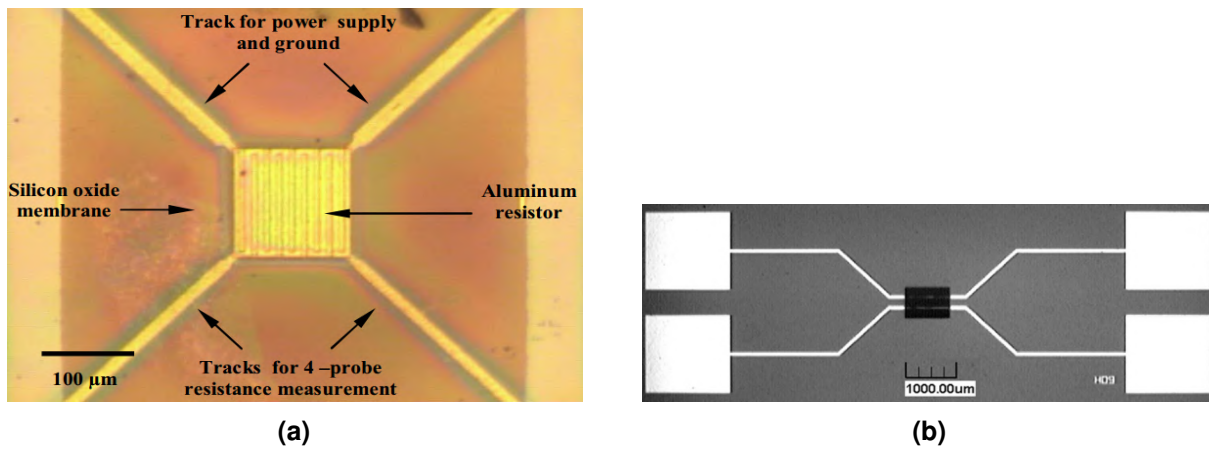


Figure 2.7 (a) An image of a wall-shear stress sensor developed by Haneef et al. (2007). The aluminium sensing element is located at the center of a silicon oxide membrane. (b) An image of MEMS wall double hot-wire developed by Buder et al. (2008).

detection. Xiang et al. (2010) have simplified the design and fabrication process of the thermal sensors by utilising a polysilicon bridge on a silicon substrate rather than the silicon-nitride diaphragm. Moreover, the sensor sensitivity increased as the bridge is fully exposed to the flow. Ghouila-Houri et al. (2016) and Ghouila-Houri et al. (2020) have reported the development and experimental investigation of a anemometric thermal wall-shear stress sensor, operating in both constant current mode and constant temperature mode, which is also sensitive to the flow direction for the separation detection, which can be seen in Figure 2.8. The authors used the sensor design presented by Romain et al. (2013) and Viard et al. (2013), which is a compromise between the robust but slow and power consuming hot-films and the fast and sensitive but fragile characteristics of hot-wire as the sensor consists of four 1mm long and 3 μm wide hot-wires suspended by periodic 7 μm wide and 600 nm high silicon oxide bridges to support the hot-wire structure, over a cavity to allow efficient thermal insulation.

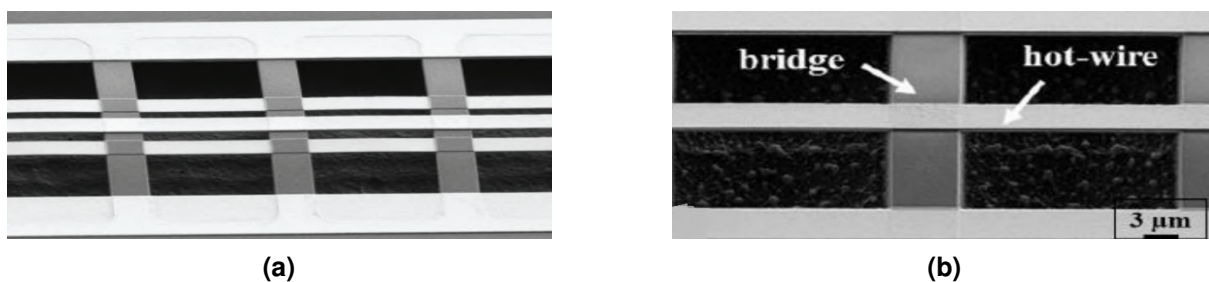


Figure 2.8 (a) SEM image of the hot-wire sensor suspended by a silicon oxide bridges. Taken from (Ghouila-Houri et al., 2016). (b) SEM image of the hot-wire micro sensor fabricated by Ghouila-Houri et al. (2020).

Shown in Figure 2.9a is a novel type of hot-wire micro-sensors that were developed by Löfdahl et al. (2003) for the measurements of the near wall region instantaneous velocity gradient. Hot-wires were positioned in the range of $50\ \mu\text{m}$ to $250\ \mu\text{m}$. The sensor tests have concluded that computational estimates as well as experimental results showed that this arrangement of the micro hot-wire sensor can be a valuable tool for the study of the fluid flow near the wall region.

A nano-wire based thermal anemometry probe was emerged by Bailey et al. (2010) and Hultmark et al. (2012) for the velocity fluctuations measurement. Shown in Figure 2.9b is the sensing element structure consists of a free standing nano-wire of $60\ \mu\text{m} \times 2\ \mu\text{m} \times 100\ \text{nm}$, which is smaller than the commercially available hot-wires, and it is suspended between two pads. The operating characteristics of this sensor are similar to the conventional hot-wire probes, and the difference is the enhanced spatial resolution due to smaller size, enabling the measurements in higher Reynolds number flows (as high as 1.2×10^6). In a similar work, Zhao et al. (2012) have designed specific structures of non-scale ($260\text{nm} \times 3.36\ \mu\text{m} \times 460\ \mu\text{m}$) hot-wire sensors, made of Platinum to obtain velocity components and their gradients, which allows the wall-shear stress calculation; see Figure 2.10a. A micro hot-film multi-array (typically five arrays) probe was manufactured and tested by Borisenkov et al. (2015) for turbulence measurement with sub-Kolmogorov resolution. The overall scale of the sensor is approximately $500\ \mu\text{m}$, as shown in Figure 2.10b, which is six times smaller than the similar type of sensors used in the experiments (Gulitski et al., 2007a,b). Similar to its larger multi-array hot-

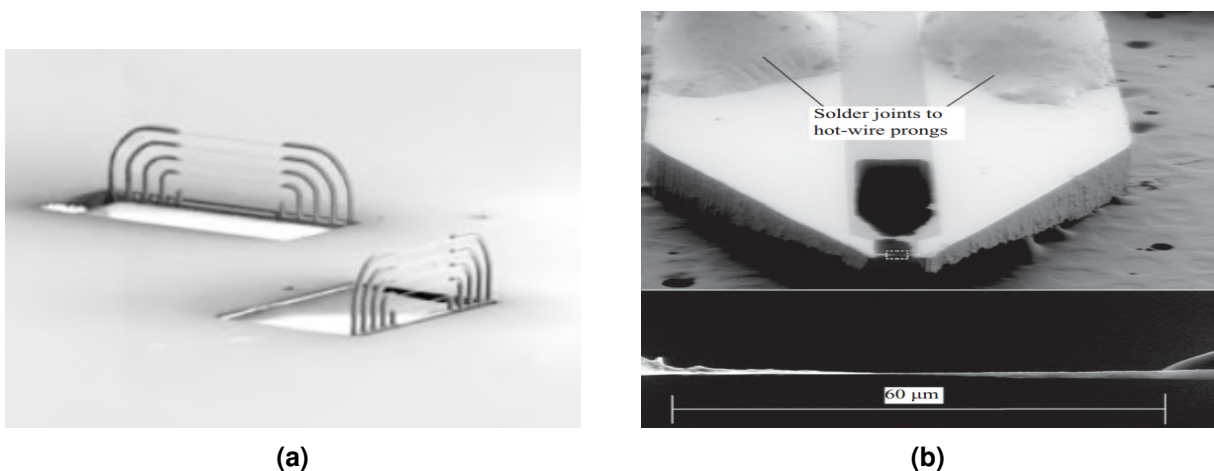


Figure 2.9 (a) A SEM image of two five-wire micro-sensors developed by Löfdahl et al. (2003). (b) SEM images of the nano-wire based thermal wall-shear stress sensor developed by Bailey et al. (2010).

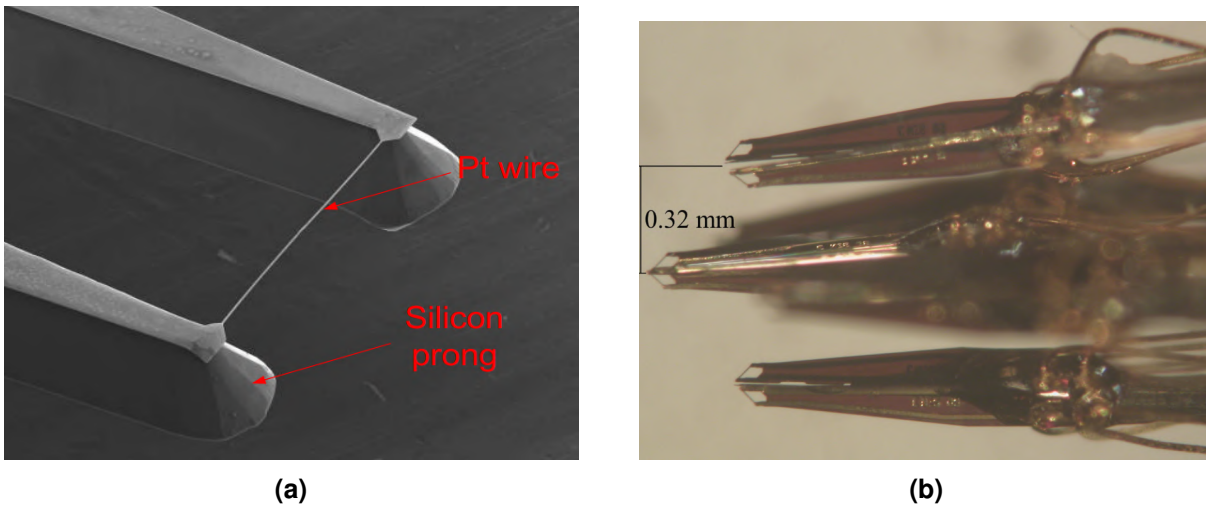


Figure 2.10 (a) A SEM image of two five-wire micro-sensors developed by Löfdahl et al. (2003). (b) Top view of the tip of a multi-array micro hot-film sensor. Taken from (Borisov et al., 2015)

wire counter parts, this multi-array probe consists of four hot-film sensors, enabling the measurements, along with all three components of the velocity fluctuations, also all nine components of the velocity gradients tensor.

Ito et al. (2010) have presented a sub-micro-scale flow sensor with a suspended Platinum hot-film that is 40 nm thick, 800 nm wide, and 6 μm long, and carbon nanotube (CNT) fins, as shown in Figure 2.11. The experimental tests of this device showed that the suspending hot-film probe in this configuration improves the thermal insulation as there is no heat loss with the surrounding substrate and utilising the CNT fins improves the heat transfer to the flow. The performance of this device was tested in a 8mm long micro-channel and the sensor was not implemented to a macroscopic turbulence channel flows or boundary layer flows. No data for the sensor performance was reported.

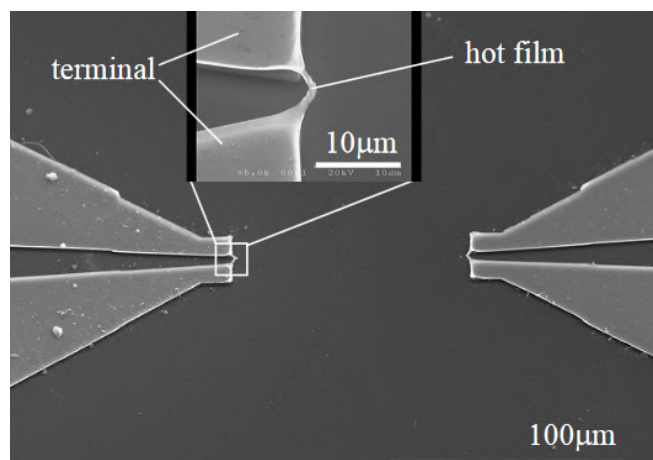


Figure 2.11 A SEM image of the sensor with suspended hot-film and CNT fins presented by Ito et al. (2010).

Calorimetric thermal sensors use at least one thermal sensor upstream or downstream of the heating element to detect the asymmetry of the temperature profile generated around the element due to the fluid flow (Chew et al., 1998; Khoo et al., 1998). Unlike anemometric thermal wall-shear stress sensors, the calorimetric thermal sensors are able to measure the direction of the wall-shear stress. However, the output of these types of sensors is non monotonic, implying that their performance range is limited as discussed by Elwenspoek et al. (2001) and Weiss et al. (2017)

Continuing the idea presented by Haneef et al. (2007), De Luca et al. (2015) developed a single thermopile calorimetric SOI CMOS MEMS thermal wall-shear stress sensor. A double thermopile configuration was also integrated to the sensor to allow the comparison of the performance with the single thermopile configuration. Shown in Figure 2.12 is the sensor structure, which comprises of a $400\ \mu\text{m}$ long and $2\ \mu\text{m}$ wide tungsten hot-wire and three silicon based thermopiles, patterned over a silicon oxide membrane. The sensor sensitivity reported to be $4\ \text{V}/\text{Pa}$ for lower values of wall-shear stresses (less than $0.1\ \text{Pa}$) and then it drops under $100\ \text{mV}/\text{Pa}$ for the wall-shear stress value of $0.5\ \text{Pa}$, which is due to the strongly nonlinear output of the sensor. Moreover, the authors reported that using the novel single thermopile configuration improves the signal to noise ratio, compared to the double thermopile configuration. As it can be seen in Figure 2.12b, the sensor packaging requires further modifications and development.

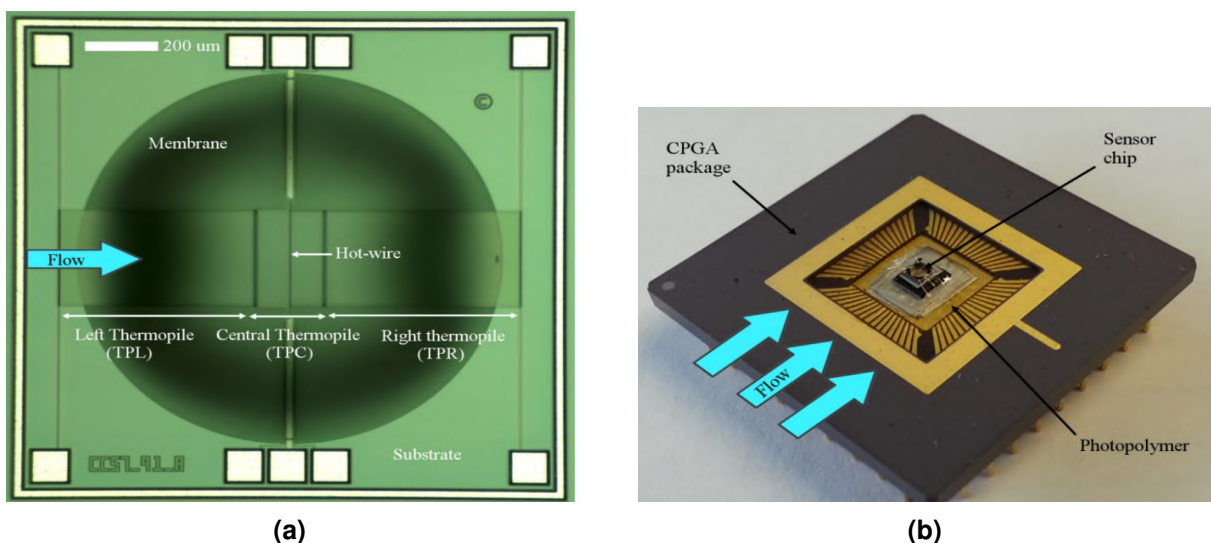


Figure 2.12 (a) An image of the calometric thermal wall-shear stress sensor, (b) A photo of the device wire bonded and mounted on a CPGA package. Taken from (De Luca et al., 2015).

Weiss et al. (2016, 2017) presented the operation principle of a MEMS calorimetric thermal wall-shear stress sensor based on the thermal wake generated by a heated beam over a cavity, followed by their static and dynamic characterisation (Weiss et al., 2017b). This sensor was composed of three beams suspended over a cavity as it is illustrated in Figure 2.13. The central beam is the heater and the beams on its sides are the upstream and downstream detectors. The heater beam heats up the flow and generates a heat wake which travels toward the downstream detector. The difference between the resistance of the upstream and downstream detectors provide the value of the cooling velocity and hence the wall-shear stress values. The sensor's characterisation have shown a 1% repeatability error and a cut-off frequency of 800 Hz for an average wall-shear stress of $\tau_w=1$ Pa. This value for the cut-off frequency in the thermal sensor needs to be further improved for the turbulence measurement applications and hence, this design requires supplementary modifications. Furthermore, the size of the cavity around the sensing beams could result in complicated recirculation pattern and, hence, the cavity size needs to be redesigned with a compromise between the flow disruption and thermal insulation.

The advent of carbon nanotube (CNT) sensing element in thermal sensors started a broad interest for the micro/nano scale wall-shear stress sensor development. Using the CNT as the the sensing element can significantly enhance the spatial resolution of the device due to a reduced size of 1-5 μm in length and 1-10 nm in diameter for single-walled nanotubes, and 10-50 nm in diameter for multi-walled carbon nanotubes

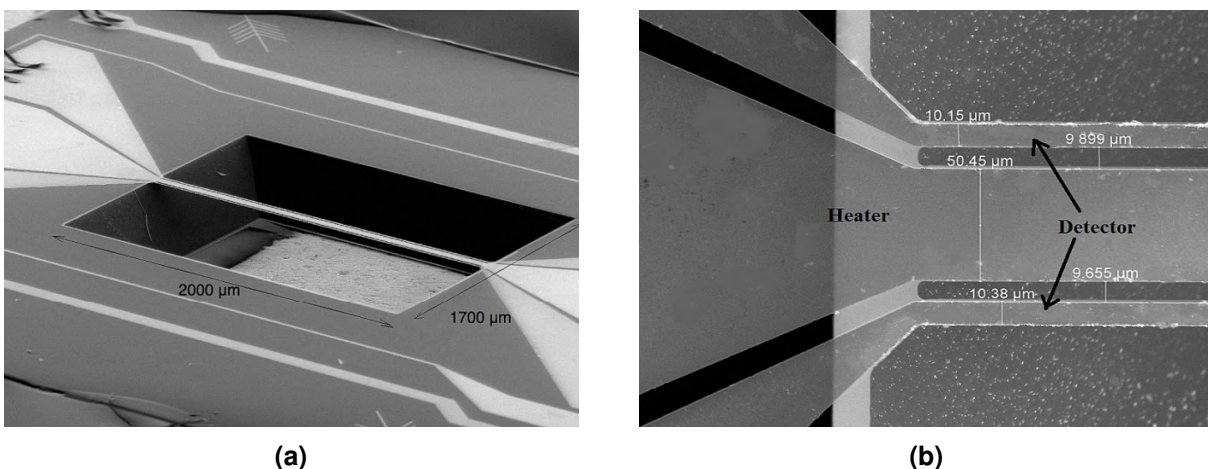


Figure 2.13 SEM images of the calorimetric thermal sensor developed by Weiss et al. (2017). (a) The beams are suspended over a cavity. (b) Three beams configuration where the central beam is the heater and the beams on its sides are the detectors.

(Tung et al., 2007a). Moreover, the electrical properties of the CNT make them suitable to be integrated with the electrical circuits (Sinha et al., 2006). Wong and Li (2003) developed a technique to form post-growth multi-walled carbon nanotube across gold micro-electrodes using AC electrophoresis to build up a resistive element with the aim to use it as the sensing element in the micro/nano thermal wall-shear stress sensors. The frequency of the devices utilising this multi-walled carbon nanotube was estimated to exceed 100 kHz in constant current operation mode. Tung et al. (2007b) reported the development of a thermal shear stress sensor using multi-walled carbon nanotubes as the sensing element. The sensing element was generated by randomly aligning the nanotubes into a conductive trace of 360 μm long and 90 μm wide between two micro-electrodes. Laminar micro-channel test of this device suggested that the multi-walled carbon nanotube based sensor is more applicable for testing in environments where a small thermal mass is required, and hence, the CNT sensor has not been tested in turbulent flows. Considering this, Bai et al. (2010) developed a CNT based wall-shear stress sensor using the single-walled carbon nanotubes bundles as the sensing element, with the aim to conduct measurements in turbulent flows. The sensitivity of the sensor reported to be in the order of mV/Pa (10-100 mV/pa) for low wall-shear stress values ($\tau_w < 1$ Pa). Observation of the results showed that there is a data scattering in the curves for the sensing elements when the input voltage was high (around 4 V). This can be explained due to the thermal expansion related to the self-heating in the element at large input voltage. The thermal expansion results in bundles dislocation from the electrodes due to the difference in the thermal expansion coefficients.

Thermal based wall-shear stress sensors are effective in measuring both the mean and fluctuating wall-shear stress values simultaneously. However, they possess some limitations. One of the very first limitations of these sensors is their dependency on the thermal properties of the fluid, and as a result of this, the fluid used in the measurement environment should be the same as the fluid used in the calibration and characterisation of these devices. A common challenge in using the thermal based devices is their calibration against a known mean value and to keep the calibration drift to a minimum (Agrawal et al., 2019), making it onerous to get a unique calibration curve to relate the heat transfer to the wall shear stress. Another limitation of these sensors is the contribution of any heat transfer and temperature variations to the measurement errors.

It is well-known that the mean/reference temperature drift result in measurement errors in thermal sensors. In addition to the temperature drifts, the heat transfer from the sensing element to the substrate (normally in hot-film based sensors) influences the sensor performance. This frequency-dependant conductive heat transfer into the substrate reduces the sensor's sensitivity and introduces complications into the sensor dynamic response (Naughton and Sheplak, 2002). Heat transfer to the substrate is not the only problem, as the heat transfer to the flow also can contribute in flow perturbations, which can result in additional 5% errors (Sheplak et al., 2002). Thermal sensors are not intrinsically sensitive to the flow direction as well. To put this in context, the instantaneous reverse flow is a known near-wall phenomena (Lenaers et al., 2012), where detecting these events is important in wall-bounded turbulence studies. Due to the directional insensitivity of the thermal wall-shear stress sensors, it is not possible to measure the reverse flow events or in another words the thermal sensors are not able to detect $\tau_w < 0$ (Örlü and Vinuesa, 2020).

2.2.1.2 Surface fences and micro-pillars

Another type of indirect wall-shear stress measurement technique is to use surface fence sensors and micro-pillars. Classical surface fences have a blade that protrudes into the viscous sub-layer, $y^+ < 5$, and the fluid flow generates a pressure difference on either side of the blade, which is proportional to the wall-shear stress (Higuchi, 1983, 1985; Patel, 1965). The measurement of the pressure gradient using a manometer provides an indirect bidirectional quantification of the wall-shear stress. However, this technique suffers from poor sensitivity and a long response time. To overcome these limitations, Von Papen et al. (2002) developed an alternative miniaturized MEMS-based fence to identify the pressure gradient by measuring the deflection of a flexible silicon fence. The deflection of the silicon fence was measured by integrating four piezoresistors connected to a Wheatstone bridge. Fluid flow induces a bending stress in the fence and these piezoresistors are implemented in the point on the fence structure that experience the maximum value of the stress. Change in the fence stress, changes the value of the electrical resistance of piezoresistors, which can be related to the wall-shear stress.

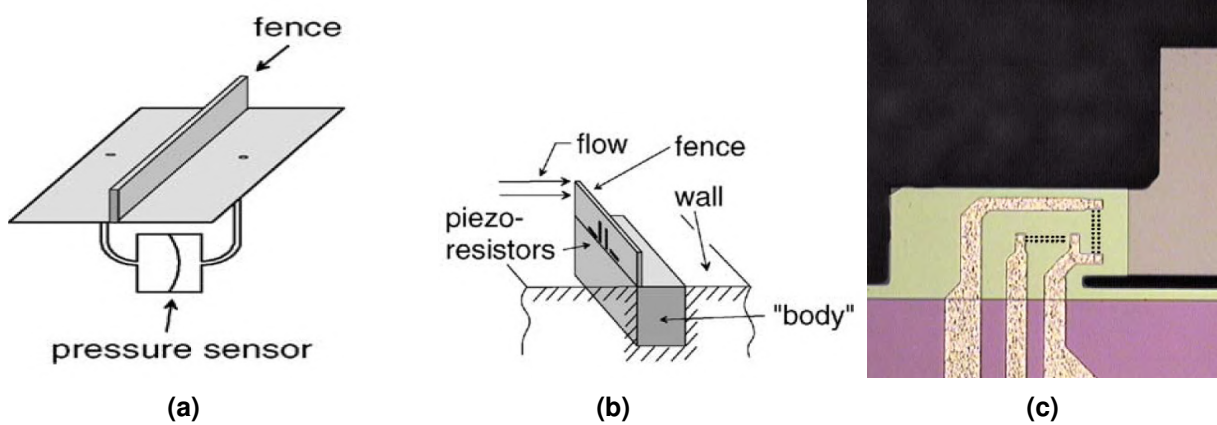


Figure 2.14 (a) A schematic drawing of a classical surface fence featuring a rigid blade with pressure tappings implemented on both side of it; (b) The MEMS-based surface fence using piezoresistors; (c) A close-up image of a surface fence device. Taken from (Von Papen et al., 2002).

The sensor structure consists of a 100-300 μm high and 7-10 μm thick silicon fence and a body for handling and packaging. As depicted in Figure 2.14, a rectangular slit was cut from the fence at the base in order to concentrate the stress and as a result of this, the fence plate was connected to the wall at the edges of the base. Enhancing the stress concentration as a result of adding the rectangular slit increases the sensitivity as well as the measurement resolution compared to a simple rectangular fence. The sensitivity of the sensor reported to be $0.5 \text{ mV}/(\text{VNm}^2)$, with a reported measurement range of 6 N/m^3 , and a resolution of 20 mN/m^3 . Attaining a better sensitivity and a higher resolution motivated von Papen et al. (2004) and Schober et al. (2004) to develop the second generation of MEMS-based surface fence sensors. This was done by increasing the surface area of the fence. Shown in Figure 2.14c, a stepped beam was introduced to the sensor structure to enlarge the stress concentration area, without increasing the value of the stress significantly. Similar to the first generation sensors, a rectangular slit was cut from the base so that the fence base is only fixed at the edges. This modification resulted in an improved sensitivity of $1 \text{ mV}/(\text{VNm}^2)$ and a resolution of 10 mN/m^3 for the sensor designed by von Papen et al. (2004), and a resolution of 20 mN/m^2 for the sensor developed by Schober et al. (2004).

Schiffer et al. (2006) designed a new MEMS surface fence wall-shear stress sensor based on two trapezoidal shaped beams with a height of 1000-1500 μm and a rectangular sensing element of 700 μm and a width of 5000 μm facing. Using a new packaging, the height of the sensing element can be adjusted allowing for the adjustments based on

different boundary layer thicknesses. The sensor calibration in a wall-shear stress range of $-0.3 \text{ Pa} < \tau_w < 0.3 \text{ Pa}$, resulted in a sensor sensitivity of $6 \text{ mV}/(\text{VNm}^2)$ and a resolution of up to 10^{-4} N/m^2 . Later, Savelsberg et al. (2012) carried out characterisation tests on the device introduced by Schiffer et al. (2006) by calibrating the device and testing it in a vortex cell flow. The MEMS surface fence sensor was calibrated against a Preston tube and then moved to the bottom of a vortex cell to measure the mean wall-shear stress over a range of reference velocities. The test result indicated that since the response of the device is closely cosinusoidal, orthogonal components of the wall-shear stress vectors can be obtained. However, the spanwise length of the surface fence that ensures this cosinusoidal behaviour, results in significant limitations specially in accurate determination of the fluctuating wall-shear stress values. Moreover, the test results also cleared that the natural vibration frequency of the sensor restricts the useful spectral range and the higher frequency content of the spectra was also affected by the poor spatial resolution in the spanwise direction.

Ma and Ma (2016) performed optimization analysis to improve the bending stress and the sensitivity of the sensors. Several sensors were designed and fabricated with the sensing element of 5 mm , a thickness of $20 \mu\text{m}$, and a height of either 1700 or $2200 \mu\text{m}$. The calibration of this device also performed alongside with a Preston tube over a range of $-0.7 \text{ Pa} < \tau_w < 0.7 \text{ Pa}$ and it indicated a sensitivity of $2.3 \text{ mV}/(\text{V.Pa})$, which is a 13% improvement compared to the sensors with the same thickness. The main drawback of the surface fence sensors is their limited spatial resolution due to the large

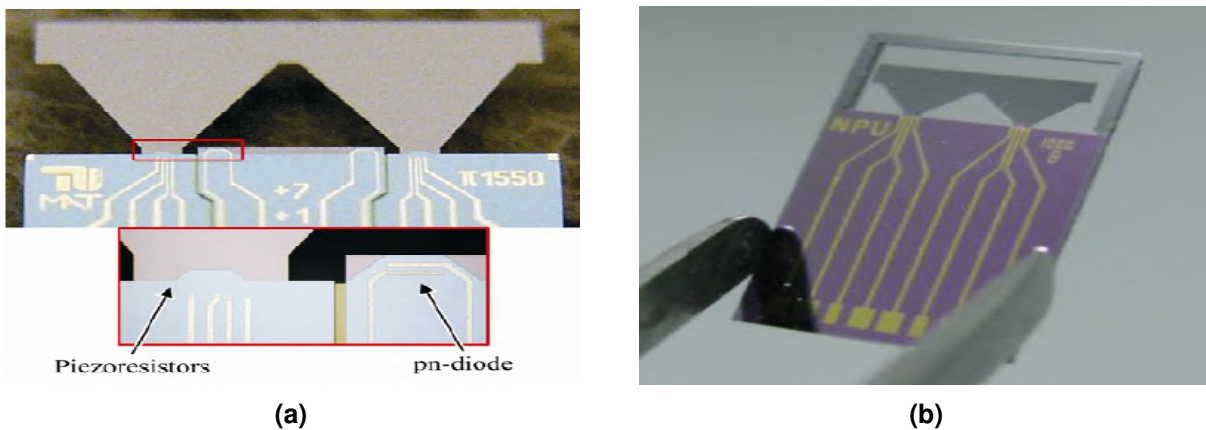


Figure 2.15 Images of micro surface fences with trapezoidal cantilevers. (a) An image of the device developed by Schiffer et al. (2006), (b) Image of the device developed by Ma and Ma (2016).

spanwise direction length of the sensing element (2 mm - 10 mm) as well as the increased surface area of the device. Moreover, in the surface fence sensors with Piezoresistive transduction the temperature effects should be considered in the sensor performance.

Micro-pillars wall-shear stress sensor (MPS3) is a method developed to accurately measure the fluctuating wall-shear stress. The array of elastic micro-pillar is placed at the wall and the deflection of the pillars due to the near wall velocity gradient of the fluid flow determines the values of the wall-shear stress. Initially, several research groups investigated the concept of using artificial hairs for flow sensing (Chen et al., 2003; Fan et al., 2002; Ozaki et al., 2000). Two techniques of forming the hairs (a) in the wafer plane and (b) perpendicular to the wafer plane were suggested based on these studies. Fabrication of the hairs in the wafer plane is straightforward due to the surface micro-machining methods, however, combining the surface micro-machined hairs into high density arrays is challenging (Ozaki et al., 2000). Li et al. (2000) introduced the utilisation of the plastic deformation magnetic assembly (PDMA) technique to erect the hairs out of the wafer plane. Dijkstra et al. (2005) presented the possibility of fabricating SU-8 photoresist-based artificial sensory hairs perpendicular to the wafer, which is shown in Figure 2.16a. The sensor structure was consisted of an artificial hair of 470 μm in length and 20 μm in diameter. As the fluid flows, sensory hairs move around in the flow. Capacitive transduction was utilised for the hair movement detection, by means of implementation of electrodes on a membrane which is connected to the base of the hair. An array of sensors was designed to increase the overall capacitance and hence the total sensitivity of the system as depicted in Figure 2.16b. One of the drawbacks of the SU-8 based sensory hairs sensor is that the hair length is constant on a given substrate, except when multiple layers of SU-8 are used. Moreover, the artificial sensory hair system is not sensitive enough and the sensitivity needs to be increased. Based on the author's investigation, the increase in the sensor's sensitivity can be obtained by increasing the length of the artificial hair up to 1 mm, which could protrude out of the viscous sub-layer.

Brücker et al. (2005) presented a sensor film with arrays of flexible PDMS micro-pillars patterned on it, coupled with optical techniques as the detection method, where the micro-pillars tip deflection due to the fluid flow was captured using an optical setup.

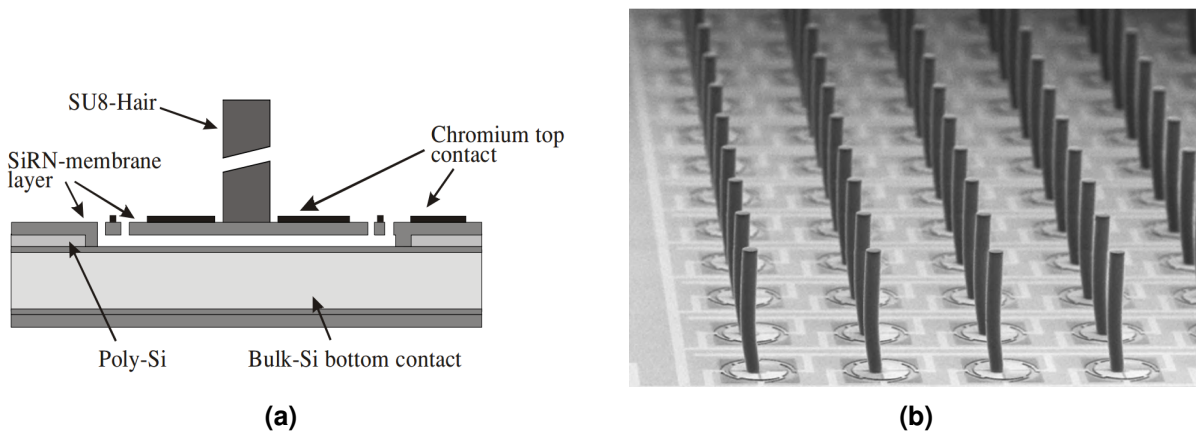


Figure 2.16 SU-8 based sensory hair with capacitive read out. (a) A schematics of the sensor structure with SU-8 hair; (b) The SEM image of array of sensory hairs. Adopted from (Dijkstra et al., 2005).

Here, two types of optical detection techniques were implemented. In the first method, the micro-pillars were illuminated from behind and due to their transparent nature, they act as fibre optic and they could transmit the light to the tip, where their image was recorded by an image sensor. The second method was based on coating the pillars tip with Gold as a reflective material and then illuminating the tips from the side and then record the deflection using an image sensor. The resolution of measurement in this technique is however limited by the optical system. Experimental investigation revealed that the gold coating could be washed-off, which results in a huge reflectivity reduction. Furthermore, this technique requires high speed cameras and optical access in the test rigs. Using the same concept, Große and Schröder (2007), Große et al. (2008), and Grosse et al. (2010) developed PDMS micro-pillar wall-shear stress sensors to measure the mean wall-shear stress in turbulent shear flows. The height of the pillars was $350 \mu\text{m}$ and their diameter was $45 \mu\text{m}$. The devices were calibrated in a plate-cone rheometer and then tested in a turbulent pipe flow. A highly magnifying telecentric lens was coupled to a high speed camera to detect the bending of the micro-pillars and to determine their displacement. This technique provides a good accuracy for high Reynolds number ($Re \geq 10000$) flows, however, for the flows with low Reynolds number the error in the micro-pillar tip displacement determination becomes extremely high due to the optical setup limitations.

Brücker et al. (2007) investigated the dynamic response of the micro-pillars and pillars array in an oscillating pipe flow. The pillar tested had a length of $700 \mu\text{m}$ and a diameter of $50 \mu\text{m}$ and the tests revealed a natural frequency of 173 Hz for this

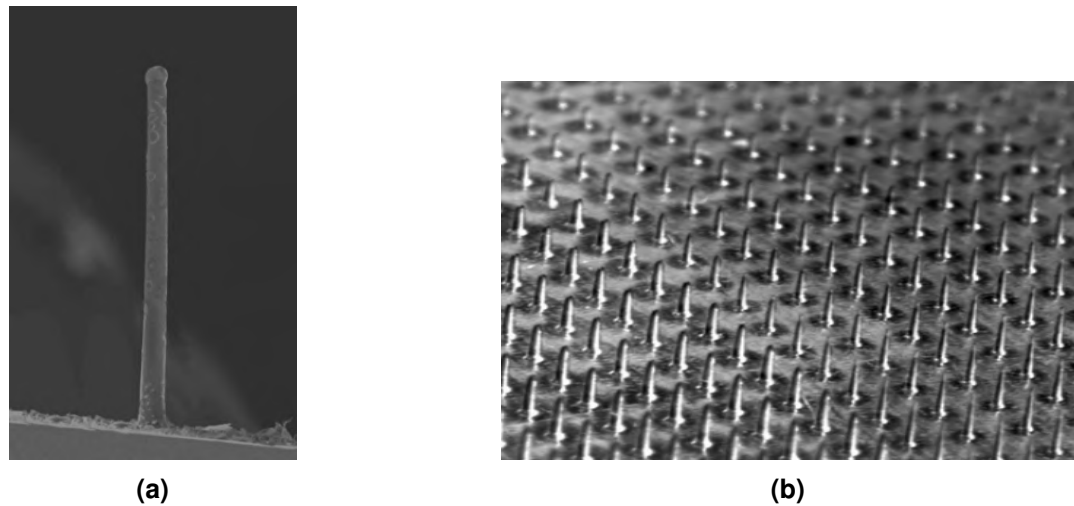


Figure 2.17 (a) The SEM image of a single micro-pillar; (b) An image of a micro-pillar array. Taken from (Große and Schröder, 2007)

micro-pillar. This investigation also indicated that for air flows, micro-pillars are affected by the large ratio of pillars density to that of air, which leads the system to resonate. Moreover, the base vibration of the sensor arrays can result in large measurement errors. To overcome this issue, the authors suggested the modification of the pillars geometry in a way to make the pillars smaller and stiffer, which can shift the natural frequency to higher values. This compromises the sensor sensitivity and also requires larger magnification in optical setup to achieve higher accuracy and higher resolution. This means the total number of micro-pillars will be limited due to a reduced field of view.

Gnanamanickam and Sullivan (2012) proposed a novel method to fabricate high aspect ratio micro-pillars. A micro-drill was manufactured by an electric discharge machine (EDM) and was utilised to form micro-holes in a wax sheet to produce a mould for micro-pillars array formation. In a following investigation, Gnanamanickam et al. (2013) characterised the fabricated micro-pillars. The flow tests suggested that, due to the low magnitude of the wall-shear stress in air flows, the micro-pillar sensors require a higher sensitivity and aspect ratio. Achieving a higher aspect ratio in the pillars is limited by the size of the viscous sublayer.

Although micro-pillar wall-shear stress sensors offer high spatial resolution due to their small diameter, the resolution of the measurements are limited by the resolution of the optical setup. Fluctuating wall-shear stress measurements in the turbulent boundary layer demands high speed image sensors which are costly and bulky. Additionally,

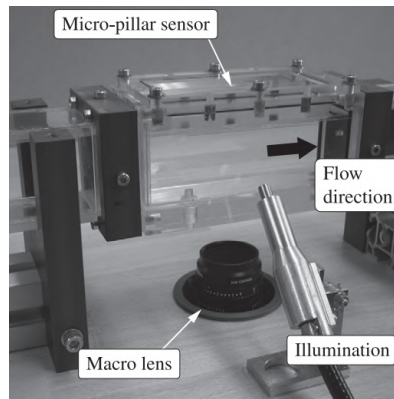


Figure 2.18 An image of a test setup for a micro-pillar wall-shear stress sensor. As it can be seen, the system requires bulky optics and optical access in the test rig. Taken from (Gnanamanickam et al., 2013)

due to their field of view and working distance they may not be suitable for use in macro-scale wind tunnel facilities. This measurement technique can be intrusive in higher Reynolds number flows where the thickness of the boundary layer is normally in the order of 10's of microns. Subsequently, the micro-pillars can protrude out of the viscous sublayer and disrupt the flow. In addition, as discussed, the micro-pillar deflection is proportional to the near wall velocity gradient which eventually links to the wall-shear stress. Micro-pillar sensors integrate the flow field in the direction normal to the wall, meaning any non-constant distribution of statistical turbulence characteristics along the micro-pillar length can not be detected. Hence, the values of these statistical terms measured with the micro-pillars can not be interpreted as the wall-shear stress characteristics (Große and Schröder, 2007).

2.2.1.3 Indirect optical methods

First introduced by Naqwi and Reynolds (1987), and later miniaturized by Fourquette et al. (2003) and Modarress et al. (2000), a sensing system was developed by modifying the conventional Laser Doppler Anemometer (LDA) for the measurement of the instantaneous velocity gradient within the flow's boundary layer, where the value of the wall-shear stress can be interpolated from the near-wall velocity gradient. Here, the sensor produces diverging fringes extended up to $66 \mu\text{m}$ into the linear region of the boundary layer by means of the interference between two closely spaced waves emerging from a surface below the flow to create a measurement volume. A pair of narrow windows with $1 \mu\text{m}$ in width and $400 \mu\text{m}$ in length were patterned $10 \mu\text{m}$ apart

by etching a $0.1 \mu\text{m}$ thick layer of chromium deposited on a glass substrate where a laser beam was focused to generate the waves. Particles were seeded on the flow to scatter the light at the Doppler frequency as they pass through the measuring volume and then the scattered light passes through one of the windows where it was collected by a detector that is implemented below the surface. Due to the linear velocity profile in the viscous sublayer, the light scatters at a single frequency for all the particles. The magnitude of the laser beam wavelength and the light scatter frequency can be directly related to the velocity gradient at the wall and, by taking the fluid viscosity into the account, the wall-shear stress value can be quantified (Obi et al., 1996; Örlü and Vinuesa, 2020).

Using this method, it is easy to vary the size of the measuring volume and change its location in the flow. It is able to detect flow reversals and this technique does not require calibration prior to the flow measurements. Additionally, this technique provides a higher spatial resolution compared to the conventional LDA method, since only one particle enters the measurement volume at a time, and as a result of this the signal only corresponds to this single particle instead of integrating over the measuring volume. However, the construction of the instrument in this sensor is complex as the device requires precise alignment since it is sensitive to vibrations. In addition, as suggested by Naqwi and Reynolds (1987), the signal rate can be low to enable data post processing and the energy spectra evaluation due to the behaviour of the scattering particles in the vicinity of the wall as well as weak signals in side scatter arrangement.

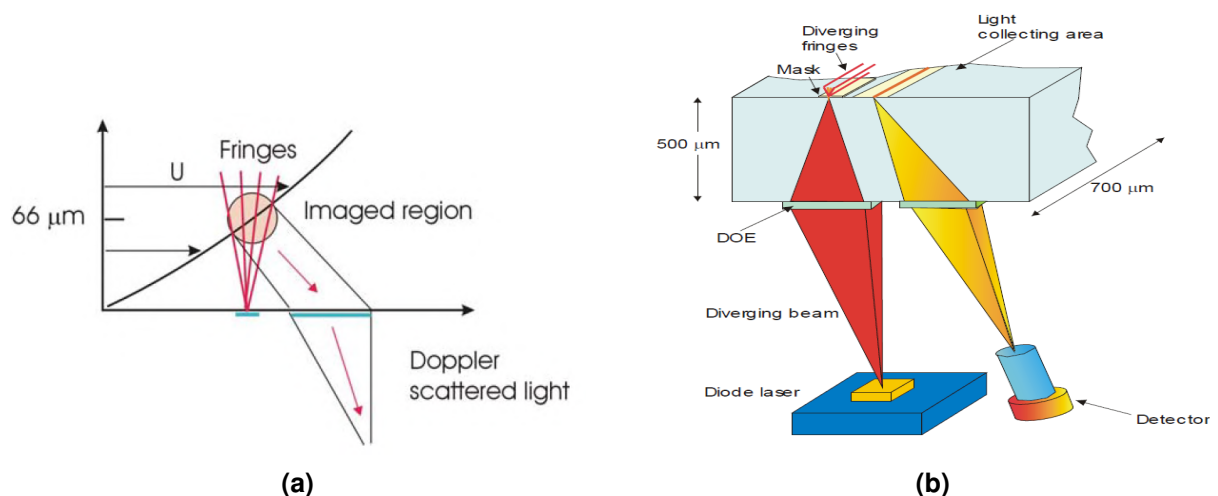


Figure 2.19 (a) Schematics of the indirect optical MEMS wall-shear stress sensor. (b) 3D schematics of the optical sensor based on LDA. Taken from (Modarress et al., 2000).

2.2.2 Direct measurements

Direct MEMS wall-shear stress sensors respond to the momentum transfer at the wall and measure the displacement of a flush-mounted movable floating element structure as a result of applied wall-shear stress (Naughton and Sheplak, 2002). The floating element is suspended and free to move using different configurations of micro-springs. As the fluid, flows over the MEMS devices, the floating element moves in the direction of the flow while remaining parallel to the surface. The lateral displacement of the floating element is directly related to the wall-shear stress, via the micro-spring elasticity, and can be measured via different transduction schemes. Despite the macro-scale floating element devices that suffer from numerous limitations such as limited spatial and temporal resolutions, the micro-machined floating element devices offer higher spatial and temporal resolutions, which are essential for turbulence measurements. Additionally, microfabrication methods allow the size of the gaps to be in the order of the viscous length scale, $o \sim (u_\tau/\nu)^{-1}$ (Schlichting and Gersten, 2016), and hence, the measurement errors due to the existence of gaps in the structure are negligible. Another source of measurements error in the conventional floating element sensors is misalignment in the sensor structure since most of the devices are manufactured by assembling multiple parts. This error, however, is negligible in the MEMS-based floating element devices due to the bulk micromachining process, where all parts of the MEMS devices can be monolithically fabricated from a same wafer, where the determining factor for the misalignment is the substrate's surface flatness. Different transduction techniques were integrated into the MEMS-based floating element wall-shear stress sensors to capture the floating element displacement. Three major transduction techniques developed for

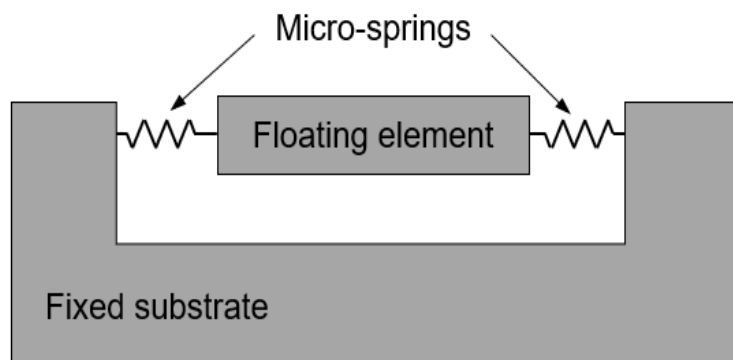


Figure 2.20 A schematic view of floating-element wall-shear stress sensors.

this purposes are capacitive, piezoresistive, and optical transduction methods, which are discussed in the following sections.

2.2.2.1 Sensors with capacitive transduction

Realizing the merits of micro-fabricated wall-shear stress devices, Schmidt et al. (1988) and Schmidt (1988) developed the first MEMS floating element wall-shear stress sensor for turbulence measurement in low speed air flows. The device was fabricated from the surface micromachining of polyimide/aluminium, where an integrated differential capacitive transduction and an integrated pair of matched P-MOS transistor were utilised to readout the sensor displacement. The sensor floating element size was reported to be $500 \mu\text{m} \times 500 \mu\text{m} \times 30 \mu\text{m}$, where four micro-beams were connected to the four corners of it acting as the micro-springs. The length of the micro-spring was reported to be $1000 \mu\text{m}$, with varying width of 10 to $20 \mu\text{m}$ and a thickness of $30 \mu\text{m}$. A schematic view of the sensor cross section with the integrated differential capacitance readout is shown in Figure 2.21. Three passivated electrodes were implemented on to the surface of the substrate underneath the floating element, alongside with an embedded conductor on the bottom surface of the floating element to track the changes in the capacitance due to the exerted wall-shear stress. The sensor calibration in a laminar air flow rig in a wall-shear stress range of $0.1 \text{ Pa} \leq \tau_w \leq 1 \text{ Pa}$, demonstrated a sensitivity of 52 mV/Pa which was in a good agreement with analytical models. Polyimide is susceptible to moisture and therefore the device suffered from the mechanical sensitivity drifts due to the moisture dependant stress. Additionally, the sensor was affected by the

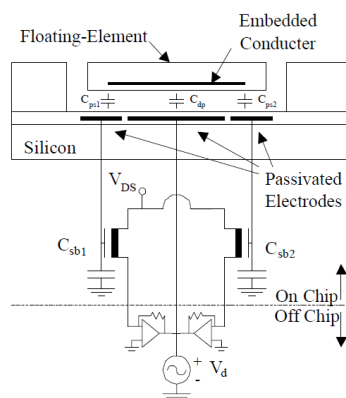


Figure 2.21 A schematic cross section view of floating-element wall-shear stress sensors with differential capacitance readout. Taken from (Schmidt et al., 1988)

electromagnetic interference (EMI) due to the high input impedance. Utilising front side wire bonding was another drawback of this device, since the wires can result in flow disruption around the device.

Pan et al. (1999), Hyman et al. (1999), and Patel et al. (2002) introduced the first capacitance MEMS wall-shear stress sensor using comb fingers, based on differential capacitive and a capacitive force feedback, using polysilicon surface micromachining technology. Illustrated in Figure 2.22, is the sensor structure, which consists of a folded-beam suspension, with the comb fingers arranged in the leading edge and trailing edge of the device. The displacement of the floating element changes the overlap area between the comb fingers that results in the capacitance variations. The difference in the capacitance on two sides of the floating element is then calibrated against the wall-shear stress. Sensor calibration performed in a 2D laminar flow channel in a wall-shear stress range of up to 10 Pa, where the sensor showed a linear response up to $\tau_w=4$ Pa. The sensor sensitivity was reported to be 1.02 V/Pa for this range. This was a promising development in the history of wall-shear stress sensors, however, the device was not flush and front side wire-bonding was employed, which results in flow disruption around the sensor die. No dynamic response was reported.

Zhe et al. (2005) designed and developed a floating element sensor for low magnitude wall-shear stress in which the displacement measurement of the floating element were accomplished by a differential capacitance measurements. The device structure

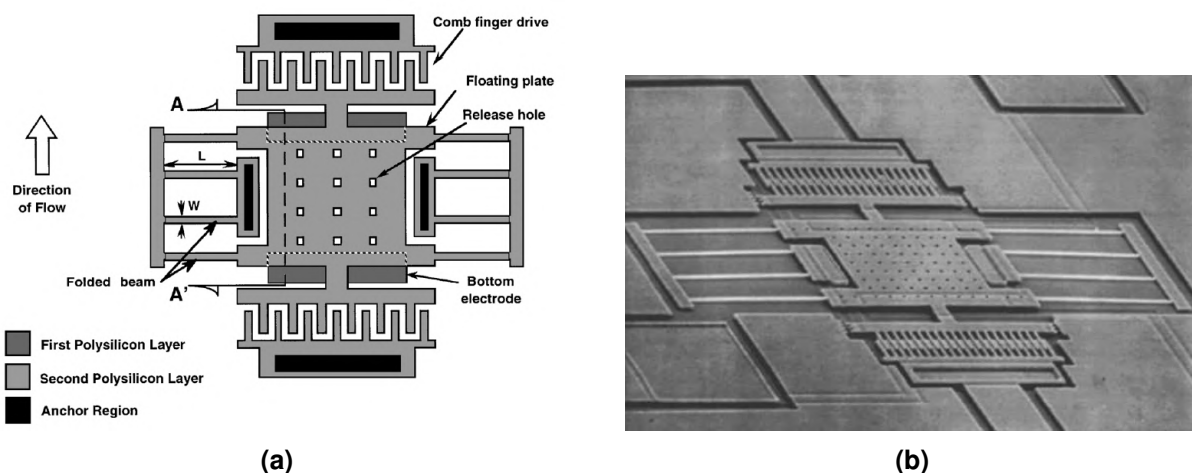


Figure 2.22 (a) Top view of the floating element with comb fingers (b) A SEM image of the MEMS wall-shear stress using comb fingers. The sensor displacement is measured via the differential capacitance from the comb finger electrodes. Adapted from Pan et al. (1999).

consisted of a $500\ \mu\text{m} \times 200\ \mu\text{m}$ floating element connected to the end of a $3000\ \mu\text{m}$ long and $10\ \mu\text{m}$ wide cantilever beam, which acts as the micro-spring and result in a resonant frequency of 531 Hz; see Figure 2.23. The beam structure alongside with two other electrodes that are formed on the walls on either sides of the beam form the differential capacitive system. The results of the air flow experiments in a laminar flow channel showed a sensitivity of 337 mV/Pa over a wall-shear stress range of up to 0.2 Pa, and a minimum detected wall-shear stress of 0.04 Pa with an accuracy of 8 %.

McCarthy et al. (2003) and Tiliakos et al. (2006, 2007) attempted to develop a shear stress sensor for the hypersonic aeropropulsion tests and high temperature applications, using a silicon carbide force-feedback capacitive detection scheme. The device was fabricated by depositing a layer of silicon carbide onto a silicon substrate to perform in a wall-shear stress range of 10-1000 Pa. A significant residual stress added to the silicon carbide during the fabrication process, which resulted in the comb fingers to curl, which consequently reduced the sensor capacitance. No value were reported for the sensor performance, and only the survivability of the sensor was investigated.

Chandrasekharan et al. (2009) and Chandrasekharan et al. (2011) developed another type of differential capacitive wall-shear stress sensor by using asymmetric interdigitated comb finger structure. The structure of the sensor consisted of a $2000\ \mu\text{m} \times 2000\ \mu\text{m} \times 45\ \mu\text{m}$ floating element, which is tethered by four $1000\ \mu\text{m} \times 23\ \mu\text{m} \times 45\ \mu\text{m}$ micro-beams on its four corners. The comb fingers with asymmetric gaps of $3.5\ \mu\text{m}$

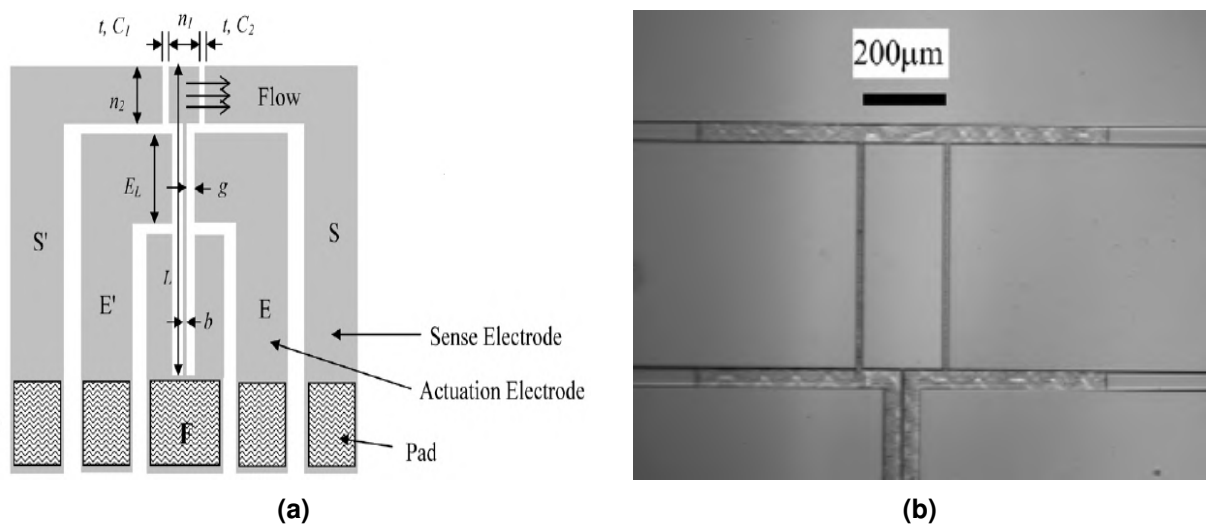


Figure 2.23 (a) The schematic view of the top surface of the sensor developed by Zhe et al. (2005). (b) A photo from the top surface of the device showing the floating element and the long cantilever beam. Taken from (Zhe et al., 2005).

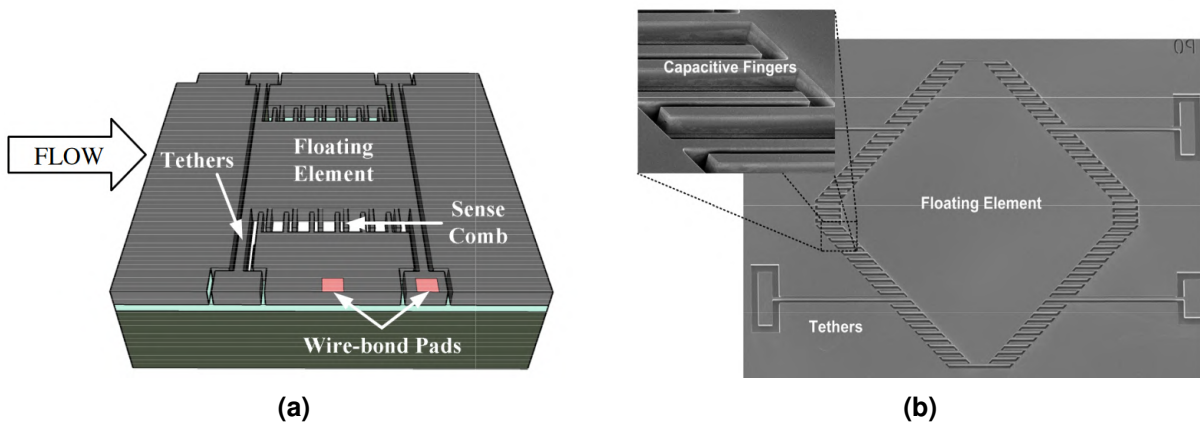


Figure 2.24 (a) The schematic view of the differential capacitive sensor developed by Chandrasekharan et al. (2011). (b) The SEM image of the capacitive sensor developed by Sells et al. (2011). Images are taken from (Sells et al., 2010) and (Sells et al., 2011).

and $20\ \mu\text{m}$ were designed on two sides of the floating element and between the micro-springs to form the differential capacitors. A two-mask fabrication process were used to pattern the sensor structure on a nickel metal plate. Electrical pads were formed at the end of the micro-springs for the wire-bonding purpose. The sensor tests showed a sensitivity of $7.66\ \text{mV/Pa}$, a resonant frequency of $6.2\ \text{kHz}$, and a minimum detectable signal of $14.9\ \mu\text{Pa}$. Furthermore, the sensor was susceptible to humidity that arose drifts in the mean value of the wall-shear stress. As a result of this, the sensor can only be used to detect the values of fluctuating wall-shear stress.

Sells et al. (2011, 2010) reported the development of a MEMS capacitive wall-shear stress sensor with passive wireless detection electronics. Shown in Figure 2.24b is the structure of this device, where the $1500\ \mu\text{m} \times 1500\ \mu\text{m}$ floating element was rotated 45° from the conventional floating element structure, and the comb fingers were placed on each side of the floating element. An indicator coil was integrated into the capacitive comb fingers to establish an electrical resonant LC-tank circuit where the frequency response can be monitored. In this design, Nickel layer was replaced by a highly doped silicon device layer followed by a hydrophobic passivation layer to mitigate the issues with the mean wall-shear stress measurement error due to the humidity. A value of $474\ \text{kHz/Pa}$ was reported for the sensitivity of the device for the measurements up to $\tau_w = 4\ \text{Pa}$, as well as a minimum detectable signal of $4.1\ \text{mPa}$. Although the device was able to measure the mean wall-shear stress values, the fluctuating wall-shear stress values were not attained for this device.

Following the developments done by Chandrasekharan et al. (2011), Meloy et al. (2011, 2012) coupled the comb fingers capacitive MEMS sensor with a synchronous modulation/demodulation system to improve the mean wall-shear stress measurements. The sensor structure was similar to the one developed by Chandrasekharan et al. (2011), and it was fabricated utilising a Silicon on Pyrex processing, with a $1000\ \mu\text{m} \times 1000\ \mu\text{m} \times 45\ \mu\text{m}$ floating element and four micro-springs of $1000\ \mu\text{m} \times 15\ \mu\text{m} \times 45\ \mu\text{m}$. The reported sensitivity, resonant frequency, and minimum detectable signal of the device are 10.8 mV/pa, 4.7 kHz, and 6.5 mPa respectively.

Employing the inductively coupled plasma (ICP) etching techniques on a SOI wafer using a single mask, Lv et al. (2013) fabricated a sensor in which the floating element displacement detection were accomplished by using a differential capacitance measurement. With a similar structure to the conventional floating element devices, the floating element dimensions is $1037\ \mu\text{m} \times 1000\ \mu\text{m} \times 26\ \mu\text{m}$ and the micro-spring dimensions is $800\ \mu\text{m} \times 10\ \mu\text{m} \times 26\ \mu\text{m}$, with the interdigitated comb fingers formed on the floating element sides. The device characterisation performed in a laminar flow cell in a wall-shear stress range of 0-35 Pa, where the sensitivity was calculated to be 27 mV/Pa and the repeatability of the sensor was within 4.9 %. Similar to previous devices, front side wire-bonding was employed for the electric connections, which results in flow disruptions. Moreover, only the mean wall-shear stress values were reported with no dynamic response characterisation.

Inspired by Patel et al. (2002), and by employing a similar structure, Zhao et al. (2014) designed and fabricated a differential capacitive wall-shear stress sensor by using four layers of surface micromachining including the copper and nickel electroplating. Micro-machined bumps were added to the sensor surface to increase the sensitivity. A direct capacitance to digital converter IC was used to measure the differential capacitance change due to the wall-shear stress. The sensor was tested in a laminar flow rig with three different channel heights, showing a sensitivity of 77 aF/Pa. Adding the bumps in this design increased the errors in the sensitivity measurements, by adding complexity into the fluid-structure interaction and changing the surface topology. In addition to this, existence of large gaps and bumps in the sensor structure resulted in the pressure sensitivity to be larger than the predicted value by an order of magnitude and play a significant role in the measurement errors. Moreover, the sensor showed a slow

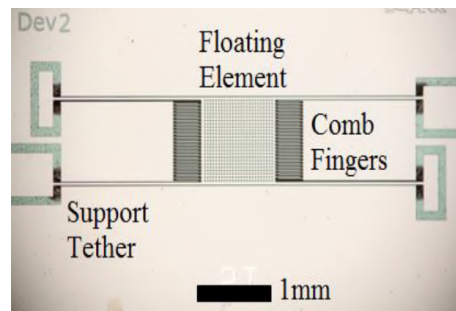


Figure 2.25 An image of the differential capacitive wall-shear stress sensor using TSVs technology. Taken from (Barnard, Meloy and Sheplak, 2016).

drift in the capacitance due to the temperature and humidity sensitivity. No dynamic behaviour was reported in this study. As discussed, front side wire-bonding was used for the capacitive sensors to provide the connection between the electrodes on the sensor element and the interface circuit. Normally, an encapsulation is used for the flow protection that extend well into the flow and results in changing the flow behaviour. To eliminate this issue, Barnard et al (Barnard, Meloy and Sheplak, 2016; Barnard, Mills, Meloy and Sheplak, 2016) utilised the through silicon vias (TSVs) technology to develop a differential capacitive MEMS wall-shear stress sensor with the aim to eliminate the need for front side wire bonds. This allows for a smooth surface for the turbulence measurement and reduces the flow disturbance. As shown in Figure 2.25, the sensor structure is similar to that of Chandrasekharan et al. (2011), with interdigitated comb fingers patterned on two sides of the floating element and between the micro-springs. The synchronous modulation/demodulation system that was employed by Meloy et al. (2012), was used in this sensor as a interface circuit. Sensor characterisation included a sensitivity of 1.36mV/Pa at 1.128 kHz, a resonant frequency of 3.4 kHz, and a minimum detectable wall-shear stress of 1.1 mPa. This was an extension to the previous efforts in the development of the capacitive MEMS wall-shear stress sensors, to make a smooth surface around the sensor, and inspired the future researchers to use this technique for the wall-shear stress sensor development. However, the fabrication process of the sensor structures with TSVs is significantly costly and the overall performance of the device is limited by the TSVs quality.

Utilising the TSVs method for the backside connection, another differential capacitive MEMS wall-shear stress sensor was developed by Ding et al. (2018). As illustrated in Figure 2.26 , the $1180 \mu\text{m} \times 680 \mu\text{m} \times 45 \mu\text{m}$ floating element is supported by four

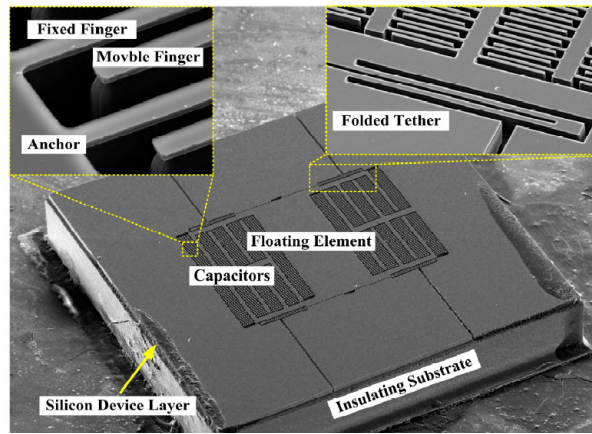


Figure 2.26 A SEM image of the differential MEMS wall-shear stress sensor developed by Ding et al. (2018).

folded-beams, acting as micro-springs, and the comb fingers were patterned on the sides of the floating element. The sensor was calibrated over a wall-shear stress range of 0-65 Pa, showing a repeatability error of 4.7 %. No sensitivity and dynamic characterisation were reported for this sensor.

Mills et al. (2017, 2018) utilised a low-cost backside electrical connections for the differential capacitive MEMS wall-shear stress sensors. As it is depicted in Figure 2.26, three separate electrodes were formed on the sensor structure to form two capacitors, which were defined by the primary and secondary comb finger gaps. The sensor structure was composed of a $2000 \mu\text{m} \times 400\mu\text{m} \times 60 \mu\text{m}$ floating element which was suspended by four folded-beam micro-springs with a length of $1600 \mu\text{m}$ and a width of $28 \mu\text{m}$. The sensor calibration and characterisation yielded a sensitivity of 38.8 mV/Pa , a bandwidth of 1.4 kHz , and a minimum detectable wall-shear stress of $60 \mu\text{Pa}$.

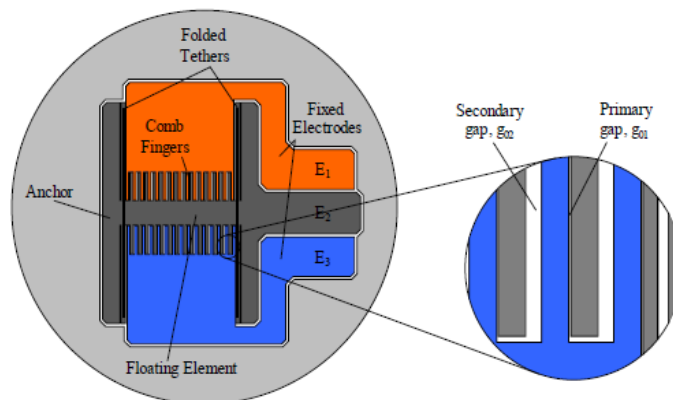


Figure 2.27 A schematics of the differential capacitive MEMS wall-shear stress sensor by Mills et al. (2017).

In order to minimise the temperature sensitivity of the capacitive MEMS wall-shear stress sensors, Mills et al. (2021) integrated a temperature-compensated amplifier circuit into the sensor and the synchronous modulation/demodulation circuit. For this purpose, a linearised negative temperature-coefficient (NTC) thermistor was used in the amplifier's feedback loop to cancel off the positive temperature coefficient of the sensor head. The sensor tests for the temperature sensitivity demonstrated ten times reduction in temperature sensitivity.

The capacitive MEMS wall-shear stress sensors are promising for the flow measurement applications as their fabrication and packaging is straightforward. Nevertheless, revealed that they are sensitive to electromagnetic interference (EMI), temperature, and moisture. In addition, using the capacitive sensors in liquid flows is challenging and requires further packaging developments to isolate the sensing fingers from the surrounding medium.

2.2.2.2 Sensors with Piezoresistive transduction

Ng et al. (1991) and Shajii et al. (1992) extended the work by Schmidt et al. (1988) to develop a floating element MEMS sensor with piezoresistive transduction for high wall-shear stress measurement of 1 kPa up to 100 kPa in polymer extrusion applications. The sensor structure with a floating element size of $120\ \mu\text{m} \times 140\ \mu\text{m}$ and four $30\ \mu\text{m} \times 10\ \mu\text{m}$ micro-springs, was patterned on a $5\ \mu\text{m}$ silicon device layer. The $5\ \mu\text{m}$ dielectrically isolated silicon layer were fabricated using the wafer bonding technology, allowing the piezoresistive property of the silicon to be used in a half-bridge electrical configuration to transduce the applied shear stress into an electrical signal. In this half-bridge arrangement, one of the resistors experiences a tensile strain, while the second resistor experiences a compressive strain, which results in decreasing resistance in the first resistor and increasing resistance in the second resistor. To implement this, despite the conventional sensor structure designs, in this design the micro-springs were formed in line with the flow direction, as illustrated in Figure 2.28, so that two of the micro-springs undergo a tensile strain, while the two other undergo a compressive strain, resulting in the resistance change. The device was tested in a cone and plate

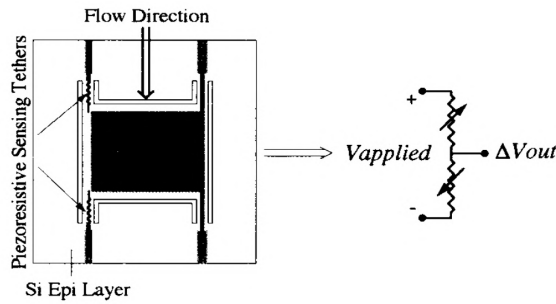


Figure 2.28 A Schematic view of the floating element sensor with piezoresistive readout. The micro-springs are formed in line with the flow, so that the deflection is normal to the micro-spring direction to generate axial strain in the piezoresistors. Taken from Schmidt et al. (1988)

viscometer, where the sensitivity was measured to be $13.7 \mu\text{V}/\text{V.kPa}$. This value for the sensor sensitivity is too low to be used for turbulence measurements.

Barlian et al. (2007, 2006) reported the development of a floating element MEMS wall-shear stress sensor with a piezoresistive transduction for underwater measurements. As shown in Figure 2.29, a pair of sidewall-implemented piezoresistors were used alongside with a pair of top-implemented piezoresistors at the root of the micro-springs, to detect the in-plane and out of plane deflection of the device by means of a Wheatstone bridge configuration, respectively. Triplex layers of oxide-nitride-oxide passivation were coated on the device surface using a PECVD process for underwater testings. Sensor static characterisation was performed by utilising a piezoelectric cantilever to deflect the floating element. The tip of the cantilever beam was placed in the gap between the floating element and the substrate to displace the floating element laterally. The result

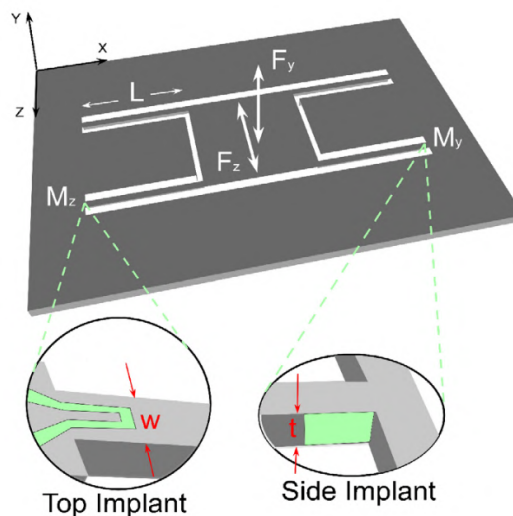


Figure 2.29 Schematics of the piezoresistive MEMS wall-shear stress sensor with top and side-wall implementation developed by Barlian et al. (2007). Taken from (Barlian et al., 2007).

was a lateral sensitivity of 0.063 mV/Pa and a minimum detectable shear stress of 2.3 mPa. The test results indicated a significant scatter in the data, which were reported to be due to the uncertainty in the measurements (Barlian, 2009).

Li et al. (2008, 2006) also developed a piezoresistive MEMS wall-shear stress sensor by using side-implemented, diffused resistors into the end cap of the silicon micro-springs (tethers). The device deflection as a consequence of the applied wall-shear stress induces a stress field in the structure and varies the resistance of the implemented resistors. As illustrated in Figure 2.30, a fully active Wheatstone bridge was formed by the side-implemented piezoresistors, to track the changes in the resistance and ultimately to quantify the wall-shear stress values. The sensor structure with a $1000\ \mu\text{m} \times 1000\ \mu\text{m}$ floating element and four $1000\ \mu\text{m} \times 30\ \mu\text{m}$ micro-springs was fabricated on a silicon-on-insulator (SOI) wafer with $50\ \mu\text{m}$ device layer. The sensitivity of the device was measured to be $4.24\ \mu\text{V}/\text{Pa}$, tested in a wall-shear stress range of up to 2 Pa. Dynamic characterisation of the device reported a resonant frequency of 6.7 kHz and a minimum detectable wall-shear stress of 11.4 mPa. The experimental investigation of the sensor suggested that the sensor sensitivity alters with temperature variations and that the device is susceptible to thermal drift. Moreover, piezoresistors self-heating was also present in the calibration of the device, affecting its performance. Microfabrication issues and complexities also affected the sensor performance and resulted in notable variations in the piezoresistors resistance values. This increased the pressure sensitivity of the device and introduced errors in the sensor readings.

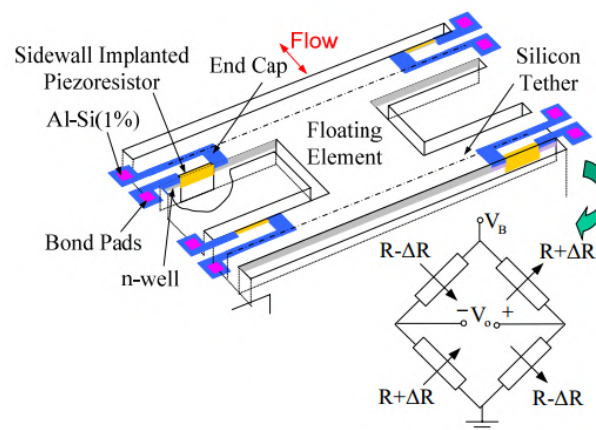


Figure 2.30 Schematics of the MEMS wall-shear stress sensor with side-implemented piezoresistors. Taken from (Li et al., 2008).

2.2.2.3 Sensors with optical transduction

The first optical MEMS wall-shear stress sensor was developed by Padmanabhan et al. (1996, 1997). The sensor's displacement detection technique was based on a floating-element shutter and integrated photodiodes. As shown in Figure 2.31a, a pair of photodiodes were implemented underneath the floating element, while subjected to laser source illumination. The laser source was located opposite the floating element. The working principle of the sensor can be explained as when there is no flow, the exposed areas of the photodiodes are similar and as a result of this the differential photo-current is zero. As the flow moves over the sensor, the floating element acts as an optical shutter, and its displacement changes the exposed areas on the photodiodes. The difference in photodiodes areas produces a differential photo-current that is proportional to the sensor displacement and the applied wall-shear stress. The sensor with a floating element size of $500 \mu\text{m} \times 500 \mu\text{m} \times 7 \mu\text{m}$ and four micro-springs of $500 \mu\text{m} \times 10 \mu\text{m} \times 7 \mu\text{m}$ was calibrated in a laminar flow rig, and showed a linear response up to 5 Pa. The sensor's response sensitivity to the incident light intensity variations, motivated Padmanabhan et al. (1997) to develop a novel sensor by utilising a split diode approach. In this new design, the photodiodes were placed closer to each other by placing an aperture at the middle of the floating element. One of the photodiodes was divided into an upstream and downstream sections, while the second diode was implemented underneath the central aperture, eliminating any sensitivity to the intensity variations, as illustrated in Figure 2.31b. The sensor was calibrated in a range of 0-1 Pa, where the results indicated a 94 % reduction in the sensitivity to the laser intensity variations.

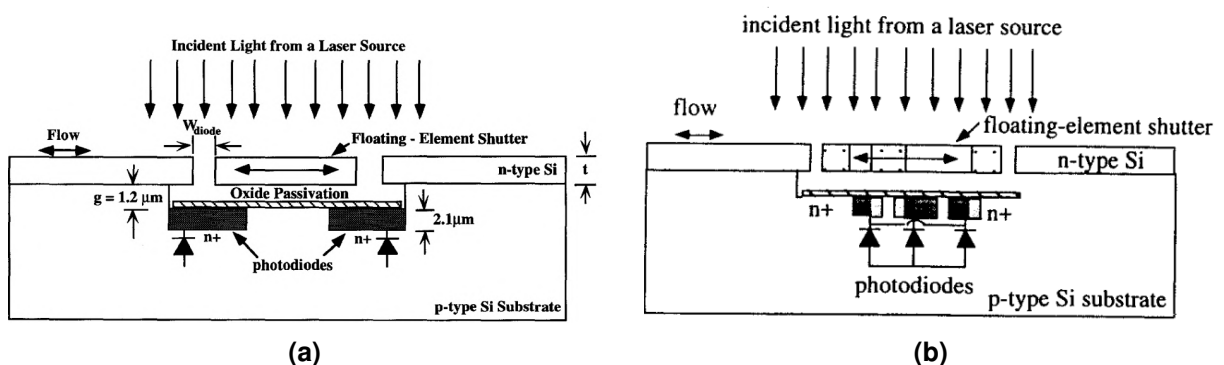


Figure 2.31 (a) The Schematic view of the detection principle for the sensor with integrated photodiode. (b) A Schematics of the optical sensor with split diode configuration. Taken from (Padmanabhan et al., 1996) and (Padmanabhan et al., 1997).

Unlike the capacitive sensors, this sensor showed to be immune to EMI and it was insensitive to pressure fluctuations. Nevertheless, this method depends on an external light source, which is installed at the top surface of the device, where in most of the cases it is inside the experimental setup. This results in measurement uncertainties because of the different distances in the calibration rig and the actual flow measurement experiments. Moreover, the front side wire-bonding was implemented in this sensor, resulting in flow disturbance around the device.

Tseng and Lin (2003) utilised micro-Fabry–Perot interferometry to develop an optical wall-shear stress sensor. Fabricated from layers of SU-8, a $1500\ \mu\text{m} \times 1500\ \mu\text{m} \times 20\ \mu\text{m}$ flexible membrane was used to protect a $200\ \mu\text{m} \times 200\ \mu\text{m}$ micro mirror with a height of $400\ \mu\text{m}$ that acts as the sensing element. Shear force on the flexible membrane due to the fluid flow induces a displacement in the micro mirror. As represented in Figure 2.32, the end surface of a fibre optic cable was placed on the reflective side of the micro mirror to create a Fabry-Perot interferometers by sending and detecting the reflected incident light from the micro mirror structure to pose interference with another reflected light. The interference spectrum is effected by the distance of the micro mirror and the fibre optic surface as well as the light wavelength, and hence, the applied wall-shear stress is detected by the shift in the interference spectrum. This sensor's tests demonstrated a sensitivity of $1.538\ \text{nm}/\text{Pa}$ and a minimum detectable wall-shear stress of $0.25\ \text{Pa}$. The tests also indicated a significant temperature sensitivity of $3.4\ \text{nm}/\text{K}$ which requires further developments for the thermal compensation.

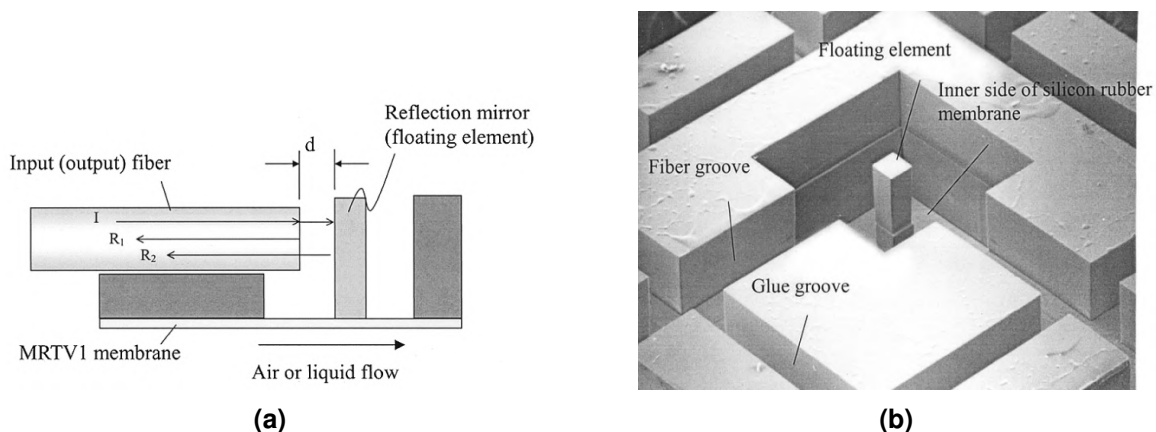


Figure 2.32 (a) A schematic cross section view of the sensor using the micro-Fabry–Perot interferometry. (b) A SEM image of the fabricated optical sensor with the micro mirror (floating element) is shown at the middle of the picture. Taken from (Tseng and Lin, 2003).

Horowitz et al. (2004) employed the geometric Moiré fringe pattern interferometry as the transduction technique to develop an optical MEMS wall-shear stress sensor. The sensor was fabricated by anodic bonding of a silicon wafer to a Pyrex wafer. Aluminium optical gratings were patterned on the back side of the floating element as well as the top surface of the Pyrex wafer, to form the Moiré fringe pattern. The Moiré fringe pattern optically amplifies the mechanical displacement of the sensor, which makes it simpler to track the sensor's displacement in nanometer scales. A 5X microscope objective was placed inside the sensor packaging which was coupled with a line-scan charge-coupled device (CCD), to track and record the displacement of the Moiré fringe pattern. The calibration of the device with a floating element size of $1280 \mu\text{m} \times 500 \mu\text{m} \times 10 \mu\text{m}$ resulted in a linear sensitivity of 13 pixels/Pa up to $\tau_w = 1.3 \text{ Pa}$, showing a limited linear performance of the sensor, and a minimum detectable wall-shear stress sensor of 6.2 mPa. The sensor's resonant frequency was reported to be 1.7 kHz with a flat-band of less than 500 Hz. The test results indicated that the Moiré fringe pattern transduction offers immunity to EMI and it is insensitive to the pressure fluctuations. However, using the objective lens and the large size of the CCD make the overall sensor packaging significantly bulky, since this requires a laboratory microscope to track the sensor displacement as shown in Figure 2.33. Additionally, the size of the data recorded by the CCD alongside with its low sampling rate restrain the sensor's performance.

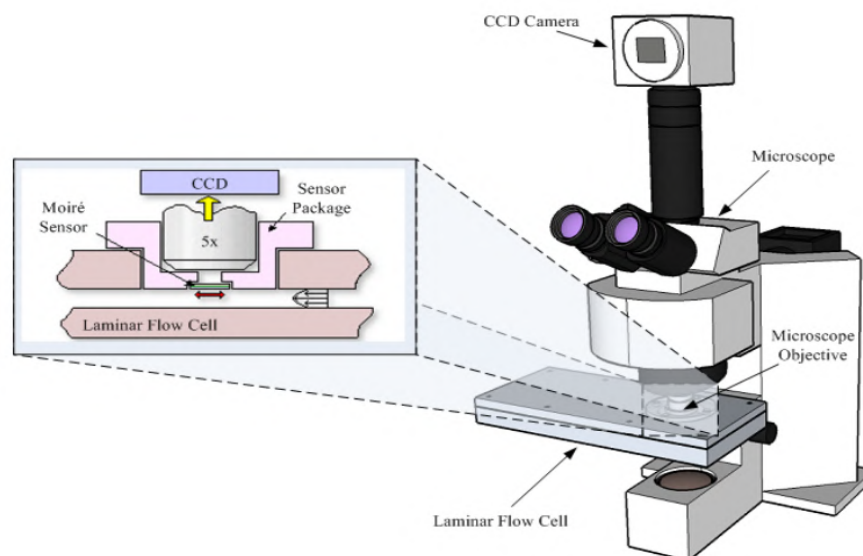


Figure 2.33 Illustration on using an laboratory microscope to observe the MEMS sensor displacement. Taken from (Chen, 2012).

Ioppolo et al. (2008) and Ayaz et al. (2011) reported the development of an optical MEMS wall-shear stress sensor using the whispering gallery mode (WGM) shifts of dielectric micro-resonator, which is based on tracking changes in the optical modes of a dielectric PDMS micro-sphere due to the shear force. Shown in Figure 2.34 is the sensor structure where a $125\ \mu\text{m}$ silica beam, which acts as a lever, is attached to a $800\ \mu\text{m}$ by $800\ \mu\text{m}$ flat plate that acts as a sensing surface. The other side of the silica beam is attached to another plate and as the sensing surface deflects under the wall-shear stress, the silica beam compresses the micro-sphere against the backstop, which consequently deforms the micro-sphere and shifts its optical mode. A fibre optic cable was used to transfer the light from a tunable laser source, whilst tapered in the section where the micro-sphere was placed on. A photodiode was implemented on the other end of the fibre optics cable to measure the transmitted light intensity. The position of each whispering gallery mode in the spectrum is based on the morphology of the micro-sphere, and thus, it changes with the PDMS micro-sphere deformation due to the applied force. The sensor was calibrated by using a cantilever beam that was mounted on a stage to exert the force to the sensor. A sensitivity of $15.145\ \text{pm}/\text{Pa}$ was reported for the calibration range of $0\text{--}2\ \text{Pa}$, and the resonant frequency of the device was measured to be $300\ \text{Hz}$ with a linear performance of up to $100\ \text{Hz}$. The low value of the sensor's sensitivity alongside with a limited bandwidth indicate that this sensor requires further optimisation and development for turbulence measurements. Although the sensor is immune to EMI, its performance significantly depends on the mixing ratio of the PDMS that is used during the micro-sphere fabrication.

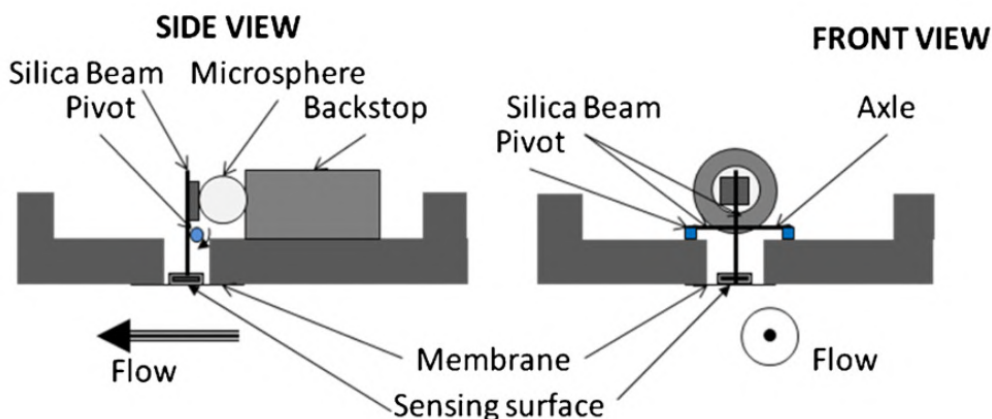


Figure 2.34 The schematic view of the WGM based sensor. Taken from (Ayaz et al., 2011).

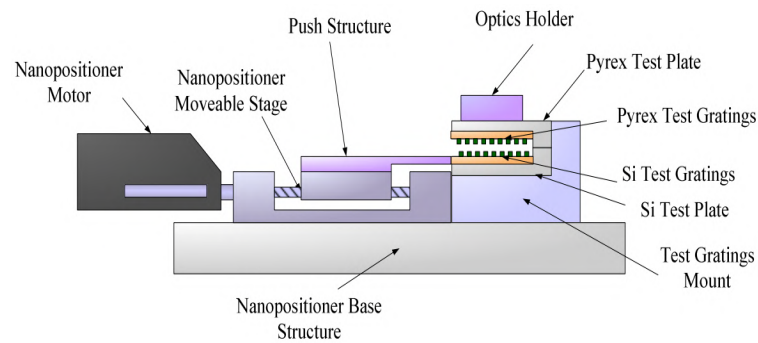


Figure 2.35 A schematics of the optical test bed developed to mimic the Moiré fringe pattern and to check the ability of the fibre optics bundle approach for Moiré fringe pattern displacement quantification. Taken from (Chen et al., 2010).

Inspired by Horowitz et al. (2004), Chen et al. (2014, 2010) developed the second generation of the sensor with the Moiré fringe pattern by miniaturizing the overall sensor packaging. The sensor structure was designed similar to the previous studies by utilising the classical straight $1260\ \mu\text{m} \times 10\ \mu\text{m}$ micro-springs on four corners of a $1500\ \mu\text{m} \times 1000\ \mu\text{m}$ floating element. Fibre optics were used to reduce the size of the sensor packaging and to improve the sensor robustness compared to the microscope-based sensors. Two bundles of 16 fibre optics cables were used to constantly send the light from the light source to the sensor at the same time, and to transmit the light from the sensor die to 16 photodiodes. A proof of concept setup was developed as illustrated in Figure 2.35 to mimic the sensor with the Moiré fringe pattern and to investigate the capability of the miniaturized sensor with the fibre optics bundle in detecting the small displacements. The test results from this proof of concept test-bed showed a mechanical sensitivity of $12.4\ \text{nm}/\text{Pa}$, which was calculated by using multiple Moiré fringe shift estimation methods. Employing the fibre optics bundle in the sensor was a step forward toward miniaturizing the overall sensor packaging, which resulted in elimination of the sensor's sensitivity to EMI and out of plane motions, which makes this technique robust for the turbulence and harsh environments measurements. Though, this device suffered from various factors such as spatial debris on the Moiré fringe pattern, uneven spacing of the fibres, varying sensitivity between the photo-detectors, and scrambled transmit-receive fibres. Moreover, since all the fibre optics were illuminating the sensor at the same time, the device suffered from the presence of optical cross-talk between adjacent source-receive fibre pairs. This is due to the fact that a portion of the reflected light from each fibre optics is detected by the adjacent receiving fibre optics. This

cross-talk needed to be quantified and resulted in measurement error. In addition, manufacturing misalignment in the fibre optics array resulted in signal intensity reduction and interference. The overall size of the device that plays an important role in the sensor performance, also was limited by the size of the fibre optics core and cladding, which explains the reason for the relatively large size of the floating element on this sensor.

Built upon previous research efforts in utilising the Moiré fringe pattern transduction in wall-shear stress sensors, Mills et al. (2016, 2015) developed a sapphire optical MEMS wall-shear stress sensor for high temperature applications and harsh environments. Picosecond pulsed laser micromachining was used to pattern a 2 mm × 2 mm floating element and four folded-beam micro-springs of 2 mm × 70 μm on the sapphire substrate. Optical gratings were generated using platinum thin-film to provide the ability of measurements in a theoretical maximum temperature of 800°C. Four channels of sapphire fibre optics and four photodiodes were used to form a quadrature configuration to detect the Moiré fringe pattern shift; see Figure 2.36. In this arrangement, four discrete segments on the Moiré fringe pattern were selected and four 120 μm fibre optics cables with a spacing of 250 μm were used to measure the intensity on each segments. The output voltage from each section on the pattern was then recorded to calculate the phase shift and the displacement of the Moiré fringe pattern eventually. Sensor characterisation results presented a sensitivity value of 76.8 μV/Pa that corresponds to a theoretical mechanical sensitivity of 1.8 nm/Pa, a resonant frequency of 3.5 kHz, and a minimum detectable wall-shear stress of 4.6 mPa. Using the quadrature configuration was a modification to the previous generations of the sensors with the geometric Moiré

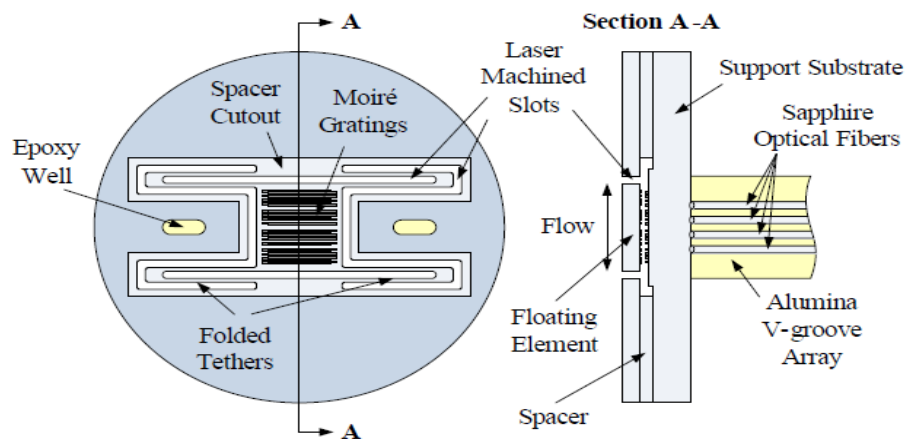


Figure 2.36 Sapphire wall-shear stress sensor with Moiré fringe transduction and four fibre optics for high temperature applications. Image is taken from (Mills et al., 2016).

fringe pattern, by means of reducing the number of fibre optics and also enhancing the sensor performance by reducing the cross-talk effect existing between the receiving fibre optics. However, the poor performance on two channels in the sensor affected the total sensor performance and prevented an accurate estimation of the Moiré fringe pattern phase shift in the quadrature configuration. Moreover, due to direct implementation of the fibres, the overall sensor size is limited by the size of the fibre optic cables and the spacing between them. Improvement is required in some areas in the sensor fabrication on the sapphire substrate and in the sapphire fibre optics array fabrication, such as the survivability of the gratings in high temperature, substrate bonding, and the laser machining of the floating element, which introduce thermal damages to the device and results in trapezoidal micro-springs cross section. On top of these, although the sensor was designed for harsh environment and for high temperature applications, its characterisation was performed in the lab environment. In the lab environment the temperature did not go beyond the room temperature, and therefore the effect of high temperature on the sensor performance is unknown and requires further investigation.

2.3 Summary

This chapter reviewed various techniques that are used in the wall-shear stress measurement, their merits and limitations. The measurements methods categorised into direct and indirect based on their transduction, and macro-scale (conventional) and MEMS-based devices based on their sensing element size. Section 2.1 reviewed the conventional techniques for the wall-shear stress measurements such as Pitot tubes, Preston tubes, Stanton tubes, and oil film interferometry. As discussed, these techniques suffer from poor spatial and temporal resolutions by reason of their size, and their performance does not satisfy the turbulence measurement requirements. Realising the limitation of the conventional methods, Section 2.2 presented the direct and indirect MEMS-based measurement techniques. Different transduction schemes were employed in the sensors; each showing promises and drawbacks for which more research and development is required.

A summary of the MEMS-based wall-shear stress sensors specifications is presented in Table 2.1. Indirect MEMS wall-shear stress sensors include thermal sensors, micro-fences, micro pillars, and indirect optical techniques. Wall-shear stress sensors with thermal transduction are effective in measuring both mean and fluctuating values of the wall-shear stress. Nonetheless, they are influenced by the thermal properties of the fluid and therefore, they should be used for measurements in the same environment as they are being calibrated. Moreover, these sensors are susceptible to temperature drift, which makes it difficult to get a unique calibration curve to relate the heat transfer to the wall-shear stress. In addition to the temperature drifts, the heat transfer from the sensing element to the substrate influences the sensor performance and introduces additional error into the measurement. Furthermore, these devices are not capable of directional measurement and, as a result of this, they cannot be used to detect the reversal events in the fluid flow.

Surface fences poses limited spatial resolution due to the large length of the sensing element in the spanwise direction, leading to an increased surface area. In addition to poor spatial resolution, the piezoresistive transduction on these devices can be affected by temperature variations. The small diameter of micro-pillar devices results in a high spatial resolution. Nevertheless, the measurement resolution is limited by the resolution of the optical facilities that are used to capture the micro-pillar displacement. Capturing the fluctuations in the turbulent boundary layer requires high speed image sensors. The optical instrumentation, which is integrated into the micro-pillar sensing system, is normally costly and bulky, making it challenging to execute wind tunnel measurements. Additionally, the micro-pillars can protrude out the viscous sublayer in higher Reynolds numbers thereby resulting in flow disruption.

Indirect sensors with optical transduction demonstrate higher performance among the MEMS-based indirect techniques since they provide high spatial resolution and do not require calibration. Despite this, further development is required before the commercialisation of these devices, since this sensor requires complex instrumentation with precise alignment. As discussed, the data rate on these devices can be too low to enable the post processing of the acquired data.

Direct MEMS wall-shear stress sensors were introduced and reviewed in Section 2.2.2. These sensors are promising as they can directly measure both the value and

direction of the wall-shear stress. Capacitive, piezoresistive, and optical transduction methods are used to read the displacement of the sensors under the shear force.

The fabrication of the capacitive MEMS wall-shear stress devices is straightforward and their sensitivity to temperature can be eliminated if a differential capacitance is used. However, these devices are susceptible to EMI and parasitic capacitance, which can influence the noise floor of the sensor and consequently the minimum detectable shear stress. Employing these sensors in liquid flow measurements is challenging and demands further packaging development to isolate the sensing fingers. Using TSVs technology eliminates the front side wire-bonding on the sensor die, however, utilising this method is costly and the sensor's performance is significantly influenced by its quality.

Devices with piezoresistive transduction can be used for measurement in both gas and liquid flows. Resistance variation due to the wall-shear stress is measured using a Wheatstone bridge. Balancing the Wheatstone bridge can be challenging and can result in an increased normal stress (pressure) sensitivity. The device performance is also effected by temperature variations.

Optical MEMS wall-shear stress sensors are immune to EMI and temperature effects since there are no electronics on the device. The lack of electronics on the sensor chip also eliminates the need for electrical connections to the sensor dies, which provides the opportunity for using low temperature electronics in a remote location. These sensors can also be used for measurements in conducting fluid flow. The packaging of the optical sensors are more complex compared to the capacitive and piezoresistive devices due to the implementation of optical elements and any misalignment in the optical system results in a poor performance of the sensor.

The principle of the optical MEMS sensors developed in this study is base on the direct measurement of the wall-shear stress using the floating element displacement detection. Here, the optical transduction is developed by employing the Moiré fringe pattern. The use of Moiré fringe pattern to measure the wall-shear stress is known in the prior art, the novel aspect of the developed sensors is in the way the movement of the Moiré fringe pattern is being tracked, which is done by utilising a rippling optoelectronics. In addition to the novel optoelectronics, serpentine micro-springs are employed in this study to achieve higher mechanical sensitivity over a reduced are, compared to the

A Review on Wall-Shear Stress Measurement Methods

classical micro-spring. The developed MEMS wall-shear stress are also are tested in the wind tunnel for instantaneous wall-shear stress measurement within the turbulent boundary-layer flows.

Table 2.1 Summary of the specifications of the MEMS wall-shear stress sensors.

Author	Type	Transduction	Sensing element size	Micro-spring size	Sensitivity	Resonant frequency	Minimum detectable wall-shear stress	Dynamic range
Sheplak et al. (2002)	Indirect	Thermal	N/A	N/A	11 mV/Pa	N/A	9 μ Pa/Hz	N/A
Haneef et al. (2007)	Indirect	CMOS Thermal	130 μ m \times 130 μ m	N/A	22 mV/Pa	N/A	N/A	up to 1.5 Pa
Von Papen et al. (2002)	Indirect	Surface fence	300 μ m \times 130 μ m	N/A	0.5 mV/(VNm ²)	N/A	Up to 6 N/m ³	-0.3Pa - 0.3 Pa
Schiffer et al. (2006)	Indirect	Surface fence	500 μ m \times 1500 μ m \times 700 μ m	N/A	6 mV/(VNm ²)	N/A	N/A	-0.3Pa - 0.3 Pa
Ma and Ma (2016)	Indirect	Surface fence	500 μ m \times 2200 μ m \times 70 μ m	N/A	2.3 mV/(V/Pa)	N/A	N/A	-0.7Pa - 0.7 Pa
Brücker et al. (2007)	Indirect	Micro-pillar	700 μ m \times 50 μ m	N/A	N/A	173 Hz	N/A	N/A
Schmidt et al. (1988)	Direct	Capacitive	500 μ m \times 500 μ m \times 30 μ m	1000 μ m \times 10 μ m \times 30 μ m	52 μ V/Pa	N/A	10 mPa	10 mPa - 1Pa
Pan et al. (1999)	Direct	Capacitive	N/A	N/A	1.02 V/Pa	N/A	N/A	Up to 10 Pa
Zhe et al. (2005)	Direct	Capacitive	500 μ m \times 200 μ m \times 50 μ m	3000 μ m \times 10 μ m \times 50 μ m	337 mV/Pa	N/A	40 mPa	0.04 Pa - 0.2 Pa
Chandrasekharan et al. (2011)	Direct	Capacitive	2000 μ m \times 2000 μ m \times 45 μ m	1000 μ m \times 23 μ m \times 45 μ m	7.66 mV/Pa	6.2 KHZ	14.9 μ Pa	14.9 μ Pa - 1.9 Pa
Sells et al. (2011)	Direct	Capacitive	1500 μ m \times 1500 μ m	N/A	474 kHz/Pa	N/A	4.1 mPa	4.1 mPa - 4 Pa
Meloy et al. (2011)	Direct	Capacitive	1000 μ m \times 1000 μ m \times 26 μ m	800 μ m \times 10 μ m \times 26 μ m	27 mV/Pa	4.6 KHZ	N/A	Up to 1.8 Pa
Barnard, Meloy and Sheplak (2016)	Direct	Capacitive	N/A	N/A	1.36 mV/Pa	3.4 KHZ	1.1 mPa	1.1 mPa - 1.9 Pa
Mills et al. (2017)	Direct	Capacitive	2000 μ m \times 400 μ m \times 60 μ m	1600 μ m \times 28 μ m \times 60 μ m	38.8 mV/Pa	1.4 KHZ	60 μ Pa	60 μ Pa - 1.9 Pa
Shajii et al. (1992)	Direct	Piezoresistive	120 μ m \times 140 μ m \times 5 μ m	30 μ m \times 10 μ m \times 5 μ m	13.7 μ V/V.kPa	N/A	1 kPa	1 kPa - 10 kPa
Li et al. (2008)	Direct	Piezoresistive	1000 μ m \times 1000 μ m \times 50 μ m	1000 μ m \times 30 μ m \times 50 μ m	4.24 μ V/Pa	6.7 KHZ	11.4 mPa	11.4 mPa - 2Pa
Tseng and Lin (2003)	Direct	Optical	1500 μ m \times 1500 μ m \times 520 μ m	N/A	1.538 nm/Pa	N/A	250 mPa	N/A
Horowitz et al. (2004)	Direct	Optical	1280 μ m \times 500 μ m \times 10 μ m	547 μ m \times 6 μ m \times 10 μ m	13 Pixels/Pa	1.7 KHZ	6.2 mPa	6.2 mPa - 1.3 Pa
Ayaz et al. (2011)	Direct	Optical	800 μ m \times 800 μ m	N/A	15.145 μ m/Pa	0.3 KHZ	N/A	Up to 2 Pa
Chen et al. (2010)	Direct	Optical	1500 μ m \times 1000 μ m	1260 μ m \times 10 μ m	12.4 nm/Pa	N/A	N/A	N/A
Mills et al. (2016)	Direct	Optical	2000 μ m \times 2000 μ m	2000 μ m \times 70 μ m	76.8 μ V/Pa (1.8 nm/Pa)	3.5 KHZ	4.6 mPa	4.6 mPa - 1.9 Pa

Chapter 3

MEMS Wall-Shear Stress Sensors

Modelling and Development

Important characteristics of MEMS wall-shear stress sensors such as sensor's sensitivity, resonant frequency, accuracy, and resolution depend on the mechanical structure of the devices as well as optoelectronics that are used as a part of sensors transduction technique. Hence, it is crucial to develop mechanical models for the sensor's structure alongside with test-beds to investigate and optimize the optoelectronics parts of the sensors.

This chapter provides information on the development of the MEMS wall-shear stress sensors. This includes details on the sensors structure's mechanical modelling using analytical and Finite-Element-Analysis (FEA), design and development of the sensors optical transduction technique, and optoelectronics that are forming the sensors control unit.

3.1 Sensors Mechanical Modelling

Mechanical design of the sensor structure is the key aspect of the sensor performance in turbulent flow measurement. Sensor's structure highly determines the spatial and temporal resolutions of the device measurement by forming the sensor's sensitivity as well as its resonant frequency. Mechanical structure of the MEMS wall-shear stress sensor consists of a central shuffle mass called the floating element, which has a width of W_e , a length of L_e , and a thickness of T , suspended on each side by up to four

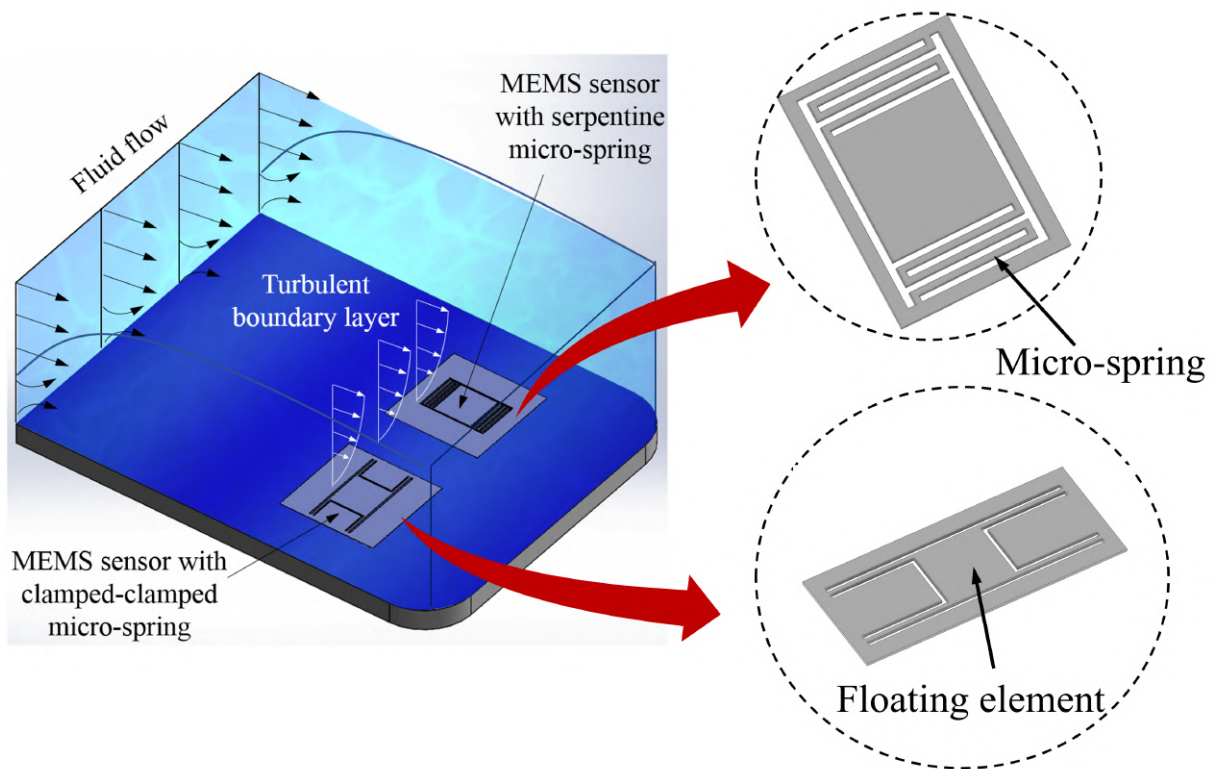


Figure 3.1 MEMS wall-shear stress sensor structures. Devices with clamped-clamped and serpentine micro-springs are designed for wall-shear stress measurements. As the air flows over the MEMS device, the floating element is free to move, courtesy of the micro-spring arrangements, in the direction of the fluid flow, whilst remaining parallel to the aerodynamic surface.

specially designed micro-springs, which are anchored to a fixed substrate. As illustrated in Figure 3.1, clamped-clamped and serpentine micro-springs are designed in this study to provide high mechanical sensitivity and ability of wall-shear stress measurements in air flows over a range of Reynolds numbers, alongside with having appropriate resonant frequencies.

As the air flows over the MEMS device, the floating element is free to move, courtesy of the micro-spring arrangements, in the direction of the fluid flow, whilst remaining parallel to the aerodynamic surface. The lateral displacement of the devices is directly related to the applied wall-shear stress, τ_w , via the micro-spring geometry. As the sensor deflects under the shear force, micro-springs act as restoring springs to resume the sensor's floating element to its equilibrium position. Euler-Bernoulli beam theory and energy methods are applied to the devices structure to obtain the equivalent stiffness of the micro-springs, devices mechanical sensitivity, equivalent mass, and resonant frequency of the devices. The Poisson ratio and Young's modulus are assumed to be constant. Floating element and the micro-springs are considered to be symmetric,

homogeneous, and linear. Moreover, the floating element is considered to be rigid, which means it moves rigidly under the shear stress force.

3.1.1 Clamped-clamped micro-spring model

In this configuration, the floating element is suspended by four beams acting as micro-springs. The length and the width of the beams are considered to be L_t and W_t . One side of each micro-beam is connected to each corner of the floating element whilst the other end is connected to a fixed substrate. Static deflection of sensors can be modelled over one half of the device as a result of floating element and micro-springs symmetry (Schmidt, 1988); please see Figure 3.2a. The floating element of the device is assumed to move rigidly under the shear force (Schmidt, 1988). This means the shear force

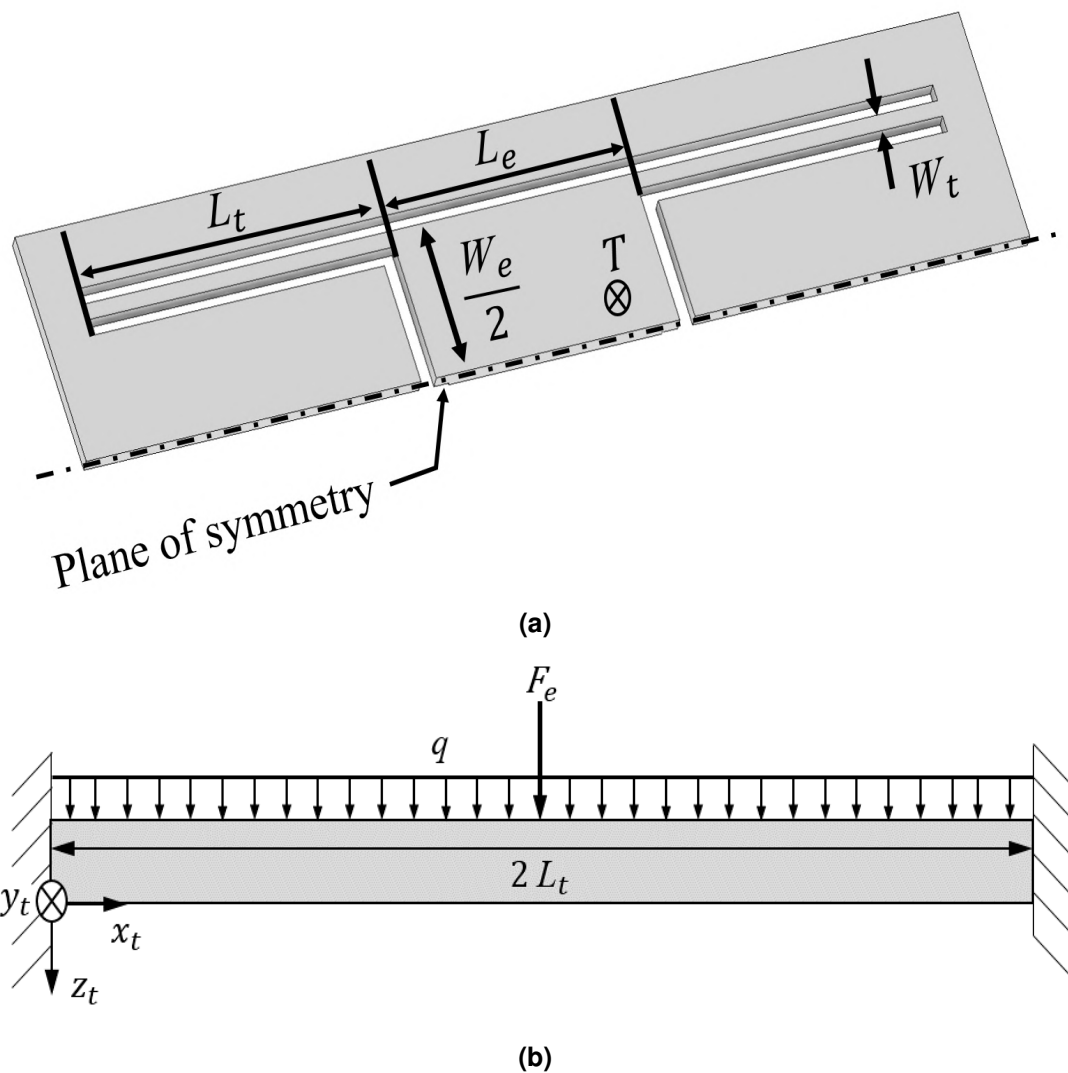


Figure 3.2 Mechanical modelling of MEMS devices with clamped-clamped micro-springs. (a) Half plane model, (b) Mechanical model of clamped-clamped micro-spring.

applied to the floating element by the flow can be modelled as a single point force acting at the center of the equivalent micro-beam model

$$F_e = \frac{1}{2} \tau_w W_e L_e \quad (3.1)$$

This force is divided by two, since there are two sets of clamped-clamped micro-springs in this configuration. Moreover, as a result of rigid displacement of the floating element, the connecting ends of each micro-beam pair to the floating element have identical deflection and slope, each set of micro-springs can be treated as a clamped-clamped beam of length $2L_t$ as it is shown in Figure 3.2b. The distributed shear-force per unit length, q , acting on the surface of each micro-spring is expressed by

$$q = \tau_w W_t \quad (3.2)$$

Considering that the micro-springs length is much larger compared to their width, $L_t \gg W_t$ and that the device deflections are small compared to the thickness of the device (normally by two orders of magnitude), the Euler-Bernoulli beam theory (Beer et al., 2006) can be used to obtain the deflection and stiffness of the micro-springs. In addition, to use the Euler-Bernoulli theory to simplify the model, the micro-spring material is considered to be isotropic and homogeneous. In the Euler-Bernoulli beam theory, the rotation of the beam's cross sections is negligible compared to the bending deformation. Moreover, the angular distortion of the beam due to shear is neglected. When plane sections of the beam remain plane and normal to the beam's centerline, the displacement field of any point in the beam's cross section can be expressed as

$$\begin{aligned} u(x, y, z) &= -z \frac{\partial w(x)}{\partial x} \\ v(x, y, z) &= 0 \\ w(x, y, z) &= w(x) \end{aligned} \quad (3.3)$$

where u, v , and w are the displacement components corresponding to x, y , and z axis respectively. Corresponding strain field can be given by

$$\varepsilon_{xx} = \frac{\partial u}{\partial x} = -z \frac{\partial^2 w}{\partial x^2} \quad (3.4)$$

$$\varepsilon_{yy} = \varepsilon_{zz} = \varepsilon_{xy} = \varepsilon_{yz} = \varepsilon_{zx} = 0$$

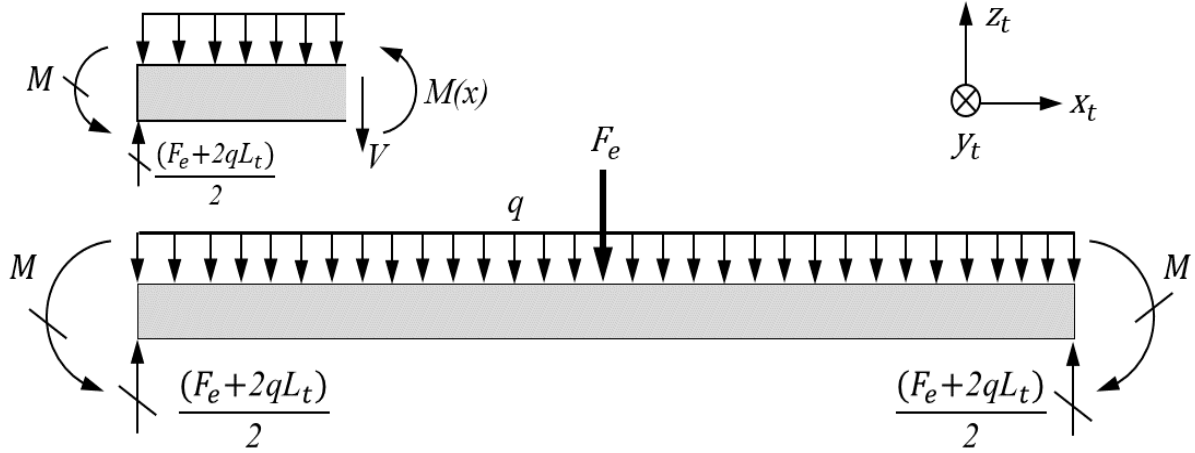


Figure 3.3 Free body diagram of the clamped-clamped micro-spring.

The Euler-Bernoulli beam equation can be obtained using Equation 3.4 as

$$EI \frac{\partial^2 w}{\partial x^2} = -M(x) \quad (3.5)$$

where E is the Young's modulus and I is the beam's cross section moment of area. $M(x)$ is the moment applied to the beam as a result of external loads and can be derived as

$$M(x) = -q \frac{x^2}{2} + \frac{(F_e + 2qL_t)}{2} x - M \quad (3.6)$$

where M can be written as

$$M = \frac{F_e L_t}{4} + \frac{q L_t^2}{2} - \frac{q L_t^2}{6} \quad (3.7)$$

Applying the clamped-clamped beam's boundary conditions

$$\begin{aligned} w(x) \Big|_{x=0} &= 0 \\ \frac{dw(x)}{dx} \Big|_{x=0} &= 0 \\ \frac{dw(x)}{dx} \Big|_{x=L_t} &= 0 \end{aligned} \quad (3.8)$$

and by substituting Equation 3.1, Equation 3.2, and Equation 3.6 in Equation 3.5 , the deflection of the clamped-clamped micro-spring under the wall-shear stress can be derived as

$$w(x) = \frac{\tau_w}{4ETW_t^3} [2W_t x^4 - (2W_e L_e + 8W_t L_t) x^3 + L_t (3W_e L_e + 8W_t L_t) x^2] \quad (3.9)$$

The displacement of the MEMS wall-shear stress sensor with clamped-clamped micro-spring is equal to the deflection of the modelled clamped-clamped beam at the center point, $x = L_t$ (Schmidt, 1988)

$$\delta_{\tau_w} = w(L_t) = \frac{\tau_w W_e L_e}{4ET_t} \left[\frac{L_t}{W_t} \right]^3 \left[1 + 2 \frac{W_t L_t}{W_e L_e} \right] \quad (3.10)$$

and total stiffness of the structure with clamped-clamped micro-spring is

$$K_{cc} = \frac{\tau_w W_e L_e}{\delta_{\tau_w}} = 4ET_t \left[\frac{W_t}{L_t} \right]^3 \left[\frac{1}{\left(1 + 2 \frac{W_t L_t}{W_e L_e} \right)} \right] \quad (3.11)$$

3.1.2 Serpentine micro-spring

Serpentine micro-springs are used as the second type of suspension for the MEMS wall-shear stress sensors as shown in Figure 3.1. The serpentine micro-spring is generated by repeated meanders. In the MEMS wall-shear stress sensor, the length of each meander is L_c and the width of the each meander is L_t . As it is depicted in Figure 3.4, each meander consists of a span beam and a connector beam.

The sections that span the width of the meanders are the span beams, and the components that connect the span beams are connector beams. Mechanical sensitivity of the MEMS wall-shear stress device enhances significantly by adding extra meanders to the micro-spring. In addition, using serpentine micro-spring reduces the occupied area compared to classic clamped-clamped micro-spring which has same values of sensitivity. In the current MEMS wall-shear stress sensor design, floating elements and micro-springs are connected by a connector beam. Moreover, all the span beams have identical length and the thickness is fixed across the devices.

In order to derive the stiffness of the serpentine micro-spring, the boundary conditions are determined at the ends of the micro-spring. Similar to the clamped-clamped micro-spring case, the floating element considered to move rigidly under the fluid flow resulting in guided-end boundary condition at the connecting end of the serpentine micro-spring to the floating element. To find the stiffness in one direction, rotation and displacement in other directions are chosen to be zero. Free body diagram of the serpentine micro-spring with n number of folding (meander) is illustrated in Figure 3.5. The micro-spring is divided into the beam sections and reaction forces and moments at each end of beams are determined by applying the Newton's third law. These forces and moments are determined in terms of the forces and the moments at the end section of the serpentine micro-spring and then the moments in each section can be expressed in terms of the position in the beam. In case of serpentine micro-spring, energy methods are used to derive the force and the moments at the connecting point to the floating element. The deflection of the micro-spring is extracted by applying the theorem of least work or Castiglino's theorem (Beer et al., 2006). Based on this theorem, the deflection can be derived using the first partial derivatives of the total strain energy with respect to a given load.

$$\delta_i = \frac{\partial U}{\partial F_i} \quad (3.12)$$

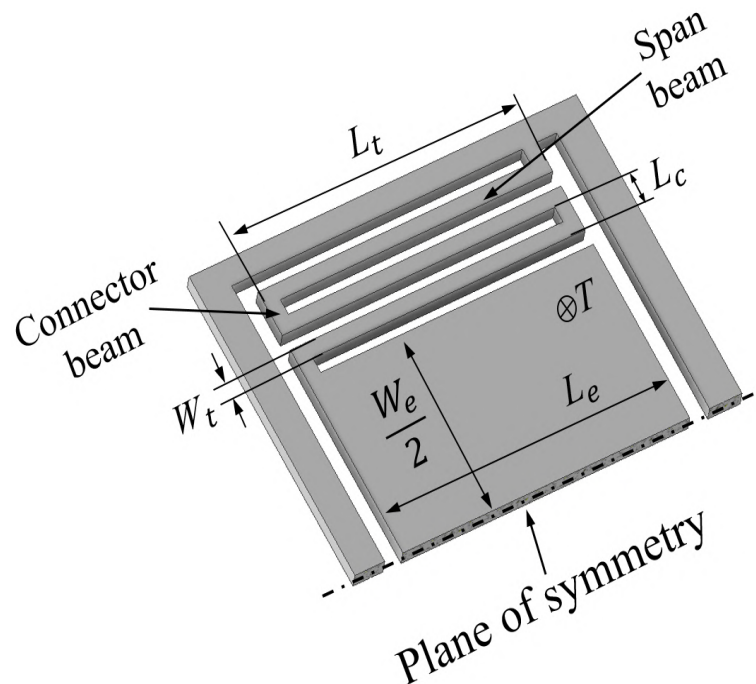


Figure 3.4 Mechanical Model of a MEMS wall-shear stress device with serpentine micro-spring

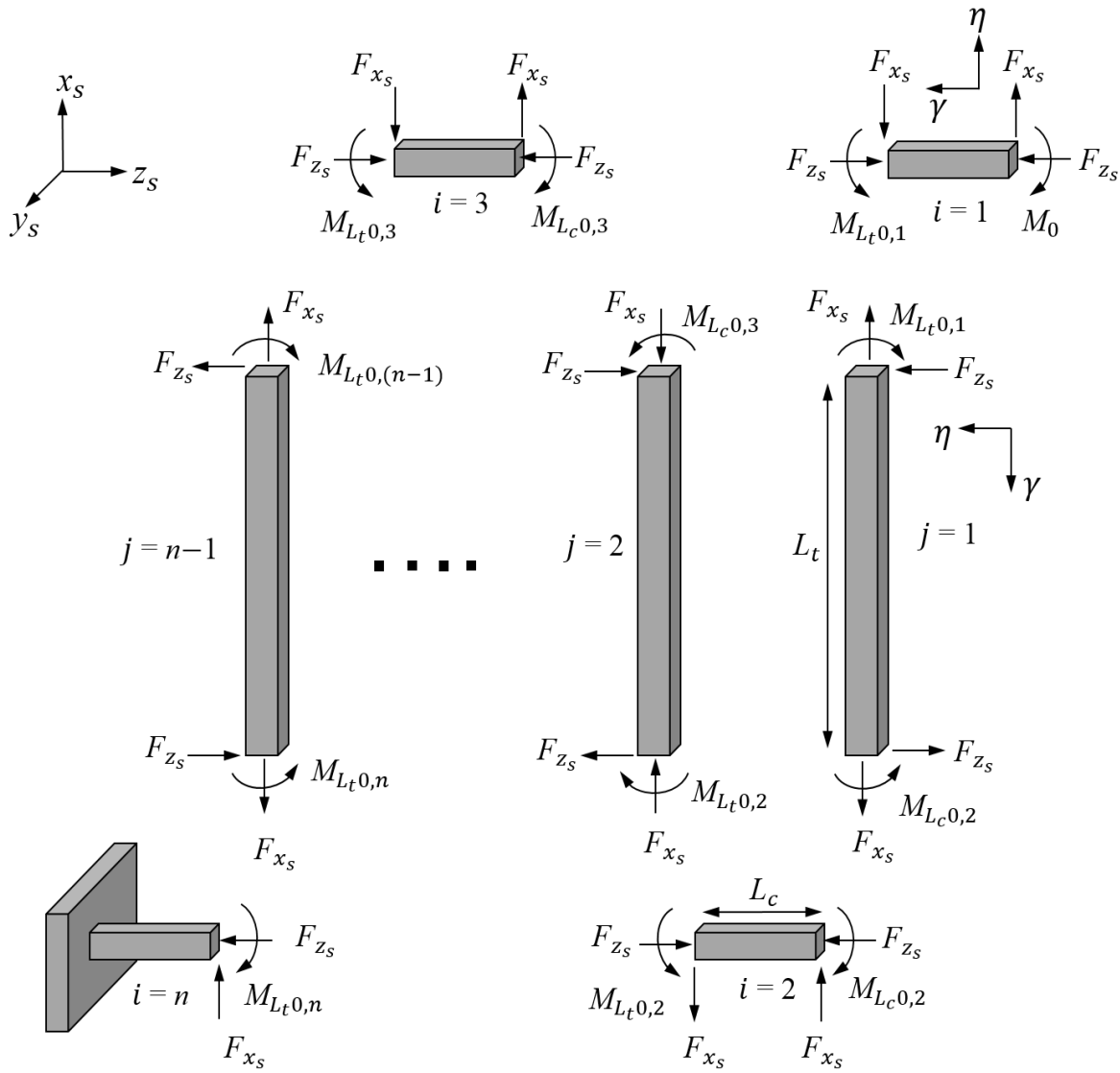


Figure 3.5 Free body diagram of the serpentine micro-spring

It can be seen in Figure 3.5 that the number of span beams, indexed $j = 1$ to $j = n - 1$, is one less than the number of connector beams, indexed $i = 1$ up to $i = n$. The length of the span beams are L_t , the length of the connector beams are L_c , the width of the connector beams and span beams are equal to w_t , and the thickness of the micro-spring is T . Span beams and connector beams have their own coordinate system, $\eta - \gamma$, where γ -coordinate is alongside each beam section length. From the micro-spring's free body diagram, the moment in i th connector beam can be expressed as (Fedder, 1994)

$$M_{L_c,i} = M_0 - F_{z_s} [\gamma + (i - 1)L_c] - \left[\frac{1 + (-1)^i}{2} \right] F_{x_s} L_t \quad (3.13)$$

for $i = 1$ to n , and the moment in the j th span beam is

$$M_{L_t,j} = M_0 - jF_{z_s}L_c + F_{x_s} \left[(-1)^j \gamma - \left(\frac{1+9-1}{2} \right)^j L_t \right] \quad (3.14)$$

for $j = 1$ to $n - 1$. The total energy in the micro-spring then can be expressed as

$$U = \sum_{j=1}^{n-1} \int_0^{L_t} \frac{M_{L_t,j}^2}{2EI_{L_t}} d\gamma + \sum_{i=1}^n \int_0^{L_c} \frac{M_{L_c,i}^2}{2EI_{L_c}} d\gamma \quad (3.15)$$

where E in the Young's modulus, and I_{L_t} and I_{L_c} are the moment of inertial for the span beams and connector beams, respectively. In order to calculate the serpentine micro-spring deflection in x_s direction the displacement in z_s and y_s directions and the micro-spring rotation are considered to be equal to zero.

$$\begin{aligned} \delta_{x_s} &= \frac{\partial U}{\partial F_{x_s}} \\ \delta_{z_s} &= \frac{\partial U}{\partial F_{z_s}} = 0 \\ \Psi_0 &= \frac{\partial U}{\partial M_0} = 0 \end{aligned} \quad (3.16)$$

Similar to x_s direction, mechanical stiffness of the serpentine micro-spring in z_s can be calculated using following considerations

$$\begin{aligned} \delta_{x_s} &= \frac{\partial U}{\partial F_{x_s}} = 0 \\ \delta_{z_s} &= \frac{\partial U}{\partial F_{z_s}} \\ \Psi_0 &= \frac{\partial U}{\partial M_0} = 0 \end{aligned} \quad (3.17)$$

Hook's law (Singiresu et al., 1995) can be applied alongside Equation 3.17, Equation 3.16, and Equation 3.15 to derive the stiffness of the serpentine micro-spring in z_s and x_s directions. The equivalent stiffness can in each direction is expressed in terms of odd or even number of foldings, n , in the micro-spring. For odd number of foldings

$$K_{z_s} = \frac{24EI_{L_t}[(\tilde{I} + L_t)n - L_t]}{(n-1)L_t^2 [(3\tilde{I}^2 + 4\tilde{I}L_t + L_t^2)n + 3\tilde{I}^2 - L_t^2]} \quad (3.18)$$

where

$$\tilde{I} = \frac{L_c I_{L_t}}{I_{L_c}} \quad (3.19)$$

and

$$K_{x_s} = \frac{24EI_{L_c}}{nL_c^2 \left[\left(\frac{L_c I_{L_t}}{I_{L_c}} + L_t \right) n^2 - 3L_t n + 2L_c \right]} \quad (3.20)$$

For serpentine micro-spring with even number of foldings

$$K_{z_s} = \frac{24EI_{L_t} [(\tilde{I} + L_t)n^2 - 3L_t n + 2L_t]}{L_t^2 [(3\tilde{I}^2 + 4\tilde{I}L_t + L_t^2)n^3 - 2(5\tilde{I} + 2L_t)L_t n^2 + (5L_t^2 + 6L_t\tilde{I} - 9\tilde{I}^2)n - 2L_t^2]} \quad (3.21)$$

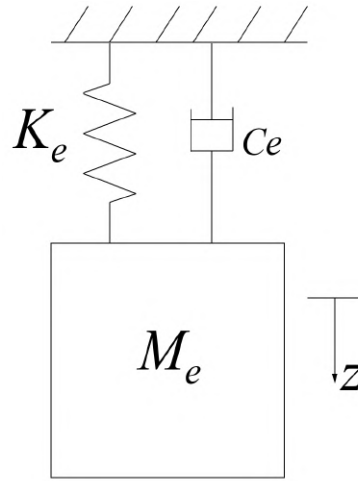
and

$$K_{x_s} = \frac{24EI_{y_s, L_t} [(3\tilde{I} + L_t)n - L_t]}{L_c^2 n [(3\tilde{I}^2 + 4\tilde{I}L_t + L_t^2)n^3 - 2(5\tilde{I} + 2L_t)L_t n^2 + (5L_t^2 + 6\tilde{I}L_t - 9\tilde{I}^2)n - 2L_t^2]} \quad (3.22)$$

3.1.3 Dynamic modelling of MEMS wall-shear stress sensors

Turbulence is a time varying phenomena and it contains frequency contents. MEMS wall-shear stress sensors are used to measure the time varying components of the wall-shear stress in the turbulent flow making it essential to consider the dynamics response of the device. Particularly, it is crucial to find the first resonant frequency of the MEMS wall-shear stress device structure. To detect and measure the turbulent flow fluctuations, the resonant frequency of the MEMS wall-shear stress sensors must be higher than the frequency spectrum of the turbulent flow. Lumped Element Modelling (LEM) is employed to find the device's dynamic characteristics. Assuming that the deflection in the MEMS devices is linear, and considering the floating element as the shuffle mass connected to the micro-springs, 1D MEMS wall-shear stress sensors can be considered as a lumped single degree of freedom (SDOF) mass-spring-damper vibrating system, as illustrated in Figure 3.6. For SDOF system, the equation of motion can be written as

$$M_e \frac{\partial^2 z}{\partial t^2} + C_e \frac{\partial z}{\partial t} + K_e z = F(t) \quad (3.23)$$



(a)

Figure 3.6 Lumped element models for the MEMS devices where 1D sensors are modelled as a SDOF system.

where M_e , is the equivalent mass, C_e , is the equivalent damping, K_e is the equivalent stiffness, and $F(t)$ is the driving force. The frequency response for the SDOF mass-spring-damper system is

$$H(j\omega) = \frac{1}{(j\omega)^2 M_e + (j\omega) C_e + K_e} \quad (3.24)$$

where j is the imaginary unit. Considering $\omega = 2\pi f_{res}$, the undamped resonant frequency of the system is expressed as (Singiresu et al., 1995)

$$f_{res} = \frac{1}{2\pi} \sqrt{\frac{K_e}{M_e}} \quad (3.25)$$

The existence of damping in the system can be a sequence of the drag generated by the fluid flow that is passing through the gap between the sensor floating and the fixed substrate underneath the floating element. This is known as slide film effect, which occurs when two plates are separated by a distance and slide parallel to each other.

Assuming the air flow to be incompressible and considering the fact that the floating element displacement is lateral, the fluid flow in the gap can be considered to be Couette flow (White, 2016) and its velocity can be expressed as (Schmidt, 1988)

$$u_x(y) = u_{fe} \left(\frac{y}{h_{gap}} \right) \quad (3.26)$$

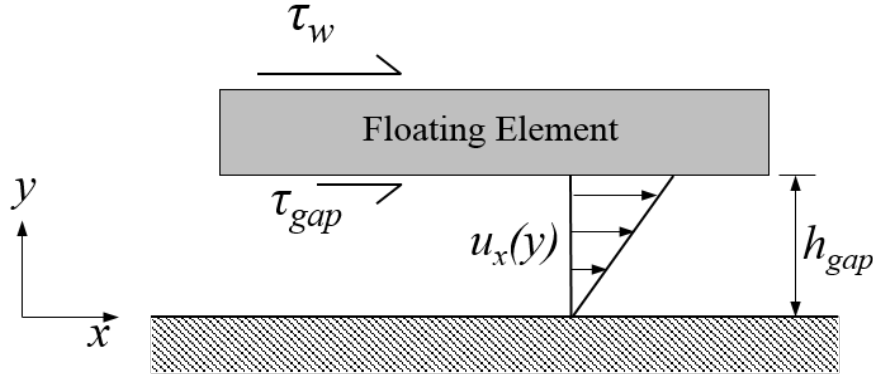


Figure 3.7 Slide-film damping between the sensor floating element and the fixed substrate. τ_{gap} is the shear stress that is applied to the lower surface of the floating element due to the fluid flow through the gaps in the sensor.

In previous equation, h_{gap} is the height of the gap between the floating element and the fixed substrate and U_{fe} is the velocity of the floating element. The drag force induced by the shear-stress in the gap is

$$F_{drag} = \tau_{drag} L_e W_e = \mu \frac{\partial u_x(y)}{\partial y} L_e W_e = \mu L_e W_e \frac{u_{fe}}{h_{gap}} \quad (3.27)$$

Considering $u_{fe} = \frac{\partial x}{\partial t}$, the damping coefficient is derived as

$$C_e = \frac{\mu L_e W_e}{h_{gap}} \quad (3.28)$$

3.1.4 Pressure gradient effects

Existence of gaps around and floating element and between the floating element and the fixed glass substrate, induce additional forces to the floating element in the flows with large pressure gradients. The effect of these additional forces should be quantified so that to reduce the measurement errors in environments with a different pressure gradient or zero pressure gradient environments. As shown in Figure 3.8, the first source of these additional forces is the additional shear stress induced by the flow passing through the gap between the floating element and the fixed substrate, τ_{gap} , which can be expressed as

$$\tau_{gap} = -\frac{g}{2} \frac{\partial P}{\partial x} \quad (3.29)$$

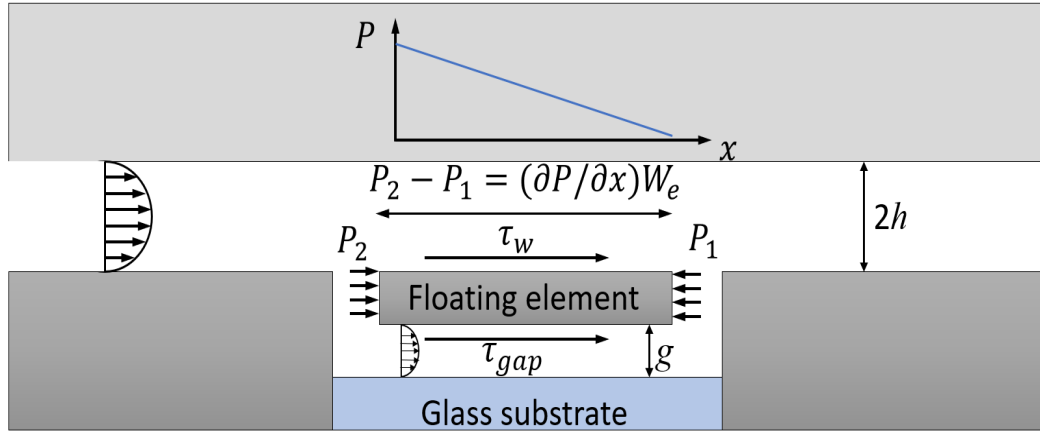


Figure 3.8 Illustration of the pressure gradient acting on the sides of the floating element and the additional wall-shear stress term on the bottom face of the floating element.

in which g is the gap size between the floating element and the fixed substrate, and $\partial P/\partial x$ is the pressure gradient across the length of the floating element. Other source of the additional forces, is due to the pressure difference acting on the leading edge, P_2 , and the trailing edge, P_1 , of the floating element, which is written as (Schmidt, 1988)

$$P_2 - P_1 = W_e \left(\frac{\partial P}{\partial x} \right) \quad (3.30)$$

The sum of all these forces can be written as

$$\Sigma F_x = \tau_w (W_e L_e) + \tau_g (W_e L_e) + (P_2 - P_1) (L_e T) \quad (3.31)$$

and hence the total effective wall-shear stress, τ_{eff} , on the sensor in the calibration rig can be obtained by dividing the resultant force to the floating element areas as

$$\tau_{eff} = \tau_w + \tau_{gap} + \left(\frac{\partial P}{\partial x} \right) T \quad (3.32)$$

3.1.4.1 Computational Fluid Dynamics Modelling

In order to further investigate these effects and verify the theory, the fluid flow in the calibration rig and around the sensor is modelled using computational fluid dynamics (CFD) in ANSYS Fluent. With the flow being laminar, incompressible, and the duct being uniform, 2D fluid analysis is selected. The fluid flow is fully developed by the time it reached the sensor, only a shortened length of $2000 \mu\text{m}$ is chosen over the actual

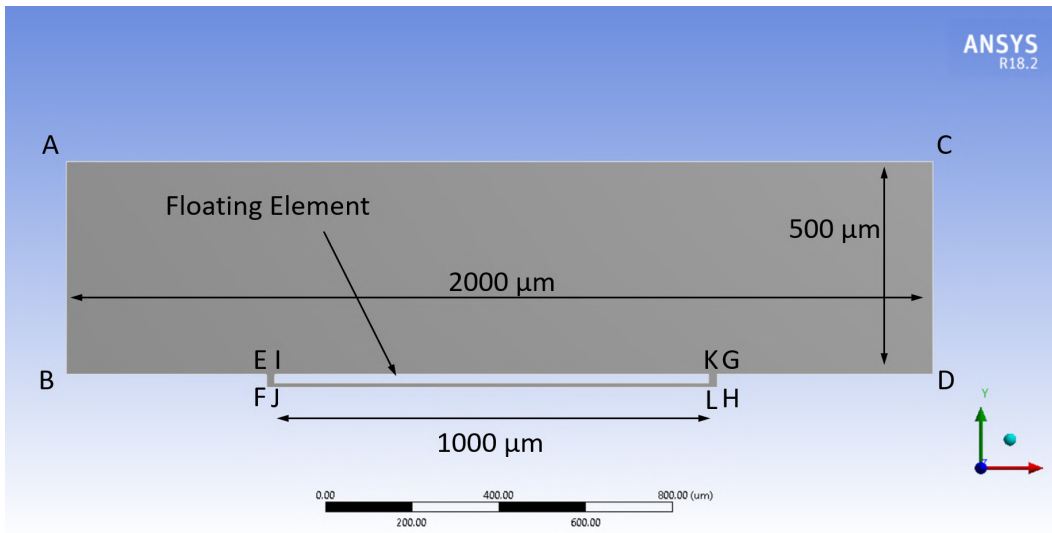


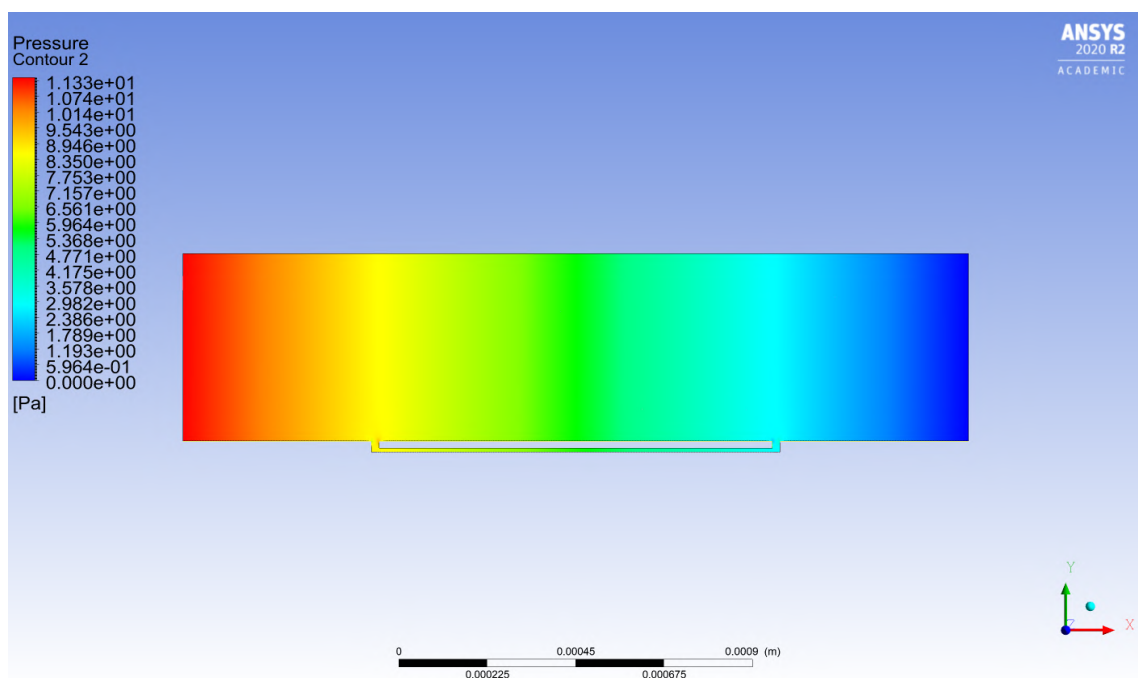
Figure 3.9 2D geometry of the calibration rig with the floating element placed at the center of it. The flow boundary conditions are a fully developed laminar flow velocity inlet and a atmospheric pressure outlet.

length of 2m to allow for a more defined mesh to be set for the program to calculate. A 2D floating element with a length of 1000 μm is placed at the center of the model, flush with the bottom wall, with the gaps presented around it, as depicted in Figure 3.9. The gap size between the floating element and the substrates on its leading and trailing edges is set to be is selected to be 20 μm , while the gap between the floating element and the glass substrate, g , is taken to be 10 μm . The solution is solved for steady-state conditions to provide results for a fully-developed flow, which is a representative of the flow in the calibration duct as the differential pressure values are taken when the flow is fully-developed. The boundaries are labelled from A to L. Boundary AB is the flow inlet where the flow enters and it is set as a fully developed velocity inlet. As this is a fully developed flow, the inlet velocity profile, $u(y)$ is expressed as the parabolic function of (White, 2016)

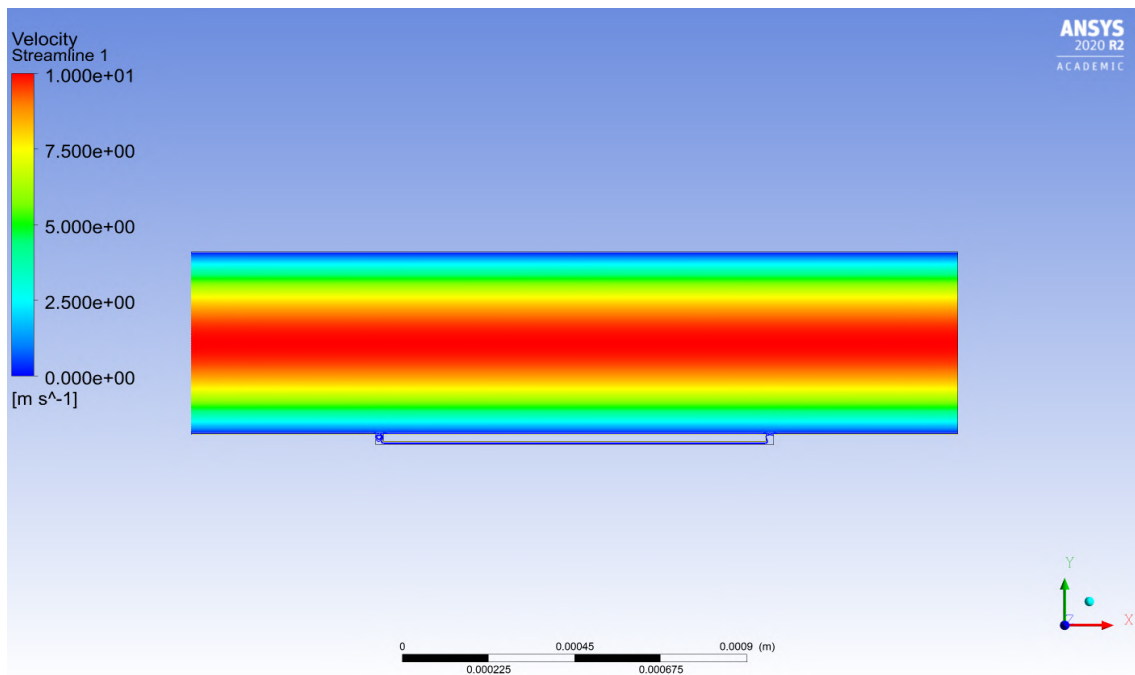
$$u(y) = \frac{Q}{A} \left[1 - \left(\frac{y-h}{h} \right)^2 \right] \quad (3.33)$$

where, Q , is the flow rate, A is the cross section area of the rig, and h , is the channel's half height. Boundary CD is set as a pressure outlet, where the flow exists the rig. This is open to atmosphere and hence, the gauge pressure is set to zero. Boundaries, AC, BE, EF, GH, and GD are set as stationary walls with no slip condition. Similarly, the floating element's surface, which are represented by IK, IJ, JL, and KL are set to be stationary walls with no slip conditions.

A residual convergence criterion of $1e-6$ allows the values to reach a steady solution and the resultant decision to be based on a single repeatable value. This solution needs to be independent of the mesh resolution to ensure that it is accurate. Adaptive mesh sizing with a element size of $2.5 \mu\text{m}$ was set so that there would be adequate number of elements in the model, specially in the gaps around the sensor. Two inflation layers were used in the flow inlet and outlet, and in the gap areas for a more precise analysis. The contour maps for the pressure distribution and the velocity profile along the rig are presented in Figure 3.10. It can be seen that the pressure decreases linearly across the rig as expected. Moreover, based on the velocity profile, it is clear that the flow is fully-developed at the inlet, with a maximum velocity of 10 m/s at the centerline. The values of the wall-shear stress are obtained for the top surface of the floating element, τ_w , and the bottom surface of the floating element, τ_g , and illustrated in Figure 3.11. For the maximum velocity of 10 m/s in the rig, $\tau_w = 1.43 \text{ Pa}$ and $\tau_g = 0.028 \text{ Pa}$, meaning that the value of the wall-shear stress on the bottom surface is 1.9% of the wall-shear stress on top surface. The additional wall-shear stress due to the pressure gradient on two sides of the floating element is also obtained to be equal to 0.11 Pa , which is equal to $0.07 \tau_w$. The effective wall-shear stress for this model then can be calculated as $\tau_{eff} = 1.56 \text{ Pa}$, which is 9% larger than τ_w .



(a)



(b)

Figure 3.10 (a) A contour plot showing the pressure gradient in the rig across the sensor. (b) A contour map showing the velocity profile in the rig. It can be noticed from the velocity contour that the flow is fully-developed when it enters the model.

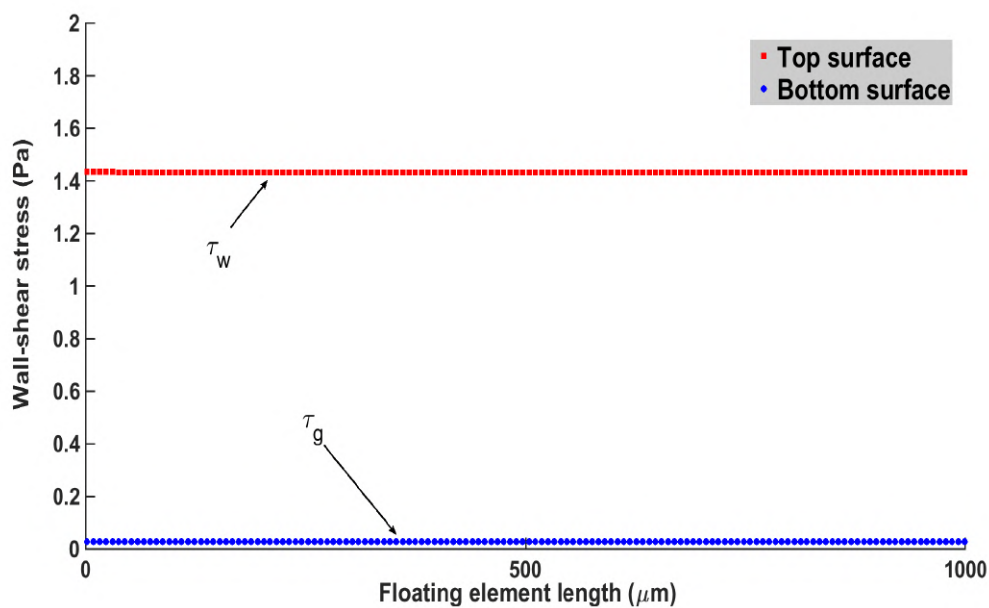


Figure 3.11 Wall-shear stress values on the top and bottom surface of the floating element obtained by CFD modelling .Blue circles represent the wall-shear stress values on the bottom surface of the floating element, τ_g , and red squares represent the wall-shear stress on the top surface of the floating element, τ_w .

These results show that the additional forces on the floating element, which are due to the large pressure gradient, can affect the sensor’s reading, and hence it is necessary to quantify them.

3.1.5 Finite Element Analysis

Finite Element Analysis (FEA) is performed on 1D sensor models with both clamped-clamped micro-springs and serpentine micro-springs to verify the analytical models of the MEMS wall-shear stress devices. Finite element analysis is performed in static structural and Modal environment of ANSYS[®] software Workbench to analyse and calculate static deflections and dynamic behaviour (resonant frequency) of the sensors. Mechanical properties of silicon that are used for model validation, are presented in Table 3.1. A fine mesh is used in the model structures and fixed support constraint is applied to the end of the micro-springs and shear stress is applied to the top surface of the devices models to find the deflection under the wall-shear stress and compare the results with analytical models results.

Table 3.1 Mechanical properties of Silicon used for model verification.

Property	Value
Density (ρ)	2330 kg/m^3
Young's modulus (E)	168.9 GPa
Poission's ratio (ν)	0.27

The displacement contour of the MEMS wall-shear stress sensors with clamped-clamped micro-spring and serpentine micro-spring are illustrated in Figure 3.12. It can be seen that the displacement of the floating elements are equal to the displacement of at the end of the micro-springs, which means the floating elements undergo a rigid displacement. Floating element's displacement is calculated over a range of wall-shear stress, $0Pa < \tau_w < 2Pa$, for both analytical model and FEA model. The models comparison for 1D devices in Figure 3.13 shows that analytical model and FEA results are in excellent agreement. Three different sensor sizes are selected in this case and the simulations are preformed on the models. Based on the model, the deflection of devices under the wall-shear stress are linear. This is crucial in the turbulence measurement and the sensors should perform linearly to have an enhanced spatial detection performance. This is also important in dynamic characteristics of the devices as any nonlinearity produces harmonic distortion in the frequency domain (Naughton and Sheplak, 2002).

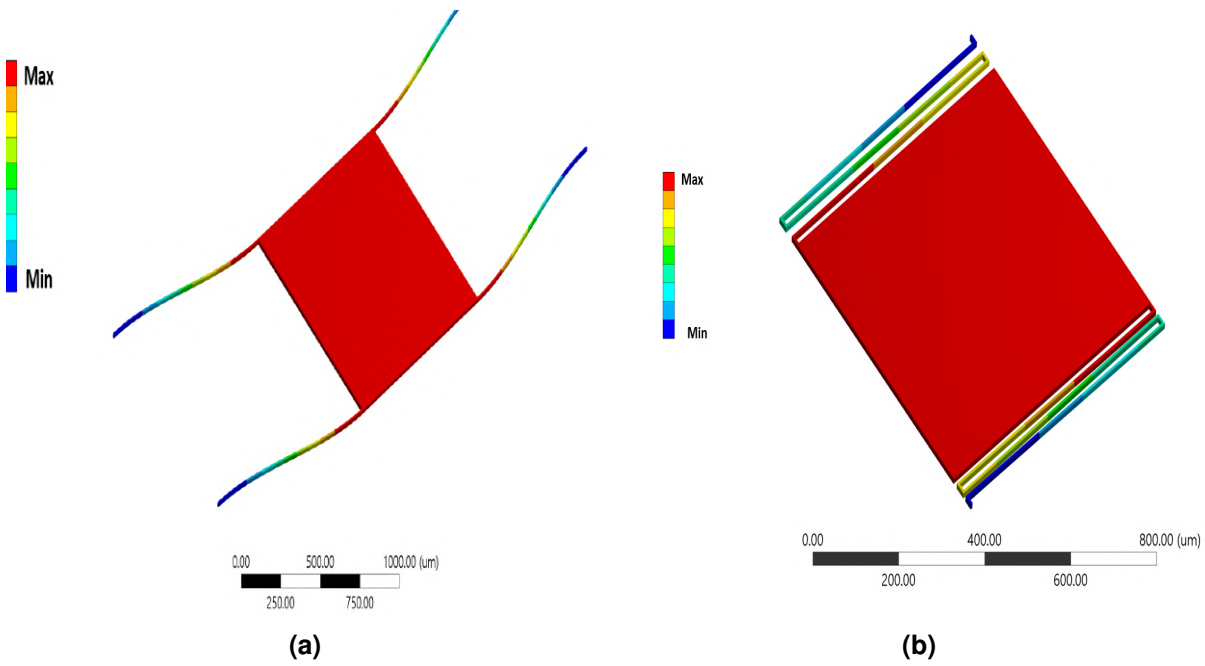


Figure 3.12 MEMS wall-shear stress sensors deflection model using FEA. (a) sensor with clamped clamped micro-spring. Sensor’s specifications in this model are $W_e = 1000\mu m$, $L_e = 1000\mu m, L_t = 1000\mu m, W_t = 7\mu m$, and $T = 20\mu m$, (b) sensor with serpentine micro-spring. Sensor’s specifications in this model are $W_e = 800\mu m$, $L_e = 800\mu m, L_t = 800\mu m, W_t = 7\mu m$, $T = 20\mu m$, and $n = 4$.

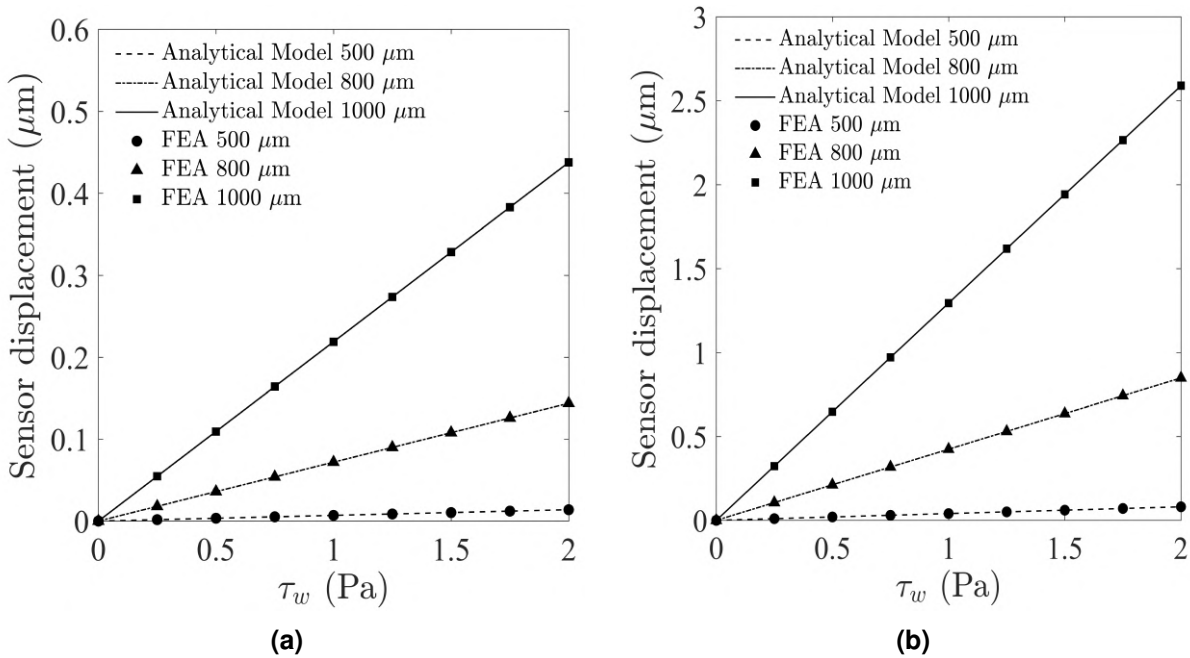


Figure 3.13 MEMS wall-shear stress sensor displacement. (a) Device with clamped-clamped micro-spring, (b) Device with serpentine micro-spring. Dashed lines (- - -) and black circles (●) represent the analytical model and FEA for devices with $W_e = 500\mu m$, $L_e = 500\mu m, L_t = 500\mu m$ respectively, dashed-dot line (- · - · -) and black triangles (▲) represent analytical model and FEA for devices with $W_e = 800\mu m$, $L_e = 800\mu m, L_t = 800\mu m$ respectively, and solid line (—) and black squares (■) represent analytical model and FEA for devices with $W_e = 1000\mu m$, $L_e = 1000\mu m, L_t = 1000\mu m$ respectively. Devices thickness and micro-spring width considered to be fixed and equal to $20\mu m$ and $7\mu m$.

Table 3.2 Sensors resonant frequency validation results.

Micro-spring	$W_e(\mu m)$	$L_e(\mu m)$	$L_t(\mu m)$	$W_t(\mu m)$	$T(\mu m)$	n	Analytical (kHz)	FEA (kHz)
Clamped-Clamped	900	900	1000	7	20	-	1.72	1.76
Serpentine 1D	900	900	900	7	20	4	1.1	1.069
Serpentine 2D	1000	1000	1000	7	20	4	2.79	2.83

It is clear from Figure 3.13 that the devices with serpentine micro-spring have higher mechanical sensitivity compared to devices with clamped-clamped micro-spring, making them more suitable for wall-shear stress detection in low speed fluid flows.

Modal analysis is carried out to predict and calculate the resonant frequencies of the devices. The results of the resonant frequency estimation using LEM and FEA methods are presented in Table 3.2. The mode shape of the devices in their first resonant frequencies are similar to the case of static displacement: see Figure 3.12.

Effect of micro-springs geometry on the static and dynamic performance of the sensors should be investigated in order to find the optimum parameters for the sensors. These effects are crucial for precise and quantitative wall-shear stress measurements in turbulent boundary layer flows. A larger sensitivity (lower stiffness) of devices is required, especially in low Reynolds number flows, to minimise the minimum detectable wall-shear stress. Moreover, a large resonant frequency is required, larger than turbulence frequency contents, for high sensor temporal resolution, which requires large mechanical stiffness in the devices. This is known as gain-bandwidth tradeoff (Horowitz et al., 2004), which is the compromise between the gain of the devices (sensitivity) and the devices bandwidth.

It can be seen in Figure 3.14 and Figure 3.15 that increasing the micro-spring length, L_t , decreases the sensors stiffness which results in larger mechanical sensitivity. However, this results in the reduced resonant frequency of the device. Width, W_t , of the micro-springs has the opposite effect so that increasing the width in the micro-springs leads to larger stiffness or smaller sensitivity and larger resonant frequency. The stiffness of the serpentine micro-spring in the flow direction is two orders of magnitude less than the stiffness in spanwise direction. This means that the deflection of the device in the spanwise direction is much smaller compared to the flow direction. Increasing the number of meanders reduces the stiffness in the micro-spring as illustrated in

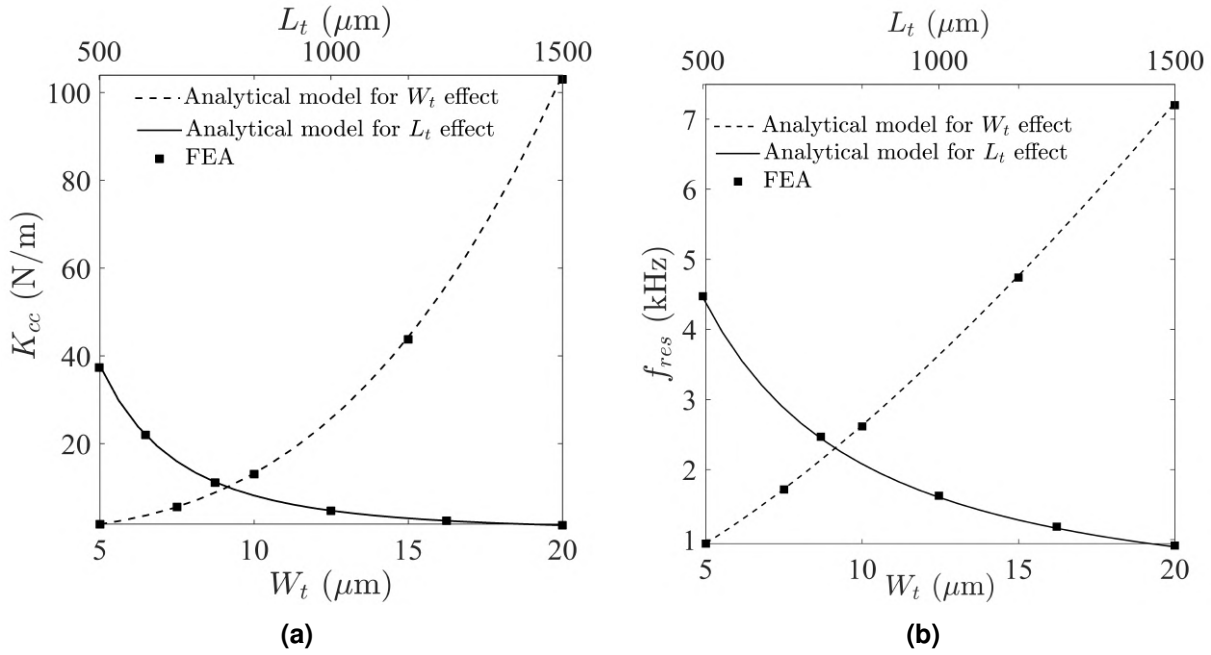


Figure 3.14 Clamped-clamped micro-spring geometry effects. (a) Effect of micro-spring width and length on mechanical stiffness, (b) Effect of micro-spring width and length on resonant frequency. Solid line (—) represent the analytical model for L_t effect, dashed line (- - -) represent the analytical model for W_t effect, and black squares (■) represent the FEA results.

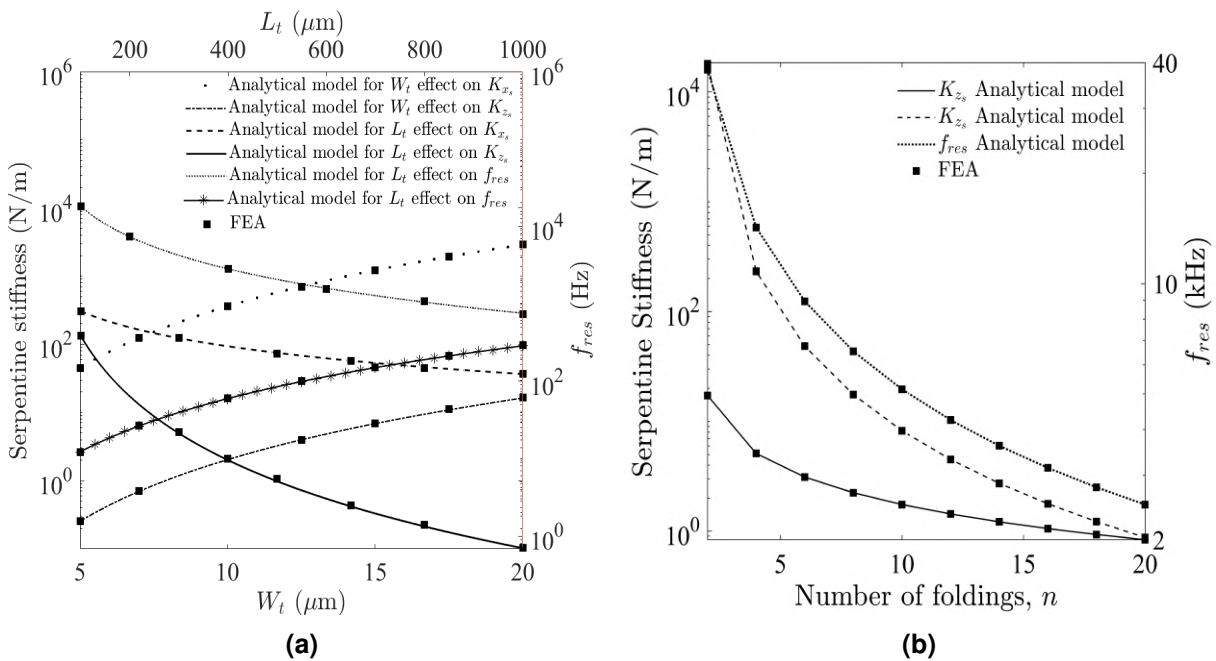


Figure 3.15 Serpentine micro-spring geometry effects. (a) Effect of micro-spring width and length on mechanical stiffness and resonant frequency, (b) Effect of number of foldings on mechanical stiffness and resonant frequency. all the lines are analytical models and black squares (■) represent the FEA results.

Figure 3.15b, however, as the number of folding increases ($n > 10$), the stiffness of the micro-spring in spanwise direction reduces sharply, which leads to the the sensor displacement in the spanwise direction. This means the number of the foldings should be designed so that to the wall-shear stress devices with serpentine micro-spring have adequate sensitivity in the streamwise direction.

In addition to the sensitivity and resonant frequency on the sensors, there are other factors that should be considered in the MEMS wall-shear stress design. For instance, the size of the floating element should be small enough to satisfy the spatial requirement of turbulent flow in different flow speeds. The maximum sensor length scale can be determined by using Equation 1.12 as $L_{max} \leq 20 \frac{\nu}{u_\tau}$. Assuming the free stream velocity is $U_\infty = 6m/s$, the sensor sensing length would be in the order of $1000\mu m$. So the smaller floating element sizes will reduce the effect of spatial averaging in the turbulence measurement. Another factor that should be considered in the sensor performance is the effect of the gap between the floating element and the fixed surrounding substrate. The size of these gaps should be smaller than several wall units to ensure that the gap will not disrupt the flow (Mills, 2014). There are limits introducing on the gap sizes due to the lithography process and also the etching process in the microfabrication, since etching through the silicon layer of $20\mu m$ thickness require a $10-20 \mu m$ gap. The wall unit for a $U_\infty = 10m/s$ flow is $50\mu m$ and for for a $U_\infty = 20m/s$ flow is $25\mu m$, which are larger than the normal gap sizes. Therefore the effect of the gaps around the floating element can be considered to be minimal.

3.2 MEMS sensors optoelectronics

This section provides an overview of the sensors optical Moiré fringe pattern transduction technique. This includes the theory behind designing the Moiré fringe pattern for different devices as well as the methods to read out data from the pattern and relate it back to measure the applied wall-shear stress. Different parts of the optoelectronics that are designed as the sensors control unit are discussed and experimental test-beds are developed to verify the theoretical models and investigate the performance of the optical elements and the electronics circuit of the devices.

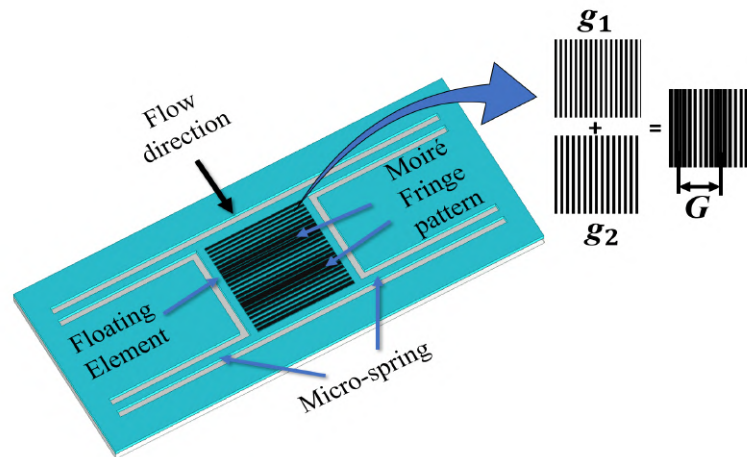


Figure 3.16 schematics of Moiré fringe pattern generated on the sensor.

3.2.1 Moiré fringe pattern optical transduction

The deflection of the MEMS wall-shear stress sensors is on the order of ten's of nanometers depending on the Reynolds number. Therefore, to detect the sensor's motion, displacement of a Moiré fringe pattern, which amplifies the motion of the sensor, is being tracked in time. The Moiré fringe pattern is an optical phenomenon and it occurs during the microfabrication process via the supposition of two sets of finely spaced gratings with slightly different pitches. When these two sets of gratings are superimposed and aligned parallel to one another, a periodic optical pattern is formed which is consisted of dark and light bands (Amidror, 2009). The explanation to the formation of these periodic dark and light bands is due to an interaction between overlaid grating sets. Areas where individual gratings of the grating sets fall on top of each other appear brighter compared to the areas where the gratings fall between each other as shown in Figure 3.16. One of the gratings sets is fixed on a transparent substrate that is bonded to the Silicon substrate, whilst the other gratings set is formed

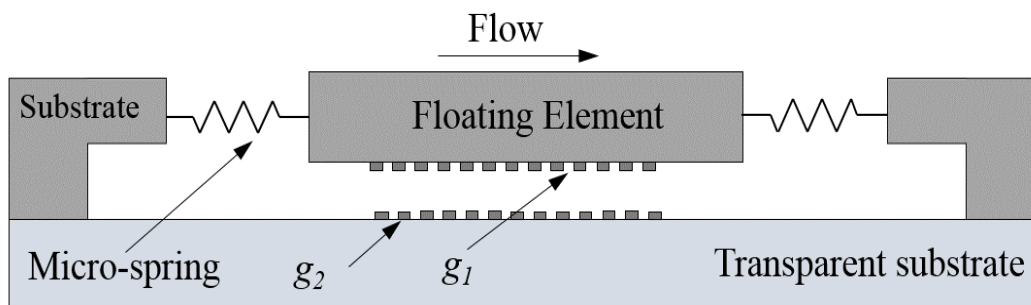


Figure 3.17 schematics of Moiré fringe pattern generated on the sensor.

on the floating element and it is free to move with the sensors structures, which causes the amplified relative displacement of the Moiré fringe pattern: see Figure 3.17. The spatial pitch of gratings sets are defined as g_1 and g_2 , where the width of the individual gratings are considered to be half the value of the gratings set pitch in the design of the MEMS wall-shear stress sensors. Based on the pitch of each optical grating set, the spatial period of the formed Moiré fringe pattern, G , can be expressed as (Stevenson and Jordan, 1989)

$$\frac{1}{G} = \frac{1}{g_1} - \frac{1}{g_2} \quad (3.34)$$

where this equation can be rearranged as

$$G = \frac{g_1 g_2}{g_2 - g_1} \quad (3.35)$$

Displacement of the first set of the optical gratings that are fixed on the floating element, due to the wall-shear stress, δ_{τ_w} , leads to an amplified displacement of the Moiré fringe pattern, Δ , in the same direction

$$\Delta = \delta_{\tau_w} \left(\frac{G}{g_1} \right) \quad (3.36)$$

in which the term G/g_1 is the amplification factor of the Moiré fringe pattern transduction. The displacement amplification characteristics of the Moiré fringe pattern makes it a useful transduction technique that can boost small mechanical displacements in MEMS sensors and provides the ability to measure these small displacements. Optical gratings that are forming the Moiré fringe pattern can be defined as a set of rectangular binary pulse trains. The transmittance function of individual gratings in each gratings set can be expressed as a Fourier series (Mills, 2014)

$$T_1(\chi, Y) = a_0 + \sum_{i=1}^{\infty} \left(b_i \cos\left[\frac{2\pi i}{g_1}(\chi - f(\chi, Y))\right] + c_i \sin\left[\frac{2\pi i}{g_1}(\chi - f(\chi, Y))\right] \right) \quad (3.37)$$

and

$$T_2(\chi, Y) = d_0 + \sum_{j=1}^{\infty} \left(e_j \cos\left[\frac{2\pi j}{g_2}(\chi) + f_j \sin\left[\frac{2\pi j}{g_2}(\chi)\right]\right] \right) \quad (3.38)$$

where $f(\chi, \Upsilon)$ is the local displacement at the point (χ, Υ) in the χ direction and $a_0, b_i, c_j, d_0, e_j,$ and f_j are constants. As a result of a uniform displacement of the floating element due to wall-shear stress the local function for the gratings set number one can be considered as $f(\chi, \Upsilon) = \delta_{\tau_w}$ and the transmittance function for the first gratings set can be simplified as

$$T_1(\chi, \Upsilon) = a_0 + \sum_{i=1}^{\infty} \left(b_i \cos \left[\frac{2\pi i}{g_1} (\chi - \delta_{\tau_w}) \right] + c_i \sin \left[\frac{2\pi i}{g_1} (\chi - \delta_{\tau_w}) \right] \right) \quad (3.39)$$

Considering the grating profiles as rectangular pulse trains and since the width of gratings in each grating sets is designed to be half the pitch of the grating sets, as depicted in Figure 3.18, the constants in the Fourier series can be derived as

$$\begin{aligned} a_0 &= \frac{1}{2} \\ b_i &= \frac{2}{i\pi} \sin\left(\frac{i\pi}{2}\right) \\ c_i &= 0 \\ d_0 &= \frac{1}{2} \\ e_j &= \frac{2}{j\pi} \sin\left(\frac{j\pi}{2}\right) \\ f_j &= 0 \end{aligned} \quad (3.40)$$

and the Transmittance functions for the grating sets can be simplified as

$$T_1(\chi, \Upsilon) = a_0 + \sum_{i=1}^{\infty} \left(b_i \cos \left[\frac{2\pi i}{g_1} (\chi - \delta_{\tau_w}) \right] \right) \quad (3.41)$$

and

$$T_2(\chi, \Upsilon) = d_0 + \sum_{j=1}^{\infty} \left(e_j \cos \left[\frac{2\pi m}{g_2} (\chi) \right] \right) \quad (3.42)$$

It is shown in Figure 3.19 that the Moiré fringe pattern is formed by superposition of two transmittance function of gratings sets expressed in terms of binary square wave trains with slightly different pitches. The amplified displacement of the Moiré fringe pattern can also be observed due to a small shift in the transmittance function of one of the gratings sets. Multiplying the gratings transmittance functions and using

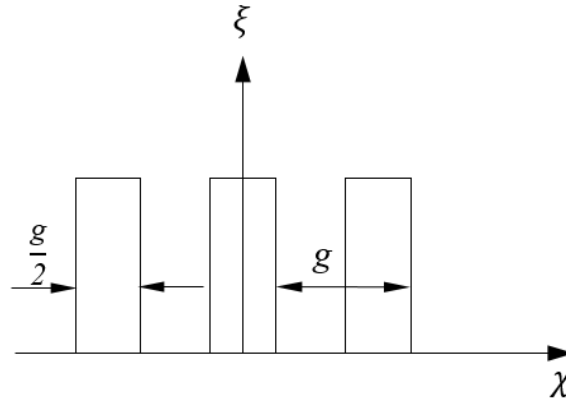


Figure 3.18 Binary square-wave representation of the Moiré fringe pattern gratings. The width of the grating is considered to be half the spatial pitch of the grating set.

trigonometric identity equations gives

$$\begin{aligned}
 T_1(\chi, \Upsilon) \cdot T_2(\chi, \Upsilon) &= a_0 d_0 + a_0 \sum_{j=1}^{\infty} \left(e_j \cos\left[\frac{2\pi j}{g_2}(\chi)\right] \right) + \\
 &\quad d_0 \sum_{i=1}^{\infty} \left(b_i \cos\left[\frac{2\pi i}{g_1}(\chi - \delta_{\tau_w})\right] \right) + \quad (3.43) \\
 \frac{1}{2} \sum_{i=1}^{\infty} \sum_{j=1}^{\infty} b_i e_j &\left(\cos\left[\frac{2\pi i}{g_1}(\chi - \delta_{\tau_w}) - \frac{2\pi j}{g_2}(\chi)\right] + \cos\left[\frac{2\pi i}{g_1}(\chi - \delta_{\tau_w}) + \frac{2\pi j}{g_2}(\chi)\right] \right)
 \end{aligned}$$

The last term in Equation 3.43 defines the sum and difference between between the optical gratings sets and defines the fundamental Moiré fringe pattern that is formed due to the difference in spatial pitches in the gratings sets (Yokozeki et al., 1976). Considering the fundamental Moiré fringe pattern, $i = 1$ and $j = 1$, and by assuming there is no displacement, $\delta_{\tau_w} = 0$, the last term in Equation 3.43 is expressed as

$$\begin{aligned}
 \sum_{i=1}^1 \sum_{j=1}^1 b_i e_j &\left(\cos\left(\frac{2\pi i}{g_1}(\chi)\right) + \cos\left(\frac{2\pi j}{g_2}(\chi)\right) \right) = \quad (3.44) \\
 &\frac{1}{2} b_1 e_1 \cos\left(2\pi\chi\left(\frac{1}{g_1} - \frac{1}{g_2}\right)\right)
 \end{aligned}$$

The intensity profile of the formed Moiré fringe pattern can be derived by adding a DC offset to the Equation 3.44 intensity and by transforming the cosine function into a sine function

$$I(\chi) = I_0 + \underbrace{\frac{1}{2} b_1 e_1}_A \sin\left(2\pi\chi\left(\frac{1}{g_1} - \frac{1}{g_2}\right) + \Phi\right) \quad (3.45)$$

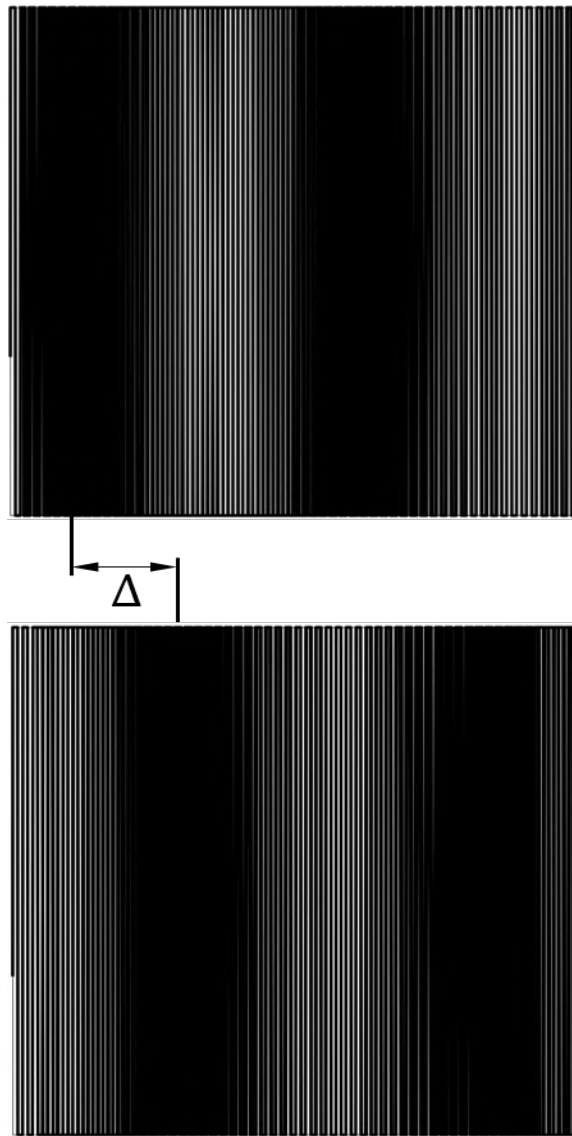


Figure 3.19 Moiré fringe pattern formation and shift based on transmittance function of grating's sets.

and by using Equation 3.34

$$I(\chi) = I_0 + A \sin\left(\frac{2\pi\chi}{G} + \Phi\right) \quad (3.46)$$

Equation 3.45 describes the periodic nature of the Moiré fringe pattern as a sinusoidal function. In Equation 3.46, I_0 defines the DC offset intensity of the Moiré fringe pattern, A defines the Moiré fringe pattern amplitude and, Φ is the phase that describes the displacement of the pattern in the flow direction.

This sinusoidal function describes the profile of an ideal Moiré fringe pattern, however, there are some factors that can lead to the non-ideal formation of the pattern and shift the

actual pattern to be different from the ideal designed pattern. Also, these non-idealities can affect the sensors transduction and sensor's data post-processing.

The nonuniform pitch or width of individual optical gratings as a result of microfabrication tolerances affects the profile of the formed Moiré fringe pattern. In addition, any angular or linear misalignment between two sets of the micro-fabricated optical gratings will change the profile of the designed Moiré fringe pattern. Another important factor, which should be considered in the MEMS wall-shear stress devices is the effect of the cavity distance between the two sets of optical gratings. The limits in the microfabrication process poses constraints on the cavity distance between the two sets of gratings. This distance defines the total contrast between the light and dark bands in the sensor and the large cavity distance ends up in loss of contrast in the Moiré fringe pattern. The loss of contrast affects the reflected light intensity and results in a poor evaluation of the sinusoidal profile of the optical pattern. Hence, the cavity distance should be designed in order to avoid any stiction between the moving floating element and the fixed transparent substrate which is bonded underneath but at the same time form the Moiré pattern with distinguishable contrast across the pattern. This distance can be justified within the 5% of the Talbot distance, T_d , (Spagnolo and Ambrosini, 2000), which depends on the gratings pitch and the light wavelength of the illumination source

$$T_d = \frac{2g^2}{\lambda} \quad (3.47)$$

Reflectivity of the material that is used to fabricate the optical gratings also influences the contrast of the Moiré fringe pattern. The material should be selected to reflect the maximum amount of the hitting light from the sensor, so that the photo-detector can distinguish the signals from dark and light bands of the fringe pattern. Gold (Au) is used to form the optical gratings on the Silicon and transparent substrate in the MEMS wall-shear stress devices due to its high reflectivity (more than 95 %) for the light sources with wavelength of higher than 550 nm. It is also widely being used in the micro-fabrication and it does not naturally oxidise.

3.2.2 Moiré fringe pattern detection technique

As discussed, Moiré fringe pattern can be expressed as a sinusoidal function. Any displacement in the sensor structure produces a transformation in the position of dark and light bands on the Moiré fringe pattern and consequently a phase shift in the corresponding sinusoidal function. Hence, the phase shift in the signal is directly related to the mechanical displacement of the sensor and eventually it can be used to measure the applied wall-shear stress. A phase shift tracking system is developed to demodulate the Moiré fringe pattern in the MEMS wall-shear stress devices. Using this method, the shape information of the Moiré fringe pattern is obtained using the signals coming out from the pattern, and the corresponding phase shift is monitored, as illustrated in Figure 3.20. This transduction technique relies on a continuous repeated scanning of the Moiré fringe pattern, using a multi-element array of rippling Light Emitting Diodes (LEDs) and a single photo-detector. This repeated scanning of the Moiré fringe pattern generates a signal, which represents the shape and the position of the optical pattern. The acquired signal is being processed to obtain the sinusoidal curve of the pattern. The amplitude of this signal corresponds to the reflected light intensity of the scanned point on the pattern, and its phase signifies the position of the dark and light bands.

The rippling LED optoelectronics consist of an array of Light Emitting Diodes (LEDs), an array of fibre optic cables, a pair of aspheric condenser lenses and a single photo-detector as shown in Figure 3.21.

To detect the light intensity across the Moiré fringe pattern, a rippling light from each LED in the LEDs drive board is launched down a dedicated fibre optic cable and is then focused on the backside of the sensors, via a pair of lenses to a small spot of light, typically 10's of microns in diameter. The diameter of the light spots depends on the size of the floating element and it can be adjusted by changing the distance between the lenses in the system so that the light spots can scan the Moiré fringe pattern area on the devices. Projected light spots are rippled in sequence at different frequencies ranging from a several hundred's of Hz up to MHz depending on the flow speed to reveal the sinusoidal response of the Moiré fringe pattern. The rippling frequency of LEDs is controlled by a micro-controller that is programmed by a computer. The focused light spots are then reflected from the Moiré fringe pattern into the single photo-detector that

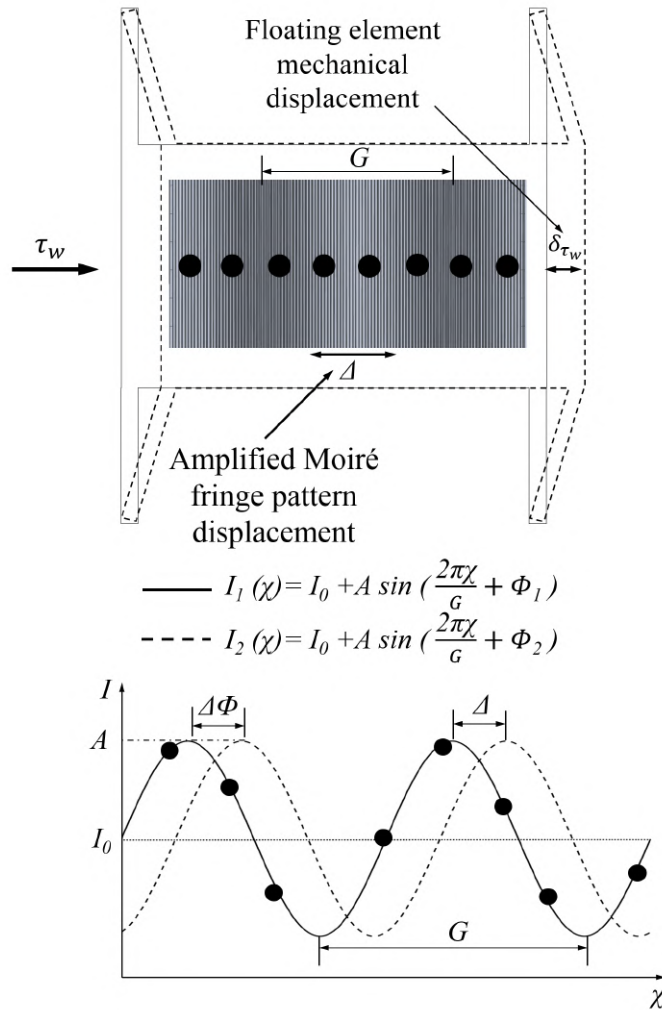


Figure 3.20 Schematics of the phase shift tracking sensor transduction. Applied wall-shear stress results in the phase shift in the corresponding sinusoidal function of the pattern.

is implemented inside the sensor packaging and is coupled to an amplification circuit. The output of the photo-detector circuit is coupled to a data acquisition (DAQ) system. The "light" bands on the Moiré fringe pattern reflect light with higher intensity compared to the "dark" bands. As the Moiré fringe pattern moves, the intensity of each reflected light spot changes accordingly and the phase of the sinusoidal response of the Moiré fringe pattern is tracked with time.

3.2.3 LED drive circuit

The illumination source type and wavelength are important parameters in the modulation of the Moiré fringe pattern on the sensors, since they influence the reflectivity of the

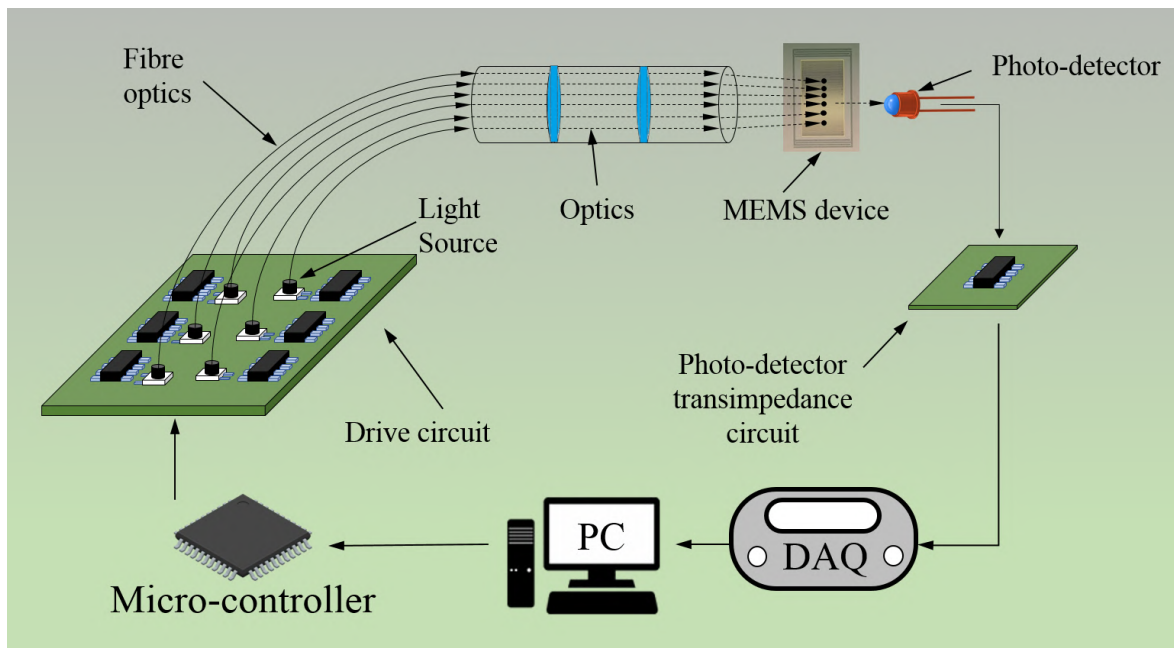


Figure 3.21 Phase shift tracking of the Moiré fringe pattern. The black dots represent the scanning light spots on the pattern. the phase shift and Moiré fringe pattern shift are shown on the sine curves.

optical gratings and consequently the contrast of the pattern. Among different types of the light sources, LEDs are an appropriate option to be used in the Moiré fringe pattern demodulation in the MEMS sensors due to their wide range of spectrum and fixed wavelengths, despite the laser diodes that have a very narrow spectrum and white light as it contains different wavelengths, which affect the contrast of the pattern. LEDs used in the sensor control unit are high power Broadcom Moonstone "ASMT-MR00-AHJ00" red LEDs with peak wavelength of 625 nm, a forward current value of 350 mA, and a forward voltage value of 2.1 v.

Arduino DUE is used as the micro-controller to program and control the rippling frequency of the LEDs in MEMS wall-shear stress sensors with rippling optoelectronics. The output current and voltage of the Arduino boards are not high enough to operate the LEDs to the required level of the brightness. LEDs are current-driven components and hence a driver circuit is designed and developed to amplify, control, and supply sufficient current to the LEDs. This LEDs driver circuit consists of "AD820N" operational amplifiers connected to NPN type Bipolar Junction Transistors (BJT), and variable resistors. The voltage of the input signals on each LED channel is transformed on two side of the dedicated resistor and then converted into the current using the operational amplifiers. When there is no input signal, no current flows to the base terminal of the BJT and the

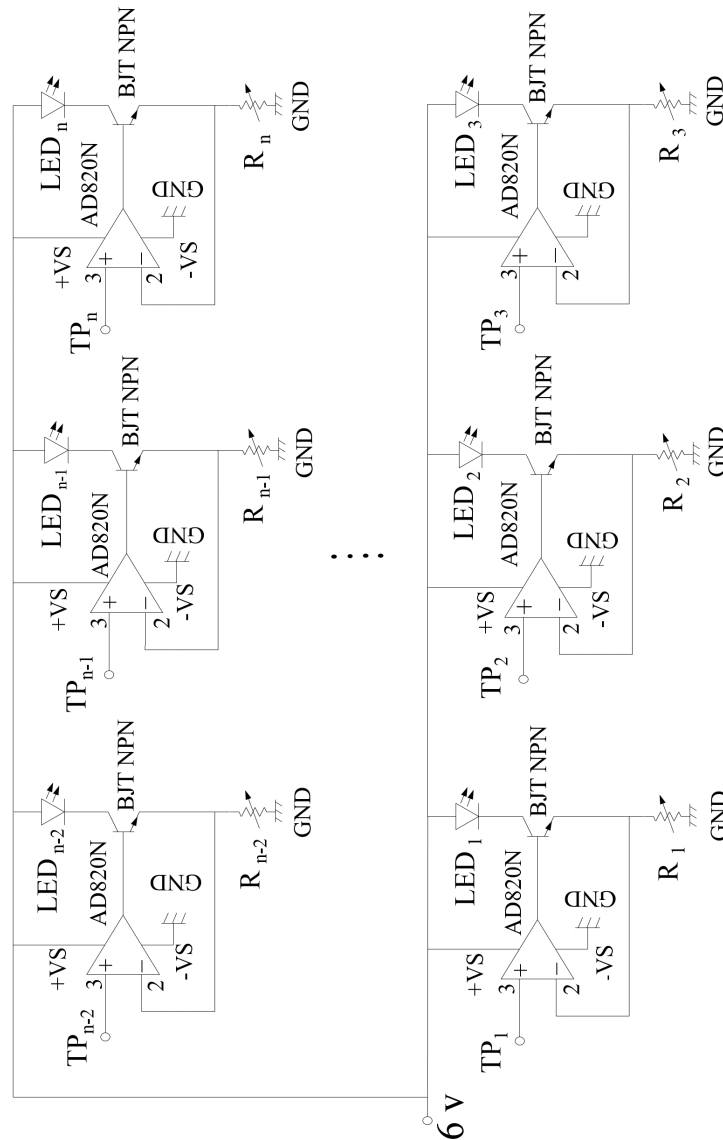


Figure 3.22 Schematics of LEDs drive circuit. "TP"s are terminal ports for each LED, where the output of the micro-controller are connected to them. The number of LEDs depend on the size of the Moiré fringe pattern.

transistor cannot turn on. As current flows through the base terminal of the BJT and a sufficient positive voltage applied to its collector terminal, the BJT acts as a current amplifier. A voltage of 6v is supplied to each LED driver channel to power the collector terminal of the BJT and the LEDs as a positive voltage is required to be applied to the the collector terminal of NPN transistors to make the driver circuit operational. This voltage is calculate based on the total voltage consumption of the circuit. The forward voltage value of the LEDs are 2.1 v, the signal voltage is 3.2v, and 0.3v is required for the BJT to operate, which results in a total voltage value of 5.6 v. Using operational

amplifiers in the circuit makes the circuit stable and reduces the effect of temperature increase on the current increase in the circuit, which results in stable illumination in the LEDs.

3.2.4 Photo-detector transimpedance amplifier circuit

The light reflected from the Moiré fringe pattern is detected by a single photo-detector that is implemented inside the sensor packaging. An option for the photo-detector is using the semiconductor photodiodes due to their fast response, high sensitivity, and their small sizes, which enable the direct integration of the photodiode inside the sensor packaging. The reflected light from the sensor produces a net charge inside the photodiode. If the photodiode is attached to an additional circuit, the net charge is transformed into a photo-current, which is linearly related to the intensity of the incident light. A dual stage transimpedance amplifier circuit is developed and coupled to a single "Vishay BPW24R" photodiode with the responsivity of 0.6 A/w for the incident light at an 620 nm wavelength, to amplify the generated photo-current and convert it to a voltage signal, which is depicted in Figure 3.23. Here the close-loop non-inverting configuration is used where the input signal is directly applied to the positive terminal of the op amps, while the negative terminals are grounded via R_2 and R_5 . Using the non-inverting configuration, no current flows into the positive terminal of the op amp and as the input impedance of this closed-loop amplifier is ideally infinite (Sedra et al., 1998). The closed-loop gain of the first stage in the circuit is expressed as

$$G_1 = 1 + \frac{R_3 + R_4}{R_2} \quad (3.48)$$

and the closed-loop gain at the second stage is quantified as

$$G_2 = 1 + \frac{R_6}{R_5} \quad (3.49)$$

The total gain of the dual stage transimpedance amplifier circuit is the product of the gains at each stage

$$G_T = \left(1 + \frac{R_3 + R_4}{R_2}\right) \left(1 + \frac{R_6}{R_5}\right) \quad (3.50)$$

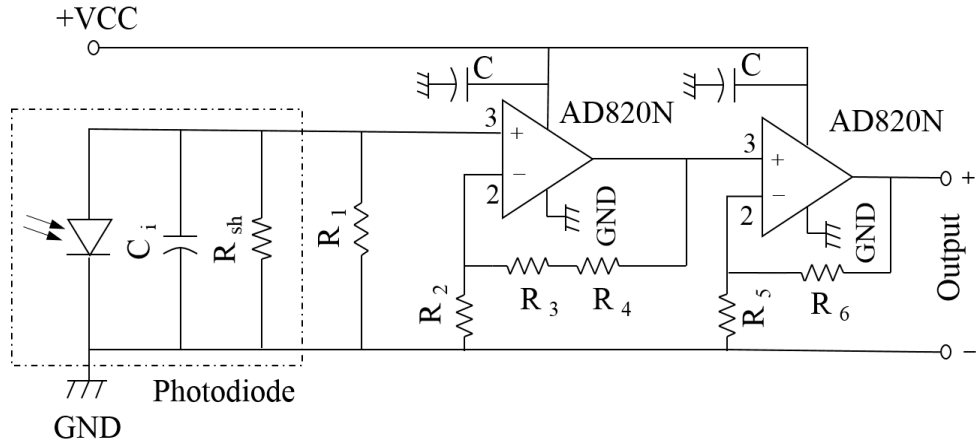


Figure 3.23 Schematics of the photodiode transimpedance amplifier circuit.

The open-loop gain, OG , of the op amp circuit reduces with frequency, and is written as (Sedra et al., 1998)

$$OG(s) = \frac{A_0}{1 + \frac{s}{\omega_b}} \quad (3.51)$$

and by considering $s = j\omega$

$$OG(j\omega) = \frac{A_0}{1 + \frac{j\omega}{\omega_b}} \quad (3.52)$$

in which A_0 is the DC gain and ω_b is the break frequency that occurs at -3 dB. The open-loop gain of the op amp decays with the frequency and reaches the unity or 0 dB at the "unity-gain bandwidth", $f_t = 2\pi\omega_t$, and for frequencies larger than break frequency, $\omega \gg \omega_b$, the open-loop gain magnitude can be expressed as

$$OG(j\omega) = \frac{\omega_t}{\omega} \quad (3.53)$$

The closed-loop gain of the non-inverting op amp is related to the frequency via the transfer function and the open-loop gain. The transfer function of the first stage non-inverting amplifier circuit with a finite open-loop gain, A , is

$$\frac{V_{o1}}{V_{i1}} = \frac{1 + (R_3 + R_4)/R_2}{1 + (1 + (R_3 + R_4)/R_2)/OG} \quad (3.54)$$

and for the second stage amplifier

$$\frac{V_{o2}}{V_{i2}} = \frac{1 + (R_6)/R_5}{1 + (1 + (R_6 + R_5)/R_2)/OG} \quad (3.55)$$

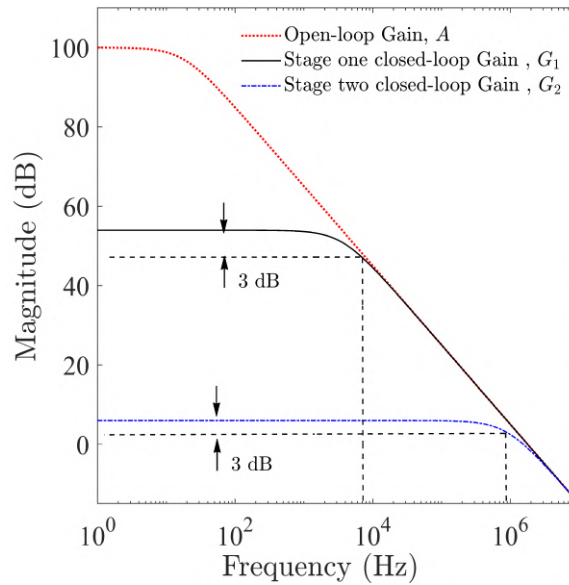


Figure 3.24 Magnitude against frequency for the open-loop gain of the amplifier and closed-loop gains for two stages of the non-inverting amplifications.

Using Equation 3.51, Equation 3.54 and Equation 3.55 can be re-written as

$$\frac{V_{o1}}{V_{i1}} = \frac{1 + (R_3 + R_4)/R_2}{1 + \frac{(1+R_3+R_4)/R_2}{\frac{A_0}{1 + \frac{s}{\omega_b}}}} \quad (3.56)$$

and

$$\frac{V_{o2}}{V_{i2}} = \frac{1 + (R_6)/R_5}{1 + \frac{(1+R_6)/R_5}{\frac{A_0}{1 + \frac{s}{\omega_b}}}} \quad (3.57)$$

The output voltage saturation and output current limit of the op amp should be considered in the circuit design to avoid clipping off the peaks in the output signal as well as the output current does not exceed the current limit, which also cause saturation in the output signal. AD820N op amp with unity-gain frequency of 1.8 MHz and an open-loop gain of 10^5 is used in both stages in the circuit. The value of the circuit's parameters are $R_1 = 10k\Omega$, $R_2 = 10k\Omega$, $R_3 = 5M\Omega$, $R_4 = 10k\Omega$, $R_5 = 10k\Omega$, and $R_6 = 10k\Omega$. The bode diagram for the magnitude of the circuit for the open-loop gain of the amplifier and closed-loop gains for both stages are shown in Figure 3.24.

3.2.5 Lens array system

The lens arrays is designed and developed to project and focus the light illuminating from the end of the fibre optics array on to the Moiré fringe pattern. Using different types

of lenses with various focal lengths and diameter, light spots with different diameters are achievable. Considering that the optical effect due to the lens thickness is negligible, the thin lens approximation (Malacara, 1994) is used to model the system. This consideration simplifies the system approximation by using the ray tracing technique which provides a good approximation of the system. Based on this method, any ray of light that is parallel to the axis of the lens, passes through the focal point of the lens, and any ray of light that passes through the center of the lens, ideally, exits the lens without refraction. The geometry of the formed image in the lens system depends on the focal length of the lens and the geometry of the object. This factors can be related together using the following equation

$$\frac{1}{d_o} + \frac{1}{d_i} = \frac{1}{f_l} \quad (3.58)$$

where d_o is the distance of the object from the center line of the lens, d_i is the image distance from the lens, and f_l is the focal length of the lens. Utilising the lens array, the image size can be smaller or larger than the object based on the system configuration. In case of MEMS wall-shear stress sensors using rippling optoelectronics, the projected light spots sizes should be smaller than the actual size of the fibre optics array. The final size of the spots on the Moiré fringe pattern is quantified by the lens magnification. The lens magnification is the ratio of the image size and the object size, and it can be related to the distance of the object and the image via the lens system geometry

$$m_{lens} = \frac{h_i}{h_o} = -\frac{d_i}{d_o} \quad (3.59)$$

in which h_i and h_o are the image height and the object height respectively. This model can be extended to systems with multiple lenses. In systems with more than one lens, distances between individual lenses affect the final image geometry. The schematics of a system with two lenses is shown in Figure 3.25. The fibre optics array is placed on the left hand side of the first lens and the final light spots with reduced size are formed on the right hand side of the second lens. Here, two lenses with different focal lengths are combined as a lens array system. Equation 3.58 is applied to this system by taking to account that the image formed in the first lens is considered the object for the second lens. For the first lens and the second lens, Equation 3.58 is expressed as

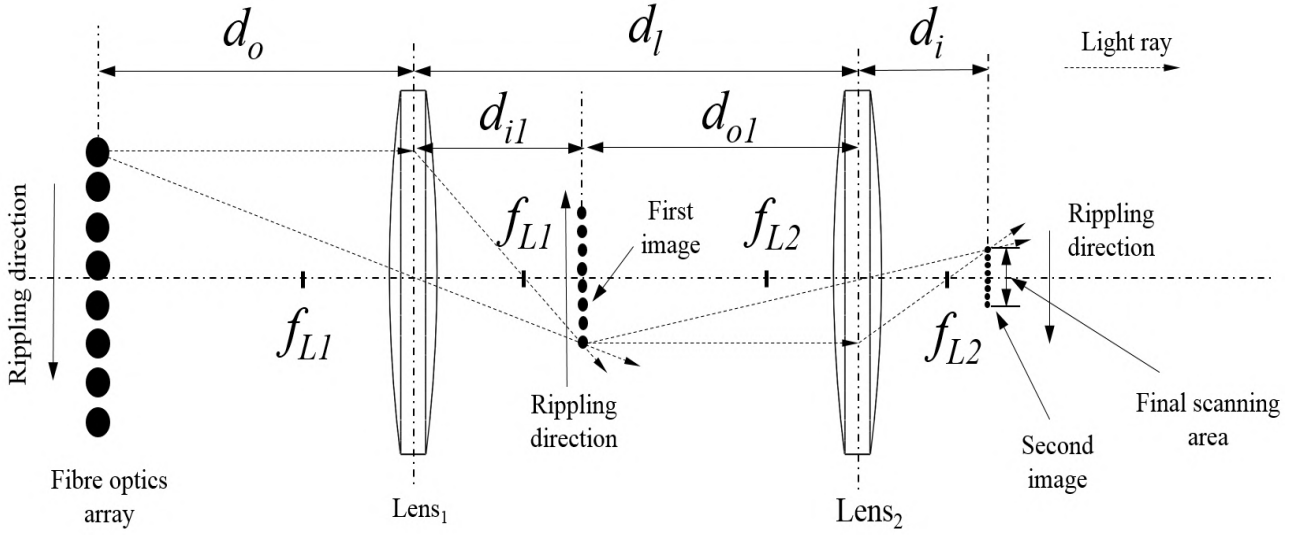


Figure 3.25 Schematics of the lens system for light spots projection.

$$\frac{1}{d_o} + \frac{1}{d_{i1}} = \frac{1}{f_{L1}} \quad (3.60)$$

and

$$\frac{1}{d_{o1}} + \frac{1}{d_i} = \frac{1}{f_{L2}} \quad (3.61)$$

Combining Equation 3.60 and Equation 3.61 and by considering $d_{o1} = d_l - d_{i1}$, the distance of the final image from the final lens is derived as

$$d_i = \frac{f_{L2} \left(d_l - \frac{f_{L1} d_o}{d_o - f_{L1}} \right)}{d_l - f_{L2} - \frac{f_{L1} d_o}{d_o - f_{L1}}} \quad (3.62)$$

f_{L1} , f_{L2} , and d_l are the focal length of the first lens, focal length of the second lens, and the distance between two lenses, respectively.

Total magnification of the lens array system is the product of the magnification of the first lens, m_{lens1} and m_{lens2}

$$m_{lensarray} = m_{lens1} \times m_{lens2} \quad (3.63)$$

Double conversion of the image in this system with two lenses results in an enhanced final magnification ratio and also the direction of the final image will be the same as the object direction, where in the case of MEMS wall-shear stress devices it means the direction of light rippling are identical on the fibre optics array and the projected light spots.

3.2.6 Material optical effects

The transmittance and reflectivity of the materials mediums on the light pass affect the reflected light intensity and consequently affects the contrast of the Moiré fringe pattern. The Transmittance intensity of the gratings sets can be written using Equation 3.43 as the product of the transmittance functions of the gratings sets

$$I_T(\chi, Y) = I_0 T_1(\chi, Y) T_2(\chi, Y) \quad (3.64)$$

and in case of the ideal Moiré fringe pattern, the reflected intensity is expressed as

$$I_R = 1 - I_T \quad (3.65)$$

In case of the real Moiré fringe pattern, however, the reflectance is less than the ideal value, as the reflectivity of gold is 0.95 and the transparent substrate does not transmit all the light shining through it. Figure 3.26 demonstrates the light propagation and reflection in the optical section of the sensor. When the light spot is projected on the backside of the sensor, it transmits through the glass substrate and the fixed gratings sets $g_{2,1}$ on this substrate. The light spot, then enters the gap between the movable structure and the fixed substrate, hits and reflects from the gratings set on the floating element, g_1 . The reflected light again hits and transmits through the fixed gratings, $g_{2,2}$, and the glass substrate for the second time and enters the photodiode. The light size changes as it enters different mediums with different refractive indexes. The intensity profile of the light also changes as it propagates and reflects from the sensor.

The intensity profile of the light projected on the sensor is considered to be governed by a Gaussian function with ζ and r coordinates, a peak intensity of I_0 , and initial radius of w_0 that is considered to be the radius of ($r_{spot} = d_{spot}/2$) projected light spot (Saleh and Teich, 2019)

$$I_G(r, \zeta) = I_0 \left(\frac{w_0}{w(\zeta)} \right)^2 e^{\left(\frac{-2r^2}{w^2(\zeta)} \right)} \quad (3.66)$$

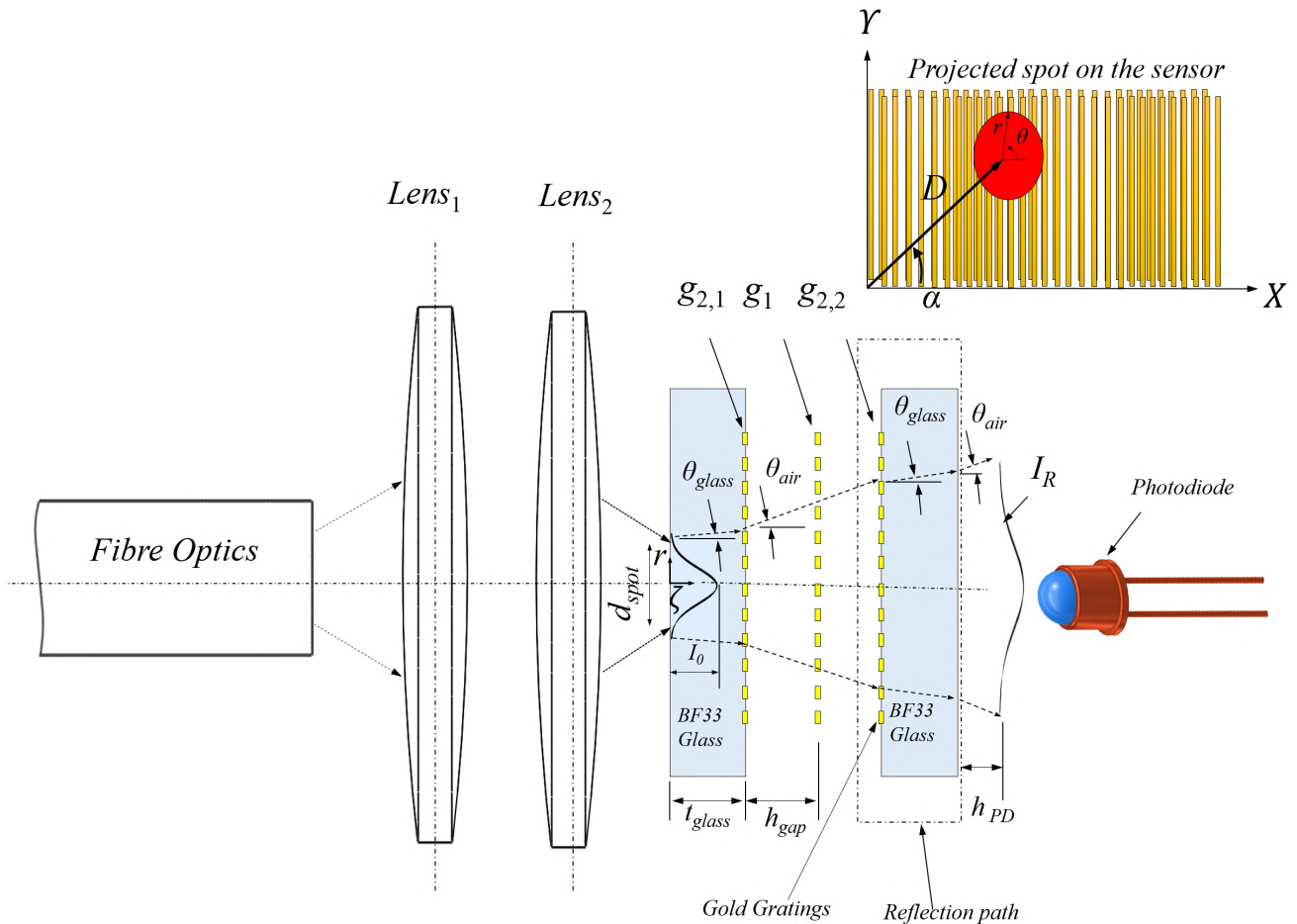


Figure 3.26 Schematic of the light transmittance and reflectivity in different mediums of the wall-shear stress sensor.

3.2.7 Lens array test-bed

An optical test-bed was developed to verify the models based on the thin lens approximation that is predicting the optical system and the final spot sizes of the lights forming on the devices. The test-bed consists of fibre optics cables with various diameters that were connected to LEDs, lenses, projection screen, and a USB microscope; see Figure 3.27. Fibre optics cables were placed in a linear array using 3D printed grooves. Optical rails were used to adjust and to measure the distance between the end of fibre optics cables to the first lens, the distance between the lenses, the distance between the image plane and the second lens, and the distance between the image plane and the USB microscope. The lenses used in the test-bed were two "Thorlabs LA1540-A-N-BK7" plano-convex lenses with 15 mm focal lengths, one "Edmund optics 32020" double convex lens with 9 mm focal length, one "Thorlabs ACL108u-A" with 8 mm focal length, and two "Edmund optics 88-283" molded Aspheric condenser lenses with 6.6

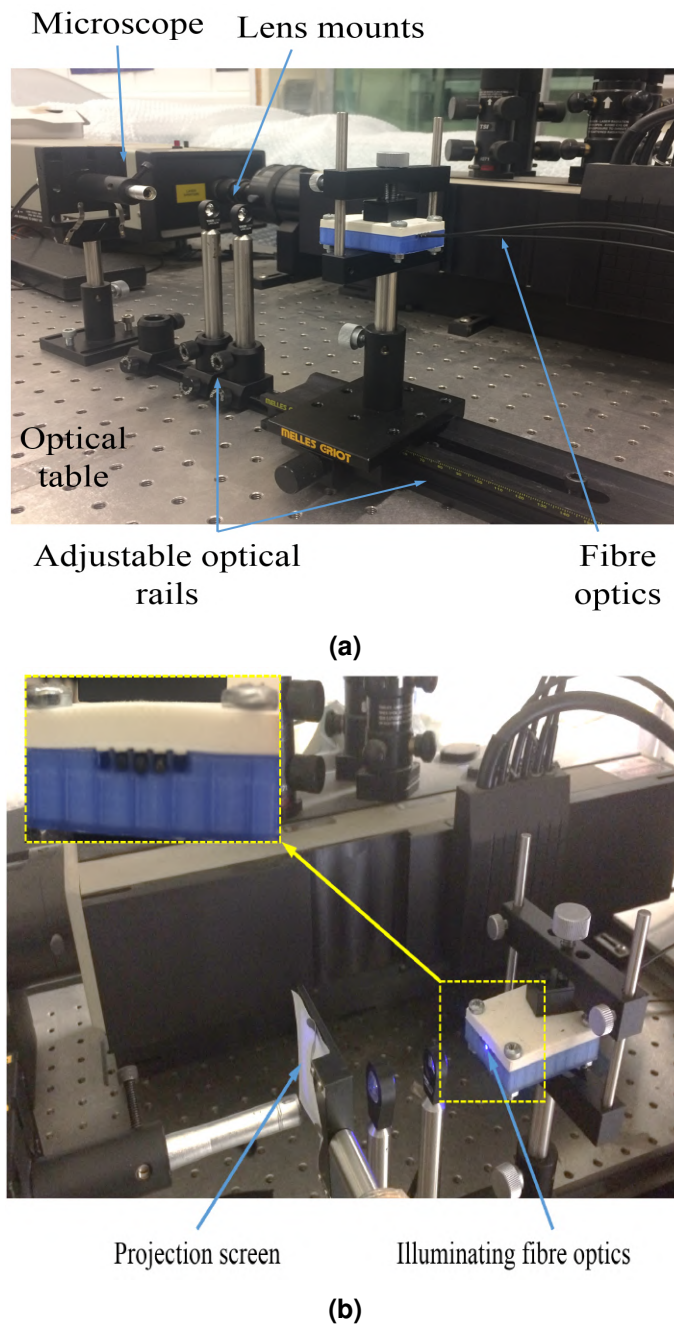


Figure 3.27 Lens array test-bed.

mm focal lengths. Fibre optics arrays with various diameters were aligned with the axis of the lenses. The source light from the LEDs board was launched down the fibre optics, passing through the lens system, and finally projected on an screen behind the second lens. The USB microscope was calibrated using a calibration target, and then was placed and focused on the other side of the projection screen, to capture the image of the projected light spots and to measure the final size of the light spots on the projected screen. Another calibration technique based on the pixel analysis and image processing was also preformed on the captured image of the light spots using

MATLAB[®] software. Using the pixels analysis reduces the error related to the USB microscope measurements. The captured image of the light spots alongside with an image of a precise graticule was imported into MATLAB software. The segments on the reference graticule was retrieved in terms of pixels number using image processing, providing the conversion ratio between the pixel numbers and the actual size in terms of micrometers on the captured image. To find the size of the light spots, the values of the pixels intensity were retrieved across the light spot image. The pixel intensity analysis was performed across the light spot images to obtain a distribution of the intensity in the image. Using the conversion ratio that was obtained from the graticule pixel analysis, the pixels numbers in X and Y direction of the image is obtained and can be converted to the physical values in micrometers. Figure 3.28a illustrates a two dimensional intensity profile of a projected light spot, captured by the microscope. Gaussian beams have a bell-shaped intensity function curve and the ends are open, which means the light spot diameter can not considered to be between the two ends of the curve. For a projected light spot, Equation 3.66 can be rewritten as

$$I_G(r) = I_0 e^{\left(\frac{-2r^2}{w^2}\right)} \quad (3.67)$$

for the point where the $r = w$,

$$I_G(r = w) = I_0 e^{-2} = \frac{I_0}{e^2} \quad (3.68)$$

intensity is equal to $1/e^2$ of the peak Intensity, which is known as $1/e^2$ width, where two points on the intensity function curve that are $1/e^2$ times the peak intensity. This analysis was performed on the intensity distributions on the light spots that were captured in the verification test-bed to find the light spots diameter. Different combinations of lenses were tested to achieve the best optical performance for the MEMS devices. Figure 3.28b displays the result of a test-bed using two Aspheric lenses with a diameter of 10 mm and a focal length of 6.6mm and "Thorlabs" fibre optics cables with core diameters of $300 \mu\text{m}$ and Numerical aperture of $\text{NA} = 0.22$. Using Aspheric lenses corrects the spherical aberration results that exists in conventional spherical lenses, which leads to a projection of the light spots to small points and avoids the formation of blurry images.

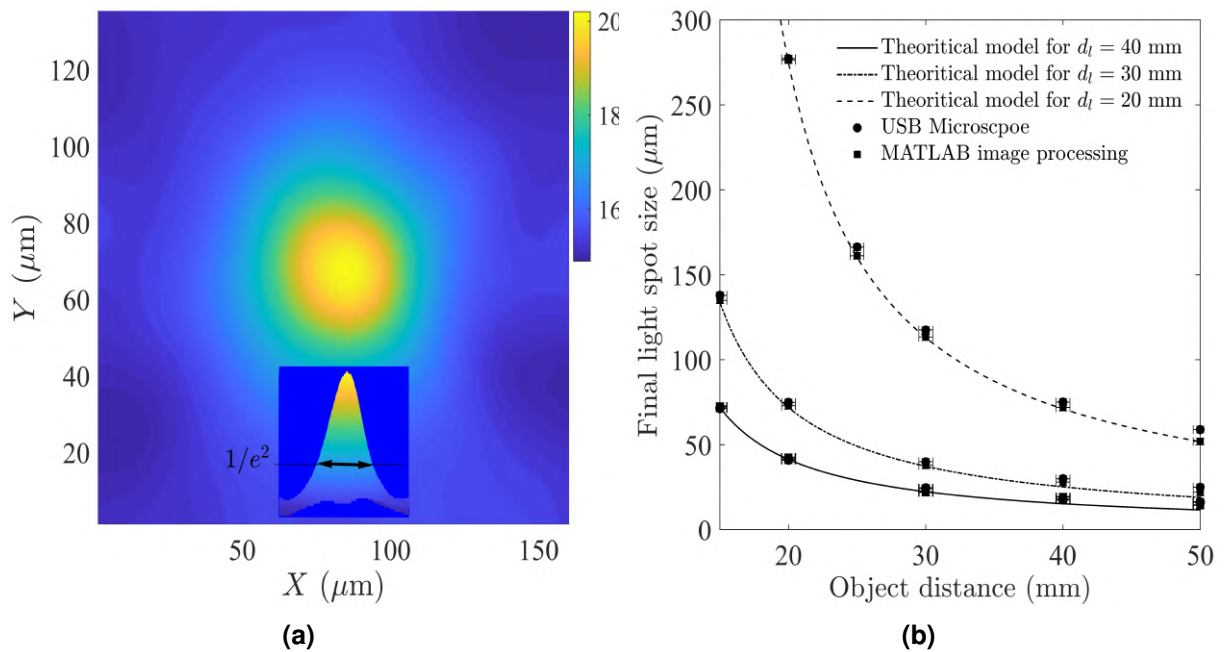


Figure 3.28 Lenses array test-bed results. (a) Intensity profile a projected light spot over an area and its intensity profile curve, $1/e^2$ method is used to measure the light spot size, (b) Model validation result for the lenses array test-bed for three different distances between the lenses.

Variation of the light spot diameter with respect to the distance of the fibre optics end to the first lens (object distance) has been measured for three different lens distances, $d_l = 20\text{mm}$, $d_l = 30\text{mm}$, and $d_l = 40\text{mm}$, showing a good agreement with the theoretical models.

Another test has been carried out with a linear array of eight fibre optics cables with $300\ \mu\text{m}$ core diameter to check the overlap of any light spots and to measure the line of scan by the rippling light spots. This is crucial as the size of the floating element and consequently the area of the Moiré fringe pattern vary on different devices, and the sensor optics should be designed accordingly, enabling the scanning of the Moiré fringe pattern on devices ranging from $300\ \mu\text{m}$ up to $1000\ \mu\text{m}$. Using Figure 3.28b, the parameters of the system has been chosen, to generate $20\ \mu\text{m}$ light spots on the projection screen. The fibre optic cables were connected to the LED driver circuit, and the rippling has been controlled using the Arduino due micro-controller. The image of the projected light spots from each fibre optics has been captured and the Pixel analysis has been performed on them to find the intensity profile for each light spot. The result presented in Figure 3.29 displays the intensity profile of the $20\ \mu\text{m}$ rippling light spots across an scanning line, χ , of $210\ \mu\text{m}$, starting from LED number one on the left side of the curve going to the last LED on the right hand side. It is clearly displayed in Figure

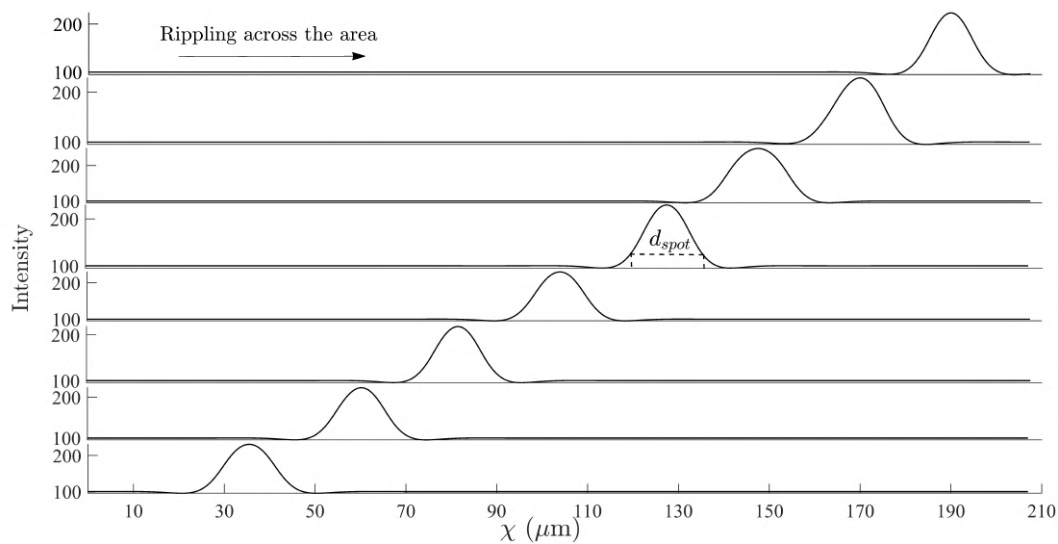


Figure 3.29 Intensity function curves of eight $20\ \mu\text{m}$ light spots across an area. The light spot size is obtained using $1/e^2$ definition.

3.29 that the light spots have minimal, providing a back to back rippling of light spots, which provides the possibility of tracking the shift in Moiré fringe patterns on small devices.

3.3 Moiré fringe pattern detection test-beds

Two optical test-beds were developed for Moiré fringe pattern tracking based on image processing, and the rippling light optoelectronics. This is essential to check the performance of the developed optoelectronics and the sensor's transduction technique, prior to the devices microfabrication. The first test-bed was based on capturing the image of the Moiré fringe pattern, and performing image processing and the second test-bed was developed to investigate the performance of the rippling optoelectronics. Two sets of gratings with $59.38\ \mu\text{m}$ and $69.38\ \mu\text{m}$ pitches were generated on lithographic film slides, generating the Moiré fringe pattern for the test-bed.

3.3.1 Moiré Fringe pattern image processing test-bed

A test-bed consisting of a precise 3-dimensional stage, a 10X objective lens, and a USB camera, was developed to check and to track the Moiré fringe pattern displacement using image processing methods; see Figure 3.30. One set of gratings was fixed, whilst the second set was attached to the displacement stage tip. the displacement of the

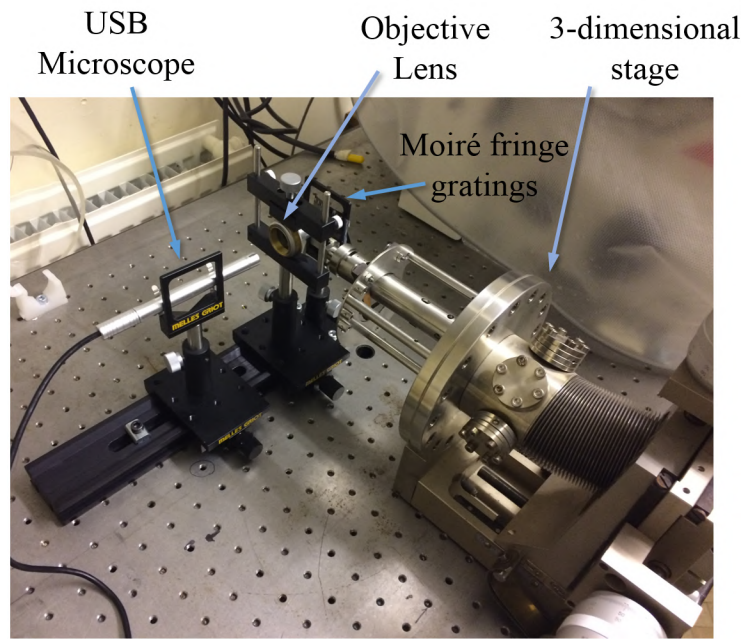


Figure 3.30 Test-bed for Moiré fringe pattern detection using image processing.

movable gratings set was precisely controlled and recorded by the stage. The objective lens and the USB camera were aligned in front of the gratings sets to capture the formed Moiré fringe pattern. The objective lens amplifies displacement of the Moiré fringe pattern and projects it to the image plane of the USB camera. Pixel analysis, as discussed in Section 3.2.7, was performed on the images captured at each displacement stage, to retrieve the intensity profile across the Moiré fringe pattern. Figure 3.31a displays the periodic dark and light bands on the generated Moiré fringe pattern using printed film slides. Intensity profile Pixel intensity analysis was carried out across 50 lines on the vertical axis of this pattern and the average intensity profile of the pattern was then obtained by averaging the intensity across the 50 lines, as shown in Figure 3.31b. The extracted intensity profiles shows the sinusoidal characteristics of the pattern. Least square curve fitting technique was performed on the average intensity profiles, to extract the amplitude, spatial period, and phase of the corresponding sinusoidal curve, mentioned in Equation 3.46, for displacement increments. Normalised sinusoidal curves for the Moiré fringe pattern at initial position and when the stage was displaced by $50 \mu\text{m}$ are illustrated in Figure 3.31c. Here, it can be observed that alterations in the intensity of any point on the pattern result in the phase shift. Furthermore, the linear relation between the phase change on the pattern, and the displacement of the gratings set is shown in Figure 3.31d.

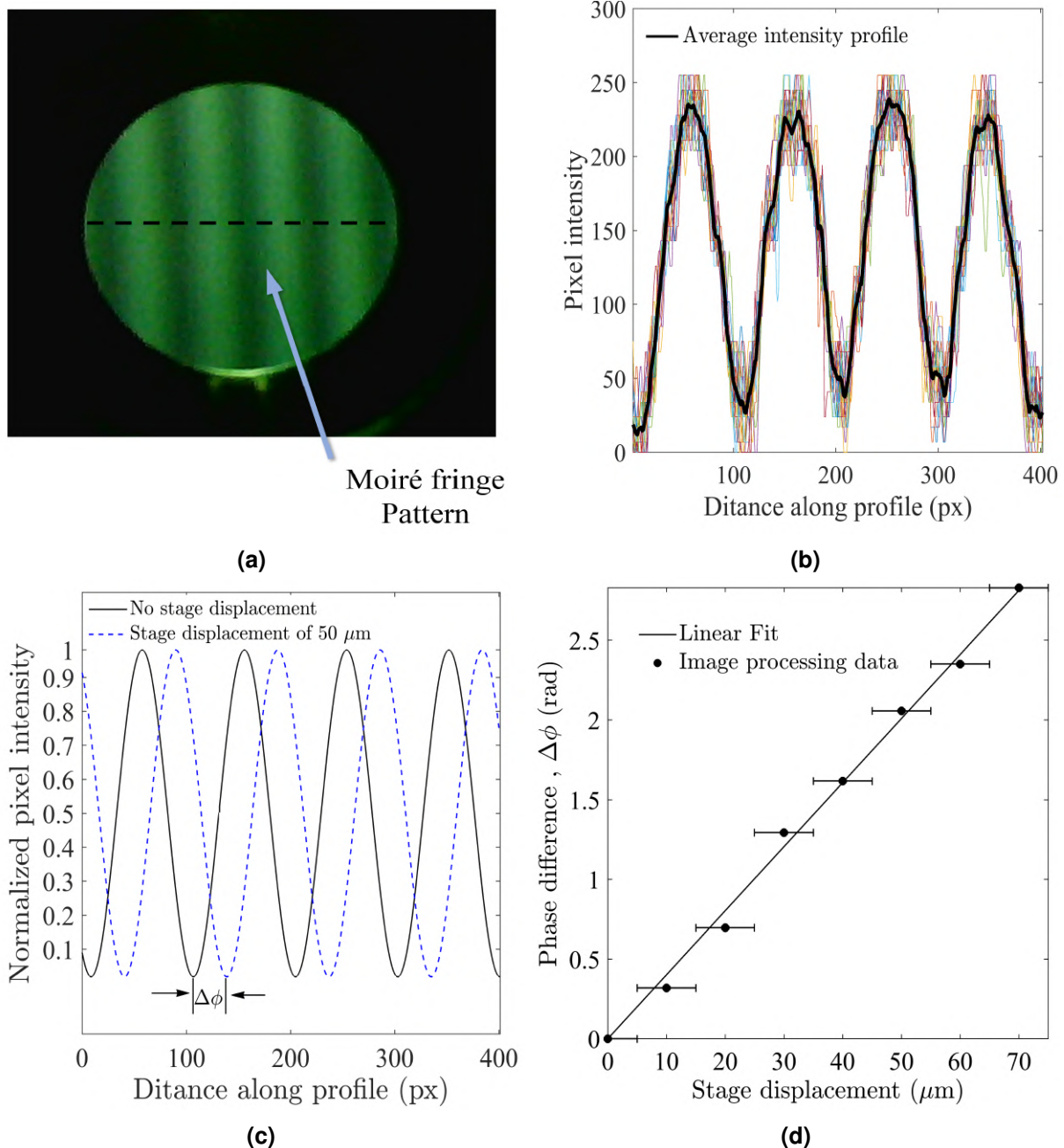


Figure 3.31 Moiré fringe pattern displacement tracking test-bed results using image processing method, (a) Generated pattern as a result of supposition of gratings sets on film slides, (b) Intensity profile across the Moiré fringe pattern area where solid black line (—) presents the average intensity profile (c) Sinusoidal curves of the initial and displaced Moiré fringe pattern, (d) Sinusoidal curve phase shift against stage displacement.

3.3.2 Moiré fringe pattern detection using rippling LEDs optoelectronics

The Moiré fringe pattern detection using image processing method test-bed is a starting point in order to investigate the phase modulation method for the Moiré fringe pattern displacement measurement, however, it is impractical in case of miniature sensors

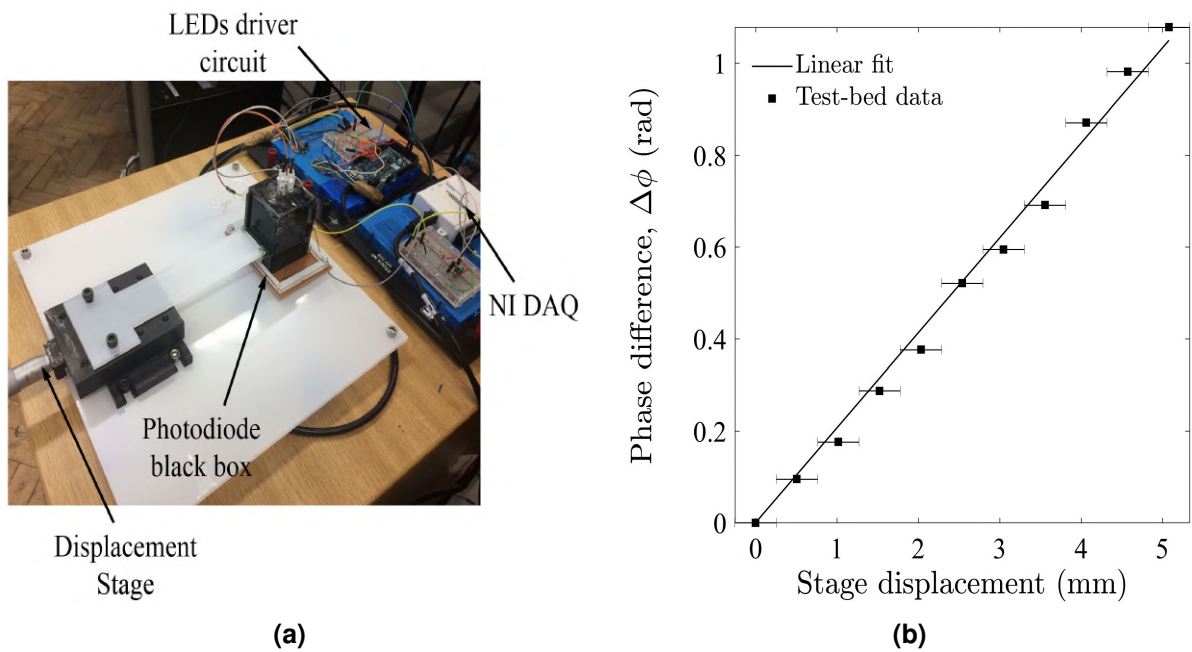


Figure 3.32 Rippling LEDs test-bed. (a) A photo of the test-bed, (b) Phase difference against displacement for the rippling LEDs method test-bed.

operating in the turbulent flows, as there would be a need for high speed image sensors. This needs a bulky sensor packaging and requires a heavy data post processing for the wind-tunnel data. Using the rippling LEDs method for phase modulation reduces the complexity of the sensors optoelectronics and provides a real-time measurement of the intensity across the pattern. A test bed on a macro-scale is set up to test the optoelectronics circuits as well as feasibility of phase modulation technique using the rippling optoelectronics. Here, two sets of gratings are placed at the top of an LED array, fitted inside a black enclosure, including a single photodiode (Vishay BPW24R) that is placed at the top of the enclosure; see Figure 3.32a.

Kingbright TC15-11SURKWA LED array is used to ripple across the gratings sets, illuminating different areas on the the Moiré fringe pattern. The photodiode is implemented at the top of the enclosure, to detect the light intensity of individual LEDs, which is connected to the photodiode transimpedance amplifier circuit, transferring the light intensity into a voltage signal. using the black enclosure reduces the effect of the environment optical noises that can be peaked by the photodiode. LEDs light intensity changes accordingly as a result of the movement of the first gratings set, which is fixed on a displacement stage with 0.254 mm accuracy. A signal processing method is used to transfer the voltage time response from the Moiré fringe pattern, at different

displacement steps into the corresponding sinusoidal curve and extract its phase against time.

Details of the signal processing method is discussed in § 6.1.1. From Figure 3.32b it can be seen that the phase shift of the Moiré fringe pattern is linearly related to displacement of the movable gratings set as expected.

3.4 Summary

In this chapter, models developed for mechanical design of the MEMS wall-shear stress sensors, using two types of micro-springs. FEA analysis carried out on the devices to verify the analytical models and investigate the effect of different parameters on the performance of the sensors. Sensors transduction technique explained alongside with mathematical models that are used to model the Moiré fringe pattern. The optoelectronics design of the sensors control unit, including circuits and optical parts, were addressed. Test-beds on the macro-scale were set up to verify the optoelectronics models and check the performance of different sections. The results from the test-beds show that the phase difference of the Moiré fringe pattern is linearly related to the wall-shear stress. This result can be used and can be extended to a miniature scale and can be used to detect the MEMS wall-shear stress devices displacements.

Chapter 4

Microfabrication and sensors packaging

After designing the structures of the micro-sensors and the parameters of the Moiré fringe pattern for different sensors, the next step is to fabricate the sensors using bulk silicon microfabrication. MEMS microfabrication processes, despite other types of microfabrication processes, are cost effective since large quantities of devices can be produced in a single process (batch processes). Moreover, due to bulk micromachining and surface micromachining, devices can be fabricated from a single material. This results in high reliability and performance of the process and devices.

In this study, the MEMS wall-shear stress sensors were fabricated using a four masks, bulk silicon-on-insulator (SOI) process to create the sensor's floating element, optical gratings, and the glass substrate. This chapter presents different steps in the micro-fabrication process of the sensors. Moreover, the detail of design and prototyping two types of sensor packaging is discussed.

4.1 Microfabrication process steps

In this part, specifications of the materials that are used in the fabrication process are introduced. The microfabrication process steps are also outlined in this section. The fabrication process utilises a four photolithography mask micromachining process to fabricate the mechanical and optical parts of the MEMS wall-shear stress sensors

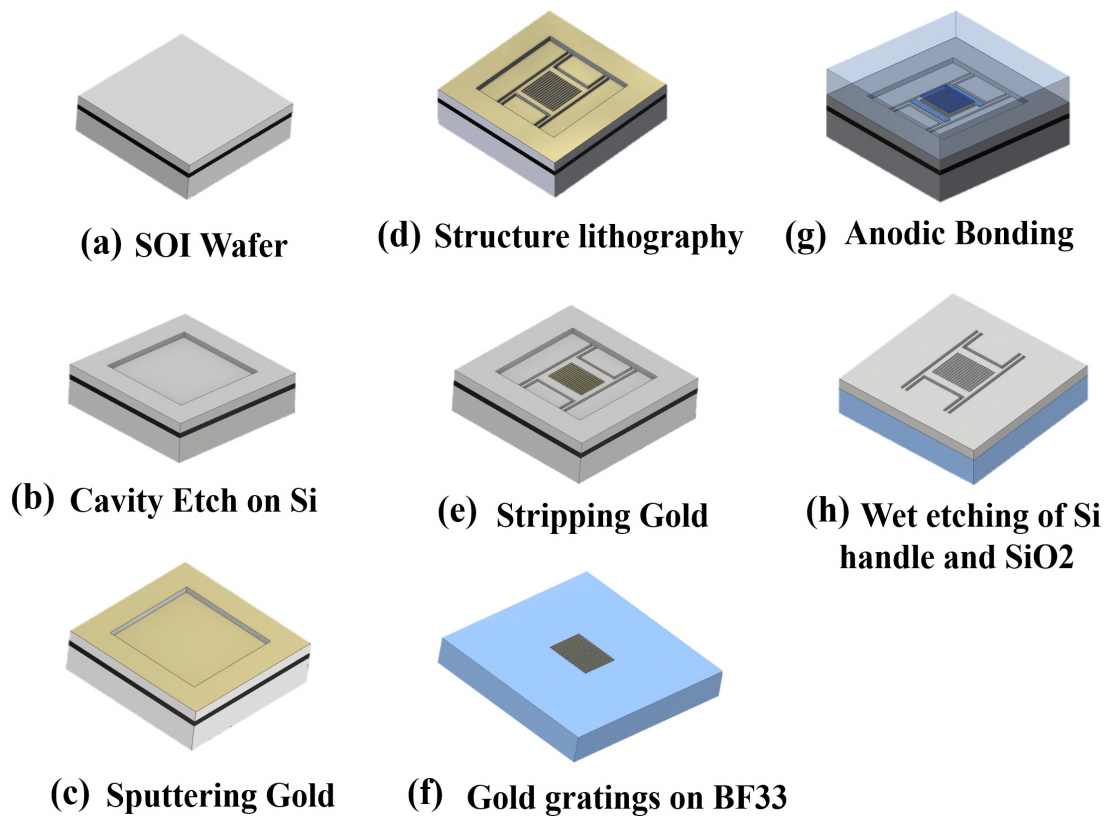


Figure 4.1 Microfabrication process flow of the MEMS wall-shear stress sensors.

structure. The microfabrication process flow is discussed in § 4.1.1. Details of each sequence in the fabrication process is also presented.

4.1.1 Microfabrication process flow

The microfabrication process steps of the optical MEMS wall-shear stress sensors are depicted in Figure 4.1. The process starts with two p-type, 100 mm diameter Silicon on Insulator (SOI) wafers. SOI wafers consist of three sections called the device layer, the insulator layer, and the handle layer. The device layer is a thin layer of silicon separated by a thin layer (normally $< 2 \mu\text{m}$) of buried oxide layer (BOX), which is normally silicon oxide (SiO_2), from the bulk handle substrate, which is also made of silicon: see Figure 4.1a. The mechanical structure of the MEMS devices are fabricated into the device layer of the SOI wafer, and hence the thickness of the device layer links to the MEMS sensors mechanical design. Based on the mechanical modelling of the MEMS sensors, a SOI wafer with a device layer thickness of $27.5 \mu\text{m}$, a box layer thickness of $2 \mu\text{m}$, and a handle layer thickness of $500 \mu\text{m}$ was selected for the devices microfabrication. The details of the microfabrication steps including the trench etch, metal deposition, structure

etch, optical gratings patterning, anodic bonding, and sensors release are discussed in the following sections.

4.1.2 Trench Etch

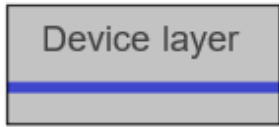
Trench etch step started with the deposition of a 7 μm thick layer of SPR220 photoresist on the surface of the device layer of the SOI wafer using a EVG coater. The photoresist was then soft baked for 3 minutes in 115°C using a EMS hotplate. The first photolithography mask is used to pattern the trench layer on the photoresist using a EVG aligner. Deep reactive Ion Etching (DRIE) is used to create a 7.5 μm deep cavity into the device layer. The trench layer is created on the device layer to provide the gap between the gratings set on the moving structures and the gratings set on the fixed BF33 glass substrate. After etching the cavity, the remaining photo-resist was stripped to provide a clean surface for the following steps; see steps 1 to 5 in Figure 4.2.

4.1.3 Gold deposition

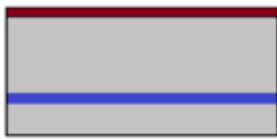
After etching the cavity, a layer of Gold (Au) was sputter-deposited across the silicon wafer via Physical Vapor Deposition (PVD) within a Balzers evaporator, to generate reflective optical grating sets. A very thin layer of chrome (Cr) and a thin layer of Nickel (Ni) were also added to the Au layer. Cr was added to Au to provide a better adhesion between Au and Si. Ni was added to Au to be used as a hard mask in the following steps. The composition ratio of these materials is 20 nm/500 nm/50 nm for Cr/Au/Ni, respectively; step 6 in Figure 4.2. Second set of the reflective optical gratings were formed on a 500 μm thick BF33 glass wafer. BF33 glass wafer was selected due to its transparency, which provides the optical access on the back side of the MEMS sensors. For this, a layer of Ti/Au with a ratio of 20 nm/500 nm was deposited over the surface of the BF33 wafer via PVD; step 17 in Figure 4.2.

4.1.4 Structure etch

The next step in the microfabrication process of the MEMS sensors was to pattern the mechanical part of the devices (.i.e floating elements and micro-springs), alongside with



1. Assign SOI wafers



2. Coat with photoresist



3. Pattern photoresist for trench etch



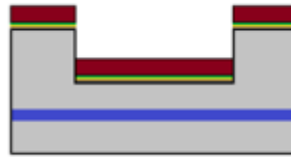
4. DRIE trenches in Si



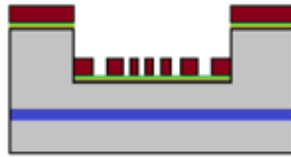
5. Remove photoresist



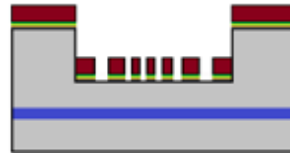
6. Deposit Cr/Au/Ni



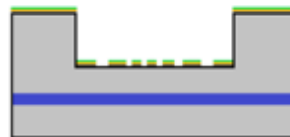
7. Coat with photoresist



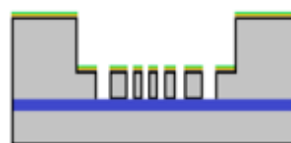
8. Pattern photoresist for floating element etch



9. Etch metal



10. Remove photoresist



11. DRIE floating element in Si



12. Wet etch Ni hard mask

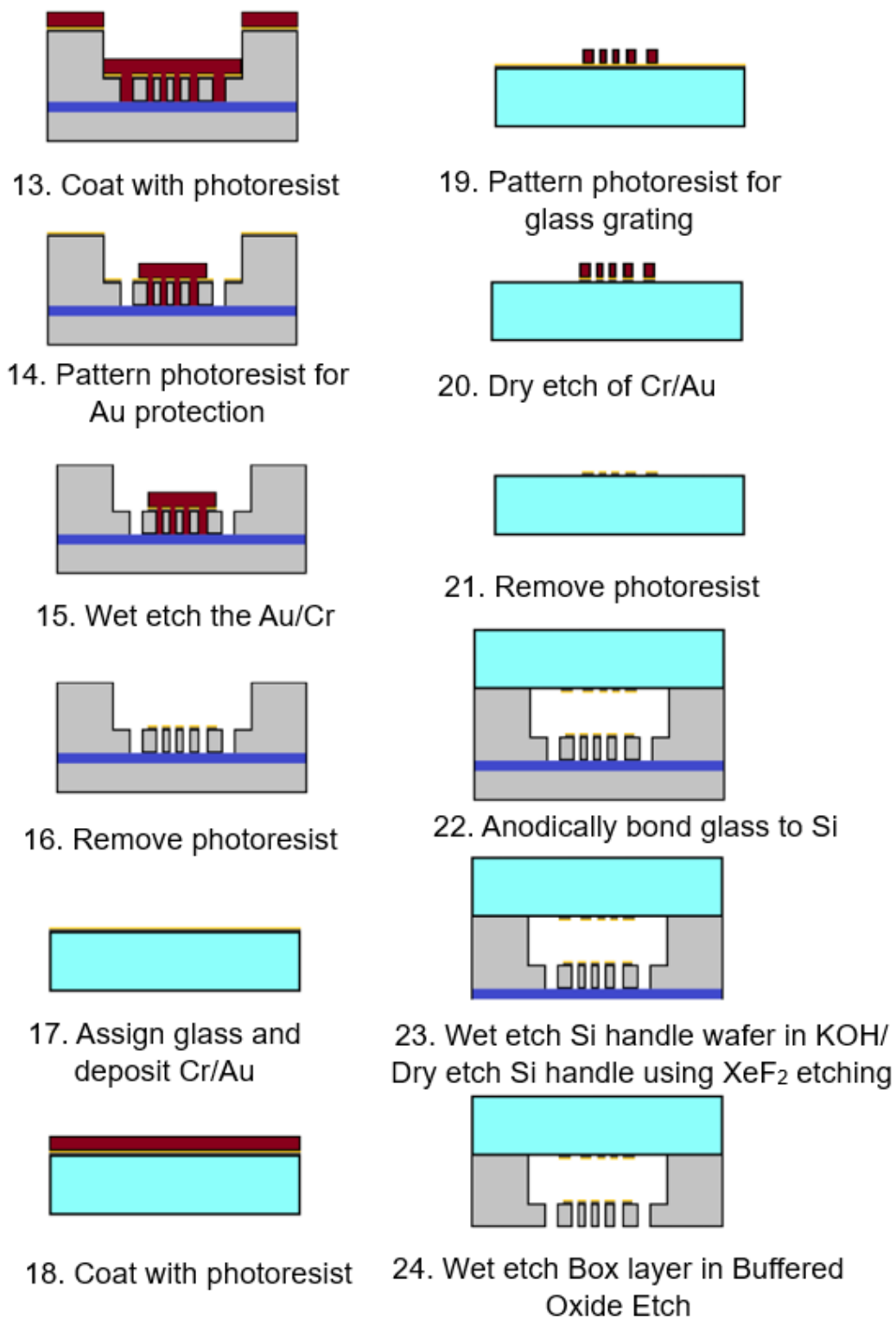


Figure 4.2 Details of the MEMS wall-shear stress sensors microfabrication process.

the optical gratings. A $3\ \mu\text{m}$ thick layer of S1813 photo-resist was coated across the device layer (including the etched cavity); step 7 in Figure 4.2. The photo-resist was then patterned using the second photolithography mask. Metal etching was conducted on the deposited metal layer (Cr/Au/Ni) via Reactive-Ion-Etching (RIE). After etching the metal layer, the photo-resist was removed from the silicon wafer. DRIE process was then utilised to etch the floating element and the micro-springs into the $20\ \mu\text{m}$ thick silicon layer. Added Ni layer (from step 6), acted as the hard mask to protect the Au layer during the DRIE process. After etching the structure into the silicon layer, Ni layer was wet etched to remove, and the device structure was left with the Cr/Au. Since the Cr/Au/Ni layer was sputter-deposited across the silicon wafer surface, a wet etching process was performed within an Acid bench to strip the Cr/Au layer away from the unwanted areas, ensuring a clean surface for the following steps. The Cr/Au layer was patterned with resist to create a block around the gratings and the Au was wet-etched using an Iodine based etchant, whilst Cr was wet-etched via a Hydrogen fluoride (HF) based etchant; steps 8 to 16 in Figure 4.2. Images of the etched silicon structure with the first set of gold optical gratings patterned on it are illustrated in Figure 4.3.

4.1.5 BF33 optical gratings

A $1.3\ \mu\text{m}$ thick layer of S1813 photo-resist was applied to the surface of the Ti/Au layer on the top of the BF33 wafer, using a EVG coater. The photo-resist was then soft-baked

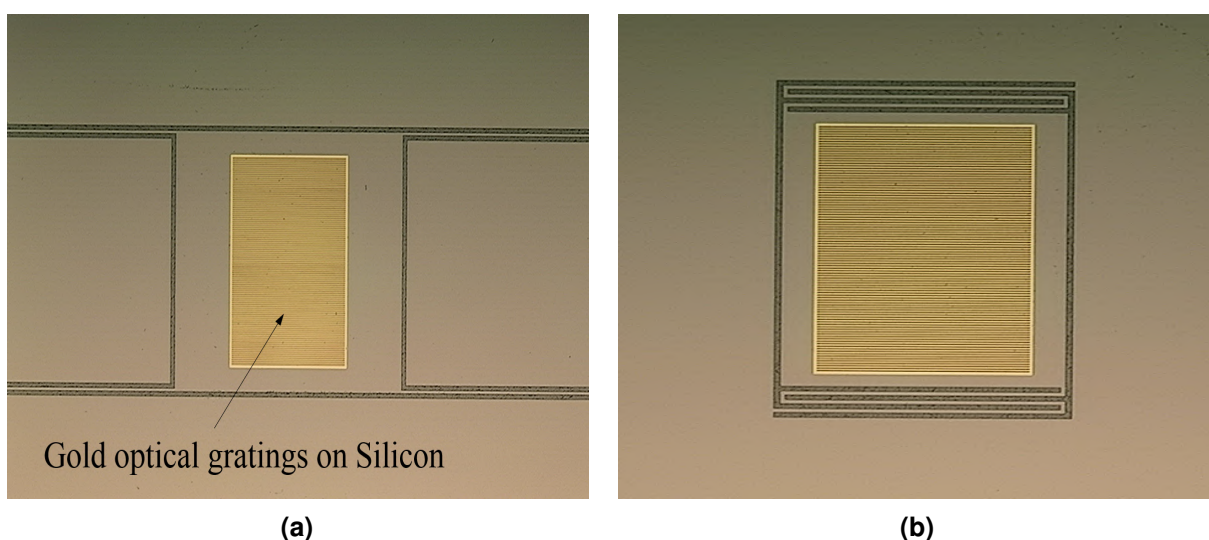


Figure 4.3 Optical images of the patterned sensors' structures as well as gold optical gratings. (a) sensor with clamped-clamped micro-spring, (b) sensor with serpentine micro-spring.

using a EMS hotplate and then exposed by EVG aligner. Dry etching of Au/Ti was then carried out using the Inductively Coupled Plasma Etching (ICP) using a STS cluster, to pattern the optical grating sets on BF33; steps 18 to 21 in Figure 4.2.

4.1.6 Anodic bonding

After patterning the metal layers on both Silicon and BF33 glass wafer, the next sequence was to bond the SOI wafer and the glass wafer. SOI and glass wafers were required to be bonded to generate the optical Moire fringe pattern and seal the cavity between Silicon and glass wafers. Anodic bonding is the method of bonding Silicon to glass. Anodic bonding process requires a relatively low temperature compared to the gold melting point to avoid the melting of the gold gratings during the bond process. SOI and BF33 wafers were aligned using a EVG aligner and heated up to $500^{\circ}C$. The anodic bonding process carried out using a EVG bonder, where an electric field was applied to the joint point of the SOI and BF33 wafer. The result was a strong bond between Silicon and glass. The schematics view of the bonded SOI and BF33 glass wafers is shown in step 22 of Figure 4.2. Shown in Figure 4.4, is the image of the bonded silicon and BF33 wafers with various sensors patterned on it.

4.1.7 Sensors release

After bonding the SOI and BF33 wafers, the next step was to remove the handle layer and buried oxide layer of the SOI wafer. This is to release the top surface of the MEMS sensors, allowing the mechanical part of the sensors to move. Here the glass layer was thick enough to act as the handle layer for the further processing. Two approaches were utilised to remove the handle and BOX layers. In the first approach, the handle layer was wet etched using Potassium Hydroxide (KOH) anisotropic etchant. Bonded SOI and glass wafers were placed in a 40 % KOH solution at $75^{\circ}C$ with etching rate of $50 \mu\text{m/hr}$ bath with the glass side protected. This was followed by an isotropic wet etching process using Hydrogen fluoride (HF) to remove the $2 \mu\text{m SiO}_2$ layer and release the sensor structure. The etching of the BOX layer stopped when it reached the silicon. At this stage, the sensors structures were released and free to move. Using wet etching methods to remove the handle and the box layers resulted in some challenges in the

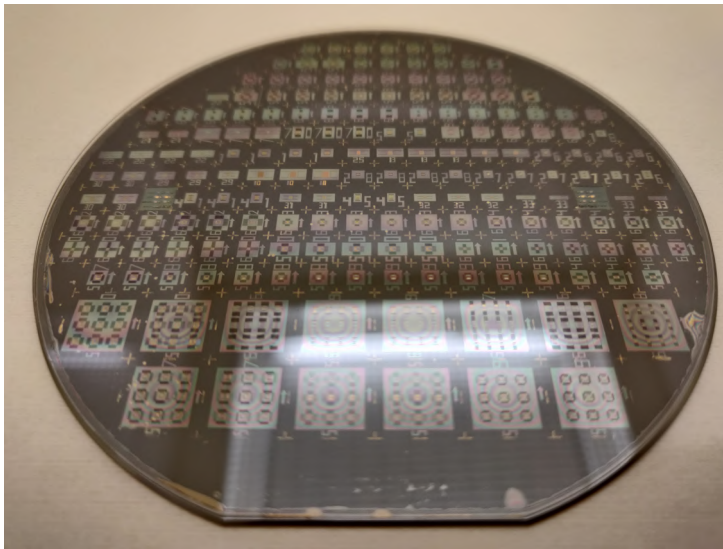


Figure 4.4 Image of the sensor devices on the bonded wafers.

microfabrication process, which resulted in the low rate success. This was mainly due the fact that the KOH could reach the patterned devices by breaking through the BOX layer. Moreover, the surface tension effects inducing from this methods, resulted in the damage to the MEMS devices, which was another reason for the low rate of success. To mitigate these issues, in the second approach, Xenon difluoride (XeF_2) vapor etching was used to remove the handle layer, followed by a vapor hydrofluoric acid (VHF) etching to remove the BOX layer. The last step in the microfabrication process was the dicing to cut the sensors into the $5\text{ mm} \times 5\text{ mm}$ dies.

Three rounds of microfabrication process were carried out to modify the individual steps involved in the process with the aim to get higher success rate in terms of the fabricating intact MEMS sensors. The list of fabricated MEMS wall-shear stress sensors and their specifications are presented in Table 4.1. Nine types of MEMS wall-shear stress sensors with different geometry were fabricated. Three out of ten sensors have serpentine micro-spring, whilst the rest of them have clamped-clamped micro-sensors. The dimensions on the fabricated devices varies from $380\ \mu\text{m}$ to 1000 for W_e , and $500\ \mu\text{m}$ to $1000\ \mu\text{m}$ for L_e . Similarly, a wide range of micro-spring dimensions were achieved, $500\ \mu\text{m} < L_t < 1700\ \mu\text{m}$, which means MEMS sensors with a range of mechanical sensitivities and resonant frequencies were fabricated that can be used for the flow measurement over a wide range of Reynolds numbers.

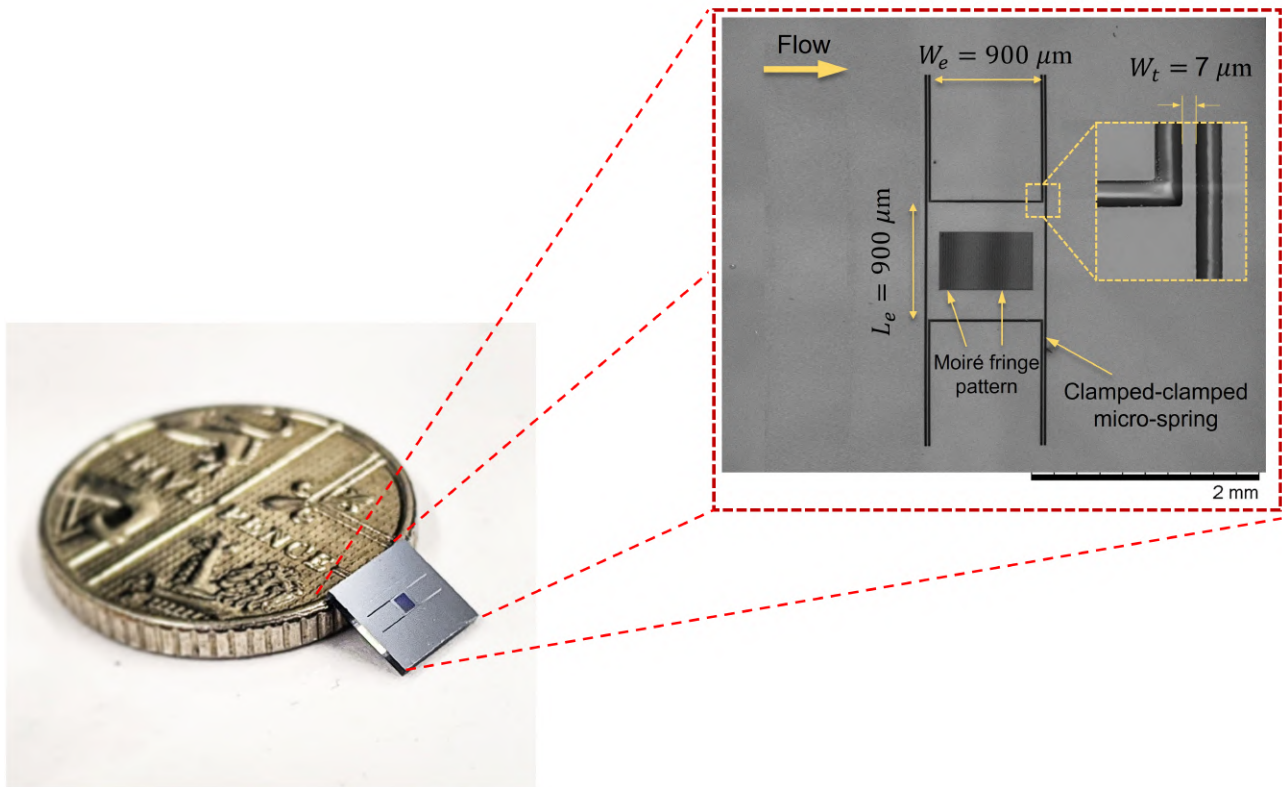
Table 4.1 Specifications of the microfabricated MEMS wall-shear stress sensors.

Device	Micro-spring type	$W_c(\mu m)$	$L_c(\mu m)$	$L_r(\mu m)$	$W_l(\mu m)$	$T(\mu m)$	n	$g_1(\mu m)$	$g_2(\mu m)$
DEV CC13	Clamped-Clamped	1000	1000	1500	7	20	-	8.8	9
DEV CC20	Clamped-Clamped	800	800	900	7	20	-	5.9	6
DEV CC23	Clamped-Clamped	500	600	1700	10	20	-	5.9	6
DEV CC25	Clamped-Clamped	900	900	1200	10	20	-	6.4	6.5
DEV SER26	Serpentine	800	500	500	12	20	3	5.9	6
DEV SER27	Serpentine	650	500	500	10	20	3	6.9	7
DEV CC30	Clamped-Clamped	1000	1000	800	10	20	-	8.9	9
DEV CC33	Clamped-Clamped	380	700	900	7	20	-	4.9	5
DEV SER68	Serpentine	670	500	500	10	20	22	8	8.1

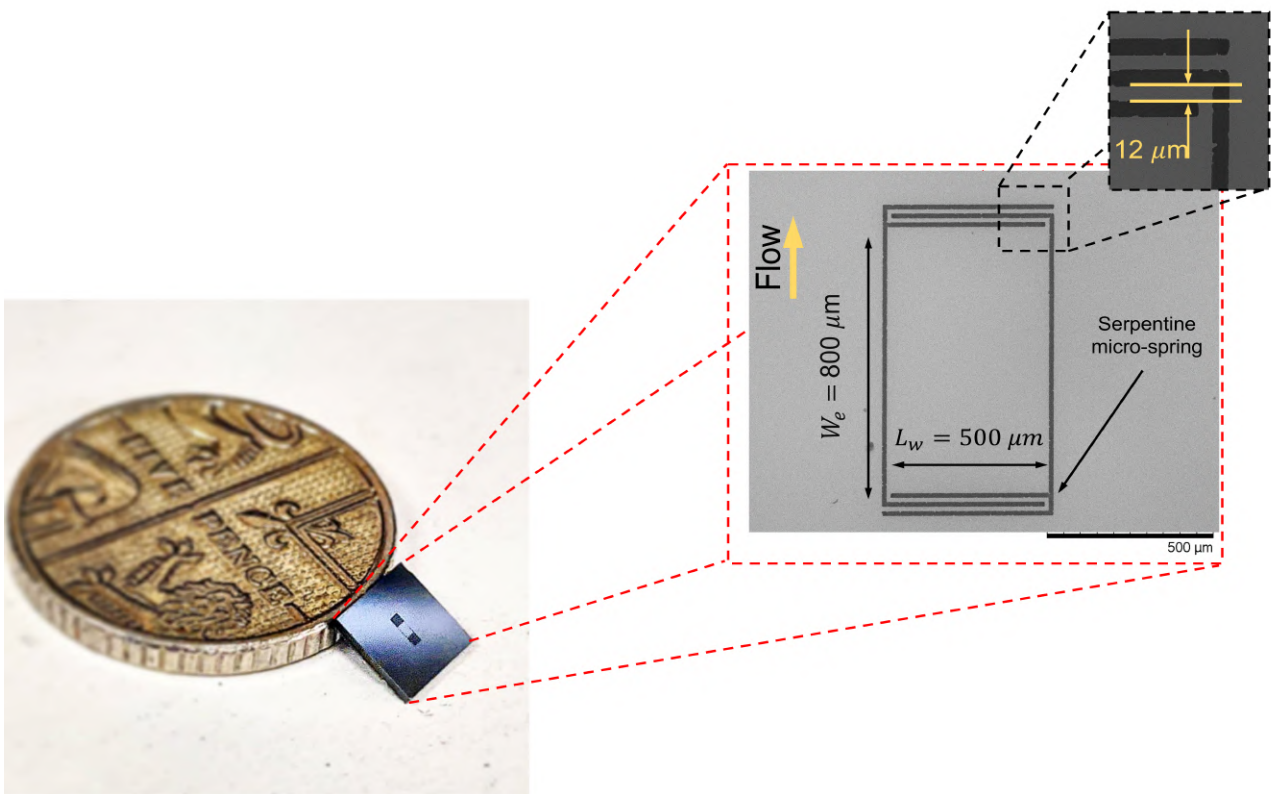
4.2 Inspection and metrology

Inspections are performed on the fabricated devices using optical light microscopy, scanning electron microscopy (SEM), and white light interferometry for the initial observation on the microfabrication results. By utilising SEM, high magnification images can be achieved from the samples. In this study, SEM was performed in a Hitachi TM3030 SEM/EDX unit at an acceleration voltage of 15 kV. SEM images of MEMS wall-shear stress sensors with clamped-clamped and serpentine micro-springs are shown in Figure 4.5. The measured size of the features on the fabricated MEMS devices are in excellent agreement with the designed parameters. Investigations were performed across the sensors dies to check the existence of any potential defects and stiction. In addition, it is important to record high quality images of the Moiré fringe patterns, which can be used in the sensors' characterisation. It can be seen that the generated Moiré fringe pattern can be clearly observed on the fabricated devices.

Residual stresses in the structure of the fabricated MEMS sensors, which are induced from the microfabrication process can potentially result in bending and curvatures in the structures (Adams and Layton, 2014). This can result in the sensor's protruding out of the viscous sub-layer resulting in errors in sensors measurement. White light interferometry (WLI) was performed on the sensors dies to measure the surface topography and step heights. This is a non-contact optical technique for surface height measurement of structures, which relies on the optical interference fringes to quantify the surface profile of the MEMS sensors by means of a beam of white light.



(a)



(b)

Figure 4.5 Images of fabricated MEMS wall-shear stress sensors with clamped-clamped and serpentine micro-springs. The mechanical structure of the MEMS sensors were fabricated at the center of 5 mm \times 5mm. MEMS sensors dies placed alongside a coin for comparison purpose. (a) SEM image of a clamped-clamped MEMS sensor, (b) SEM image of a MEMS sensor with serpentine micro-spring.

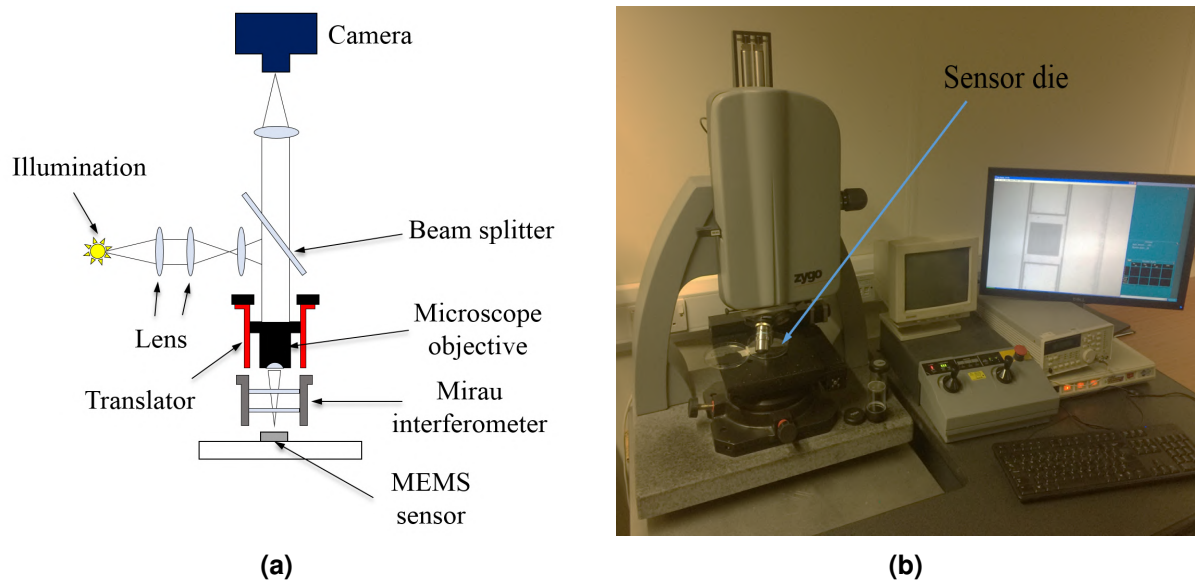


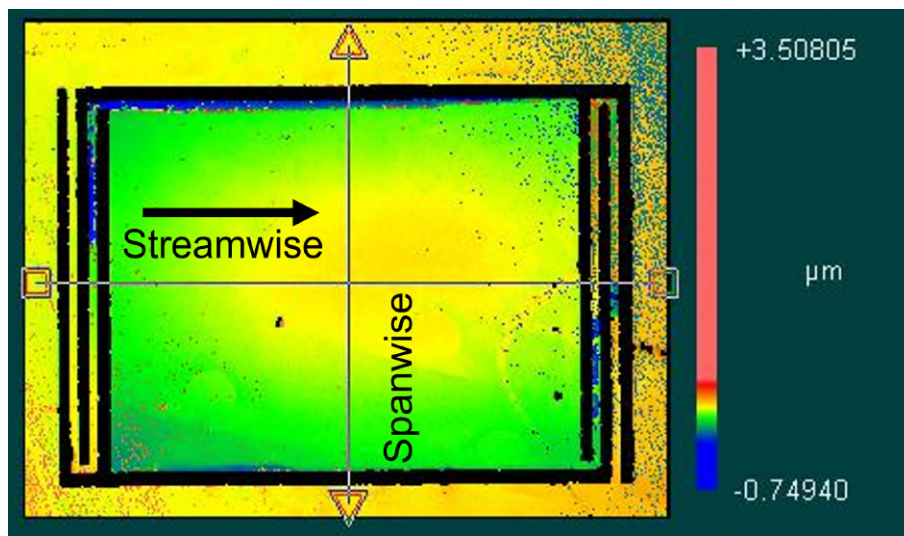
Figure 4.6 (a) Schematics of white light interferometry, (b) MEMS sensors surface profiling under Zygo interferometer.

Here, a non-contact surface analysis was performed using a Zygo NewView 5000 profiler to obtain the meteorological information of the structures of the MEMS sensors.

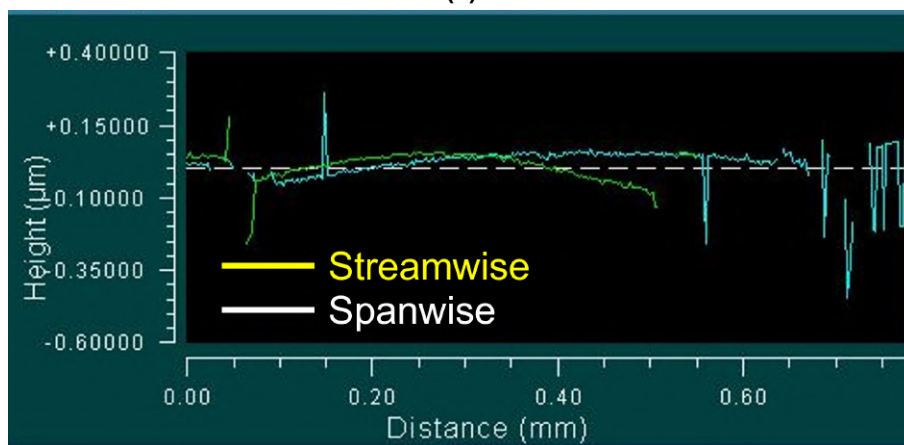
A 10X Mirau objective lens was used to focus the light beam on the MEMS sensors and capture the sensors images at the same time. MEMS sensors were fixed on the stage of and the translator of the interferometer, and moved until the fringes are appeared on the sensors surfaces on the screen. Surface scanning was performed using the planar scanning mode for a time period of 60s. The surface profile of the sensors were obtained in both streamwise and spanwise directions, as shown in Figure 4.7 for MEMS DEV SER27. The values of the maximum surface height in both streamwise and spanwise directions for the fabricated MEMS wall-shear stress sensors are presented in Table 4.2. It can be seen from the results except MEMS DEV CC25, which has a maximum height of $1.86 \mu\text{m}$, the value of the maximum height on the rest of the MEMS sensors are smaller than $1 \mu\text{m}$, which is much smaller than the thickness of the viscous sublayer in the flow. To put this in context, it can be seen in Chapter 7 that the thickness of the viscous sub-layer for the highest Measured Reloads number, is $\approx 200 \mu\text{m}$. Hence, the effect of the bending on the performance of the fabricated MEMS wall-shear stress sensors is negligible.

Table 4.2 Surface profile height measurements of the MEMS wall-shear stress sensors.

Device	Maximum height in Streamwise direction (μm)	Maximum height in Spanwise direction (μm)
DEV CC13	0.65	0.68
DEV CC20	0.54	0.57
DEV CC23	0.58	0.42
DEV CC25	1.76	1.84
DEV SER26	-0.12	-0.17
DEV SER27	0.075	0.4
DEV CC30	0.25	0.18
DEV CC33	0.065	0.05
DEV SER68	0.9	0.5



(a)



(b)

Figure 4.7 (a) Surface profile contour of MEMS DEV SER27, (b) corresponding surface profiles across the lines of scan in streamwise and spanwise directions.

4.3 Sensors Packaging

Sensor packaging is required to make the fabricated MEMS sensors functional by bringing together different parts of the transduction system together. Two types (generations) of sensor packaging were designed and developed to fix the MEMS sensors in place which enables further characterisation of the sensors within the fluid flow. The sensor packaging should be designed to allow the MEMS devices to be flush-mounted with the surface during the fluid flow measurement. Details of the design and development of both generations of the sensor packaging are presented in this section.

4.3.1 Angle sensor packaging - First generation

An illustration of the package design for the MEMS wall-shear stress devices with rippling optoelectronics is presented in Figure 4.8. In this case, the sensor packaging consisted of a main packaging body, an optical tube, and a cap to hold the sensor dies in place. All the parts were fabricated using an Autodesk Ember stereolithography (SLA) 3D printer. SLA 3D printing technology is capable of printing complex parts with high precision (geometrical tolerance is equal to $\approx 50 \mu\text{m}$). The parts were made of resins that are normally composed of epoxy or acrylic and methacrylic monomers. These resins are sensitive to light, typically UV region, and they are polymerized and harden when exposed to the light. This technique, enables the rapid fabrication of complex parts. Following the fabrication of the parts in the Autodesk Ember 3D printer, all the parts were cured and hardened in a UV curing oven. The sensor plug is the main part of the sensor packaging that accommodates the sensor dies cap, lens tube and the photodetector. The diameter of this plug was designed to be 30 mm, and a 1 mm deep step was designed at the top section of the sensor plug to guarantee that the sensor cap was flush mounted with the wall surface. It can be noticed from Figure 4.9, that there are two holes are build in to the bottom surface of the recess. The circular hole was designed to fix the photodiode inside the sensor packaging under the MEMS wall-shear stress sensor, while the rectangular window was designed to provide the light beams to be focused on the Moiré fringe pattern at the back of the MEMS sensors. To ensure that the maximum light intensity was detected by the photodetector, the optical tube was

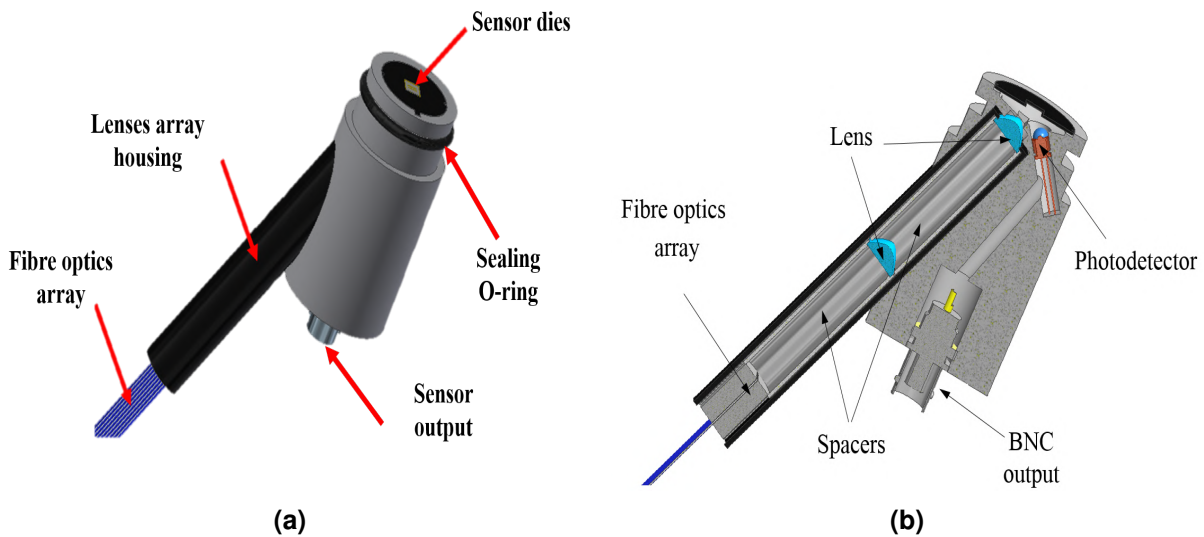


Figure 4.8 Schematics views of the sensor packaging.

assembled to the main packaging body with an angle of 28° with respect to the vertical axis, results in an angle illumination configuration.

A Vishay BPW24R photodiode was placed underneath the sensor dies with an angle of 38° with respect to the vertical axis, making a 56 degrees angle between the light tube axis and the photodetector axis. An O-ring groove was designed on the top part of the sensor plug for the sealing purposes during the measurement in the calibration rig and the wind tunnel.

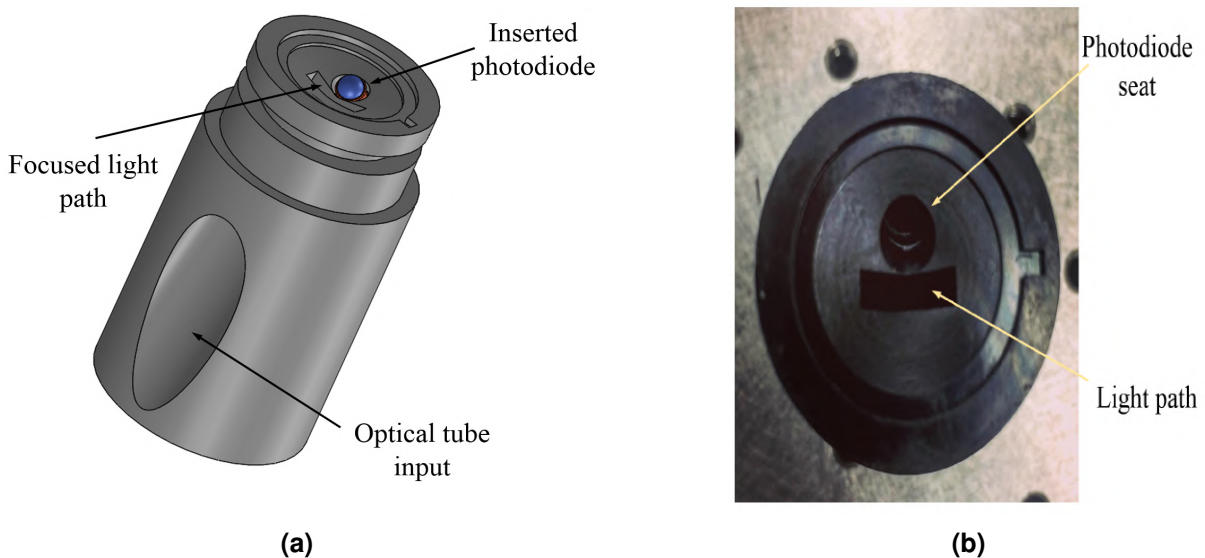


Figure 4.9 Sensor plug, (a) CAD modelling of the sensor plug, (b) Top view of a 3D printed sensor plug.

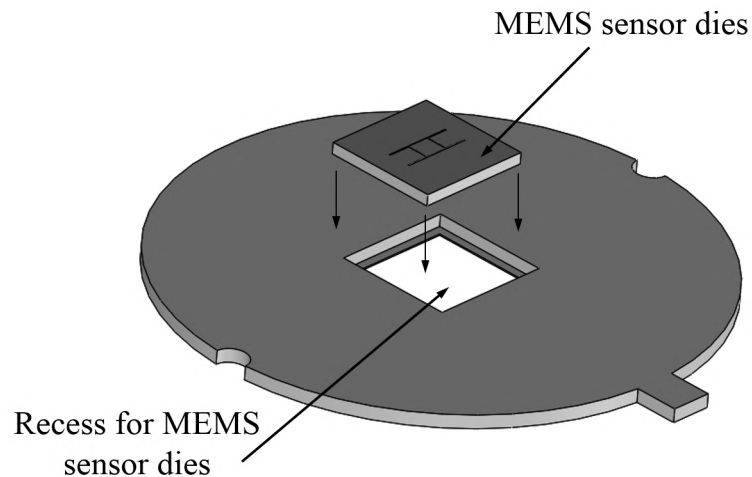


Figure 4.10 Schematics of the sensor die holder with the recess at the center. The MEMS sensor is placed into the recess and epoxied to be fixed.

A sensor cap was designed and fabricated to fix the sensor dies into the main packaging body as shown in Figure 4.10. A recess with the depth of $500\ \mu\text{m}$ was implemented at the center of the cap such that the sensor surface to be flush. MEMS sensors dies were placed and epoxied inside the recess. This sensor cap was then mounted and fixed at the top of the sensor plug part ensuring a flush and smooth surface around the sensor. A key structure was placed on the cap to be fitted into the keyhole on the package to ensure the sensor was placed in the flow direction.

Edmund optics 88-283 aspheric condenser lenses with a diameter of 10 mm were placed inside a tube alongside with the designed spacers and the fiber optics array, to form an optical pathway for the light that was shining out from the fiber optics ends toward the Moiré fringe pattern. Optical spacers were designed to fix the optical components in place and to generate the required distance between the optical components in the system and also to guarantee that the image plane of the optical system lies on the pattern on the sensors. Diameter of these elements were 11 mm and the length of these spacers are designed based on the sensor size and consequently the size of the light spots required. A different set of spacers with various lengths, varying between 10 mm up to 50 mm, were fabricated for different sensor sizes. As it can be seen in Figure 4.11, lenses were fixed inside an step provided inside the spacer tubes. The overall length of the optical tube for this type of the sensor packaging was 100 mm.

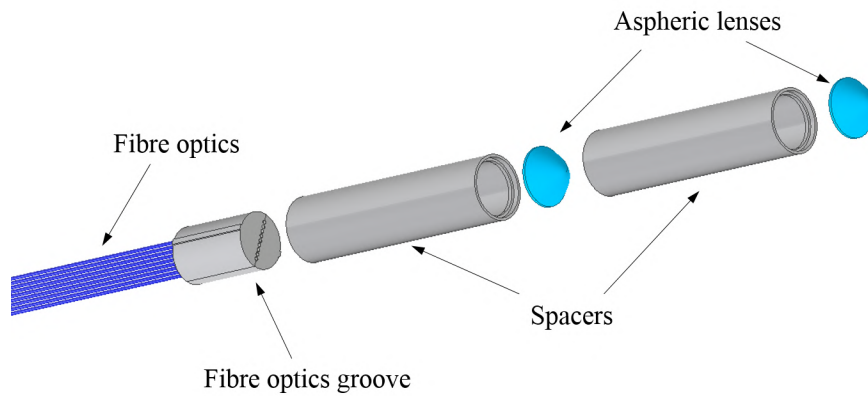


Figure 4.11 Explosive map of components inside the optical tube. The spacers are designed to fix the lenses and fibre optics groove in place and also to provide the gap between the components in the optical system. All these components are fixed inside an enclosure and then are assembled into the main sensor plug.

The fibre optics groove is designed to put the fibre optics in an equally spaced array. The process flow of the fibre optics array fabrication is illustrated in Figure 4.12. First, two semicircular pieces with diameter of 9.6 mm of are fabricated using SLA 3D printing. Fibre optics grooves with spacing of 850 μm (center to center) are made of circular profiles of 650 μm to leave enough space for the fibre optics to be fixed inside. Epoxy wells are also designed on the parts to enhance the strength of the bonding. Pillars and holes are designed and fabricated on these parts for alignment purposes and reduce any misalignment errors between these two part during assembly. Thorlabs FT300UMT multi mode fibre optic cable with a core size of 300 μm and the jacket size of the 600 μm were used. Smaller grooves with 300 μm diameter were designed at the end of each groove as it is shown in Figure 4.12a. These smaller grooves were added to ensure that only beams of light with the diameter of 300 μm were shining out of the fibre optics array into the lens system. Moreover, they reduced the effect of varying light spots profiles shinning out from different fibre optics cables. This can happen during the fibre optics polishing, where the core shape of the fibre optics cables can be slightly different. Fibre optics cables were then placed and fixed inside the micro-grooves with both ends polished. The epoxy was applied over the fibre optics and inside the epoxy wells to retain the fibre optics cables inside the first set of micro-grooves. The second part of the grooves was then aligned and assembled onto the first part and the fibre optics cables, courtesy of the alignment pillars and holes, and it was pressed down to fix and secure the fibre optics cables in place. Different parameters in the 3D printing process,

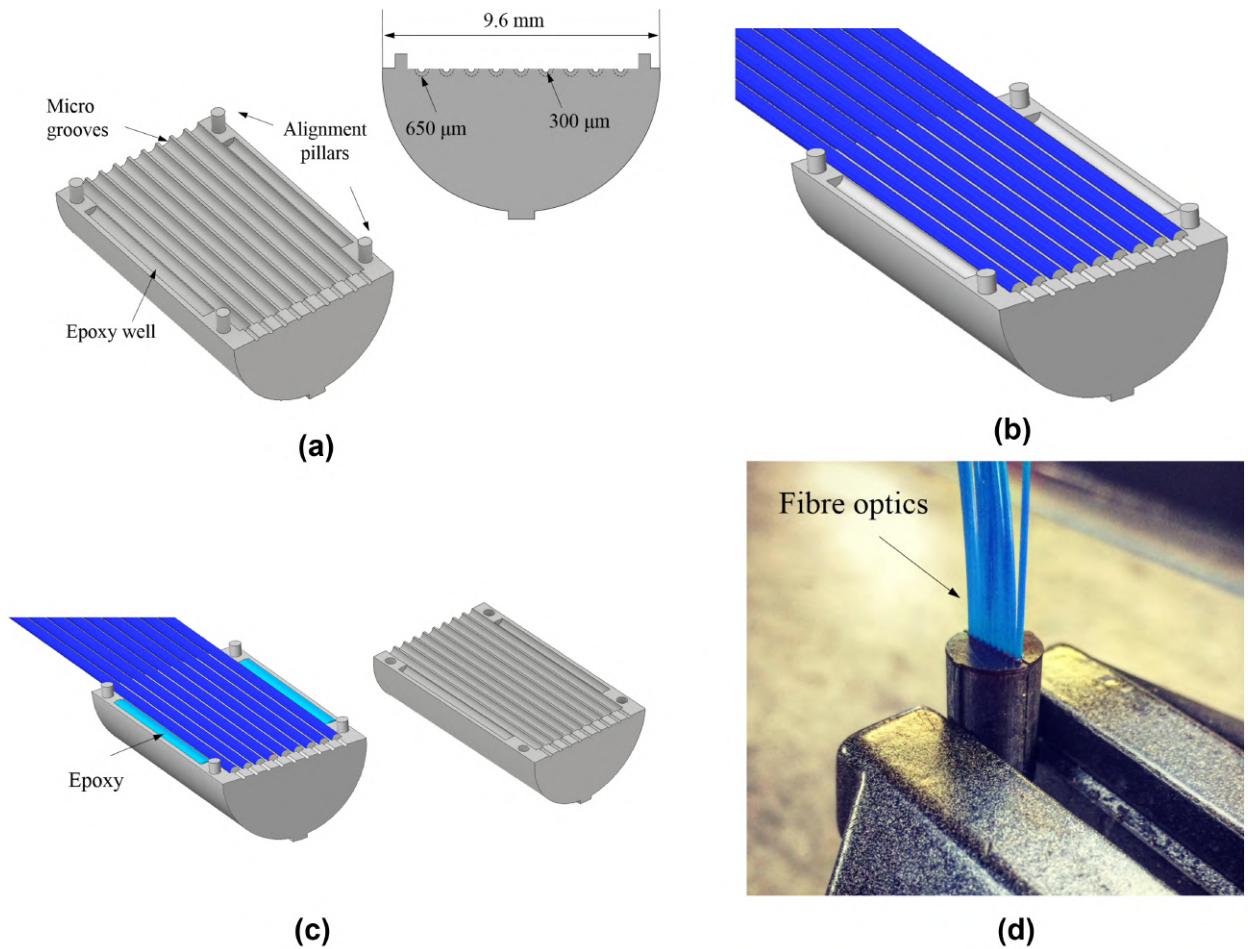


Figure 4.12 The process flow for the fibre optics micro-groove fabrication. (a) Two parts are fabricated using 3D printing technology, (b) The fibre optics are placed and retained in the grooves, (c) UV curable epoxy is applied to the first part and on top of the fibre optics, (d) Second part is assembled to the first part using the alignment pillars and holes, (e) Fibre optics are fixed inside the micro-grooves.

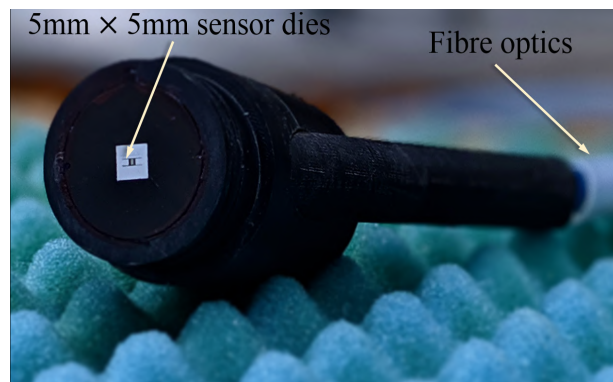


Figure 4.13 A prototype of the sensor packaging. The MEMS wall-shear stress sensor can be seen at the center of the sensor die holder.

such as the exposure time and layer height, were optimised to minimize the geometrical errors of the fabricated micro-grooves.

The final prototype of the sensor packaging is shown in Figure 4.13. A 5 mm × 5 mm sensor die was fixed and epoxied to the sensor cap. Optical components were fixed inside the optical tube and the final system was then assembled into the main packaging body. 1.5 meter long fibre optics cables are protected inside a shielding tube, to avoid any damage during the sensor handling.

4.3.2 Direct illumination sensor packaging - Second generation

The second generation of the sensor packaging was designed with the aim to reduce the overall packaging size, and to further develop it towards commercialisation. As shown in Figure 4.14, unlike the angle illumination sensor packaging, the concept of the second packaging was designed based on the direct illumination of the fibre optics light into the MEMS sensors, while the photodiode is placed in an angle with respect to the center line. Here, the sensor packaging is a cylinder with a diameter of 30 mm and a length of 50 mm. The optical tube, which is consisted of the lenses, lens spacers and the fibre optics array, was placed at the centerline of the main body of the sensor packaging. A 5 mm × 2 mm rectangular window was placed underneath the MEMS sensor dies as the optical access to the sensor and to eliminate the shining light being detected by the photodiode; see Figure 4.14b. The Vishay BPW24R IR photodiode, was placed 5 mm underneath the MEMS sensor dies in a 45 ° configuration with respect to the centerline. A customised M403-EMEF-12LS-PC-002-B fibre optics array was used to further improve the sensor packaging. The fibre optic array was consisted of 12 multi mode OM4 fibre optics cables with a core size of 50 μm and the cladding size of 125 μm that were placed in a linear array with a spacing of 250 μm in a multi-fibre termination push-on (MTP) connector. One end of the 3m long fibre optics bundle utilised a female MTP connector, which was plugged into the sensor packaging via a port designed in the optical tube, as illustrated in Figure 4.14d. The other end on the fibre optics were fixed in a male MTP connector, as depicted in Figure 4.15, that is plugged into a female MTP connector on the sensor control unit, which is discussed in § 4.4. In addition to the direct illumination technique, the smaller core size in OM4 fibre optic cables (50 μm)

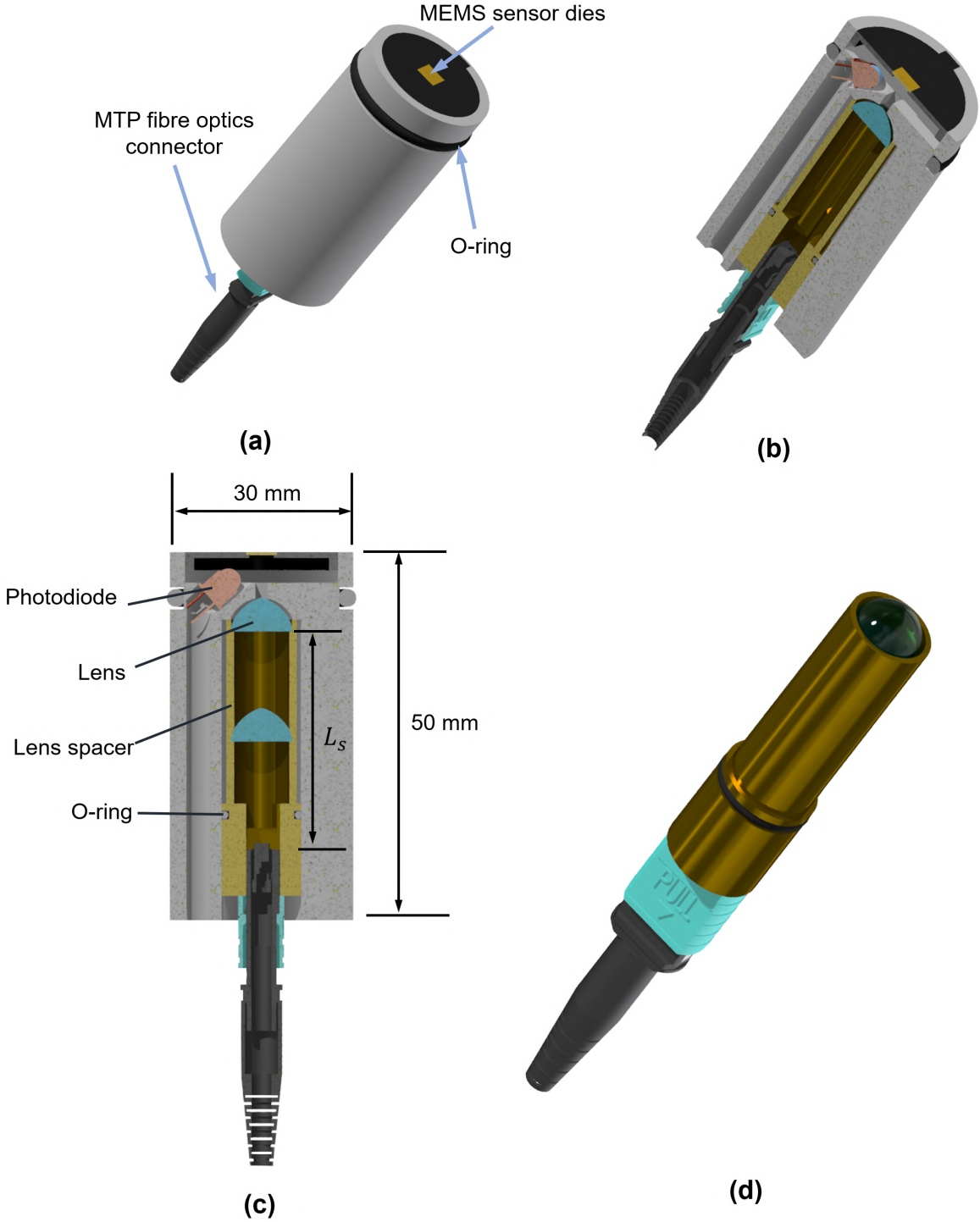


Figure 4.14 CAD modelling of the second generation sensor packaging. (a) schematics of the overall sensor packaging, (b) cross section view of the sensor packaging with one lens, (c) cross section view of the sensor packaging with two lenses, (d) the optical tube (spacer) with the female MTP connector plugged into it and. The lens can be seen at the top of the optical tube.

Table 4.3 Required length of spacers for MEMS sensor packaging

Device	L_s (mm)
DEV CC13	20
DEV CC20	25
DEV CC30	20
DEV CC26	28
DEV CC27	35

compared to FT300UMT fibre optics ($300\mu\text{m}$), which were used in the first generation of the sensor packaging, provides the opportunity to further reduce the overall packaging size. Moreover, it eliminates the errors and tolerances that are linked to the fabrication and assembly of fibre optic cabled using 3D printed grooves. In addition, by utilising the male to female MTP connection, it is possible to plug different sensors to one sensor control unit.

Shown in Figure 4.14d, is the optical tube (lens spacer) that was designed to: (1) hold the lens(es) in place, (2) provide the female MTP connector port that allows the MTP connector to be connected to the sensor packaging, and (3) to provide the distance required between the fibre optics array and the lenses. The effective length of the spacer (L_s), and the number of the lenses (one or two), are linked to the size of the MEMS wall-shear stress sensor and the Moiré fringe pattern, and it varied between 20 mm to 40 mm. Considering the analysis presented in § 3.2.5, and by using Equation 3.60 to Equation 3.62, the required length of the spacers for the MEMS wall-shear stress sensors are presented in Table 4.3.

The geometry of the sensor die holder (sensor cap) is similar to the first generation, where the thickness of the cap increased to 3 mm (1mm in the first generation), to eliminated the bending in the cap and to reduce the risk of damage during the assembly. Similar to the first generation the keyhole geometry was used to lock the sensor cap in place, whilst at the same time used to indicate the flow direction. The main body of the sensor packaging and the optical tube were fabricated using the 3D printing manufacturing in an Autodesk Ultimaker 3⁺ PLA 3D printer, and then they were machined to compensate for any geometrical tolerances that are linked to the 3D printing process. M4 Brass threaded inserts were placed into the sensor packaging body to fix the optical tube inside the packaging body by utilising M4 hex socket grub screws.

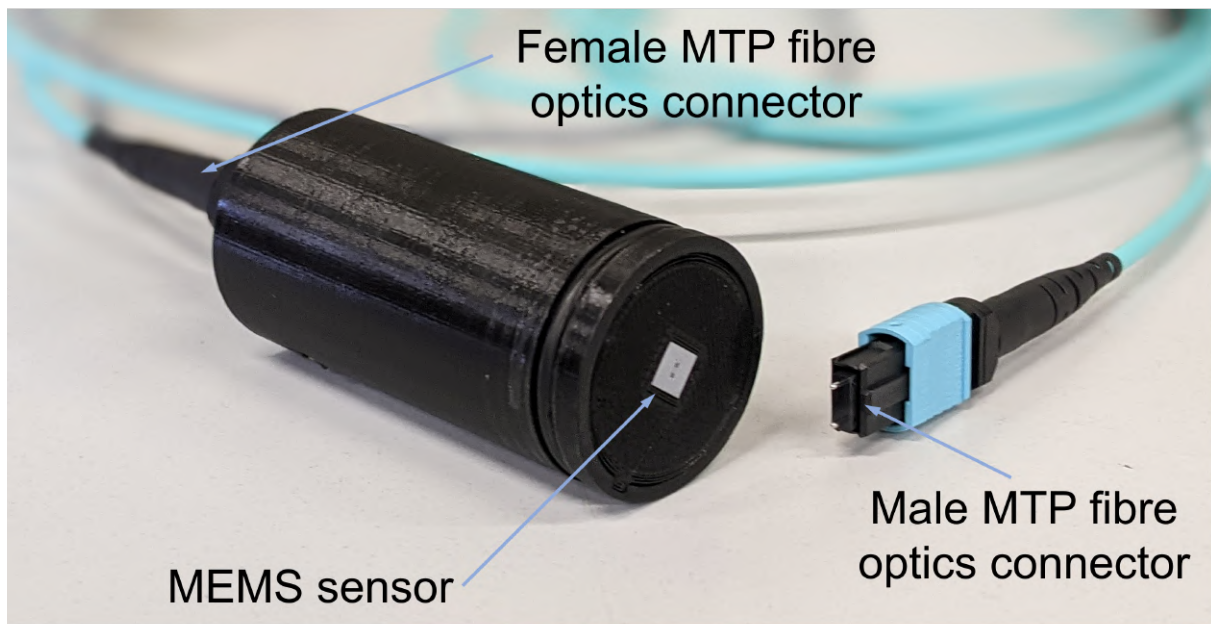


Figure 4.15 An image of a prototyped sensor packaging, with the MEMS sensor dies placed at the center of it. on end of the fibre optics array with a male MTP connector can be seen in the image, whilst the other end is plugged into the sensor packaging.

Two o-rings were utilised in the optical tube and the main packaging body to provide the sealing during the flow measurement. A comparison between the length of the sensor packaging in the first generation (100 mm) and the second generation (50 mm), indicates a 50% reduction in the overall size of the sensor packaging.

4.4 Sensor control unit electronics

A sensor control unit, which is shown in Figure 4.16, was developed to bring together all the electronics and optics that are used as a part of the sensor transduction. For this, Printed-Circuit-Boards (PCBs) were designed and fabricated for the designed circuits; reader is referred to § 3.2.3 and § 3.2.4 for the circuits schematics. Twelve Broadcom ASMT-MR00-AHJ00 red high power LEDs with a colour wavelength of 625 nm were used for the light sources. This wavelength was selected based on the reflectivity of the gold, where its reflectivity reaches $\approx 95\%$ at a wavelength of ≈ 600 nm (Shanks et al., 2016). In addition, twelve 10Ω through hole trimmer potentiometer were utilised in the LEDs drive PCB to adjust the LEDs intensity of the individual LEDs. This is important for balancing the light intensity across the twelve LEDs. The intensity of the transmitted light from all the LEDs should be identical before reflecting from the Moiré fringe pattern,

to minimise any error linked to the difference in the initial intensity of the light sources. The LEDs drive circuit is powered up by a 6 V power supply. A customised MTP (female) to ST OM4 fibre optics bundle with a length of 0.3 m was utilised to collect the light from the LEDs and transmit it to the sensor packaging. An adaptor was designed and fabricated to provide the connection the ST connector of the fiber optics to the LEDs; see Figure 4.16. The other end of the fiber optics bundle, which is a MTP ELITE 12 fibres connectors, was fixed onto the sensor control unit box. The Male MTP connector can be plugged into the port to transmit the light into the sensor packaging.

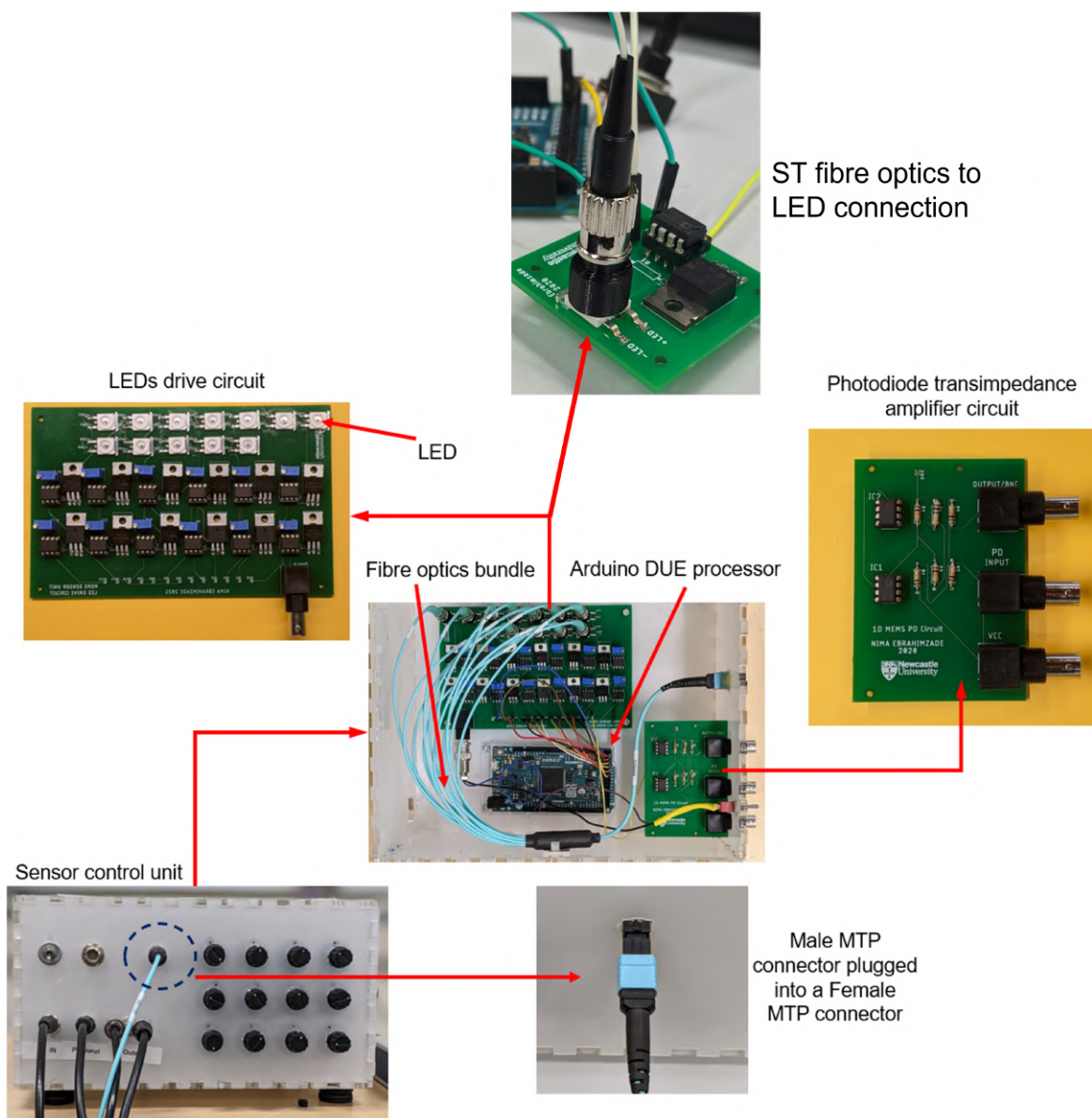


Figure 4.16 Electronics of the sensor control unit including the LEDs drive circuit's PCB, photodiode transimpedance amplifier circuit's PCB, and the Arduino DUE microprocessor. A bundle of 12 OM4 fibre optics were used to transfer the lights from the LEDs into the sensor packaging via a female to male MTP connection.

4.5 Summary

The microfabrication process of the MEMS wall-shear stress sensors has been discussed in this chapter. Devices were inspected under the SEM and surface profilometer to check for potential defects, misalignment, stiction, and failures in the sensors structures. The result of the inspection and meteorology shown that the fabrication results are in agreement with designed parameters. The design and prototyping of sensor packaging has been presented. The sensor packaging is designed to provide a flush mounted area around the sensor die and to bring all the elements of the MEMS devices together and make them operational for the flow measurement. Finally, fabricated electronics PCBs and the sensors control units have been presented.

Chapter 5

Experimental Setup

Experiments were conducted in different test rigs for calibrating the MEMS wall-shear stress sensors and to characterise their performance in turbulent flow. A laminar flow rig was developed for the sensors' calibration. Dynamics performance of the devices was characterised utilising the Stroboscopic light effect using the ZYGO profilometer. Finally, the performance of the MEMS sensors was verified inside a turbulent boundary-layer flow alongside with Hot-wire anemometry and Laser Doppler Velocimetry (LDV) inside a wind tunnel. Details of these test rigs and diagnostic tools are outlined in this chapter.

5.1 Laminar flow cell development

A calibration rig was designed and developed for the MEMS wall-shear stress sensors static calibration, as shown in Figure 5.1. The calibration rig is a high aspect ratio rectangular duct that allows the laminar fluid flow over the MEMS wall-shear stress sensors. The fluid flow velocity inside the rig increases from zero at the wall to a maximum centerline velocity at the middle of the channel. The duct height, $2h$, is controlled using thin 500 μm stainless steel shims, and the duct width, b , is set to be 80 mm ($b/2h = 1600$). The duct length is 2m ($x/2h = 4000$), allowing the fluid flow to be fully-developed (in which the velocity profile does not change) before reaching the sensors as well as the pressure tapings and to ensure the pressure drop can be measured for flows with lower speeds. The channel base is manufactured from a single piece of precision face-machined aluminium cast tooling plate CAL5®, of dimensions 2000 mm x 228 mm x 12 mm.

Experimental Setup

In order to accurately calibrate the wall-shear stress sensor using the rig, the internal surfaces of the channel are required to be extremely flat and with low surface roughness so that the flow of fluid passing through the duct is not interrupted. Ensuring that the material used for the base was of high dimensional fidelity was therefore essential. An aluminium cast tooling plate with a surface roughness of $0.4 \mu\text{m}$ was used due to its excellent resistance to corrosion.

A threaded inlet hole was located at the center of the rig entrance. A straight threaded-to-tube adapter push fitting was directly assembled into this hole, allowing for the compressed air to be fed into the channel. Milled gasket grooves were used across the full length of the channel base, on both sides. These grooves were used to house 5.7mm diameter nitrile rubber gasket cord. The dimensions of the grooves were designed for this exact gasket specification, to ensure that the sealing performance of the calibration rig is maintained at all times. A 30 mm diameter reamed hole, located 1650 mm down the flow inlet, allowed for the wall-shear stress sensor housing to be mounted directly into the channel base from below. The hole was reamed so as to ensure an interference fit between the two components, which when combined with o-rings, eliminates the possibility of leakages. Pressure tapings were placed along the centreline of the channel, as depicted in Figure 5.12a. The distance between the pressure tapings was varied ensuring that a greater range of volume flow rates could be measured with the same sensor.

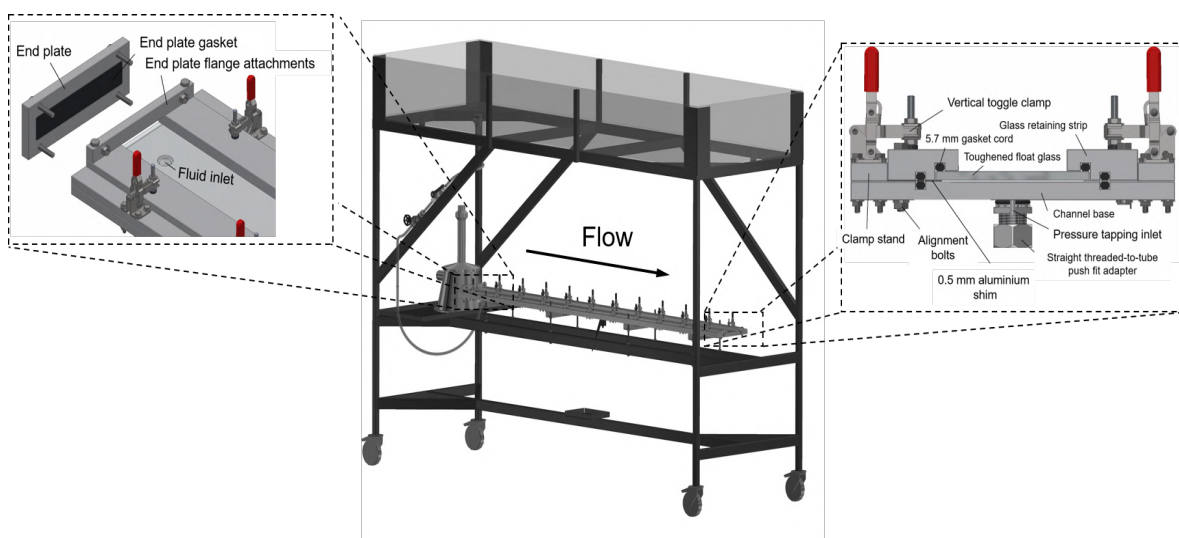


Figure 5.1 A schematics of the calibration rig. The high aspect ratio of the duct ensures that the flow is laminar and fully-developed inside the rig during the sensors' calibration.

To connect the pressure tapping holes to the pressure transducer, aluminium inlet tubes were placed into each tapping by means of adhesive, allowing for PVC piping to be plugged into them. A single piece of toughened float glass was used for the top face of the duct. The glass rested directly over the shims, forming a rectangular duct of 2000 mm x 80 mm x 0.5 mm through the centre of the channel. As illustrated in Figure 5.2b, aluminium parts were bolted into the flow-inlet end of the rig to prevent the leakage at the inlet. A rubber nitrile gasket was utilised over the plate face, which sealed the section as it compressed against the channel. To keep the components of the calibration rig stationary and to avoid leakage during the sensors calibration test, two aluminium strips were bolted to the channel to retain both the shims and the top surface glass. Gasket grooves were milled across the full length of these strips.

Compressed dry air flows into the rig through a 16 mm diameter entrance and exit the channel at the atmospheric pressure. Since the channel's aspect ratio is high, the flow inside the rig can be expressed by a Poiseuille flow where the velocity profile can be obtained as (White, 2016)

$$u(y) = \frac{6Q}{2bh} \left[\frac{1}{4} - \left(\frac{y}{2h} \right)^2 \right] \quad (5.1)$$

The air flow rate, Q , is regulated from 0 to 100 standard cubic feet per hour (SCFH), using a Dwyer RMA-8-BV flow meter with an accuracy of ± 0.5 SCFH. Here, the flow increases from zero at the top and bottom walls to a maximum value at the channel's centerline.

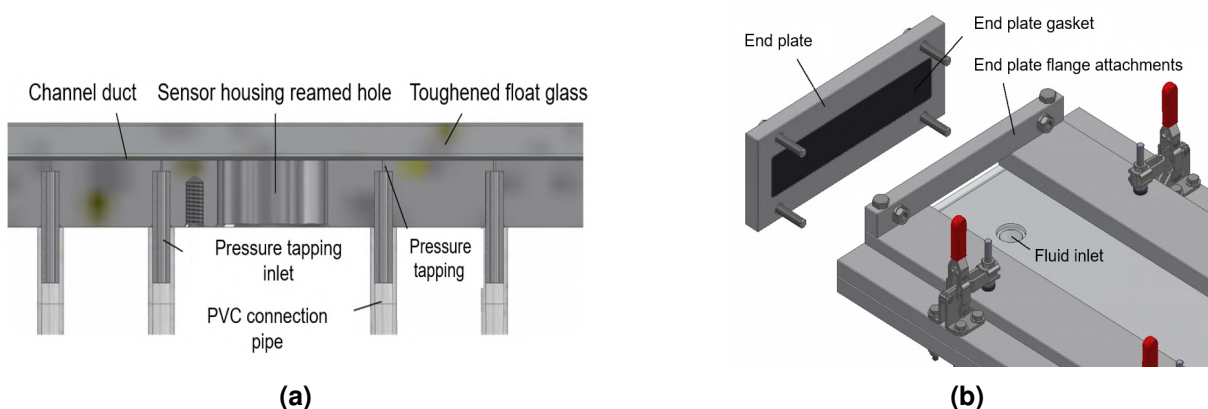


Figure 5.2 (a) Half section view of the calibration rig duct. Pressure tapings are placed on either sides of the sensor to measure the pressure gradient across the channel. (b) End plate sealing attachment.

Experimental Setup

For the highest flow rate of 100 SCFH ($0.00079 \text{ m}^3/\text{s}$) the maximum velocity (centerline velocity) is equal to 19.75 m/s. This results in a Mach number of 0.0576 for the centerline, meaning that the flow is incompressible for the highest flow rate in the rig.

The Reynolds number based on the hydraulic diameter, Re_{D_H} , is expressed as

$$Re_{D_H} = \frac{2Q\rho}{b\mu} = \frac{U_b D_H}{\nu} \quad (5.2)$$

in which ρ is the density, μ is the dynamic viscosity, and $D_H = 4A/P$ is the hydraulic diameter. The Reynolds number for the maximum measurable flow rate is calculated as 872, which is lower than the transitional Reynolds number of 2300 for channel flows, indicating that the flow remains laminar inside the calibration rig in the testing range (White, 2016). In order to check that the flow is fully developed by the time it reaches the sensor, the entrance length is calculated in the rig. The entrance length is a function of the Reynolds number and the hydraulic diameter and for the flow between parallel plates it is written as

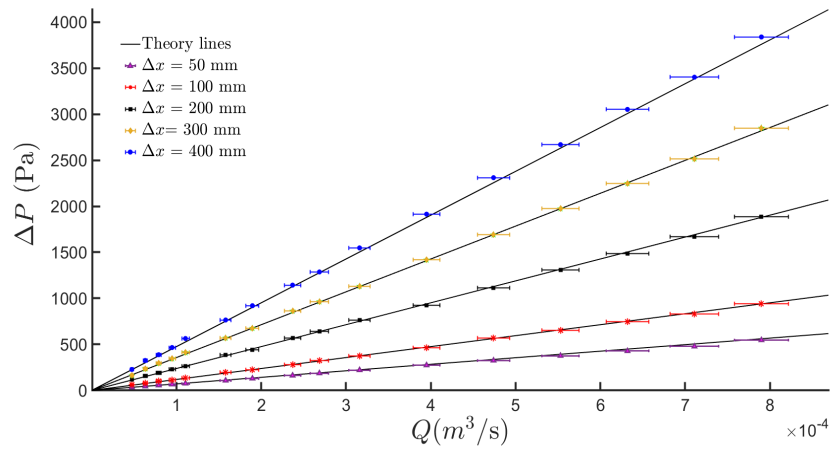
$$L_{entrance} = 0.06D_H Re_{D_H} = \frac{0.24Q\rho}{\mu} \left(\frac{2h}{b}\right) \quad (5.3)$$

The entrance length at the maximum flow rate is 79 mm that is well before the sensor location of 1650 mm down the flow entrance. This indicates that the flow is fully developed when it reaches the sensor and the pressure tapings on either sides of it.

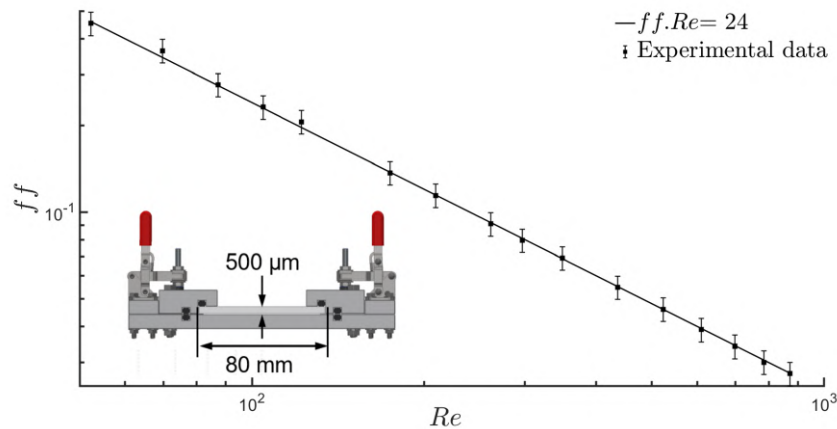
A Betz PARW 76 differential pressure manometer is used to estimate the stream-wise pressure gradient across the rig, $\partial P/\partial x$, from which the time-averaged wall-shear stress is quantified, by measuring the pressure difference, ΔP , across the pressure tapings with a known distance of Δx , installed on the lower wall of the rectangular duct with a half height of h . For a fully developed, laminar, incompressible flow, the value of the wall-shear stress is determined from (White, 2016),

$$\tau_w = -h \frac{\partial P}{\partial x} \quad (5.4)$$

Validation profiles of the calibration rig are acquired prior to the sensors' calibration. Figure 5.3a illustrates linear pressure differential, ΔP against the flow rate, measured across different pressure tapings' distances, Δx . The results are in excellent agreement



(a)



(b)

Figure 5.3 Validation profiles of the calibration rig. (a) Pressure drop across the calibration rig versus the flow rate for various pressure tapings' distances. (b) Friction factor versus Reynolds number for laminar flow in the calibration rig. The black solid line is $ff \cdot Re = 24$.

with the theory line, meaning that the flow is laminar and fully developed. Shown in Figure 5.3b is the friction factor, ff , against the Reynolds number, Re , demonstrating a laminar flow in the calibration rig up to the highest flow rate tested. Friction factor is calculated as $ff = \tau_w / (0.5 \cdot \rho \cdot \bar{U}_b^2)$, where the wall-shear stress value is determined from Equation 5.4, and the velocity is calculated from the flow rate measurement. Reynolds number is defined as $Re = 2h\bar{U}_b / \nu$, where h is the channel half height, \bar{U}_b is the bulk velocity through the calibration rig determined from the flow rate, and ν is the kinematic viscosity of the fluid (for air $\nu = 1.51 \times 10^{-5} \text{ m}^2/\text{s}$). The data collapse to the laminar curve $ff = 24/Re$, based on the Fanning friction factor definition, with error bars showing the uncertainty in the pressure drop measurement, (White, 2016).

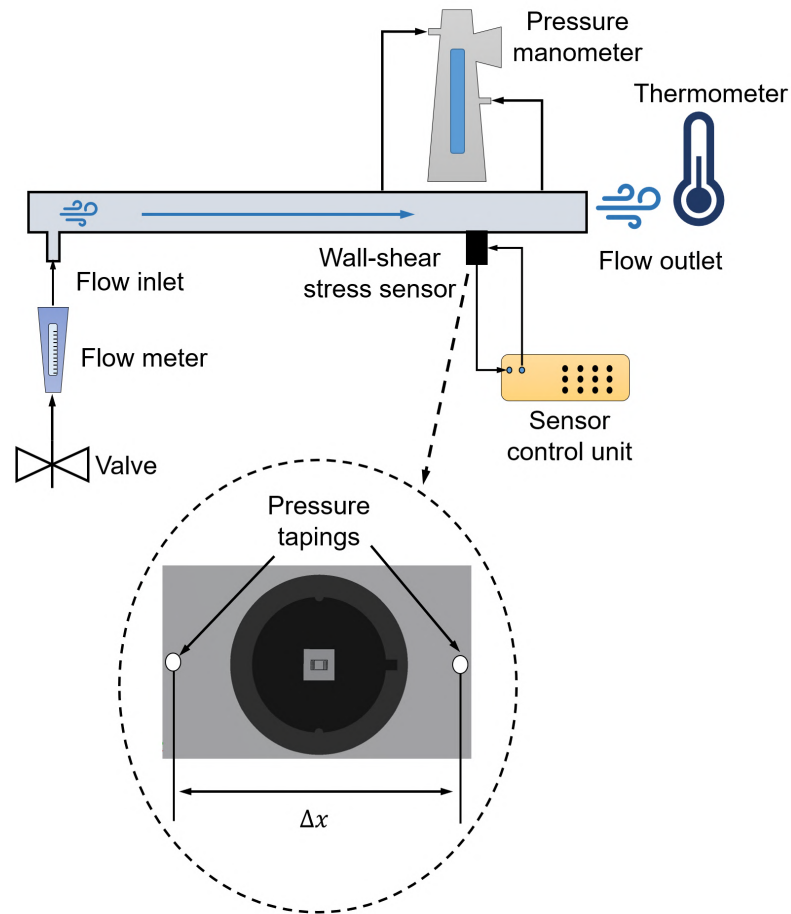
5.1.1 Sensors' calibration experimental setup

The experimental setup for the calibration of the MEMS wall-shear stress devices is depicted in Figure 5.4. The sensors' packaging was plugged into the calibration rig, whilst the floating element was flush with the bottom surface of the rig. The inlet compressed dry air flow rate was controlled by adjusting a valve, where the flow rate was measured using a Dwyer RMA-8-BV flow meter, with a relative accuracy of $\pm 4\%$. The pressure difference across the rig and on two sides of the sensors was measured using the Betz PARW 76 manometer with an accuracy of $\pm 50 \mu\text{m H}_2\text{O}$ and a dynamic range of 0 up to 400 mmH₂O. Here, the pressure taping on the upstream of the sensor was plugged into the positive port of the manometer, whilst the downstream pressure taping was connected to the negative port on the manometer, resulting in the differential pressure measurement. A Voltcraft PL-125-T2USB VS thermometer with an accuracy of $\pm 0.15\%$ was implemented at the flow outlet to record the air flow temperature during the sensor calibration, to monitor the effects of the temperature drifts on the sensors' performance. The sensors' output signal at each test point was monitored and recorded utilising a 16-bit National Instrument cDAQ-9171 card, via the sensors control unit.

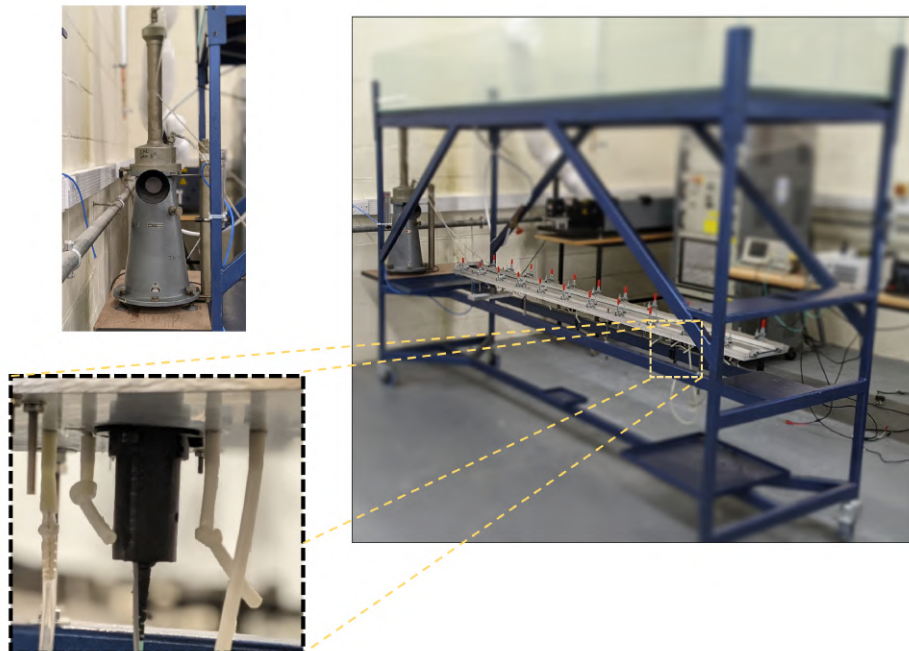
5.2 Dynamic Characterisation Experimental Setup

The sensors' dynamic characterisation was carried out under the ZYGO NewView 5000 profilometer by using the ZYGO's Dynamic Metrology Module (DMM), which was designed to measure MEMS devices as they are moving. The dynamic application freeze-frames the motion of the device under test by synchronizing the strobed light source in the NewView interferometer to the device movement with a drive signal from an Arbitrary Waveform Generator (AWG). Using the stroboscopic light source, the motion of the device can be effectively frozen, whilst adjustment of the illumination phase delay, which controls the lag between the drive signal and the illuminator strobe, allows the device's full range of motion to be examined. The schematics of the dynamic test setup is illustrated in Figure 5.5a. A Pragmatic 2416A AWG controls the frequency and the phase delay of the illuminator strobe via a NewView control unit. Moreover, the amplitude and the frequency of the piezoelectric actuator is controlled by AWG.

5.2 Dynamic Characterisation Experimental Setup



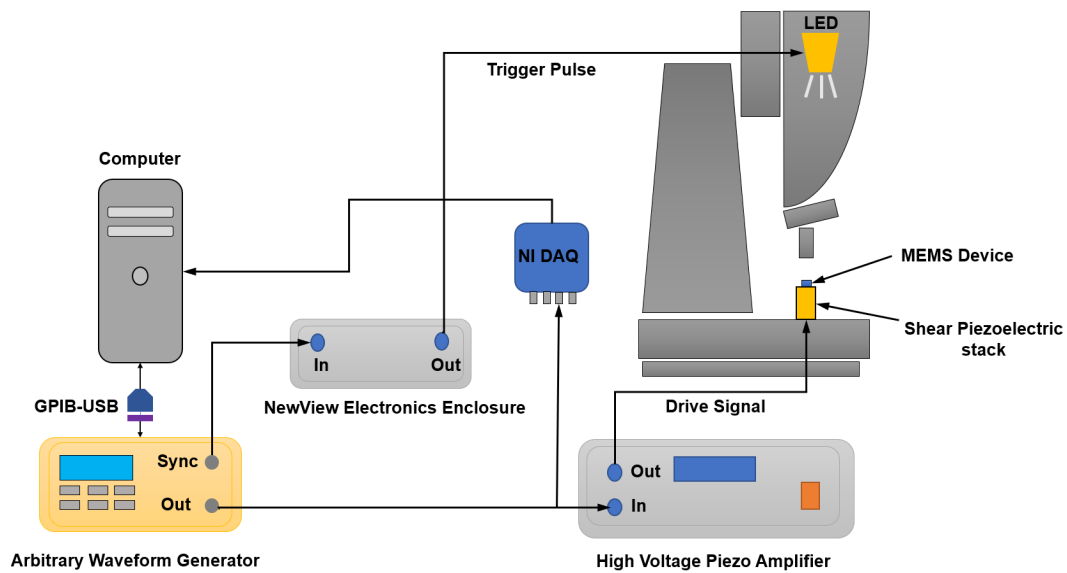
(a)



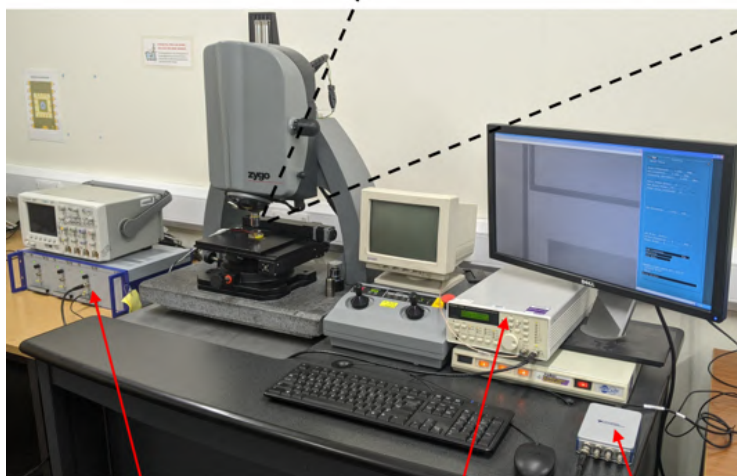
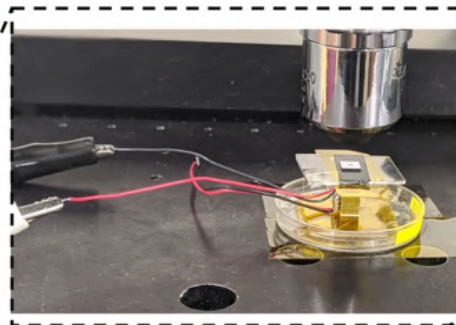
(b)

Figure 5.4 Experimental setup for the MEMS wall-shear stress sensors calibration. (a) A schematic view of the experimental setup; (b) an image of the calibration rig with the sensor plugged into it. The Betz manometer and a plugged sensor are shown in the insets.

Experimental Setup



(a)



High Voltage Amplifier

Pragmatic 2416A
AWG

NI DAQ

(b)

Figure 5.5 Experimental setup for the dynamic characterisation of the MEMS wall-shear stress sensors. (a) Shows the schematics of the setup and (b) shows the actual setup. The MEMS devices are mounted on the top surface of a 2D piezoelectric shear stack, which actuate the devices.

The drive signal from the AWG enters the Piezoelectric actuator via a high voltage E-508 PICA Piezo Amplifier Module. Sensor dies were mounted at the 5mm×5mm surface of a Thorlabs PN5FC2 low-voltage Shear Piezoelectric stack, which provides lateral displacement in x and y directions. The two-dimensional shear piezoelectric actuator consists of multiple discrete shear piezo chips bonded together using epoxy and copper foils. Positioners providing displacement along both lateral axes mate the upper end plate of one shear piezo stack to the lower end plate of another. A drive voltage of ± 200 V from the PI E-508 high voltage amplifier generates an inplane displacement of $7\mu\text{m} \pm 20\%$ on the actuator's surface. MEMS sensor dies were fixed on the surface of the Shear piezoelectric actuator using carbon tape so the streamwise direction of the sensor was aligned with the x direction on the actuator. A 10X objective lens was utilised alongside with a zoom adjustment knob with a range of 0.4-2.0X to capture the image/video of the sensor.

5.3 Wind Tunnel

The experiments are conducted in a open-loop low-speed wind tunnel that is operated using an ABB ACS880 inverter that sets the velocity of the induction motor rated at 15 kW. The motor can be adjusted to an angular velocity ranging from 0 RPM to 1000 RPM, which corresponds to a maximum attainable flow speed of ≈ 30 m/s inside the test section. The motor is directly attached to a fan that drives the flow. The air flow is passed through six meshed screens and honeycomb panel to enhance the the flow uniformity and to reduce turbulence intensity before entering the test section. The meshed screens and honeycomb panel is situated within a 6:1 contraction section from the settling chamber to the test section.

The measurements are taken inside the test section of the wind tunnel with an inner geometry of 350mm×490mm×3000mm. The boundary-layer is developed on a flat plate, manufactured from 20 mm thick Formica, and included an elliptical leading edge with a semi-major axis of 100 mm. A turbulence trip is attached to the leading edge of the flat plate, which is manufactured from 6mm thick acrylic and laser cut into a zig-zag shape with a pitch of 6mm, which are 11mm in width and extended across the

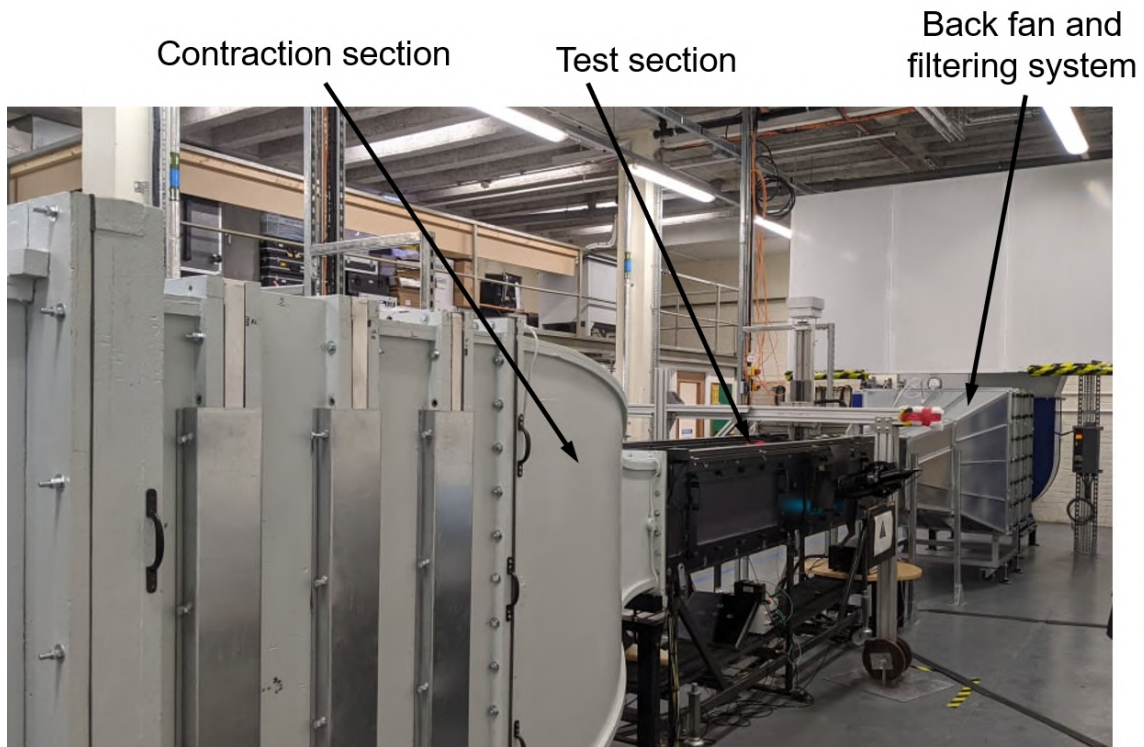


Figure 5.6 Wind tunnel facility at the Fluid Dynamics laboratory.

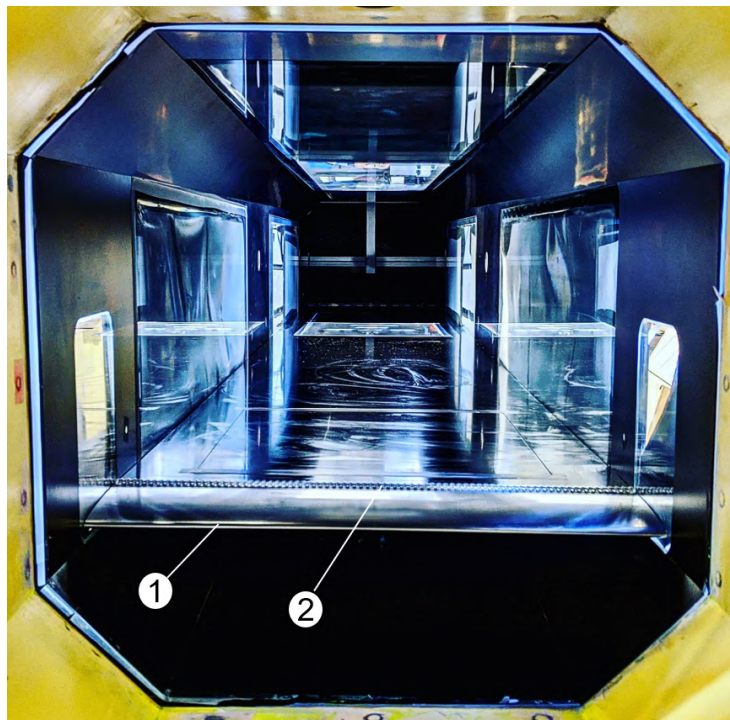


Figure 5.7 A picture of the wind tunnel test section , showing (1) the elliptical leading edge and (2) the turbulence trip.

width of the flat plate. Suggested by Elsinga and Westerweel (2012), this kind of trip generates the low speed streaks and hairpin vortices consistent with that of the wall structures found in a turbulent boundary layer.

An adjustable flap at the trailing edge of the test section is adjusted to a maximum angle of 47.6° in 3.4° increments to alter the stagnation point of the flow at the tip of the leading edge. This results in a zero pressure gradient flow along the test section and avoids the flow separation at the leading edge. After the test section, the air passes through a three stage filtration system to remove any seeding particles introduced during testing. A back fan is operating via a 18 kW induction motor that automatically adjusts in speed to prevent a pressure build up in the test section.

The flat plate in the test section is consisted of three removeable $400\text{mm}\times 350\text{mm}$ plates, which are used to mount wall-shear stress sensors flush to the surface, and are placed 100mm, 1.6m, and 2m downstream of the leading edge. Measurements are taken 1.8m downstream of the leading edge over the second removeable flat plate.

Low frequency and large scale structures can originate from the facility equipment, such as the fan that drives the flow. As a result of this, a common procedure is to high-pass filter the signals at a cut-off frequency that relates the flow's free stream velocity, U_∞ , to the length of the test section, $f > U_\infty/2L_{TS}$, where L_{TS} is the test section length. Therefore, all the turbulent boundary-layer signals obtained in this study are high-passed filtered using $f > U_\infty/2L_{TS}$, to remove the low frequency noise linked to the equipment.

5.4 Hot-wire Anemometry

The hot-wire anemometry system used is a DANTEC Dynamics StreamLine pro, which is shown in Figure 5.8, which allows multiple plug in units. For velocity measurements, DANTEC 91C10 Constant Temperature Anemometers (CTAs) are used.

A DANTEC 55P15 boundary-layer probe with a swan-neck was used for boundary-layer velocity measurements; see Figure 5.9a. The probe is connected into a DANTEC 55H22 right-angle probe support, as shown in Figure 5.9c, and held inside a mounting



Figure 5.8 DANTEC Dynamics streamLine pro with 91C10 CTA modules.

tube, which is secured by tightening the probe support chuck. This enables the sensing element to be placed in the near wall region to obtain the boundary layer measurements.

A DANTEC 55P11 free-stream probe, which is depicted in Figure 5.9b, is connected into a DANTEC 55H22 1D right-angle probe support, and is held at the back of the test section ($x=3000\text{mm}$ and $y=175\text{ mm}$), to measure the free-stream during testing. This allows variations in velocity to be taken into account as a result of motor undulations.

These probes have a platinum-plated tungsten wire with a length of 1.25mm and a diameter of $5\text{ }\mu\text{m}$. Both of the 55P15 and 55P11 hot-wire probes are operated with an overheat ratio of 1.8. This provides a high operating temperature (around 230°C), which allows a high sensitivity to the flow velocity variation whilst keeping the temperature

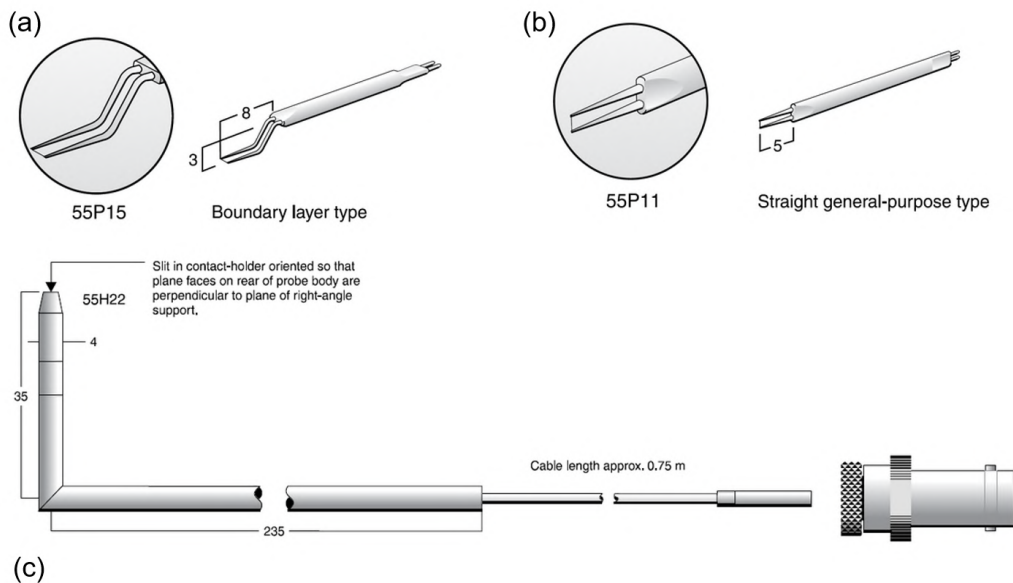


Figure 5.9 (a) 55P15 boundary-layer hot-wire probe, (b) 55P11 Free-stream hot-wire probe, (c) 55H22 1D right-angle probe support. Courtesy of DANTEC Dynamics.

below the oxidation temperature of tungsten. Both hot-wire probes were connected into the DANTEC 91C10 modules via 20m long RG58A/U 50Ω BNC cables.

5.4.1 Hot-wire probe calibration

Hot-wire probes were optimised and balanced as part of the Wheatstone bridge before the calibration. Hot-wire probes, due to the low thermal inertia of their sensing element, behave similarly to a low pass filter with a cut-off frequency on the order of 100 Hz. CTAs increase this cut-off frequency to an order of 100 kHz, which require tuning to achieve an optimum frequency response. To optimise the hot-wire probes, a square-wave is applied to the hot-wire bridges. Figure 5.10 illustrates the optimal response for hot-wire probes. This is achieved by applying a square-wave to the Wheatstone bridge, a voltage step is applied to one side of the bridge and, whilst observing the response, the anemometer gain, offset, bridge control, and cable compensator are altered to achieve the optimum signal for the hot-wire probes. The optimum signal is achieved when the signal is critically damped. For hot-wire probes, an undershoot of $0.15h$, where h is the height of the maximum point of the signal, should be present. The time taken for the signal to drop to 3% of the maximum value is defined by $t_{3\%}$. The cut-off frequency, f_c , is the frequency at which the signal is damped by -3 dB and is defined as

$$f_c = \frac{1}{1.3 t_{3\%}} \quad (5.5)$$

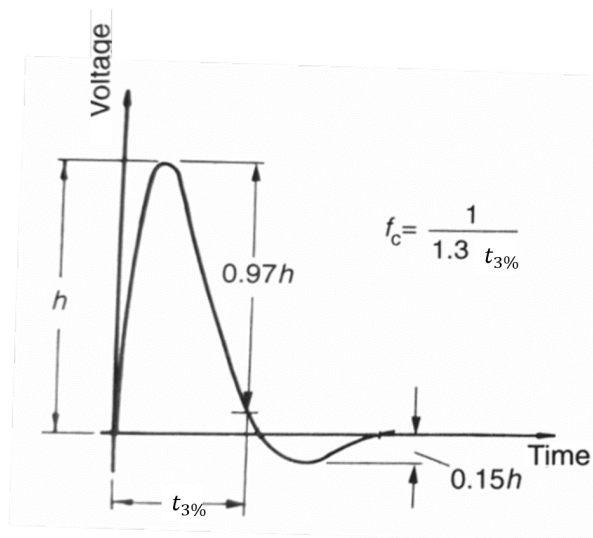


Figure 5.10 Optimum square-wave response of a Hot-wire probe. Taken from (Bruun, 1996).

Experimental Setup

The location of the diagnostic tools during the hot-wire probe calibration are demonstrated in Figure 5.11. The ambient temperature variations during the calibration and experiments are recorded using an OMEGA P-L-1/10-1/8-6-1/8-T-3 Resistance-based Temperature Detector (RTD), allowing the hot-wire data to be compensated accordingly. This RTD has a precision of 0.001°C and an accuracy of $\pm 0.1\%$. The temperature readings were sampled using LabVIEW through an OMEGA PT104A, which has an accuracy of $\pm 0.4\%$, giving a total accuracy of $\pm 0.5\%$ for the RTD setup.

Both the 55P15 and 55P11 probes are calibrated using a DANTEC Dynamics ComfortSense (FlowMaster) probe, which is supplied with a factory calibrated curve of velocity against voltage output. The Flowmaster has a uncertainty of $\pm 2\%$, which corresponds to ± 0.02 m/s. The FlowMaster probe is implemented at the back of the test section, in line with the free-stream and boundary-layer probes ($x=3000$ mm and $y=175$ mm). The traversing boundary-layer hot-wire probe, the free-stream hot-wire probe, and the FlowMaster probe are installed at the same plane in the wind tunnel, well outside any boundary-layer, inside the free stream.

For a predetermined fan speed range, the voltage output from the hot-wire probes and FlowMaster were sampled at 1 kHz for 30s at 11 different free-stream velocities, ranging from 0-15 m/s. In order to take into account for hysteresis effects, calibration is

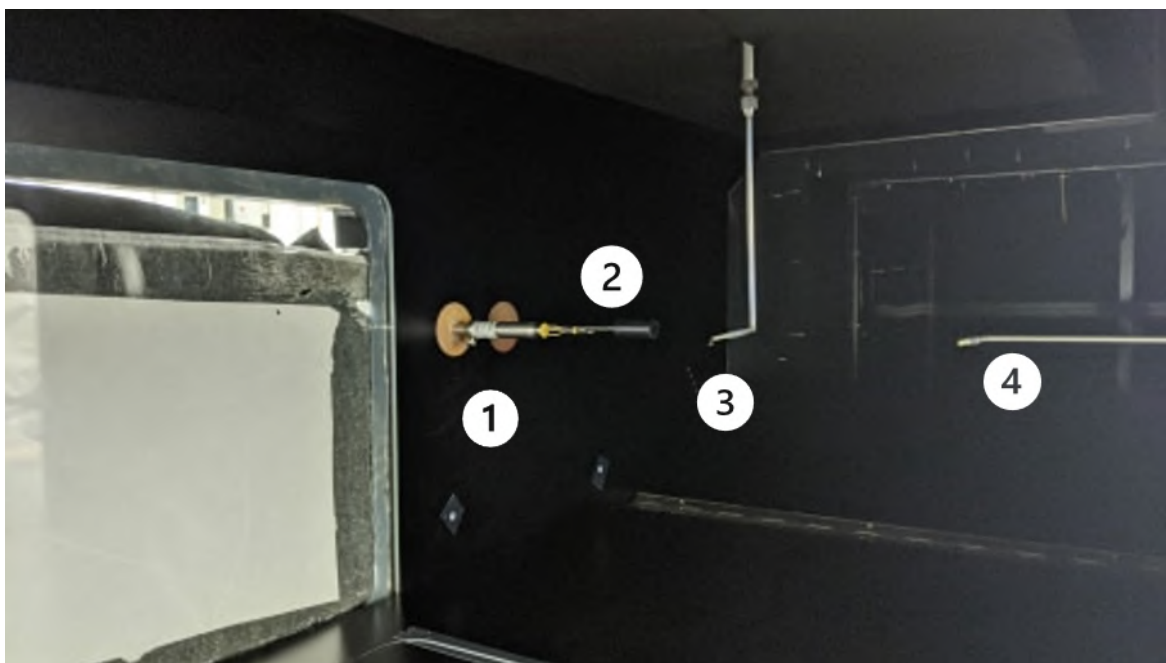


Figure 5.11 An image illustrating the diagnostic tools that are used for Hot-wire calibration and wind tunnel testings, showing (1) FlowMaster probe, (2) RTD probe, (3) boundary-layer hot-wire probe on the traverse system, (4) Free-stream hot-wire probe

done by taking points up and down the full velocity range. Moreover, to consider the ambient temperature variations on the hot-wire probes calibration, the temperature at each free-stream velocity was recorded. At each fan speed, the voltage output from the FlowMaster was averaged and then converted to velocity using the factory supplied calibration curve. Averaging the voltage output from the hot wire probe for the same fan speed, the hot wire outputs were plotted against the FlowMaster velocity to gain the calibration curve as seen in Figure 5.12. The calibration curve is fitted with a third order polynomial curve to obtain a relationship between the hot-wire voltage output and the free stream velocity.

5.4.2 Traverse System

Measurements in various locations inside the wind tunnel were enabled utilising a traversing probe mounted onto a three axis traversing system situated above and external to the test section; see Figure 5.13. The traverse system moves the traversing probe independently in the x (stream-wise), y (wall-normal), and z (spanwise) directions, using three stepper motors. The x -axis SAVEBASE Nema24 60BYGH100-410a stepper motor is rated at 4.6A and 400 steps per revolution, with each step translating to a movement of $43 \mu\text{m}$. the y and z -axis RS PRO Hybrid stepper motors are rated at 2.8A and 400 steps per revolution, with each step translating to $1 \mu\text{m}$ along the wall-normal

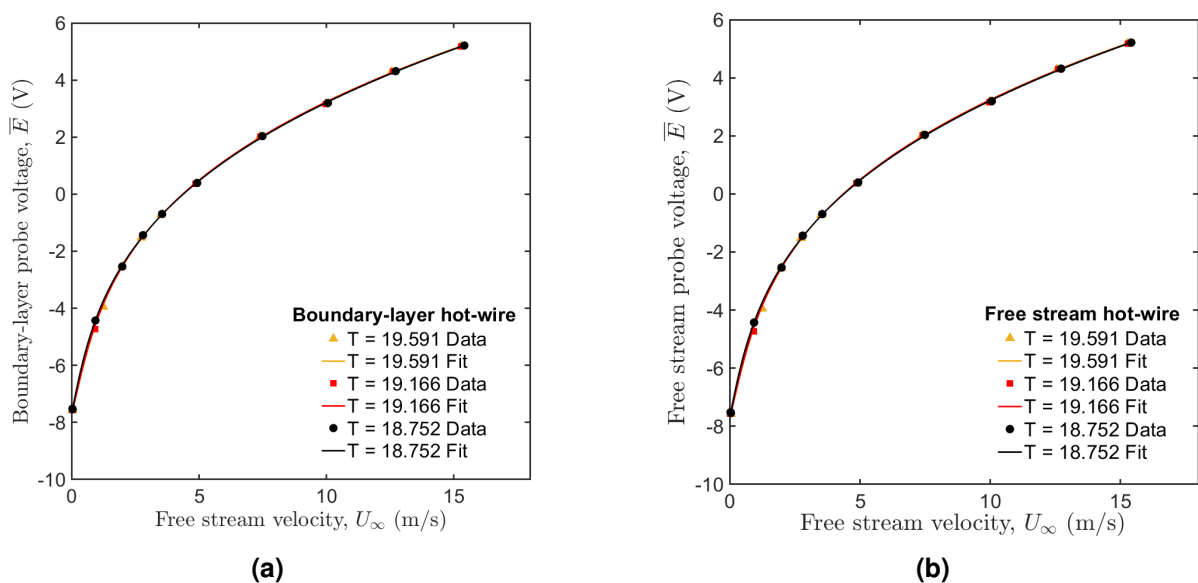


Figure 5.12 Hot-wire calibration curves over a temperature range. (a) Traversing boundary-layer hot-wire probe and (b) Free stream hot-wire probe.

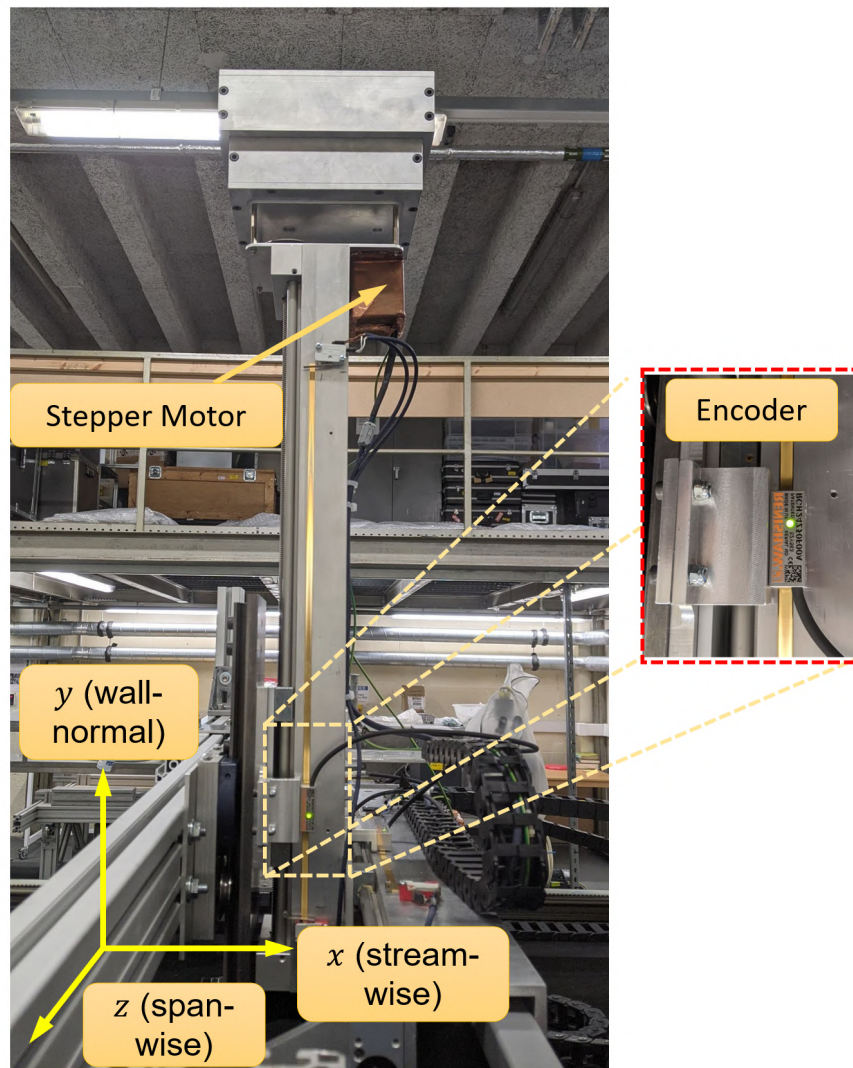


Figure 5.13 Hot-wire probes traverse system. Three stepper motors provide the movement of the hot-wire probe in three directions independently.

and span-wise directions respectively. Copper plate, 1mm in thickness, was formed into a box, placed around each stepper motor and connected to a copper grounding plate to prevent high frequency electrical noise emanating from the motors being picked up by the sensors used in the experiments. Reinshaw linear quadrature encoders along the y and z axis of the traverse system determines the relative position of the probe with a resolution of $0.5 \mu\text{m}$. Two micro switches situated at the extremities of each direction prevents the traverse system of moving beyond the dimensions of the test section. The stepper motors are connected into one drive for each axis, The drives, linear encoders, and limit switches are connected into a National Instruments (NI) UMI-7764 motion interface that connects into a NI PXI-7334 four axis stepper motion controller. The stepper motors are programmed using LabVIEW. Slots machined on the roof of the

test section allows the probe attachment, which is secured onto the y-axis plate, to be moved along the centreline of the plate and along the spanwise direction at 200mm intervals along the streamwise direction.

5.4.3 Data Acquisition

The signals from the FlowMaster and hot-wire probes are sampled using an eight channel NI 16-bit data acquisition system. The signals can be sampled up to a maximum of 1.2×10^6 sa/s and can be set to a maximum voltage range of ± 10 V. The temperature measurements are sampled on separately using an OMEGA PT104A 16-bit RTD data acquisition module. Due to the slow response time of RTD, the maximum sampling rate that can be set is 1 sa/s.

5.4.4 Near-Wall Measurements

Near wall measurements using hot-wire probes are important, particularly in this study as they can be used to quantify the wall-shear stress values and fluctuations. Nonetheless, obtaining precise data near the wall-region is challenging. Normally boundary layer hot-wire probe is being utilised for this measurements as the bent prongs situate the stem of the probe away from the viscous sub-layer.

As discussed, the probe stems are typically attached to the traverse mechanism via a probe holder, resulting in the probe movement near the wall region. As the hot-wire probe gets closer to the wall, conductive heat transfer occurs between the wire and the surface due to the lower thermal conductivity of air compared to the surface material (Turan et al., 1987). This heat transfer results in an increased voltage in the hot-wire output signal, which can be misinterpreted as a (false) velocity, instead of linearly decreasing to zero due to the no slip condition (Ligrani and Bradshaw, 1987). Hutchins and Choi (2002) suggested an empirical method for accurate near wall velocity profile measurements to a standard error of $\pm 1.8\%$. The curved prongs in the hot-wire probes are designed to prevent damage to the wire if it is traversed into the wall. However, for the near wall region measurements, it has been recommended that the probe is tilted backward as shown in Figure 5.14. This can be used to determine the position at which the probe touches the wall. The heat transfer between the probe and the wall increases

Experimental Setup

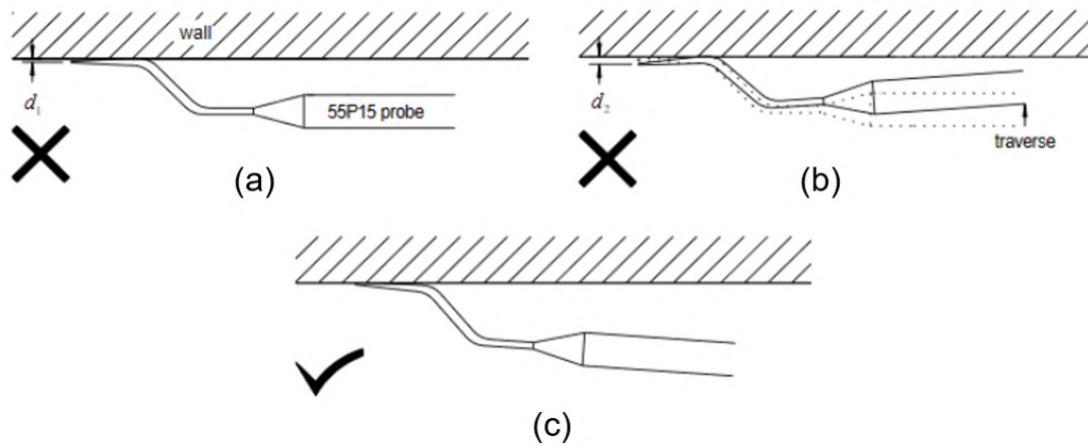


Figure 5.14 Boundary layer probe positioning. a) probe not tilted, b) probe not tilted and traversed into the wall, and c) probe tilted to allow prong tips to touch the wall. Taken from (Hutchins and Choi, 2002).

as the probe is traversed toward the wall until the tip of the prongs touch the surface. This appears as a change in gradient in the velocity profile, which is shown as A in Figure 5.14. By traversing the probe further into the wall, the tip of the both of the prongs touch the wall. Here, maximum heat transfer takes place from the hot-wire into the surface and hence, the voltage no longer increases. This point is illustrated as B in Figure 5.14. By fitting a linear line to the linear region it can be seen that the zero position is not defined as the point where either of the prong tips touch the wall, and

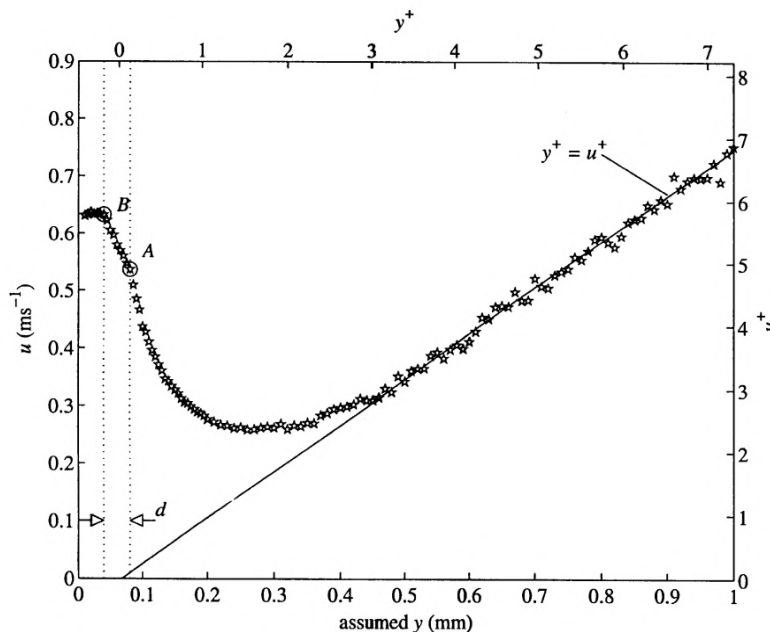


Figure 5.15 Near wall velocity profile showing the heat transfer region below $y^+ = 3$. Taken from (Hutchins and Choi, 2002).

this can be defined between them. Using this technique, the hot-wire probe can be placed into the viscous sub-layer where taking samples for 90 seconds can provide the wall-shear stress with an accuracy of $\pm 1.4\%$.

5.5 Laser Doppler Velocimetry

Laser Doppler velocimetry (LDV) is a non-intrusive measurement method, which relies on the interference of laser beams to capture the velocity of small particles in the flow. Simultaneous two-component flow velocity measurements are carried out by LDV. LDV possesses higher spatial resolution compared to hot-wire anemometry for multi-component velocity measurements in the wall-normal direction. Using the hot-wire anemometry, a spatial resolution of approximately $160\ \mu\text{m}$ can be achieved, however, they result in thermal-wake interference, aerodynamic disturbance effects, and prong-wake problems (Bruun, 1996). LDV can achieve a control volume of approximately $50 \times 250\ \mu\text{m}$ in the flow without encountering significant issues, which make the LDV suitable for near-wall measurement. Nevertheless, hot-wire anemometry and LDV can be considered as complementary measurement methods. Hot-wire anemometry possesses lower spatial resolution compared to LDV, however, it offers good temporal resolution, which is essential for frequency-domain analysis. LDV, on the other side, offers good spatial resolution but poor temporal-resolution, since it is based on random particle detection occurrence. The reason for conducting LDV measurements in this study is to quantify the wall-shear stress at the MEMS sensors location. LDV probes can be focused at the top of the MEMS sensors, enabling simultaneous flow measurement. This is, however, challenging to be achieved using hot-wire anemometry, due to the heat transfer between the hot-wire sensing element and the silicon substrate of the MEMS devices, which making it challenging to conduct simultaneous measurements with the hot-wire and MEMS sensors at top of the MEMS devices. A TSI LDV system is used for the turbulent boundary-layer profile measurements as well as the velocity profile measurements inside the viscous sub-layer, as shown in Figure 5.16. The LDV system consists of two Genesis MX series lasers STM/SLM, TEM00, providing two laser beams with a wavelength of 514 nm and 488 nm. This is a Class IV continuous wave laser with

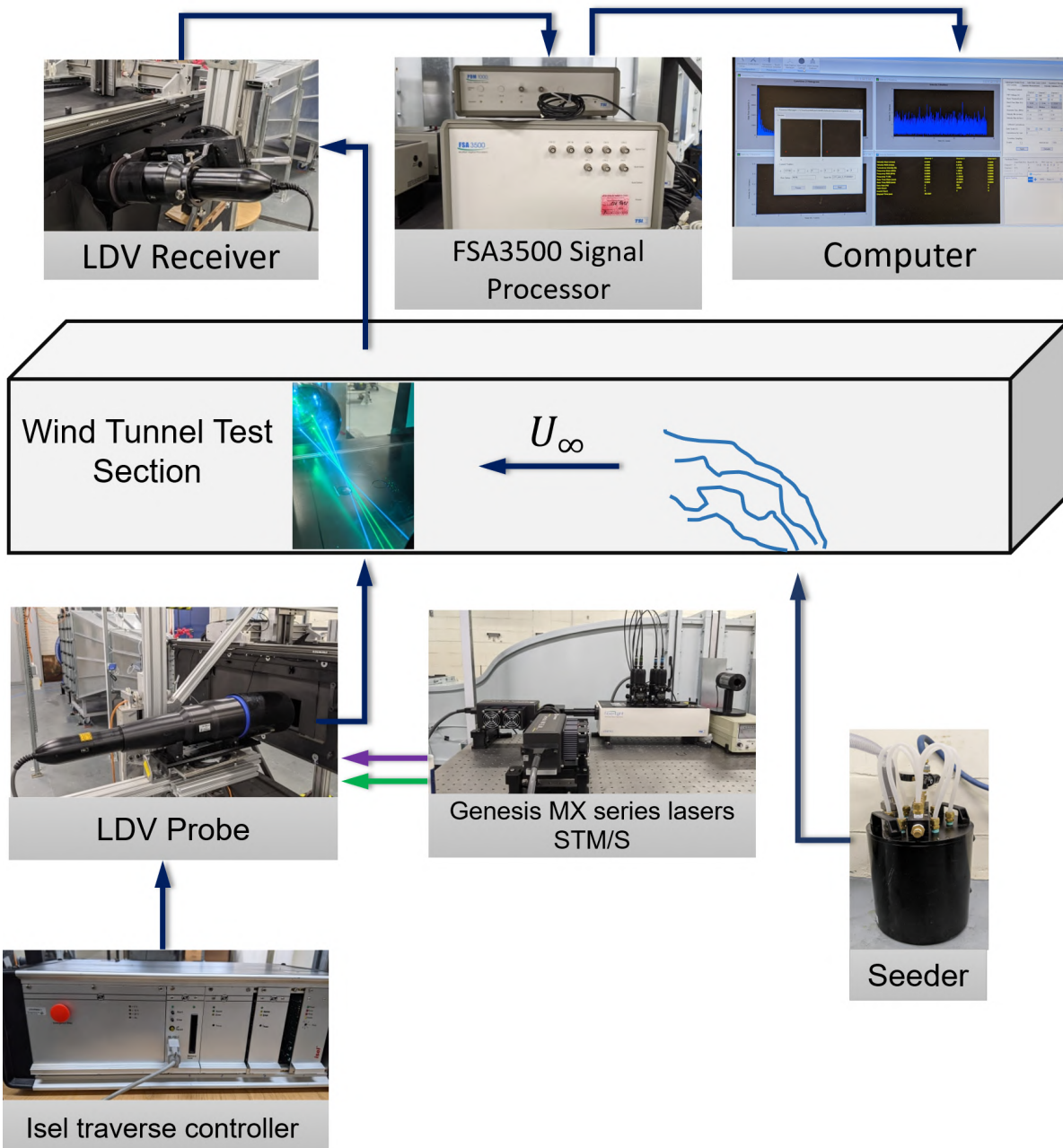


Figure 5.16 Schematics the LDV setup. Genesis MX series lasers STM/SLM providing two laser beams with a wavelength of 514 nm and 488 nm. These laser beams then are transferred in to the LDV probe, where they are projected and focused inside the wind tunnel test-section. The LDV receiver with a focal length of 300mm detect the signal and transfer it to the FSA3500 signal processor via fibre optics.

a laser power of up to 2 W. The generated beams then enter into a TSI fiberlight Multicolor beam separator, where it is reflected toward a dispersion prism by a set of mirrors. Each beam travels down its respective fibre optic cable into the fibrelight probe. A TSI RV4480 optical lens beam expander focuses the pairs of beam into the wind tunnel, where they interfere with each other and generate a fringe pattern. A dispersion prism attached between the lens and fibrelight probe reflects one of the beams by 50% of the separation to allow the probe to be traversed close to the wall. A TSI atomiser, filled with Di-Ethyl-Hexyl-Sebacat (DEHS), introduces seeding particles into the flow. As a particle moves through the fringes, light is scattered at a frequency proportional to its velocity. Since the seeded particles are very small in size (normally 1 μm in diameter), their velocity can be considered to be equal to the flow velocity. To determine the velocity direction of the particle, one of the laser beams is shifted by 40MHz by a Bragg cell to generate a fringe pattern that moves at a constant frequency of 40MHz. As the particles move towards the detector, the wave is compressed and the frequency increased above 40MHz, whereas if the particles move away from the detector the frequency decreased below 40MHz. A TSI receiver, with a focal length of 300mm, is focused into the intersection point of the beams where it picks up the scattered light and then transmit the collected signal into a FSA3500, where it is converted into velocity. The signal is mixed with another signal with a frequency ranging between 0-40MHz. The low frequency portion of this mixed signal, termed as the difference, is passed through a series of band-pass filters. This process is called downmixing and enables the optimum frequency shift to be selected to resolve flows with small or zero velocity. The fibrelight probe and receiver is attached onto a 3-axis IseI traverse system where each axis has a resolution of 80 steps/mm. A square section 90mm X 90mm aluminium extrusion assembly supports the fibrelight probe on one side of the test section and the receiver directly on the other side. A linear guide rail connected to the wind tunnel 3-axis traverse system supports the extrusion assembly to reduce the vibrations. The LDV rests on an angular stage, which is rotated so that the probe is perpendicular to the wind tunnel flat plate. Due to the nature of the LDV measurement method, a bias is introduced in the velocity measurement. This stems from the fact that a higher percentage of faster moving particles travel through the measurement volume in a given amount of time than the slower moving particles (McLaughlin and Tiederman, 1973), which results

in the measured velocity statistics being higher than normal. Additionally, since the particles are not uniformly distributed in the flow, irregular sampling is recorded in time. Correction formulas are used to correct for higher statistics values as (McLaughlin and Tiederman, 1973)

$$\bar{u} = \frac{\sum_{i=1}^N W_i u_i}{\sum_{i=1}^N W_i} \quad (5.6)$$

$$\bar{v} = \frac{\sum_{i=1}^N W_i v_i}{\sum_{i=1}^N W_i} \quad (5.7)$$

and

$$SD_u = \left(\frac{\sum_{i=1}^N W_i (u_i - \bar{u})^2}{\sum_{i=1}^N W_i} \right)^{\frac{1}{2}} \quad (5.8)$$

$$SD_v = \left(\frac{\sum_{i=1}^N W_i (v_i - \bar{v})^2}{\sum_{i=1}^N W_i} \right)^{\frac{1}{2}} \quad (5.9)$$

Where SD_u and SD_v are standard deviation values for the streamwise and spanwise velocity component, respectively, and W_i is weight function based on the weight time, t_{gi} , which can be calculated as

$$W_i = t_{gi} / \sum_{i=1}^N t_{gi} \quad (5.10)$$

where t_{gi} is captured during the LDV measurement.

5.6 Summary

This chapter discussed the details of the experimental setups and rigs that are used in characterisation and testing of the MEMS wall-shear stress sensors. The result of the sensors calibration using the laminar calibration rig is discussed in chapter 6. A laminar flow cell was developed and characterised to be used for sensors' calibration. A setup was developed using ZYGO dynamic module for the sensors' dynamic performance characterisation. The frequency response of the devices are obtained using this setup and they are discussed in chapter 6. Wind tunnel experiments are carried out, in which the flow measurements of the wall-shear stress sensors are performed alongside with hot-wire anemometry and LDV. The result of the wind tunnel experiments are presented in Chapter 7.

Chapter 6

MEMS wall-shear stress sensors' characterisation

This chapter presents the characterisation results of the MEMS wall-shear stress sensors. Characterisation tests were performed to obtain the sensors' calibration curves and to investigate their dynamic performance. Static and dynamic tests are performed on the devices with the aim to investigate the sensor performance and to determine various sensors' specifications including the mechanical sensitivity, frequency response, minimum detectable wall-shear stress, dynamic range, accuracy, and repeatability.

6.1 MEMS devices static characterisation

Sensor static calibration was carried out in the laminar flow rig, which was developed for the MEMS sensors calibration, against known time-averaged wall-shear stress values, which is determined via the pressure gradient measurement across the rig. Sensors were flush-mounted into a two dimensional laminar flow rig, where the fluid flows over it. Applied mean wall-shear stress results in the sensors' displacement, resulting in a shift in the Moiré fringe pattern on the devices. The optical pattern on each sensor is scanned with time to find and extract the time-averaged Moiré fringe pattern's phase shift. This phase shift is then utilised to determine the mechanical displacement of the sensors at each known wall-shear stress value. A linear relation is then established between the sensor displacement and the wall-shear stress, from which the sensors' sensitivity, accuracy, and repeatability can be extracted.

6.1.1 Sensors' calibration data processing procedure

After commissioning the calibration rig and characterising the sensors optoelectronics, MEMS wall-shear stress sensors were flush mounted with the bottom surface of the calibration rig. Prior to starting the sensors calibration, the location and diameter of each projected light spot on the Moiré fringe pattern was determined by capturing their image using a small calibrated Dino-Lite AM4115ZT USB microscope followed by image processing in MATLAB® software as presented in Figure 6.1. To find the size and the location of the light spots, the values of the pixels intensity were retrieved across the Moiré fringe pattern with individual light spots on it. The light intensity contour of the sensor surface and a projected light spot is illustrated in Figure 6.2b as an example. The pixel intensity analysis was performed across the light spot images to obtain a distribution of the intensity in the image. The pixel numbers in x and y directions of the image were obtained and then converted to the physical values in micrometer. The conversion ratio between the pixel size and the actual physical size in micrometer was performed by taking the known sizes on the sensors, which are precisely measured under the SEM, as the reference. As discussed in Section 3.2.7, the intensity profile of the projected light spots on the sensors is considered to be governed by a Gaussian function, and the intensity profile of the projected light spots is expressed by Equation 3.67. $1/e^2$ width analysis was performed on the intensity distributions of the light spots to find their diameter and their centre point location on the Moiré fringe pattern with

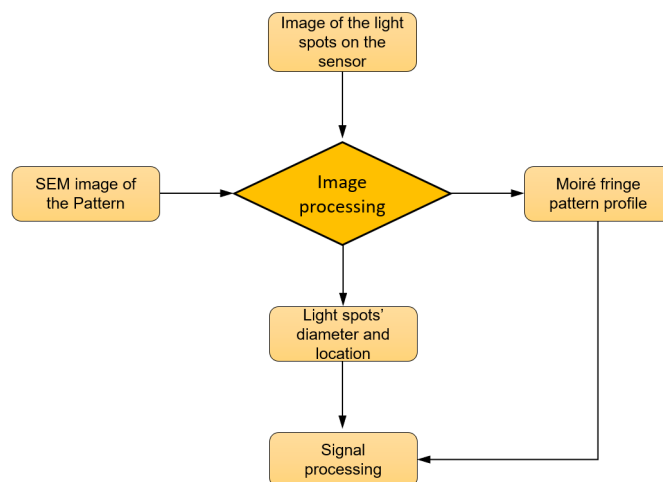
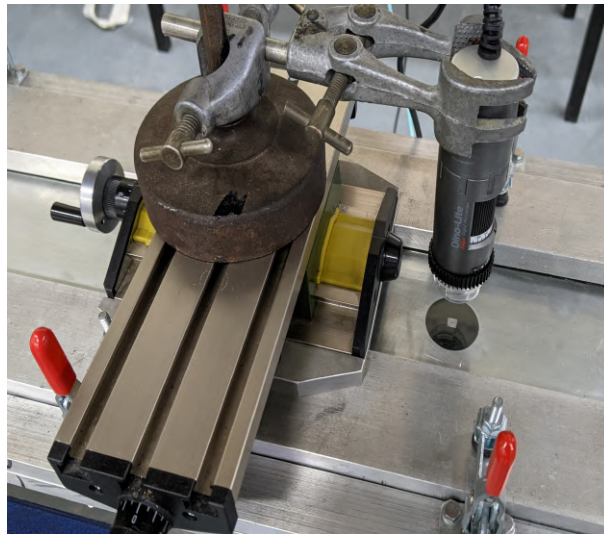
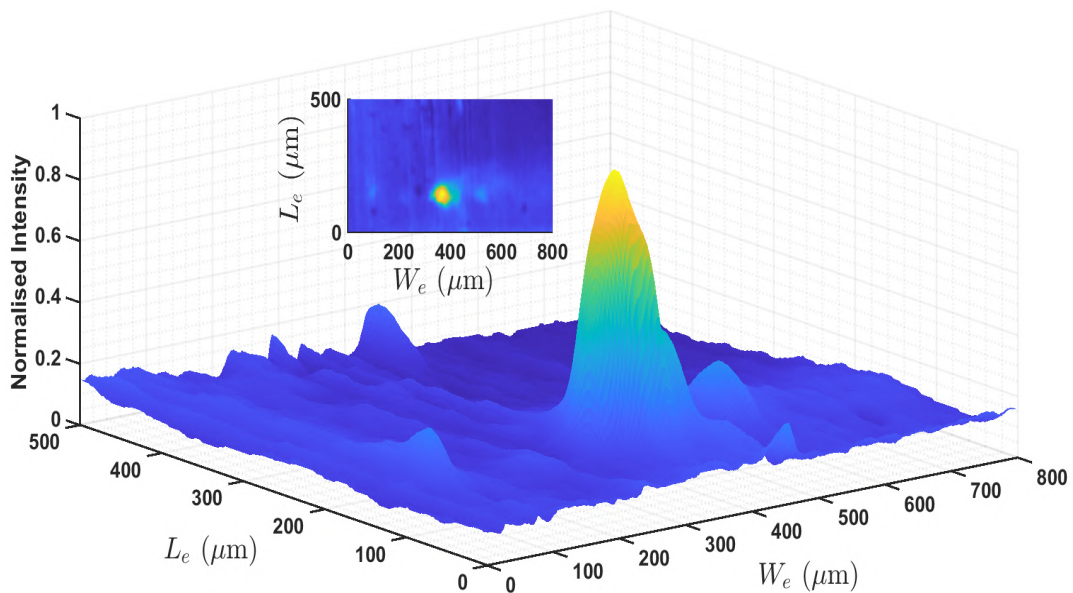


Figure 6.1 Algorithm to determine the location and diameter of the light spots on the sensor and to retrieve the Moiré fringe pattern profile. Image processing is performed on the images of the projected light spots and the SEM image of the Moiré fringe pattern.



(a)



(b)

Figure 6.2 Procedure of determining the location and diameter of the projected light spot on the sensor. (a) A USB microscope is used to take the picture of the light spots on the sensor. (b) Normalised intensity profile contour across the sensor. The inset shows the 2D contour of the light intensity on the sensor surface.

an accuracy of less than one pixel. Next step was to retrieve the sinusoidal profile describing the Moiré fringe pattern on each sensor. Illustrated in Figure 6.3a, is the SEM image of the Moiré fringe pattern on MEMS DEV CC25, with the black circles showing the location of the projected light spots on it. The intensity profile was obtained across the pattern as schematically shown with the blue thick line. The blue sinusoidal curve in Figure 6.3b represents the normalised intensity profile, I , corresponding to the blue line of scan across the Moiré fringe pattern, x , on the SEM image. The black curve shows

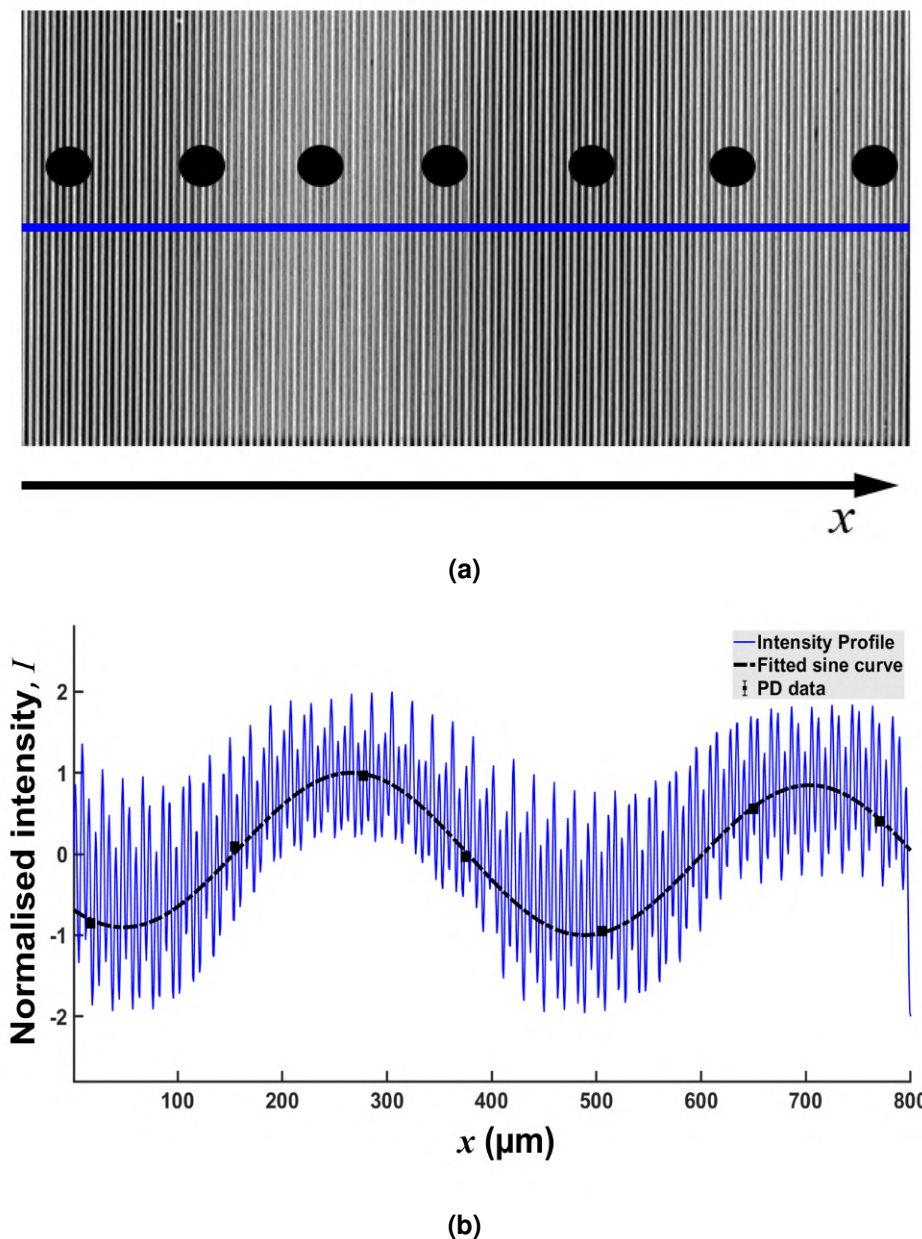


Figure 6.3 Retrieving the Moiré fringe pattern profile by image processing. (a) SEM image of the Moiré fringe pattern on a sensor. Black circles represent the location of the light spots across the pattern. This is for the device with the first generation of the packaging and seven fibre optics. (b) The resulting intensity profile of the Moiré fringe pattern with the corresponding sinusoidal curve. Black sine curve is the corresponding sinusoidal profile of the pattern obtained by applying a low-pass filtering on the image. Black squares are the photodiode voltage response of each light spot, that are in good agreement with the profile.

the averaged intensity profile, representing the characteristic sinusoidal function of the Moiré fringe pattern. This was obtained by eliminating high frequencies in the blue curve resulting from the individual gratings on the pattern, utilising the Butterworth low-pass filter. To do this, a Fast Fourier Transform (FFT) was carried out on the intensity profile of the pattern to find the frequency content, followed by the low-pass filtering of the higher frequencies. Afterwards, a sum of sinusoidal functions least square curve fitting

was carried out on the averaged curve to obtain the amplitude, spatial period, and the initial phase of the Moiré fringe pattern. This sinusoidal function can be described as the sum of multiple sine curves as

$$I(x) = A_0 \sin\left(\frac{2\pi}{G}x + \Phi_0 + \Delta\Phi\right) + \sum_{n=1}^{\infty} A_n \sin\left(\frac{2\pi}{\lambda_n}x + \Phi_n\right) \quad (6.1)$$

Here A_0 is the amplitude, Φ_0 is the initial phase, $\Delta\Phi$ is the phase shift, G is the Moiré fringe pattern spatial period on the main Sinusoidal function and A_n , λ_n , and Φ_n are the amplitude, period, and phase on the additional sinusoidal curves respectively. The additional sinusoidal functions are added to the Moiré fringe pattern due to the imperfections and errors that affect the intensity on the Moiré fringe pattern. Among the parameters in the sinusoidal function of Equation 6.1, the only varying parameter is the Phase difference, $\Delta\Phi$, due to the sensor displacement and the rest of the parameters are fixed. Once the value of the fixed parameters are obtained, the sinusoidal function is used in the least squares curve fitting algorithm on the photodiode response data, with 95% confidence intervals, to minimize the deviation between the sinusoidal function and the data from the photodiode and to calculate the value of the phase shift. Here, the least squares algorithm compare the data from the photodiode to the predicted sinusoidal function until the minimized value is obtained for the sum of the square of the residuals. When there is no flow, the value of the phase shift is equal to zero. In order to track the phase shift with time, the time response from the sensor is divided into rippling cycles, where each cycle consists of the voltage time response of the light spots, captured by the photodiode. The least square curve fitting algorithm is then performed on each cycle and with the predicted parameters for the sinusoidal function and the location of the light spots known, the phase of the Moiré fringe pattern is extracted for each cycle over time.

6.1.2 Static calibration result

The calibration of the devices is carried out in the calibration rig. The output signals of the sensors are recorded for a period of 60s at 10 kHz sampling rate, at each flow rate. The LEDs rippling frequency is set at 5 kHz during the calibration procedure. Shown in

Figure 6.4, is the calibration procedure for MEMS DEV CC20. Big black circles in Figure 6.4a demonstrates the location of the twelve projected light spots on the Moiré fringe pattern for this device. The Moiré fringe pattern profile on this device is expressed as the sum of two sinusoidal functions as

$$I(x) = 0.47\sin(0.0166x + 1.8779 + \Delta\Phi) + [0.534\sin(0.002x + 0.9512)] \quad (6.2)$$

where the first term on the right hand side of the equation is the main sine that defines the Moiré fringe pattern's period and its displacement. It can be seen from Figure 6.4b that the photodiode output data are in good agreement with the Moiré fringe pattern intensity profile. The twelve data points on this curve are the photodiode output for a single rippling cycle. The inset in this figure demonstrates the residuals of the output data with the fitted sinusoidal curve in the least squares curve fitting process. Here the residuals are defines as the differences between the photodiode output data, PD , and the predicted response value, \hat{I} .

$$Residual = PD - \hat{I} \quad (6.3)$$

It can be seen that the residuals scattered randomly, suggesting that the model fits the data well, and there is no systematic error in the data and the curve fitting process. R-squared analysis, r^2 , is used as a metric to assess the performance of the least squares curve fitting process and the goodness of the fit. R-squared measures the goodness of the fit based on the variation of the data, which is defied as the square of the correlation between the measured data and the predicted values (Hughes and Hase, 2010). R-square can be expressed as the ratio of the sum of squares of the regression, SSR , and the total sum of squares, SST , as (Coleman and Steele, 2018)

$$R - squared = r^2 = \frac{SSR}{SST} \quad (6.4)$$

or

$$R - squared = r^2 = \left[\frac{n(\sum(x_i y_i)) - (\sum x_i)(\sum y_i)}{\sqrt{[n \sum (x_i)^2 - (\sum x_i)^2][n \sum (y_i)^2 - (\sum y_i)^2]}} \right]^2 \quad (6.5)$$

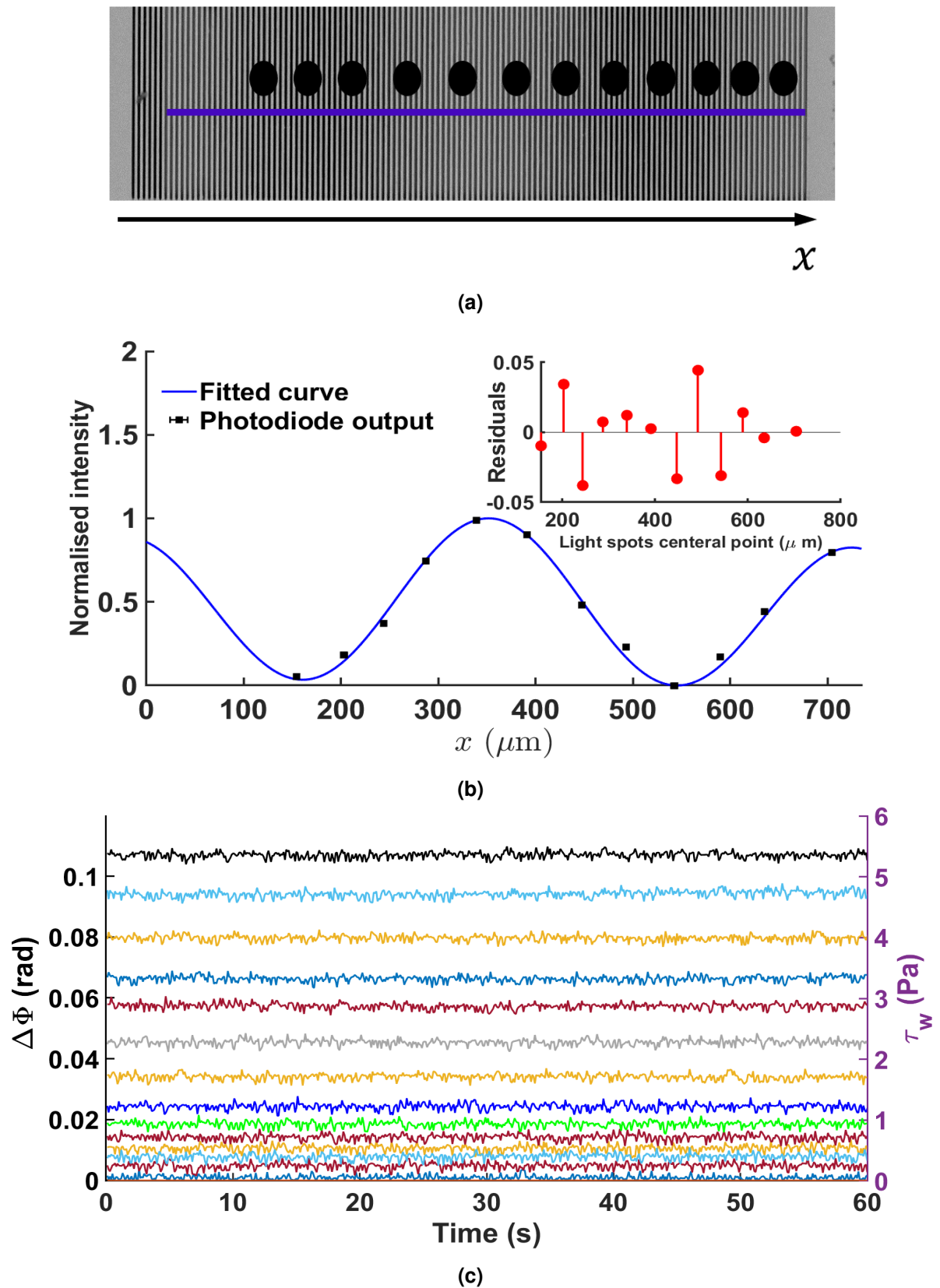


Figure 6.4 Static calibration procedure result for device number 20. (a) Shows the SEM image of the Moiré fringe pattern with the blue line presents the line of scan and black circles represent the location of the projected light spots on the pattern; (b) Shows the fitted sine curve to the photodiode output data. The inset illustrates the residuals of the photodiode output data to the sine curve; (c) Sensor's time signal at different wall-shear stress values.

Here n is the number of the samples, and x_i and y_i are the values of the data points. The R-squared value for the sum of sines function to the photodiode data is equal to 0.9943, which means that the fit explains 99.43% of the total variation in the data about the average.

To obtain the time signal of the sensor at each wall-shear stress value, the sensor's output signal is broke down into the rippling cycles of 12 LEDs, and the phase shift value, $\Delta\Phi$, is obtained for each cycle over time. This is illustrated in Figure 6.4c, where the phase shift values at each wall-shear stress level are plotted against time for a period of 60 s. It is clear from Figure 6.4c that the values of the phase shift, $\Delta\Phi$, increases as the wall-shear stress increases inside the rig. The time-averaged value of the phase shift signal is plotted against the corresponding wall-shear stress values, which provides the calibration curve for the sensor.

The calibration curve for this device is presented in Figure 6.5, showing the phase shift against the wall-shear stress. Two calibration lines are presented, showing the result with and without the pressure gradient effect correction. The dashed line, $\Delta\Phi = 0.1337\tau_w$, demonstrates the calibration curve for the case that the effect of the pressure gradient and the flow through the gaps is not considered. Employing Equation 3.32, the extra forces on the sensor and the effective wall-shear stress values is calculated.

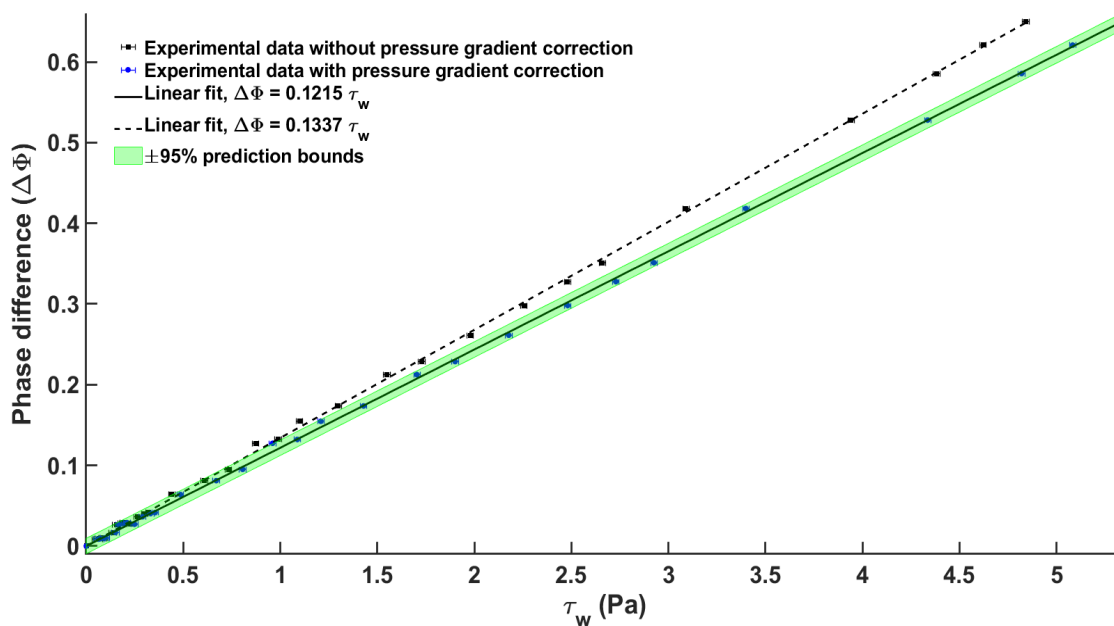


Figure 6.5 An example of the MEMS wall-shear stress sensor response with and without pressure gradient correction. It can be seen that the calibration curve shifts noticeably.

Adding the extra terms to the wall-shear stress values, shifts the calibration curve to the higher wall-shear stress values, whilst the values of the phase shift is fixed. The thick black line, $\Delta\Phi = 0.1215\tau_w$, shows the calibration curve with the correction for the pressure gradient effect. It is clear from the two curves that the values of the wall-shear stress increases notably, specially in the higher wall-shear stress values, which results in a reduced sensitivity by 9%. This correction increases the sensor accuracy, specially for the measurement in a different flow regime with a different pressure gradient environment. To put it in context, if the actual wall-shear stress is equal to 5 Pa in a zero pressure-gradient turbulent boundary layer, and the effect of the pressure gradient in the sensor calibration is neglected, the calculated wall-shear stress from the sensor reading will be $\tau_w = (0.1215/0.1337)(5) = 4.55$ Pa.

Presented in Figure 6.6, is the calibration curve for MEMS DEV CC20. Two calibration tests were carried out to investigate the environmental parameters effects on the device performance. It is clear from the calibration curve that the sensor's response for both tests is linear up to the wall-shear stress limit of 5.2 Pa. The maximum wall-shear stress is limited by the dynamic range of the Betz manometer as the the highest measurable pressure differential, DP , is equal to 400 mmH₂O. Right hand side y-axis on the calibration curve, illustrates the sensor's floating element displacement.

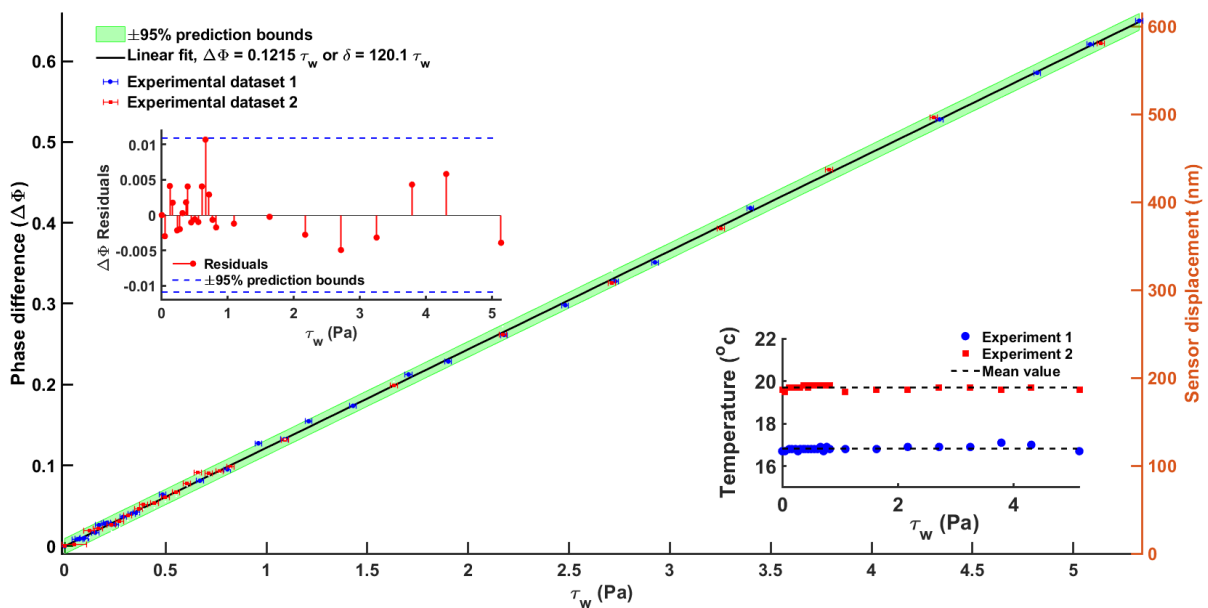


Figure 6.6 Calibration curve for device number 20. One of the insets show the the data points residuals to the linear curve fitting and the second inset show the temperature reading during the calibration for two test runs. The shaded area around the calibration curve demonstrates the $\pm 95\%$ prediction bounds in the least square curve fitting.

This is extracted by transferring the phase shift into the mechanical displacement using the measured Moiré fringe pattern period, $G = 384.6\mu\text{m}$, on the device. This results in a mechanical sensitivity of 120.1 nm/Pa for this device which is 6.7 % higher than the theoretical sensitivity of 112 nm/Pa. The difference in the measured sensitivity and the theoretical sensitivity can be linked to the microfabrication tolerances. To put this in context, side etching occurs during the etching process of the silicon. The value of this side etching depends on the etch aspect ratio, which is defined as the etching depth to the etching width (Adams and Layton, 2014). This can slightly affect the MEMS sensors performance by transforming the rectangular cross sections of the micro-springs towards a trapezoidal geometry.

Both data sets are within the $\pm 95\%$ prediction bounds of the least squares curve fitting with error bars showing the uncertainty in the wall-shear stress measurement. The inset figure on the top left side of Figure 6.6 demonstrates the residuals of the data sets in the linear least squares curve fitting. The distribution of the residuals are random, indicating that there is no systematic error in the curve fitting. Similar to the sine curve fitting, R-squared value for the linear fit is calculated to investigate the fitting performance, which is equal to $r^2 = 0.9996$ and shows that the fit explains 99.96 % of the total variation in the data about the average.

The inset figure on the bottom right side of Figure 6.6 represents the temperature measurements during the device calibration tests. It is clear that although the temperature varies by 3°C between the two tests, the sensor reading is not influenced by this variation, indicating that the wall-shear stress sensors using the optical Moiré fringe transduction is immune to the temperature drifts (Mills, 2014).

Kline (1953) discussed that if a measured quantity, Y , is a function of independent variables, X_i , of the form

$$Y = X_1^a X_2^b X_3^c \dots X_M^m \quad (6.6)$$

then the uncertainty in the quantity measurement, Y is expressed as

$$\frac{\varepsilon Y}{Y} = \pm \left[\left(a \frac{\varepsilon X_1}{X_1} \right)^2 + \left(b \frac{\varepsilon X_2}{X_2} \right)^2 + \left(c \frac{\varepsilon X_3}{X_3} \right)^2 + \dots + \left(m \frac{\varepsilon X_M}{X_M} \right)^2 \right]^{\frac{1}{2}} \quad (6.7)$$

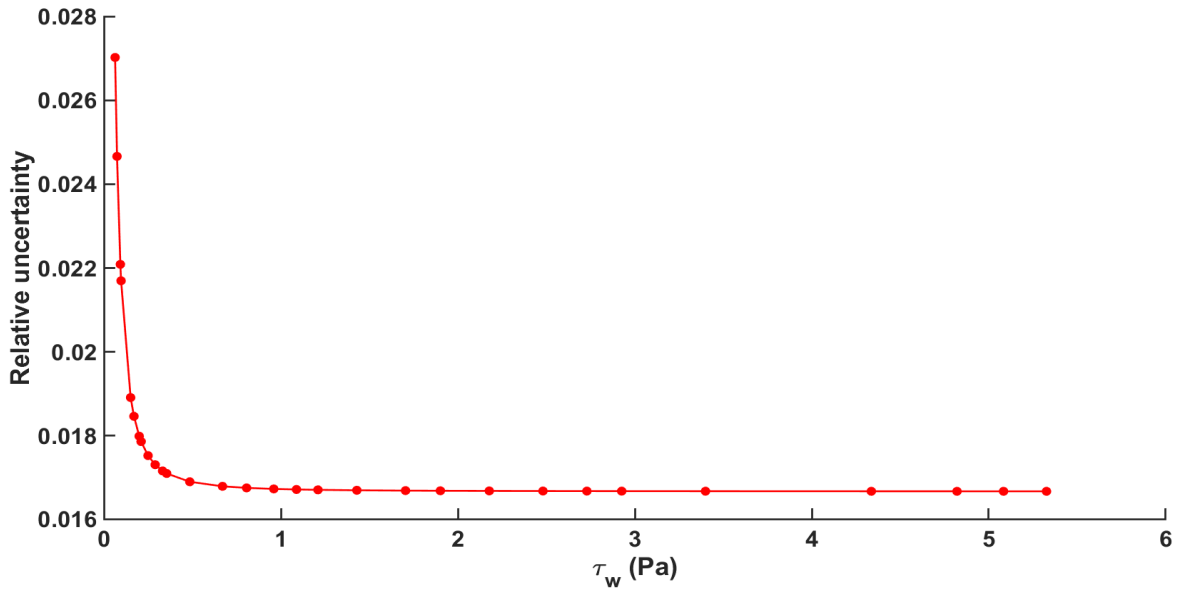


Figure 6.7 Relative uncertainty in wall-shear stress measurement.

where ε is the error. Given that the Betz manometer has an accuracy of ± 0.05 mmH₂O, and the precision machined channel flow calibration facility ensures that the relative uncertainty of the channel half-height measurements is $\pm 1\%$, the relative uncertainty in the wall-shear stress is varies from $\pm 2.7\%$ at the lower wall-shear stress values, to $\pm 1.7\%$ at the highest wall-shear stress values as illustrated in Figure 6.7 .

6.1.2.1 Repeatability error

The repeatability error of the sensor is estimated using the data points from the two experiments. The repeatability error is evolved by the inability of a sensor to reproduce the same value under identical conditions (Fraden, 2010), and it represents the maximum difference between the output signals of a sensor in two separate run cycles, Δr , and it is calculated as percentage of the input full scale (FS) as

$$\varepsilon r = \frac{\Delta r}{FS} \times 100 \tag{6.8}$$

Here, the full scale is equal to the range of the applied wall-shear stress. The maximum difference between the two tests in the calibration of MEMS DEV CC20 is equal to $\Delta r = 0.067$ Pa, and considering the the full scale value of $FS = 5.32$ Pa, the repeatability error is equal to $\varepsilon r = (0.067/5.32) \times 100 = 0.9\%$; see Figure 6.8.

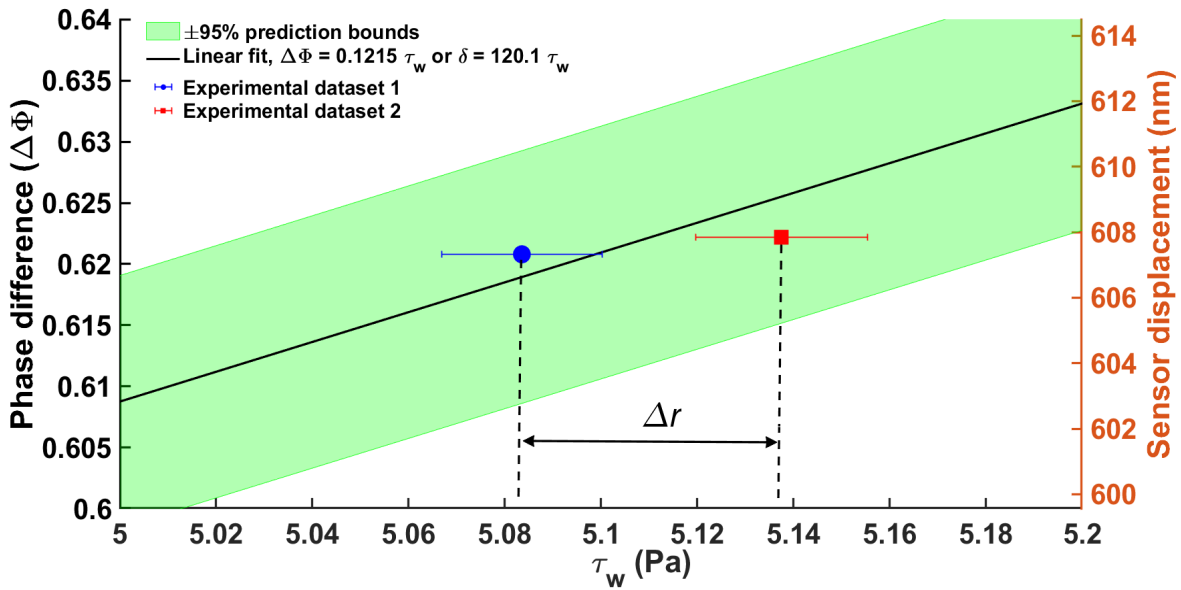


Figure 6.8 Illustration of the repeatability error quantification from the sensors calibration tests.

6.1.2.2 Accuracy

Accuracy of the MEMS sensors is derived using the highest deviation of the value measured with the sensors from the ideal value of the wall-shear stress that can be calculated from the calibration curve. To put this in context, the deviation from the calibration curve is described as a difference between the value of the wall-shear stress, which has been traced back from the sensors reading and the actual input value of the wall-shear stress. For MEMS DEV CC20, the maximum measured difference measured to be at $\tau_w = 0.96$ Pa with a phase shift of $\Delta\Phi = 0.1273$. However, tracing back the wall-shear stress value from $\Delta\Phi = 0.1273$, by considering the calibration line, $\Delta\Phi = 0.1215\tau_w$, results in wall-shear stress value of $\tau_w = 1.04$ Pa. The result overestimates the wall-shear stress by 0.08 Pa. This extra 0.08 Pa is an erroneous deviation in the measurement, or error. Therefore, in a 5.32 Pa range, the sensor relative accuracy is equal to $[1 - (0.08/5.32)] \times 100 = 98.49\%$. In other words, the relative inaccuracy of this device is equal to 1.51%. Since the sensor's reading at this point in the second run is closer to the calibration curve, it can be concluded that the inaccuracy of the sensor is due to the random error and this is not a systematic error in the sensor's measurement.

6.1.3 Noise floor

The Noise floor characterisation was performed on the sensors to determine the minimum detectable wall-shear stress (MDSS). For this, the device time series response was sampled at 10 kHz using a NI cDAQ-9171 card for a duration of 60 minutes, where there was no flow acting on the floating element. A 12 V battery was used to power up the photodiode circuit and the light sources to reduce the effect of the noise from the power line on the circuit. Figure 6.16 illustrates the phase shift, $\Delta\Phi$, noise power spectral density (PSD) for MEMS DEV CC20. The noise floor of the device is flat from 30 Hz to 5 kHz, with a value of $69.1 \text{ nrad}/\sqrt{\text{Hz}}$, which is equal to a root mean square value of $\Delta\Phi_{RMS} = 69.1 \times 10^{-9} \times \sqrt{4870} = 4.87 \mu\text{rad}$. Inserting this value into the sensor's calibration relation, $\Delta\Phi = 0.1215\tau_w$, yields a minimum detectable wall-shear stress value of $41 \mu\text{Pa}$. The sensor dynamic range defines as the ratio between the highest wall-shear stress that can be applied to the device to the minimum detectable wall-shear stress. Considering that the maximum measured wall-shear stress value in the calibration rig is equal to 5.32 Pa, the dynamic range of the devices is $41 \mu\text{Pa}$ to 5.32 Pa. The dynamic range of the sensor can be expressed in decibels as (Fraden, 2010)

$$DR = 20\log\left(\frac{\tau_w^{Max}}{MDSS}\right) = 20\log\left(\frac{5.32}{41e-6}\right) = 102.2\text{dB} \quad (6.9)$$

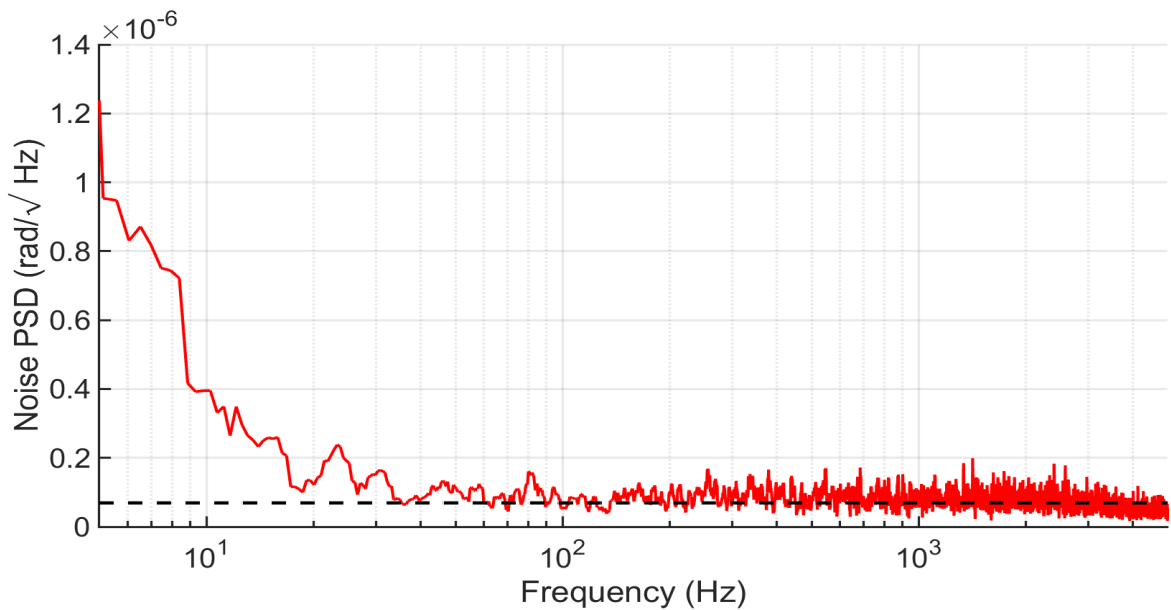


Figure 6.9 Power spectral density (PSD) of the phase shift noise. The dashed black line presents the Noise floor of the signal.

Table 6.1 Calibration results of the MEMS wall-shear stress sensors.

Device number	Micro-spring type	Sensitivity (nm/Pa)	Sensitivity (rad/Pa)	Accuracy	Repeatability	MDSS	Experimentally Verified Dynamic Range
DEV CC13	CC	730	0.285	2.1%	0.68%	17 μ Pa	17 μ Pa - 5.32 Pa
DEV CC20	CC	120	0.1215	1.51%	0.9%	41 μ Pa	41 μ Pa - 5.32 Pa
DEV CC30	CC	42	0.0094	1.4%	1.1%	485 μ Pa	485 μ Pa - 5.32 Pa
DEV SER26	Serpentine	38	0.0082	1.8%	1.24%	593 μ Pa	593 μ Pa - 5.32 Pa
DEV SER27-1	Serpentine	56	0.0161	1.76%	0.86%	295 μ Pa	295 μ Pa - 5.32 Pa
DEV SER27-2	Serpentine	53	0.0152	2.36%	1.96%	313 μ Pa	313 μ Pa - 5.32 Pa

Table 6.1 summarise the results obtained from the calibration of the MEMS-wall shear stress sensors over a wall-shear stress range of 0 to 5.32 Pa. The maximum value of the wall-shear stress on the calibration experiments was limited by the range of the BETZ manometer (0-399 mmH₂O). Three calibration experiments were carried on the MEMS sensors presented in the Table 6.1 to account for any temperature effect and to quantify the repeatability error. It can be seen that the range of the measured mechanical sensitivity of the MEMS wall-shear stress sensors varies in a range of 38 nm/Pa to 730 nm/Pa. Here, the measured mechanical sensitivity for DEV CC13, 730 nm/Pa, is 2.8 times larger than the maximum reported sensitivity of 260 nm/Pa for the device developed by Horowitz et al. (2004). To investigate the performance of sensor replicas with similar geometry, DEV SER27-1 and DEV SER27-2, were calibrated, and it can be seen that the difference between the measured sensitivities is equal to 5.3%, showing that the tolerances linked to the microfabrication process can affect the performance of sensors replicas. The value of the MDSS was determined based on the calibration coefficient of each MEMS sensor and it varies over a range of 17 to 593 μ Pa, which results in a minimum and maximum experimentally verified dynamic range of 79 to 109.9 dB. It an be noticed that although the minimum measured MDSS of 17 μ Pa for DEV CC13 is 12% larger than the minimum reported MDSS of 14.917 μ Pa on capacitive MEMS sensor that is developed by Chandrasekharan et al. (2009) which means further improvement is required for the sensor's electronics. Moreover, DEV CC30 was shown to has the highest accuracy (98.6%) based on the calibration, whilst DEV SER27-2 was shown to has the lowest accuracy (97.6%). The calibration curves of the calibrated MEMS sensors are illustrated in Figure 6.10, where a linear performance is observed in the response of the MEMS sensors.

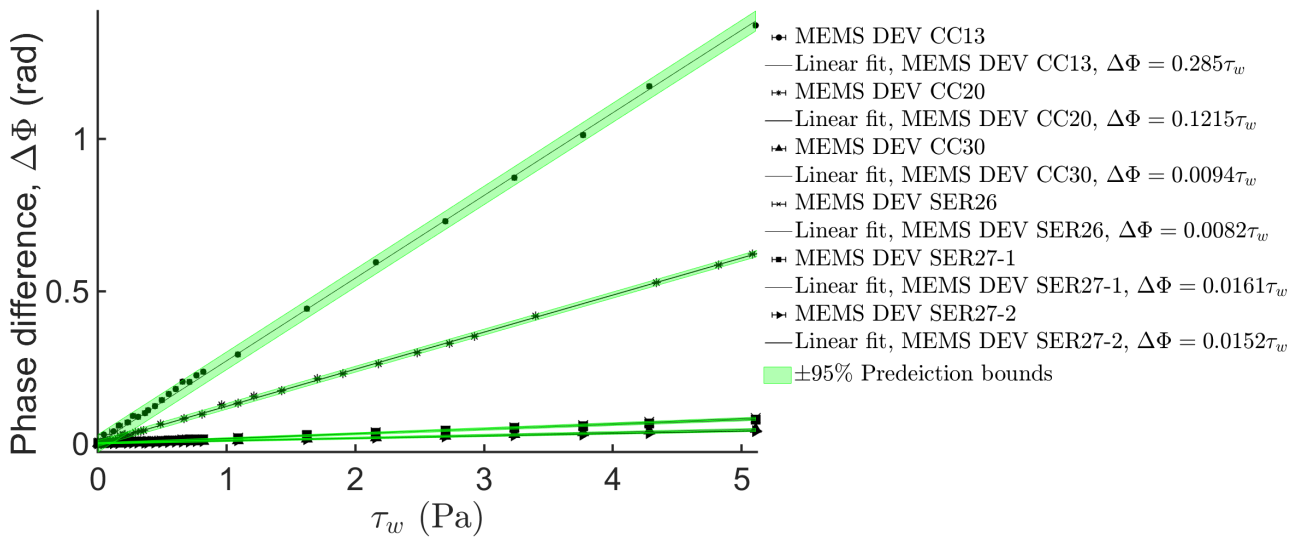


Figure 6.10 Calibration curves of the MEMS wall-shear stress sensors.

6.2 Dynamic characterisation

The aim of the dynamic characterisation is to investigate the dynamic response of the devices over a range of frequencies, and ultimately to find the resonant frequency, quality factor, and the flat band response. To detect the resonant frequencies on the devices, first, a quick frequency sweep was performed for the range of 1 Hz up to 10 kHz, which was based on the theoretical prediction. When the sensor was in its resonant frequency threshold, its image became blurry as the exposure time of image sensor on the ZYGO NewView 5000 cannot resolve the high speed movements of the device. Shown in Figure 6.11, is an illustration of a clamped-clamped MEMS sensor that is



Figure 6.11 An example of a MEMS wall-shear stress sensor at its resonant frequency. It is seen that when the sensor is actuated with the external frequencies near its resonant frequency, its image becomes blurry due to a low exposure time on the image sensor.

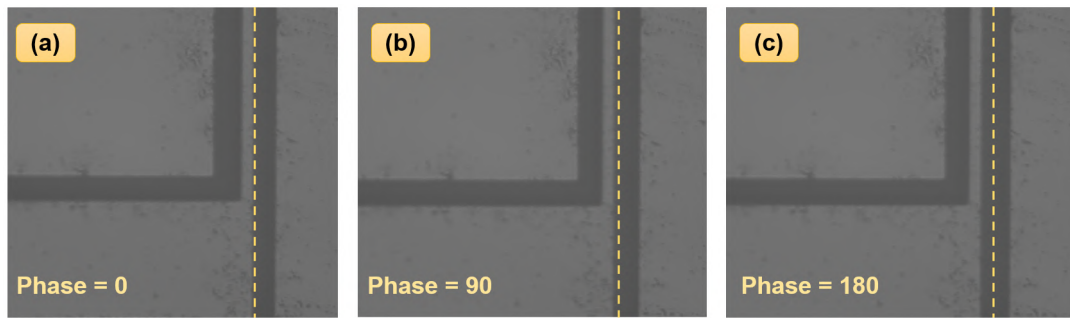


Figure 6.12 Illustration of a clamped-clamped sensor displacement at its resonant frequency using the phase delay method with (a) 0° phase delay, (b) 90° phase delay, (c) 180° phase delay. The dashed line is added to the images as a reference for the device displacement at each phase delay. It should be noticed that the images are taken at one corner of the device.

actuated at its resonant frequencies, which is blurry in the micro-spring and floating element's edge. Two approaches were used to detect the sensors' displacement amplitude at each frequency. In the first method, the drive signal frequency was set to be similar to the strobe light frequency, which resulted in a frozen image of the moving device, and then varying the phase delay between the drive signal and the trigger signal. The phase delay was altered from 0° to 360° in 45° increments, which is equal to one oscillating cycle of the device. The image of the device at each phase delay increment was then captured for the image processing, see Figure 6.12. In the second approach, the frequency of the drive signal and the strobe light were not similar. Instead, the Frequency difference between the two signals was set to be equal to one, $f_{Strobelight} = f_{Drivesignal} + 1$, while the phase delay between the two signals was set to be zero. This resulted in the visualisation of the devices' displacement at 1Hz, regardless of the actual displacement frequency. To put it in context, if the sensor displacement at 2.5 kHz is of interest, the drive signal frequency is set at 2.5 kHz, while the strobe light (trigger pulse) frequency is set to be 2.501 kHz. The result is the visualisation of the device displacement with a 1 Hz frequency, which can be recorded by the ZYGO NewView 5000 image sensor. The frequency sweep started at 10 Hz and continues up to 10 kHz. The frequency sweep increment for the frequencies close to the devices resonant frequency (which is detected using the quick scan) was set to be 2 Hz, while for the frequencies outside the resonant frequency threshold, the increment varies from 10 Hz to 200 Hz, depending on the frequencies difference to the resonate frequency. The video of the sensors' displacement was recorded for a period of 10s and a frame

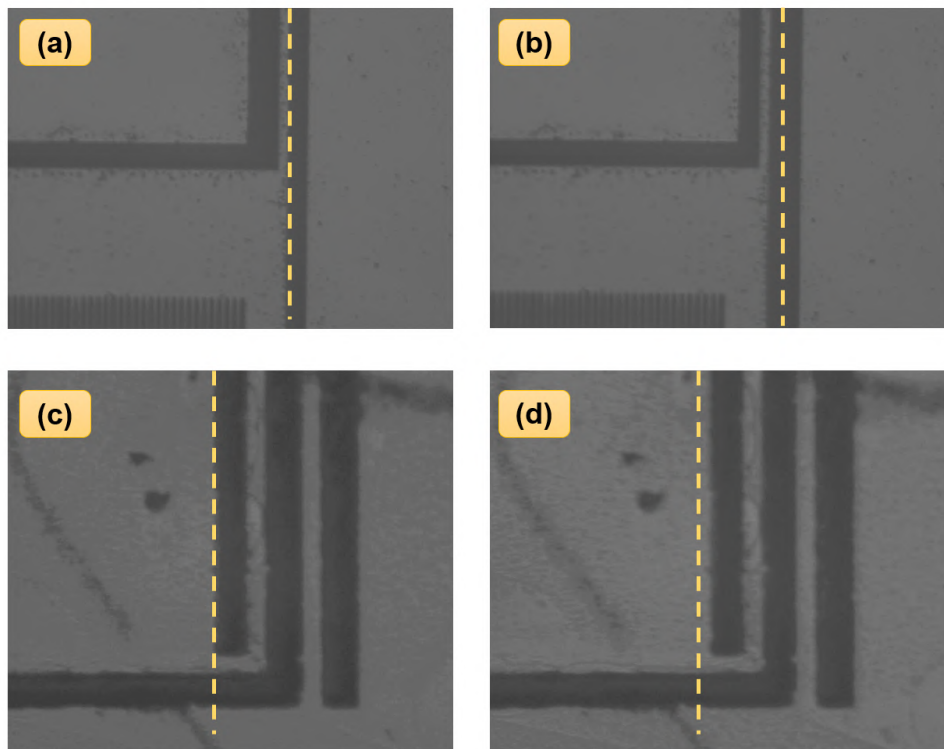


Figure 6.13 Illustration of the sensors' displacement at their resonant frequencies, using the Frequency delay method. (a) and (b) represent the displacement of a clamped-clamped device, (c) and (d) Show the displacement of a serpentine device. Dashed lines are imposed on the images as a reference to show the displacement.

rate of 30 fps at each frequency , following with an image processing algorithm to extract the amplitude.

6.2.1 Image Processing Algorithm

The captured video at each frequency was then converted into its frames. Afterwards, an image processing algorithm was performed on the individual frames to extract the sensors' displacement at different frame numbers, which ultimately provides the displacement's time response at each frequency. Shown in Figure 6.13, are two frames of the sensors' displacement at their resonant frequencies. Intensity profile of each frame was retrieved across the horizontal centerline. It can be seen in Figure 6.14 that the intensity value is varying between 250 for the silicon areas and 10 for the dark regions. After extracting the intensity profile, the distance of the floating element edge to a fixed reference was obtained, which is equal to the displacement amplitude of the sensor at each frame. The oscillation amplitudes of the sensors were recorded at different frequency, which provides the frequency response of the devices. The main

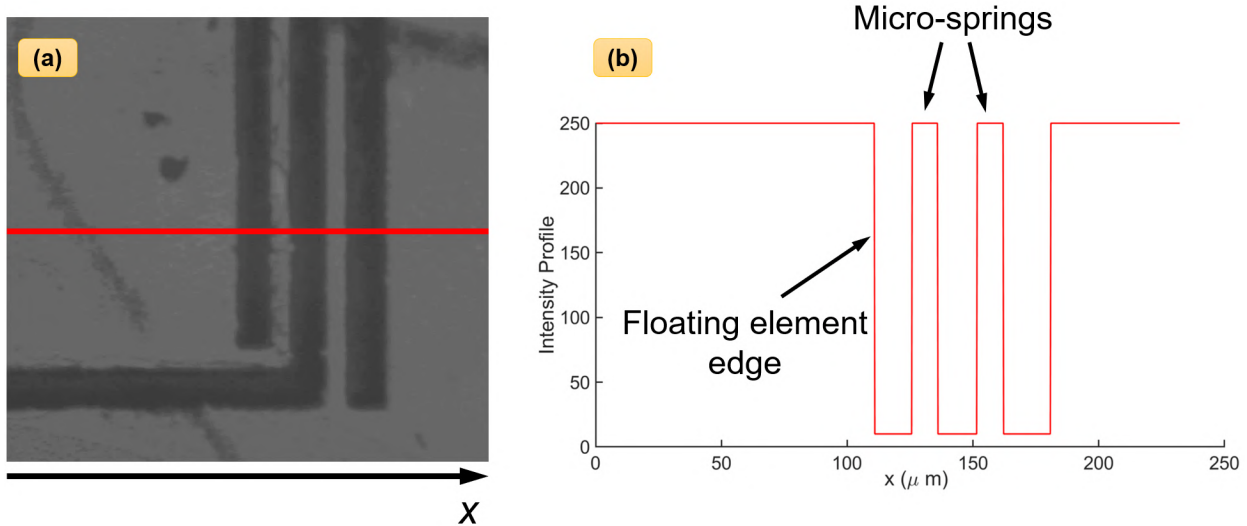


Figure 6.14 An illustration of the intensity profile across a serpentine sensor displacement frame. (a) A 20X image of a serpentine device. The red line is line of scan for the intensity profile. (b) Corresponding intensity profile of the image.

source of error in this approach is the conversion from pixel to micrometer. To reduce the errors arising from this conversion, 100 intensity profiles were obtained across the width of each image. Afterwards, the pixel width of the micro-spring was calculated at each line of scan. The mean value was then taken as the pixel width of the micro-springs. By extracting the width of the micro-springs in term of the number of pixels and also, by knowing the actual width of the micro-springs (measured under SEM), the conversion ratio from the pixel number to micro-meter was obtained.

6.2.2 Dynamic Characterisation Results

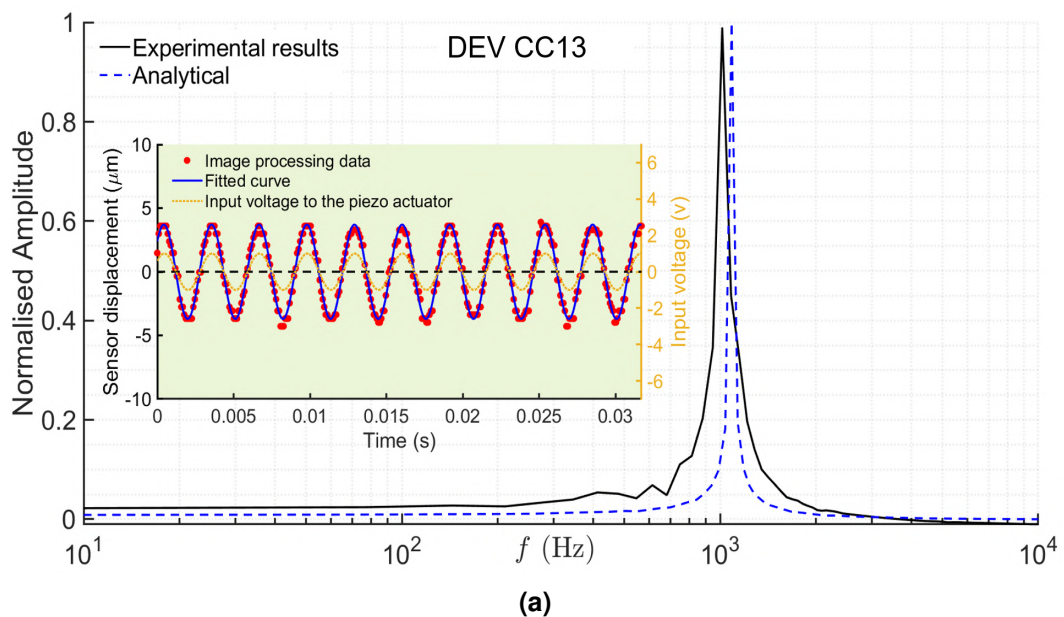
The in-plane frequency responses of the wall-shear stress sensors are presented in Figure 6.15. Here the extracted experimental data are plotted alongside with the analytical data. The analytical harmonic response for each sensor, is obtained by solving the ordinary differential equation presented in Equation 3.23 using the ODE23 solver in MATLAB, with the mass, damping, and stiffness parameters are known. The data is normalised for the comparison purpose between the experimental and analytical data, since the amplitude of the external force from the piezoelectric actuator transferred to the MEMS device is not known. The insets in the graphs show the sensors' displacement time response alongside with the input voltage to the piezoelectric actuator. The input voltage to the piezoelectric actuator is recorded at a sampling rate of 10 kHz, using a 16-

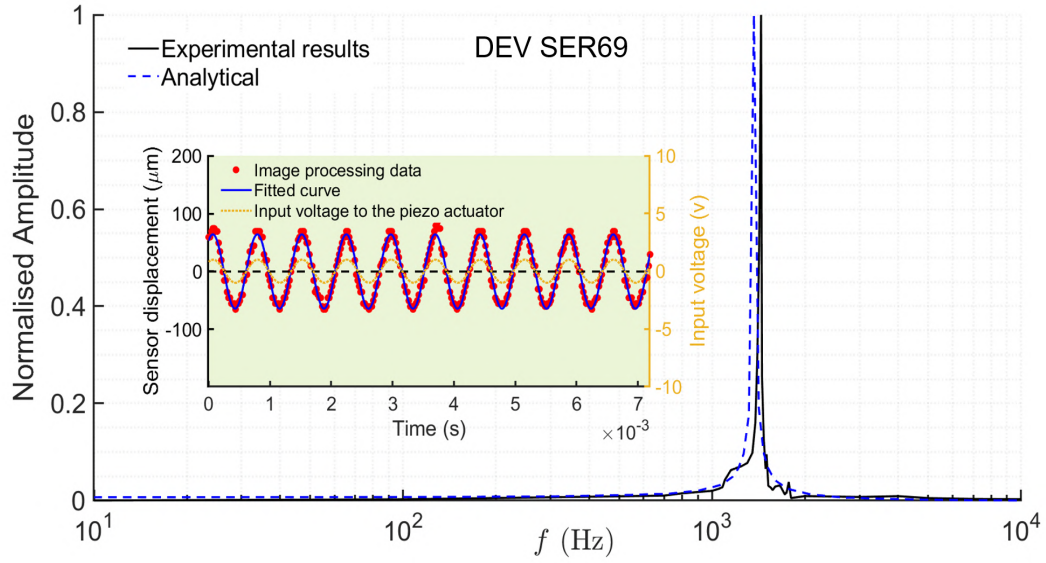
Table 6.2 Dynamic specifications of the devices.

Device number	Micro-spring type	f_0 (kHz)	Analytical f_0 (kHz)	Flat band (kHz)	Quality factor	Time delay (s)
13	CC	1.016	1.086	0.41	25.4	3.5 E-6
69	Serpentine (n = 8)	1.44	1.366	1.06	87.92	4.5 E-6
68	Serpentine (n = 26)	1.85	1.88	1.6	84.5	5 E-6
23	CC	2.62	2.61	0.9	54.2	4 E-6
25	CC	3.043	3.038	0.9	62.44	4.6 E-6
20	CC	2.835	2.872	1.817	49.2	4 E-6
30	CC	4.346	4.32	3.03	49.2	3.5 E-6
27	Serpentine (n = 3)	7.38	7.39	5.2	213.81	1.5 E-6
26	Serpentine (n = 3)	8.37	8.358	7.6	375.2	1.5 E-6

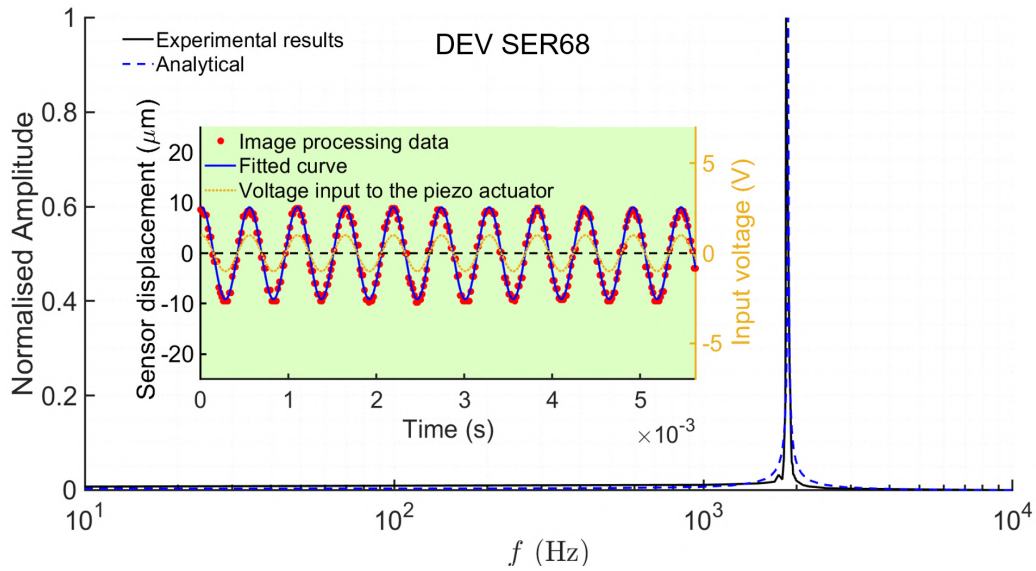
bit National Instrument DAQ card, simultaneously with the MEMS sensors' displacement recording.

Table 6.2, summarise the results of sensors' dynamic characterisation. The resonant frequencies of the devices cover a range of 1 kHz up to 8.4 kHz, ensuring that different devices can be used to measure the turbulent fluctuations in different flow speeds. It is clear from the Table 6.2 that the value of the resonant frequencies, which are obtained from the dynamic experiment, are in good agreement with the predicted analytical values, with the minimum difference of 1% for device number 26, up to a maximum difference of 6.7% for device number 13. The difference between these values can easily arise from the uncertainties in the micro-fabrication process of the devices, which affect the mass and stiffness of the wall-shear stress sensors.

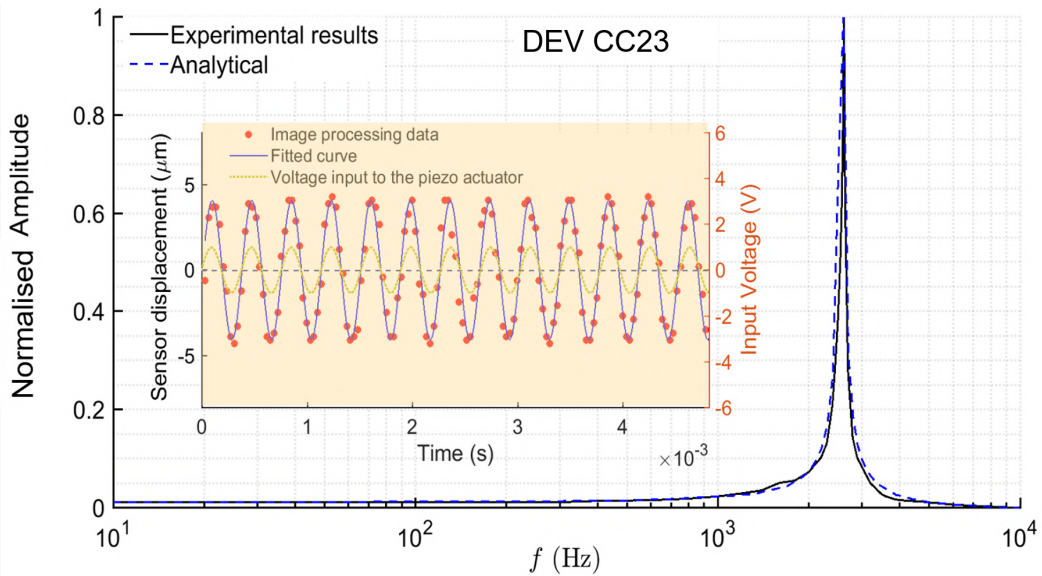




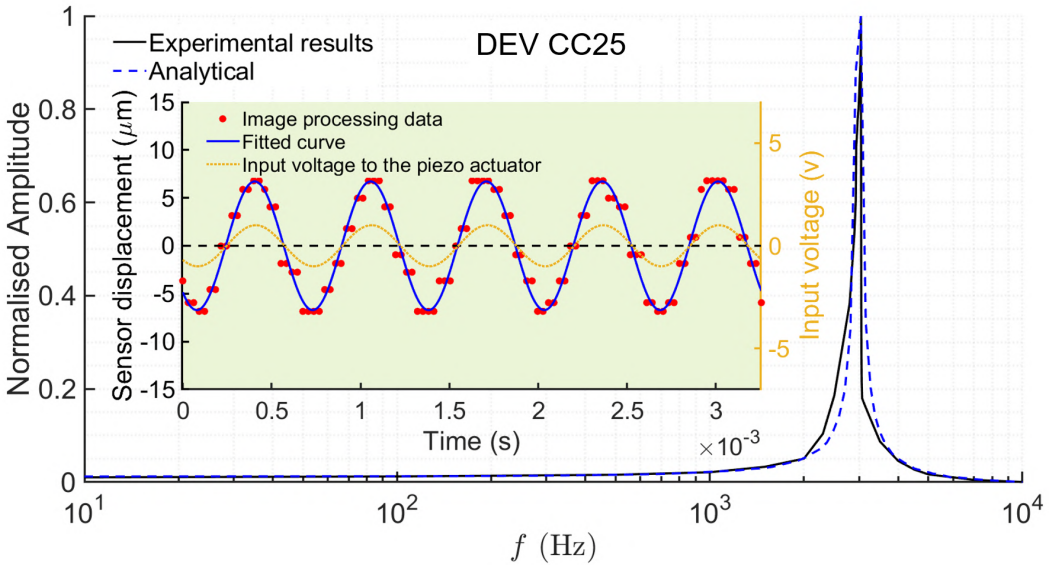
(b)



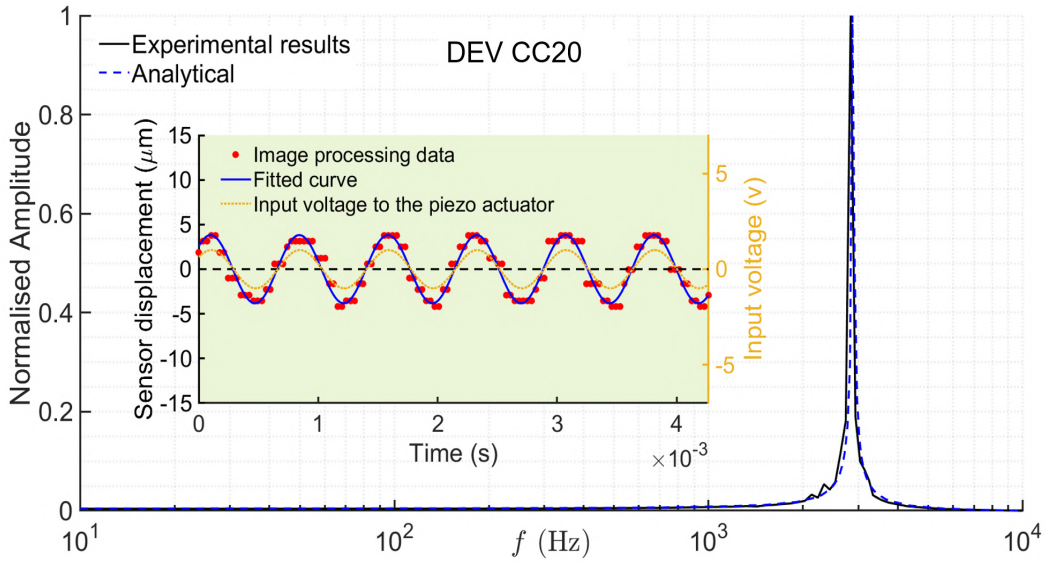
(c)



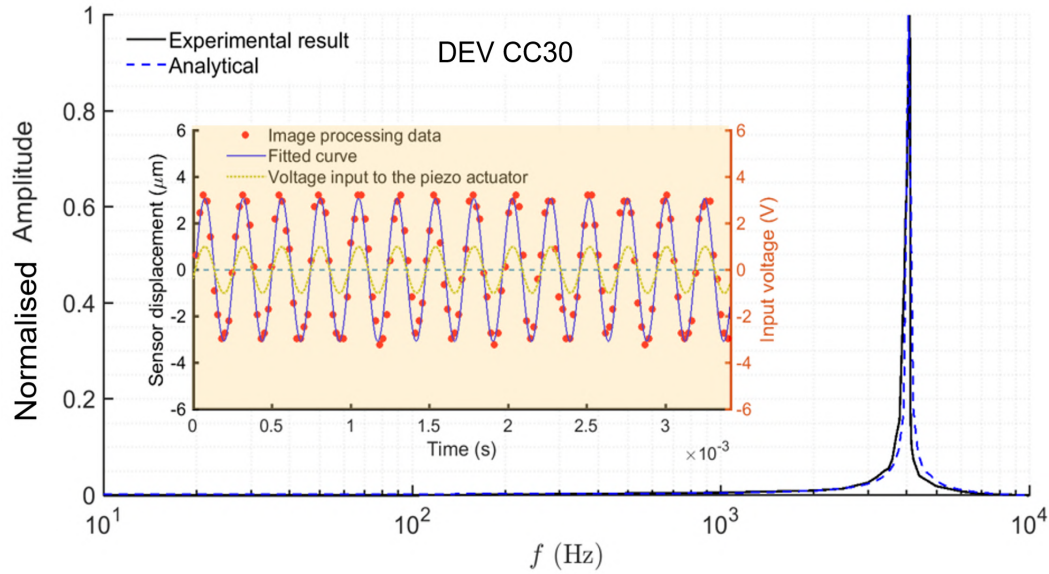
(d)



(e)



(f)



(g)

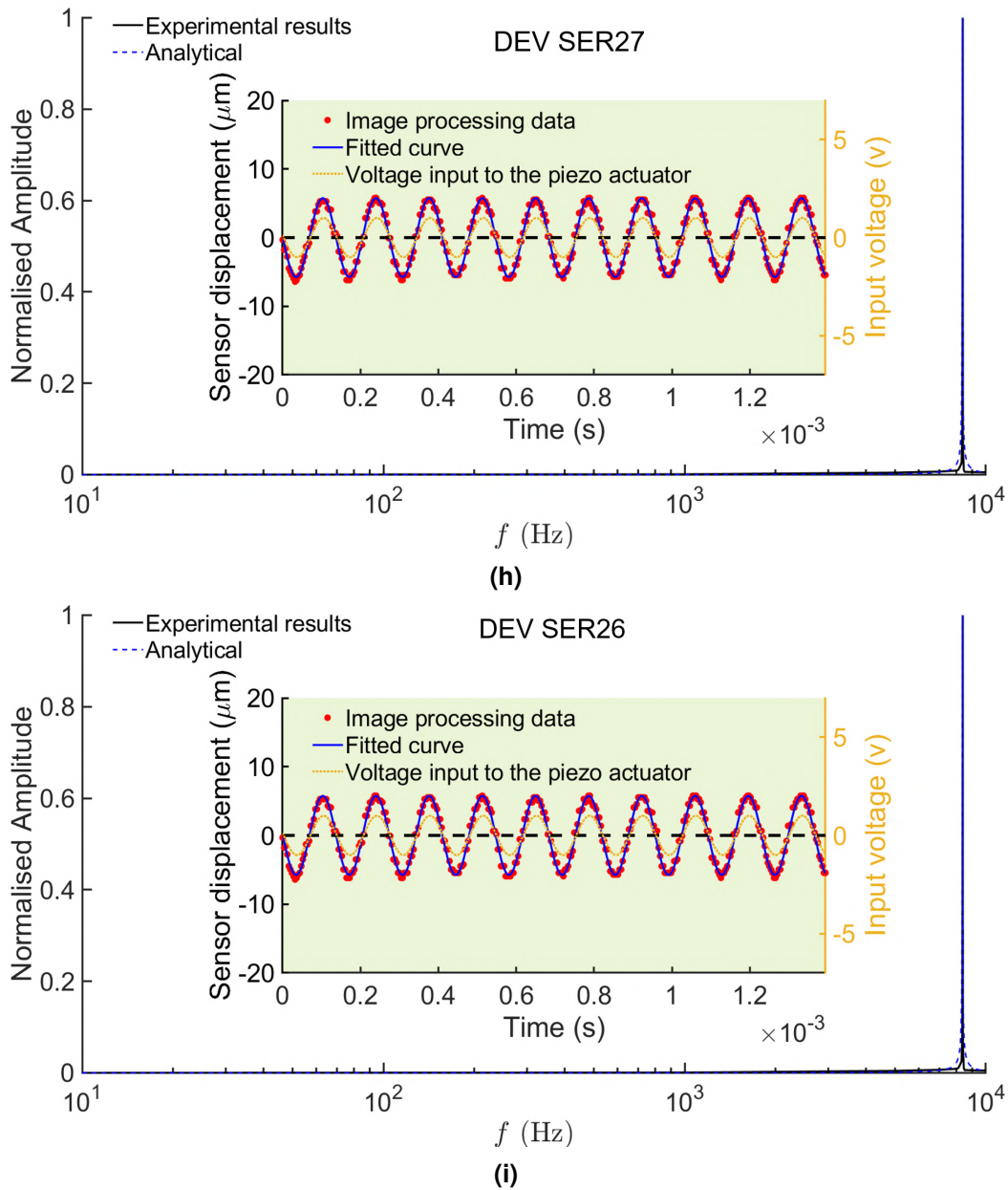


Figure 6.15 Frequency response of the MEMS wall-shear stress devices. (a) MEMS DEV CC13; (b) MEMS DEV SER69; (c) MEMS DEV SER68; (d) MEMS DEV CC23; (e) MEMS DEV CC25; (f) MEMS DEV CC20; (g) MEMS DEV CC30; (h) MEMS SEV SER27; (i) MEMS DEV SER26. The insets present the displacement time response of the sensors as well as the voltage input to the piezoelectric actuators. Thick black line represents the experimental results and the dashed blue line is derived from the analytical solution.

The flat-band based on a ± 3 dB standard is obtained for each sensor from the frequency response curve. In other words, to find the values for the flat-band region, the frequency is obtained where the amplitude is 3 dB larger than the initial amplitude. The sensors should perform in environments with frequency contents that are within the flat-band to avoid the nonphysical sensor's response near resonance. Energy losses due to the viscous damping can affect the mechanical behaviour of the MEMS wall-shear

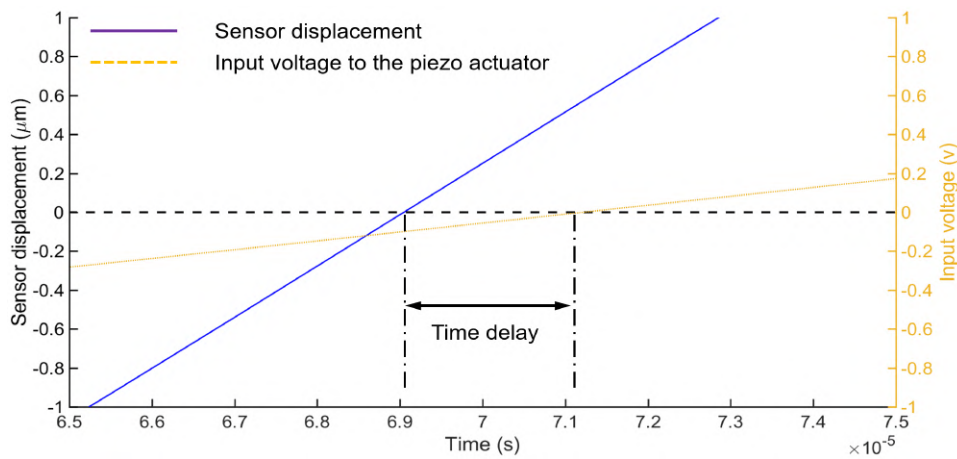


Figure 6.16 An illustration of the time delay between the actuator signal and the sensor's response.

sensors and limit their performance. These losses are quantified by means of the quality factor, Q , which is defined by the ratio of the energy stored to the energy lost during a vibration cycle (Lobontiu, 2007). Q -factor for each devices can be obtained using

$$Q = \frac{f_0}{BW} \quad (6.10)$$

where BW is the bandwidth and it is considered to be the difference between two points on the frequency response curve, where the amplitude is -3 dB below the resonant peak amplitude. It can be seen from the result table that although the Q -factors varies from 25.4 up to 357.2, for different devices, all of the sensors are under-damped ($Q > 0.5$). Q -factor can be related to the damping ratio as $Q = 1/(2\zeta\sqrt{1-\zeta^2})$, and hence the damping ratio varies from 0.019 for MEMS DEV CC13 up to 0.0013 for MEMS DEV SER26.

The phase delay between the actuator's signal and the sensor's displacement can be expressed in terms of time delay, which is shown in Figure 6.16. The results demonstrate that the response time of the devices is in the order of 1-5 μs .

6.3 Summary

The characterisation of the MEMS wall-shear stress sensors was discussed in this chapter. Sensors calibration curves were presented with and without the pressure

gradient correction and it was showed that the difference between the calibration curves for these cases is notable. The sensors calibration indicates that the sensors cover a wide range of sensitivity from 38 nm/Pa up to 730 nm/Pa, which is largest recorded sensitivity for the floating-element-based MEMS wall-shear stress sensors. Uncertainty analysis was performed on the calibration result to obtain the accuracy, repeatability, and the dynamic range of the developed sensors.

Dynamic characterisation was carried out on the devices to study their response to the frequency contents in the turbulent flow. A dynamic characterisation algorithm was developed to extract the frequency response of the devices using the ZYGO's dynamic module. It was shown that the resonant frequencies of the devices cover a range of 1 kHz up to 8.4 kHz, to cover a wider range of Reynolds numbers. Similar to the sensor calibration, dynamic parameters of the sensors such as the flat band, Q-factor, and time delay are obtained, which are summarised in Table 6.2.

Next chapter studies the implementation of the MEMS devices in turbulent boundary-layer flows to investigate the performance of the developed MEMS wall-shear stress sensors in measuring the turbulent flow.

Chapter 7

Turbulent boundary-layer measurements

Once the MEMS wall-shear stress sensors have been calibrated and their dynamic performance has been characterised, the devices are placed in a turbulent boundary layer alongside with other flow measurement methods for further characterisation and verification of their performance. In a series of wind tunnel experiments, the instantaneous wall-shear stress within the turbulent boundary layer flow is measured simultaneously by the MEMS sensors and by either hot-wire anemometry or Laser Doppler Velocimetry (LDV) using the near-wall velocity gradient technique. This chapter discusses the experimental results from the MEMS sensors, hot-wire probes, and the LDV.

7.1 MEMS and Hot-Wire Anemometry

Hot-wire anemometry measurements were conducted alongside with a MEMS sensor to quantify the wall-shear stress within the turbulent boundary-layer.

7.1.1 Canonical Turbulent Boundary-layer

In the first round of experiments, hot-wire anemometry was used to measure the canonical turbulent layer and the wall-shear stress alongside with a MEMS sensor. For this purpose, a Dantec 55P15 boundary-layer hot-wire probe was attached to the probe

Turbulent boundary-layer measurements

support secured onto the traverse system, and traversed towards the wall. For this experiment, the free stream velocity, U_∞ , was set to 5.3 m/s, generating a boundary layer thickness, δ , of 37.4 mm at the measurement location. Friction velocity, u_τ , and the kinematic viscosity, ν , are used to scale the data.

DEV CC20 MEMS sensor was mounted into the central plug of the wind tunnel flat plate which is located 1805mm ($x^+ = xu_\tau/\nu = 26537$) downstream of the test section's leading edge, and at the centerline, $z^+ = zu_\tau/\nu = 0$. In order to avoid the heat transfer between the hot-wire probe and the silicon on the MEMS sensor, the hot-wire measurements were carried out 10 mm ($z^+ = 147$) on the spanwise direction of the MEMS sensor as depicted in Figure 7.1.

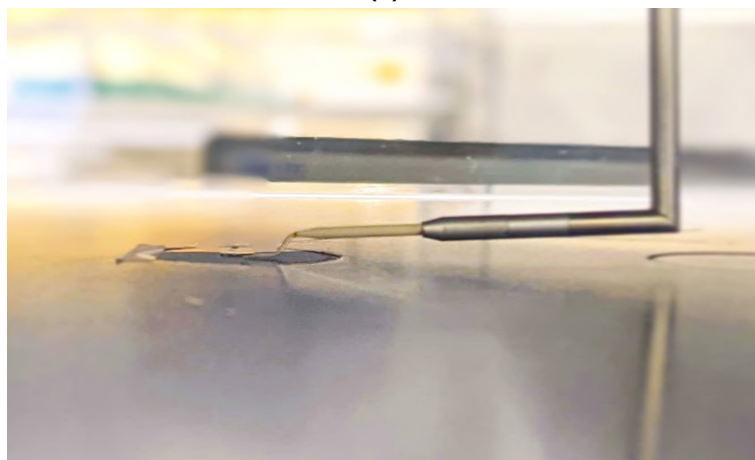
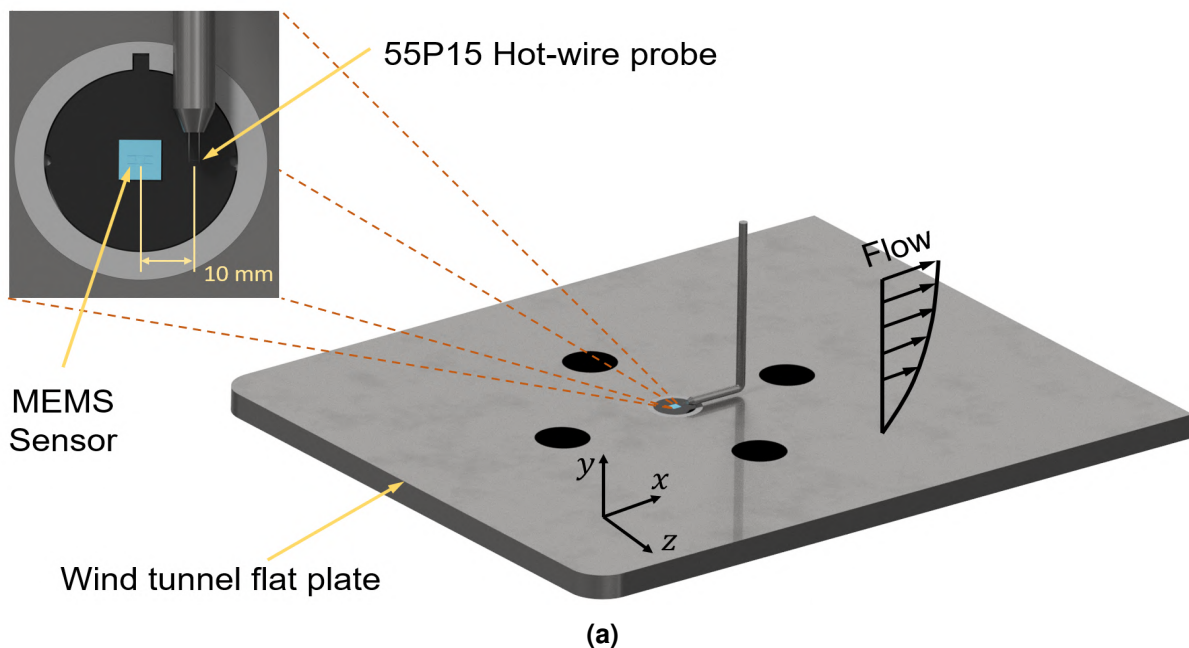


Figure 7.1 Hot-wire and MEMS measurements. (a) Schematics of the hot-wire probe and MEMS sensor in the wind-tunnel flat plate, (b) An image of the hot-wire probe traversed into the wall on the spanwise direction of the MEMS sensor.

To start the boundary-layer profile measurement, the hot-wire probe was traversed down to the wall until the output voltage increases due to the heat transfer to the wall as discussed in § 5.4.4. A LabView code is used to traverse the hot-wire probe in the wall-normal direction, where 117 data points were sampled at 10 kHz for a period of 90s at each point. To find the flow sampling time the method suggested by Tennekes and Lumley (2018) is used. For each point in the boundary-layer a total sampling time of T_s can be defined as (Whalley, 2011)

$$T_s = N\Delta t \quad (7.1)$$

in which $\Delta t = 2T_i$ is the sampling interval and N is the required number on independant samples. The integral time, T_i , can be obtained through the definition of an auto-correlation function as (Dunn and Davis, 2017)

$$R_{uu}(\tau) = \lim_{x \rightarrow \infty} \frac{1}{T} \int_0^T u'(t)u'(t + \tau) dt \quad (7.2)$$

in which τ is the time lag. Here, $R_{uu}(\tau)$ is defines the correlation of $u'(t)$ with $u'(t + \tau)$. The auto-correlation coefficient, $\rho_{uu}(\tau)$, is calculated via the normalisation of the auto-correlation function as

$$\rho_{uu}(\tau) = \frac{R_{uu}(\tau)}{R_{uu}(0)} \quad (7.3)$$

Using the auto-correlation coefficient, the integral time, T_i , is expressed as

$$T_i = \int_0^{\infty} \rho_{uu}(\tau) d\tau \quad (7.4)$$

Velocity functions at the point with the maximum turbulence intensity, $y^+ = 14$, is used to calculate the integral time. This is shown in Figure 7.2, alongside with the velocity fluctuations and the turbulence energy spectra. The integral time at this location is equal to $T_i = 7.5$ ms, which suggests that the sampling frequency of $1/\Delta t$ is required with N number of independant samples to resolve the mean velocity and the turbulence intensity of the flow. Nonetheless, from the energy spectra of the flow at this location ($y^+ = 14$), it can be seen that the flow contains smaller time and length scale, which would not be resolved by using the sampling frequency of $1/\Delta t$. Based on the energy spectra,

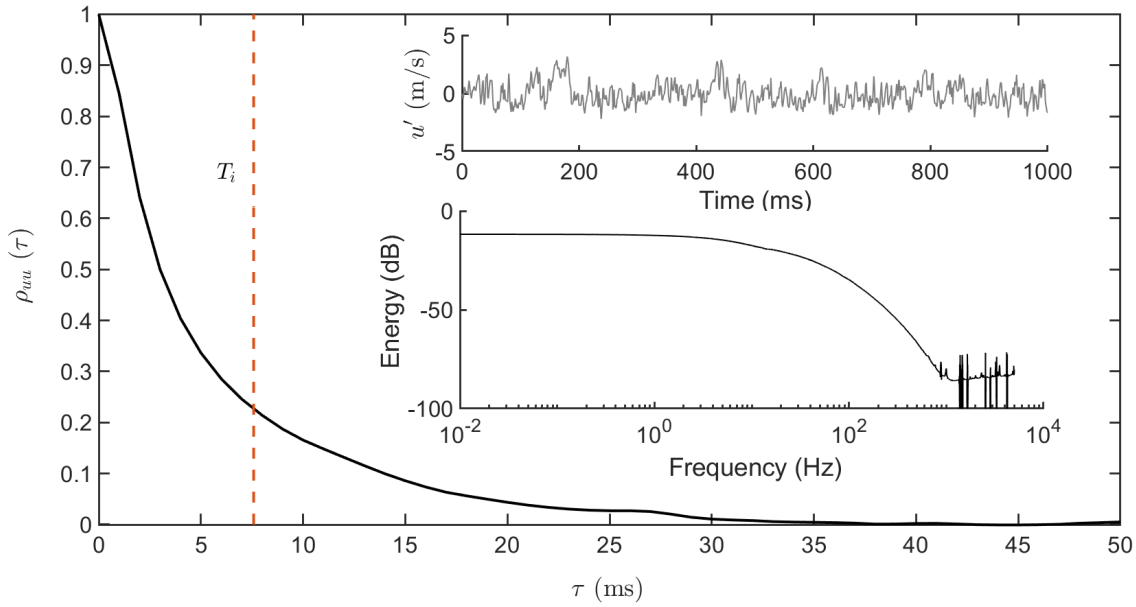


Figure 7.2 Integral time calculation for the fluctuating velocity at the location with the maximum turbulence intensity ($y^+ = 14$). The insets show the velocity fluctuations and the turbulence energy spectra at this location.

it can be seen that the turbulence has a cut-off frequency of 920 Hz. Hence, 10kHz sampling frequency is more than double the Nyquist frequency that is required to resolve the smallest scales of the turbulent flow. Whalley (2011) suggested that the number of the samples required for at each location, N , can be established using the mean velocity uncertainty analysis. The uncertainty in the mean velocity measurements can be expressed through the definition of standard deviation as

$$\sigma[\bar{u}] = \frac{1}{\sqrt{N}} \frac{u_{RMS}}{\bar{u}} \quad (7.5)$$

The number of samples required to measure the mean velocity within $\pm 1\%$ of the true mean velocity value, $\hat{\bar{u}}$, can be obtained by using the re-arranged form of Equation 7.5, as (Whalley, 2011)

$$\frac{\bar{u}}{\hat{\bar{u}}} = 1 \pm 2.57 \left(\frac{1}{\sqrt{N}} \frac{u_{RMS}}{\bar{u}} \right) = 1 \pm 0.01 \quad (7.6)$$

The value of the turbulence intensity, $TU = u_{rms}/U_\infty$, at this location is equal to 11.4%. hence, to measure the mean velocity with an uncertainty of $\pm 1\%$, a number of $N=860$ independent samples is required, which results in a minimum sampling time of $T_s = 15$ s. A sampling of time of 90s is used in the turbulent boundary-layer measurements to make sure that the flow statistics converges at each location.

Velocity data taken within the viscous sub-layer of the turbulent boundary layer is illustrated in Figure 7.3. Linear least squares curve fitting is utilised to 18 points in the linear region $3.7 < y^+ < 5$, out of 25 data points taken within the viscous sub-layer. The slope of the fitted line allows the quantification of the wall-shear stress, τ_w , and the friction velocity, u_τ , by using Equation 1.4 and Equation 1.5, respectively. For the free stream velocity of $U_\infty = 5.3$ m/s, the friction velocity is equal to $u_\tau = 0.223$ m/s. As discussed in § 5.4.4, an increase in the velocity can be seen in the region $y^+ < 3.5$, which is due to the heat transfer between the hot-wire and the surface. The data in this region, which is labeled as the wall-effect region, should be excluded from the linear curve fitting of the near-wall gradient technique to avoid inaccurate results. To find the true values of the wall-normal distance, y , for data points, the least square fit in the linear region is extrapolated so that $u = 0$ m/s. This allows the true $y = 0$ mm to be determined.

The turbulent boundary-layer profile is illustrated in Figure 7.4a, where the time averaged velocity, $u^+ = \bar{u}/u_\tau$ is plotted against the wall-normal location, $y^+ = yu_\tau/\nu$. It can be seen that the hot-wire data collapses to the the Schlichting log law (Schlichting and Gersten, 2016), in the canonical boundary-layer.

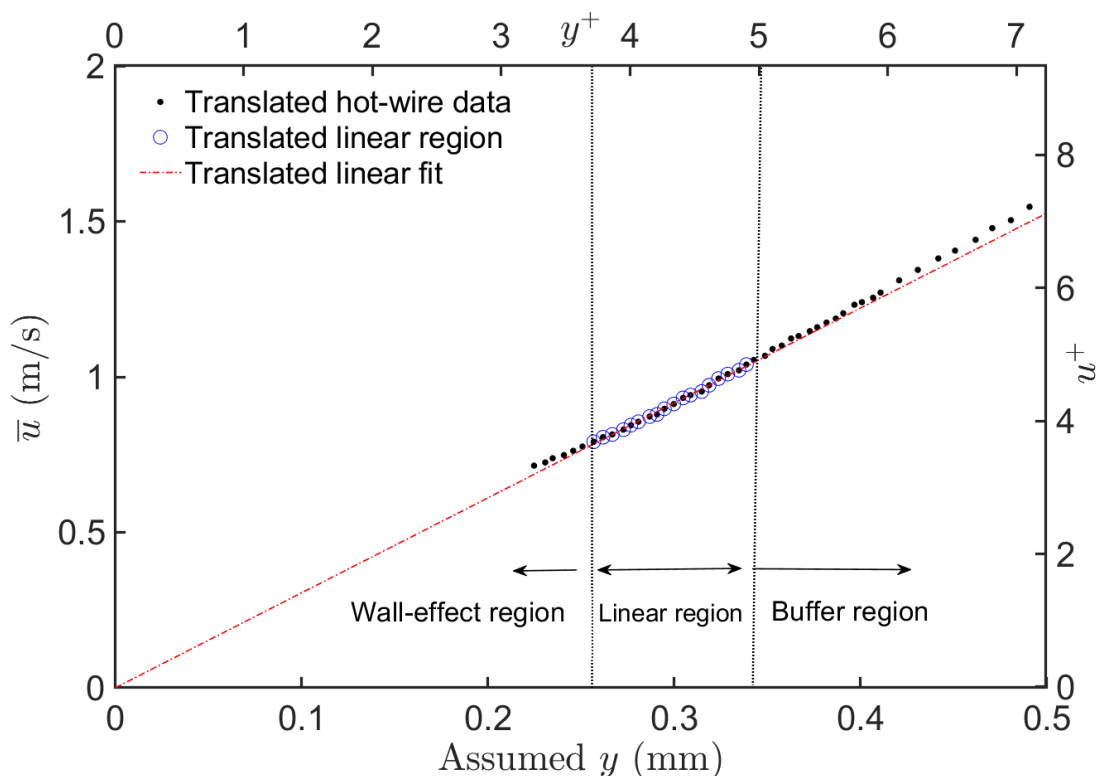


Figure 7.3 Mean value of the near-wall velocity within the turbulent boundary-layer. The points in the wall-effect region are excluded in the least squares fitting to avoid inaccurate measurements of the friction velocity.

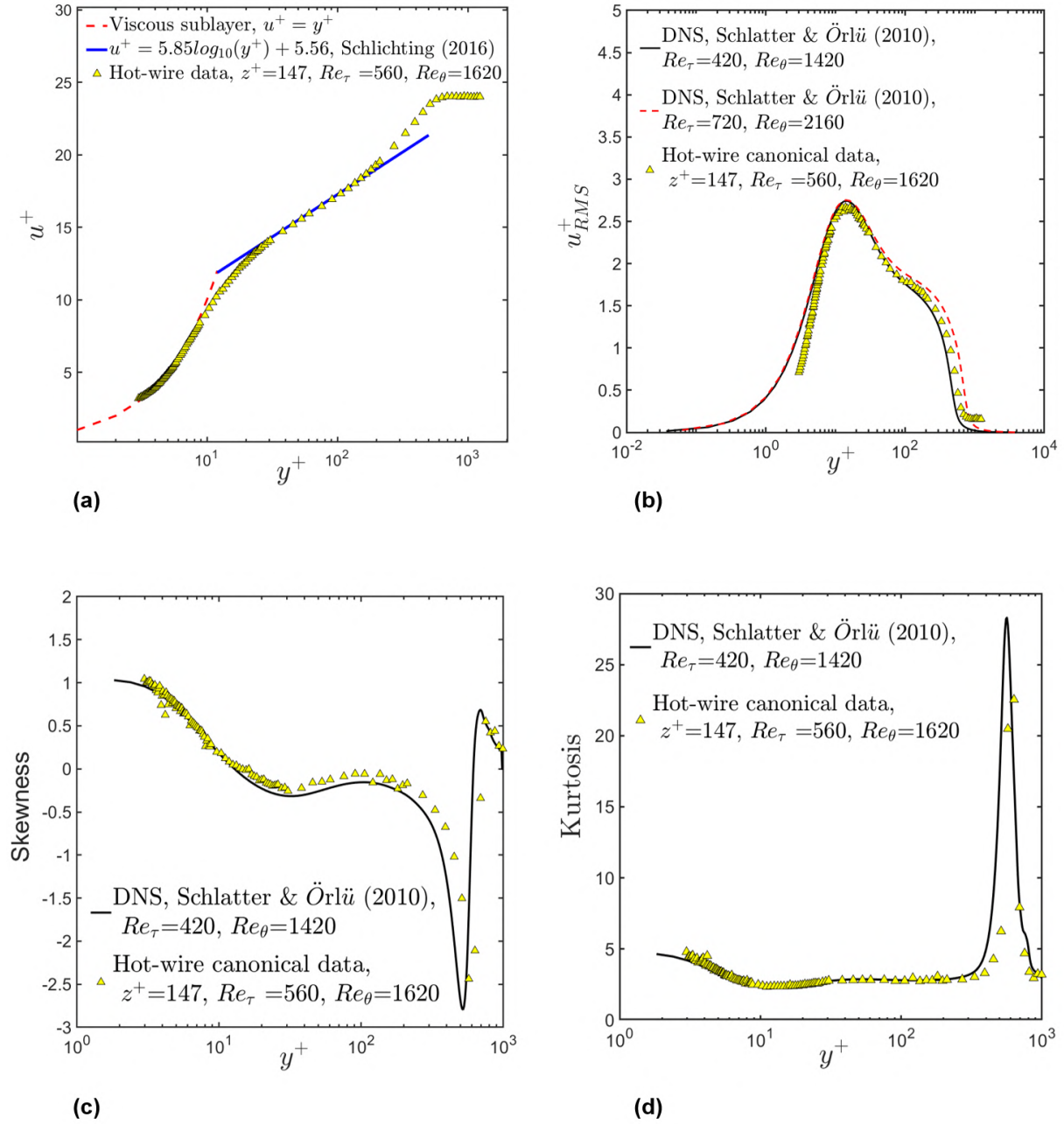


Figure 7.4 Turbulent boundary-layer canonical data measured by hot-wire. (a) Mean streamwise velocity profile, (b) turbulence intensity profile of the streamwise velocity, (c) averaged skewness profile of the streamwise velocity, and (d) averaged kurtosis of the streamwise velocity.

The displacement thickness, δ^* , of the boundary-layer is expressed as (Schlichting and Gersten, 2016)

$$\delta^* = \int_0^\delta \left(1 - \frac{\bar{u}}{U_\infty}\right) dy \quad (7.7)$$

and the momentum thickness, θ , is calculated as (Schlichting and Gersten, 2016)

$$\theta = \int_0^\delta \frac{\bar{u}}{U_\infty} \left(1 - \frac{\bar{u}}{U_\infty}\right) dy \quad (7.8)$$

The value of the displacement thickness and the momentum thickness for this turbulent boundary-layer are equal to $\delta^* = 0.0062$ mm and $\theta = 0.0045$ mm, result in a shape factor of, $H = \delta^* / \theta = 1.38$, which indicates that the boundary-layer is turbulent. The resulting Reynolds number of the flow based on friction velocity, $Re_\tau = u_\tau \delta / \nu$, is equal to 560 and the Reynolds number based on momentum thickness, $Re_\theta = U_\infty \theta / \nu$, is equal to 1620.

In addition to the turbulent boundary-layer profile, the data points are averaged and the turbulent intensity, skewness, and kurtosis profiles are obtained against the wall-normal distance. Data from Direct Numerical Simulation (DNS) are adopted from Schlatter and Örlü (2010) at relatively similar Reynolds numbers for the purpose of the comparison with the experimental data. The Reynolds number values for the first data set are equal to $Re_\tau = 420$ and $Re_\theta = 1420$, and for the second data set the values of the Reynolds numbers are $Re_\tau = 720$ and $Re_\theta = 2160$. streamwise velocity turbulence intensity profile is shown in Figure 7.4b, where the root mean square (RMS) value of the velocity, $u_{RMS}^+ = u_{RMS} / u_\tau$, is plotted against the wall-normal distance. It can be seen that profiles taken from the hot-wire measurements and the DNS data are qualitatively similar, where the difference between them is due to the difference in the Reynolds numbers. Free-stream turbulence intensity value is calculated as $TU = u_{RMS} / U_\infty = 0.46\%$. Skewness and kurtosis profiles of the turbulent boundary-layer data captured by hot-wire are presented in Figure 7.4c and Figure 7.4d alongside with the DNS data, against the wall-normal distances. Similar to the turbulence intensity profile, the experimental data demonstrate similar profiles to the DNS data from Schlatter and Örlü (2010). A slight difference can be observed between the two data sets, which is due to the difference in the Reynolds numbers. The larger difference in the higher moments skewness and kurtosis can arise from the fact that these parameters are normalised quantities.

7.1.2 Wall-Shear Stress Measurement Result- MEMS and Hot-wire

After characterising the canonical turbulent boundary-layer, an independent wall-shear stress measurement carried out utilising MEMS DEV CG20 and the boundary-layer hot-wire probe at $Re_\tau = 560$. The instantaneous wall-shear stress measurement using hot-wire carried out by measuring the instantaneous streamwise velocity from within the viscous sub-layer. For this more than 6×10^6 streamwise velocity data points were

captured with the hot-wire probe at wall-normal location of $280\mu\text{m}$ ($y^+ = 4.3$) and at $z^+ = 147$, as well as the MEMS sensor at the wall and $z^+ = 0$; see Figure 7.1 . Signals from the MEMS sensor and the hot-wire probe were sampled using a NI PXIe-1073 National Instruments DAQ card (NI DAQ) via a computer program written in the LabVIEW software.

The wall-shear stress statistics measured by the MEMS sensor and the hot-wire, such as the mean wall-shear stress, τ_w , standard deviation, SD_{τ_w} , Skewness, S_{τ_w} , and kurtosis, K_{τ_w} , are presented in Table 7.1. The sensing element geometries are normalised using the wall unit. Here the length of the sensing element can be normalised as $L^+ = L_e u_\tau / \nu$, and its width can be normalised as $W^+ = W_e u_\tau / \nu$. It can be seen that the length (spanwise direction) of the MEMS wall-shear stress sensor is equal to $L^+ = 11.81$, which is 36% smaller than the L^+ value on the hot-wire probe. However, the value of W^+ on the hot-wire is much smaller than width of the MEMS sensor. The value of the mean wall-shear stress measured by the MEMS sensor at $z^+ = 0$ is slightly underestimated by 3.3% compared to the hot-wire value. In addition, the values of the other statistical parameters measured by the MEMS sensor are smaller compared to the hot-wire measurement statistics by 10%, 2%, and 6.8% for SD_{τ_w} , S_{τ_w} , and K_{τ_w} , respectively.

The fluctuation magnitude of the wall shear stress, $\tau_{w,RMS}^+ = \tau_{w,RMS}^I / \overline{\tau_w}$, are calculated for the two independent measurement techniques. For MEMS DEV CC20, the value of this parameter was measured to be equal to $\tau_{w,RMS}^+ = 0.352$, whereas for the hot-wire measurement it is equal to $\tau_{w,RMS}^+ = 0.3885$. These values are slightly smaller than the classical asymptotic value of 0.4-0.44 that is reported by other researchers using the DNS and experimental measurements (Wu and Moin (2010) and Alfredsson et al. (1988)). However, in an experimental investigation, Österlund (1999) showed that the value of $\tau_{w,RMS}^+$ varies from 0.28 to 0.41, depending on the measurement technique. In addition, Alfredsson et al. (1988) suggested that the value of $\tau_{w,RMS}^+$, depends on the

Table 7.1 Turbulent flow wall-shear stress parameter measured by a MEMS sensor and the Hot-wire anemometry.

	Device	z^+	y^+	$w^+ = w_e u_\tau / \nu$	$L^+ = L_e u_\tau / \nu$	$A^+ = w^+ L^+$	$\overline{\tau_w}$ (Pa)	SD_{τ_w}	S_{τ_w}	K_{τ_w}	$\tau_{w,RMS}^I / \overline{\tau_w}$
$Re_\tau = 560$	Hot-wire	147	4.3	0.08	18.4	-	0.061	0.0237	1.135	4.79	0.3885
	DEV CC20	0	-	11.81	11.81	139	0.059	0.021	1.113	4.46	0.352

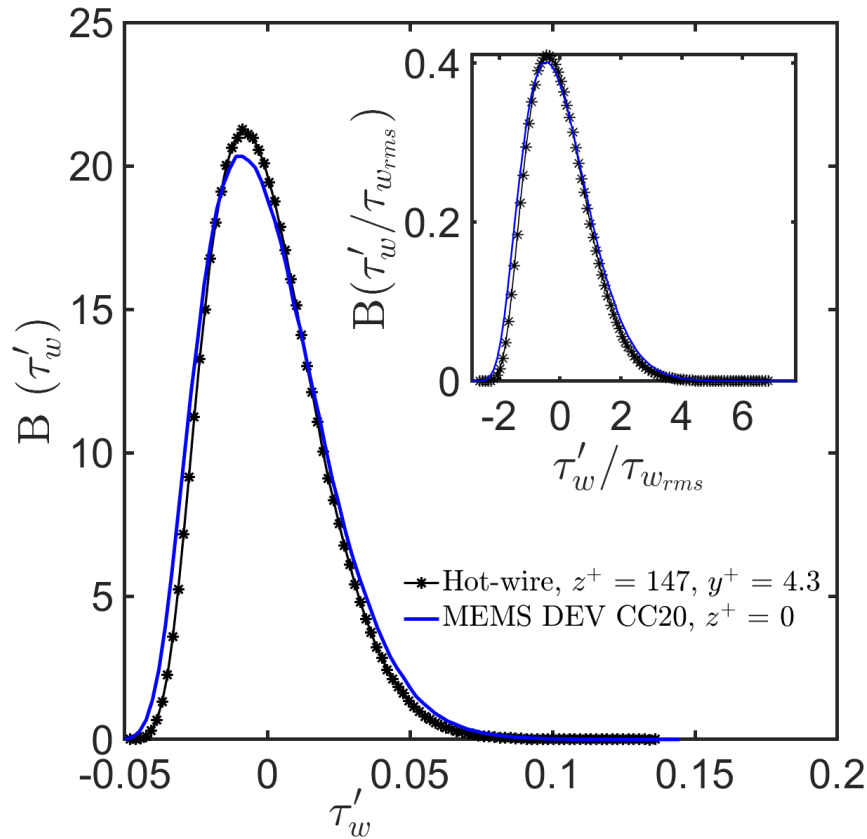


Figure 7.5 PDFs of fluctuating wall-shear stress measured by the hot-wire probe (black line with the stars) and the MEMS sensor DEV CC20 (blue line) at $Re_\tau = 560$. The inset shows the normalised PDFs of the wall-shear stress fluctuations.

spanwise geometry of the sensing element and it can decrease by increasing L^+ . The data captured here, is in agreement with the trend presented in the DNS data from Schlatter and Örlü (2010). Considering that L^+ value of the MEMS sensor is smaller than the hot-wire, it is expected that the $\tau_{w,RMS}^+$ value measured by the MEMS sensor to be larger than the hot-wire. Nonetheless, this value is smaller by 9.4 %, which can originate from the larger streamwise dimension, W^+ , of the MEMS sensor.

Probability density functions (PDFs) of the fluctuating wall-shear stress, $B(\tau'_w)$, measured by the MEMS sensor and the hot-wire probe at $Re_\tau = 560$ is depicted in Figure 7.5. Good agreement is observed between the PDFs of the two independent measurement techniques. MEMS sensor slightly overestimated $B(\tau'_w)$ for $\tau'_w < 0$. The trend changes by reaching the peak τ'_w values, where the MEMS sensor underestimated $B(\tau'_w)$ by 4.5%. This is consistent with the trend that is observed in the fluctuation magnitude of the wall-shear stress, and can arise from the spatial averaging effects in the MEMS sensor. The inset in Figure 7.5 shows the normalised PDFs of the fluctuating wall-shear stress, $B(\tau'_w/\tau_{w,RMS})$, in which it can be observed that the data between

the two measurement techniques collapse, indicating that the MEMS sensor correctly capture the wall-shear stress. It worth mentioning that, the PDF tail on the positive side for the MEMS sensor exceeds the hot-wire, indicating that the MEMS could capture the large events in the flow.

Independent measurement of the instantaneous wall-shear stress using the MEMS sensor and the hot-wire demonstrates that the MEMS sensor correctly measures the wall-shear stress. The fact that difference in the measured mean wall-shear stress is smaller than the difference in the statistics, indicates that further experimental investigations are required to underpin the performance of the MEMS sensors in the measurement of the wall-shear stress fluctuations. Hence, in the second round of the wind tunnel experiments, LDV was used to measure the wall-shear stress fluctuations at the location of the MEMS sensors, $z^+ = 0$, over a range of $Re_\tau = 600$ to 1320.

7.2 MEMS and LDV

The velocity measurements using hot-wire anemometry for higher Reynolds numbers are challenging. At higher Reynolds numbers, thickness of the boundary-layer and the viscous sub-layer, reduces. This makes it challenging to capture data near-wall region due to the heat transfer effects. Moreover, instantaneous MEMS and hot-wire measurements is challenging at the same streamwise location as a result of heat transfer between the hot-wire probe and the MEMS sensors. These challenges can be resolved by using the LDV measurements.

7.2.1 LDV Canonical Turbulent boundary-layer Measurements

In the second round of the wind tunnel experiments, LDV is used alongside the MEMS sensors for turbulent-boundary layer measurements. Forward scatter optics LDV setup, which is described in § 5.5, is used to measure the canonical turbulent boundary-layer profile and the wall-shear stress values. Laser beams of 514 nm and 488 nm are focused within the test section to measure the flow's velocity in streamwise and spanwise directions. The laser beams with the wavelength of 514 nm are used to measure the flow velocity in spanwise direction, whilst the laser beams with the wavelength of 488

nm are used to measure the streamwise velocity. Using the Flow-master software, the LDV traverse system was controlled, so that the laser beams can be traversed in $25\mu\text{m}$ increments in the wall-normal direction, y , and spanwise direction, z . A total number of 55 points were sampled for 90s in co-incidence mode so that all the collected samples can be used in determining the Reynolds stress correlations. PMT voltages for spanwise and streamwise velocity measurement were set to 550 v and 500 v, respectively. The burst threshold was set to 50 mV, with a high signal to noise ratio. Despite the hot-wire measurements, the sampling rate depends on the number of particles passing through the control volume. As a result of this, the sampling rate varies between 1 kHz for the points in the viscous sub-layer up to 40 kHz for the points in buffer region and the free-stream. The free stream velocity, U_∞ , was set within a range of 6-15m/s to investigate the sensor performance over a range of Reynolds numbers.

For each Reynolds number, three MEMS wall-shear stress sensors with various specification were implemented into the wind-tunnel flat plate. The streamwise location of the MEMS sensors were similar ($x^+ = 28067$ to 68064), whilst they were placed with a spatial pitch of 75mm ($z^+ = \pm 1166$ to ± 2828 with respect to the central sensor) across the span, as shown in Figure 7.6.

Prior to the wall-shear stress measurements, the canonical turbulent boundary-layer quantification was performed in two spanwise locations, to make sure that the canonical boundary-layer profiles are similar across the span at an specific streamwise location. This was performed to make sure that the statistical values of the turbulent flow (i.e. mean wall-shear stress, standard deviation, skewness, and kurtosis) are constant across the span. First set of the canonical turbulent boundary-layer profiles were measured at the centerline of the test section and where the central MEMS sensor was located, whilst the second data set was captured 75mm in the spanwise direction and at the location of the MEMS sensor on the right hand-side.

Since in the viscous sub-layer the velocity changes linearly with the wall-normal location, $u^+ = y^+$, the LDV probe was traversed towards the wall until the value of the mean streamwise velocity lies within $u^+ < 3$. This is to make sure that the measurement control volume is within the viscous sub-layer, $y^+ < 5$.

Similar to the hot-wire measurements, the least squares linear fit is utilised to 7-10 points within the linear region $1.7 < y^+ < 5$. To determine the true $y = 0\text{mm}$, the linear fit

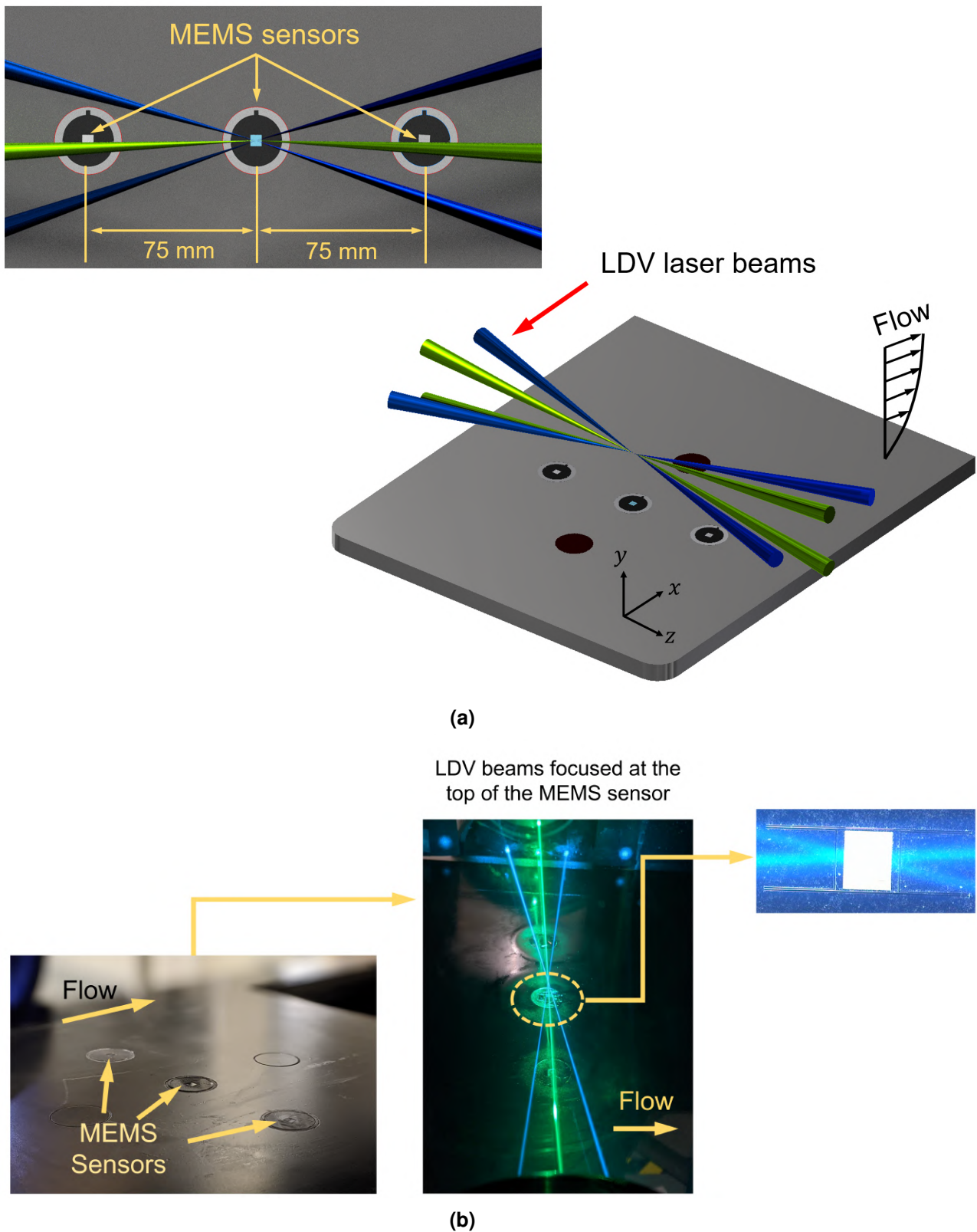


Figure 7.6 An illustration of MEMS and LDV experiments. (a) A schematic of the MEMS and LDV test. Three MEMS wall-shear stress sensors are placed across the span of the flat plate to measure the flow statistics. LDV laser beams are focused over the floating element of the central MEMS sensor, while the two other MEMS sensors are taking data across the span. (b) An image of the MEMS and LDV experiments.

Table 7.2 Canonical turbulent boundary-layer parameters.

U_∞ (m/s)	u_τ (m/s)	δ (mm)	δ^* (mm)	θ (mm)	H	Re_τ	Re_θ	$TU(\%)$
6	0.2348	40	6.9	4.8	1.43	600	1800	0.54
6.8	0.2743	38	6.6	4.6	1.4	700	2000	0.6
8.7	0.3301	37	6.3	4.5	1.39	870	2200	0.38
10	0.3858	36	5.8	4.12	1.41	910	2660	0.33
12	0.4207	35.5	5.6	4.06	1.38	1060	3300	0.42
15	0.5694	35.1	5.5	3.96	1.39	1320	3900	0.46

is extrapolated so that $u = 0$ m/s. The value of the wall-shear stress and the friction velocity are quantified by using the slope of the fitted line. For the range of measured flow speeds, the friction velocity varies in the range of $u_\tau = 0.2348$ to 0.5694 m/s, the Reynolds number based on the friction velocity varies from $Re_\tau = 600$ to 1320 , and the Reynolds number based on the momentum thickness varies from $Re_\theta = 1820$ to 3900 . Equation 7.7 and Equation 7.8 are utilised to calculate other parameters of the turbulent boundary-layer, such as the momentum thickness and the Reynolds number based on the momentum thickness. The value of these parameters are summarised in Table 7.2.

Turbulent boundary-layer profiles for $z = 0$ and $z = 75$ mm (on the right side of the Central sensor) are presented in Figure 7.7 and Figure 7.8. The mean velocity values, \bar{u} and \bar{v} , and the standard deviation for the velocity components, SD_u and SD_v , are calculated using Equation 5.6 to Equation 5.9.

Figure 7.7a and Figure 7.8a show time-averaged streamwise velocity profile taken over a range of Reynolds numbers ($Re_\theta = 1800$ to 3900) by LDV at two spanwise locations $z = 0$ ($z^+ = 0$) and $z = 75$ mm ($z^+ = 1200$ to 2860). Data that are acquired with LDV show excellent agreement with the theoretical data and collapse to the Schlichting log law in the canonical boundary-layer. LDV data are compared to DNS data that are adopted from Schlatter and Örlü (2010), for relatively similar Reynolds numbers ($Re_\theta = 1400$ to 4000). Turbulence intensity profiles for both streamwise and spanwise velocity components, u'_{RMS} and v'_{RMS} , are illustrated in Figure 7.7b and Figure 7.8b. It can be seen that the LDV data are in good agreement with the DNS data, where the difference between two data sets arises from the difference in the Reynolds numbers. LDV has

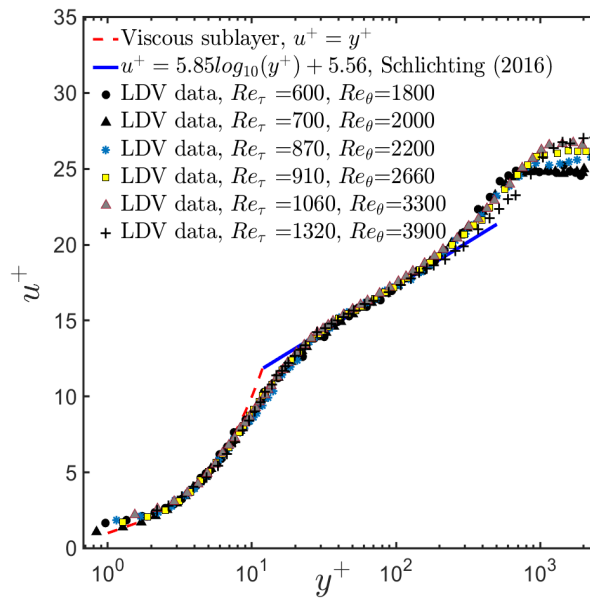
slightly underestimated $u'_{RMS} \approx 7\%$ for $y^+ < 7$ below the DNS data over the Re_τ of interest. For $y^+ > 20$, the LDV data converges on the DNS data. On the other side, LDV slightly overestimated $v'_{RMS} \approx 5\%$ for $y^+ < 170$ over the DNS data over the Re_τ of interest.

Skewness and kurtosis profiles for the streamwise velocity are presented in Figure 7.7c and 7.7d. Similar to the turbulence intensity profile, the experimental data taken by LDV show similar profiles to the DNS data. A slight difference can be noticed between the data sets, which is due to the difference in the Reynolds numbers. Shown in Figure 7.7e and Figure 7.8e, are the Reynolds stress profiles, $-\overline{u'v'}$, where the insets in Figure 7.7e demonstrate the fluctuating velocity components time series and their negative product time series. The time average of this product, $-\overline{u'v'}$, provides the Reynolds stress profiles. The Reynolds stress profiles are plotted against the DNS data obtained from Schlatter and Örlü (2010). For $Re_\tau = 600$, the LDV Reynolds stress slightly underestimated $-\overline{u'v'} \approx 2\%$ at $y^+ = 40$, and then converged to the DNS data for the remaining wall-normal locations. For $Re_\tau = 870$ and $Re_\tau = 910$ the LDV data slightly overestimated $-\overline{u'v'} \approx 1.5\%$ over the range of measured wall-normal locations. For $Re_\tau = 1060$ and $Re_\tau = 1320$, the LDV overestimated the $-\overline{u'v'} \approx 2\%$ for $y^+ < 35$, and then converged to DNS data for $y^+ > 35$.

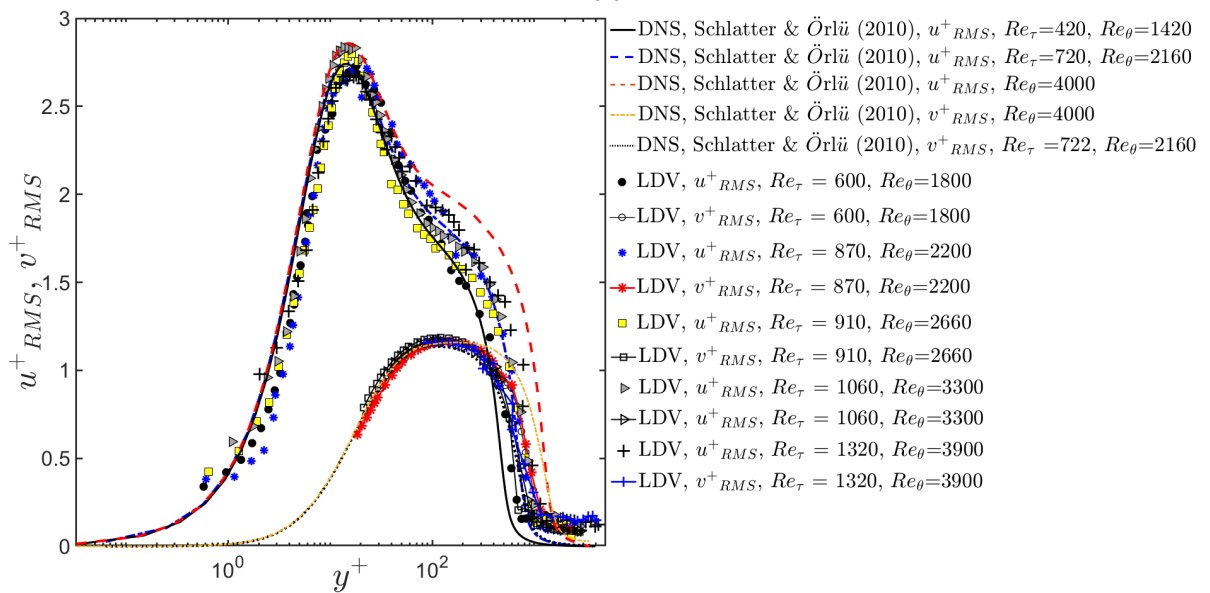
Results from canonical turbulent boundary-layer measurements ensure that the developed boundary-layer is in turbulent state. Turbulent boundary-layer profiles captured at two locations across the span show that the turbulent boundary-layer profiles are similar, and hence the turbulent flow statistics should be similar across the span at the streamwise location of interest.

7.2.2 Wall-shear stress measurement-MEMS and LDV

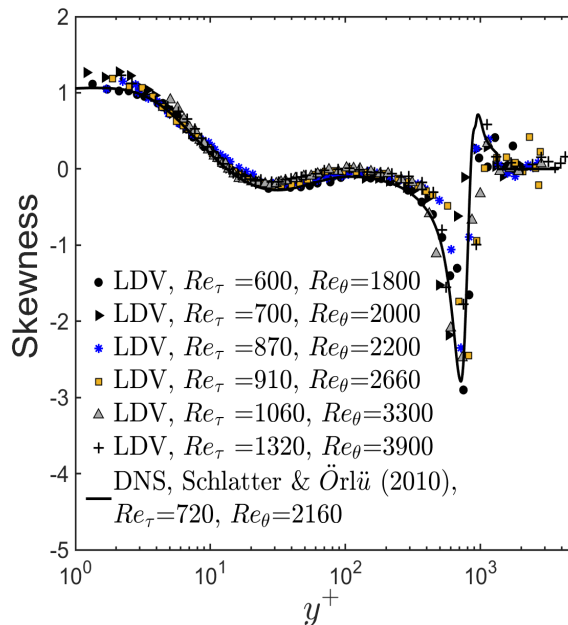
To ensure that the MEMS wall-shear stress sensors are able to capture fluctuating wall-shear stress correctly, an independent measurement of the fluctuating wall-shear stress was carried out by measuring the instantaneous streamwise velocity from within the viscous sub-layer and 150 μm to 200 μm above the central MEMS sensor. Two other MEMS wall-shear stress sensors were also implemented in $z = \pm 75$ mm on either side of the central sensor. For each Reynolds number, MEMS sensors with appropriate size, sensitivity, and dynamics characteristics were utilised to investigate the optimum



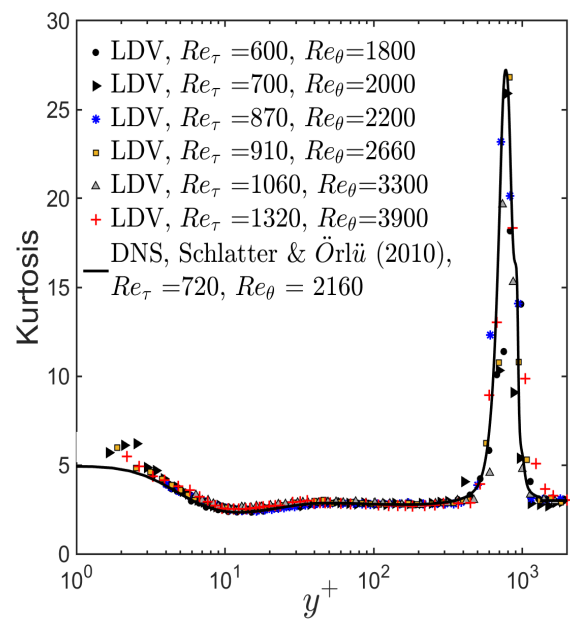
(a)



(b)



(c)



(d)

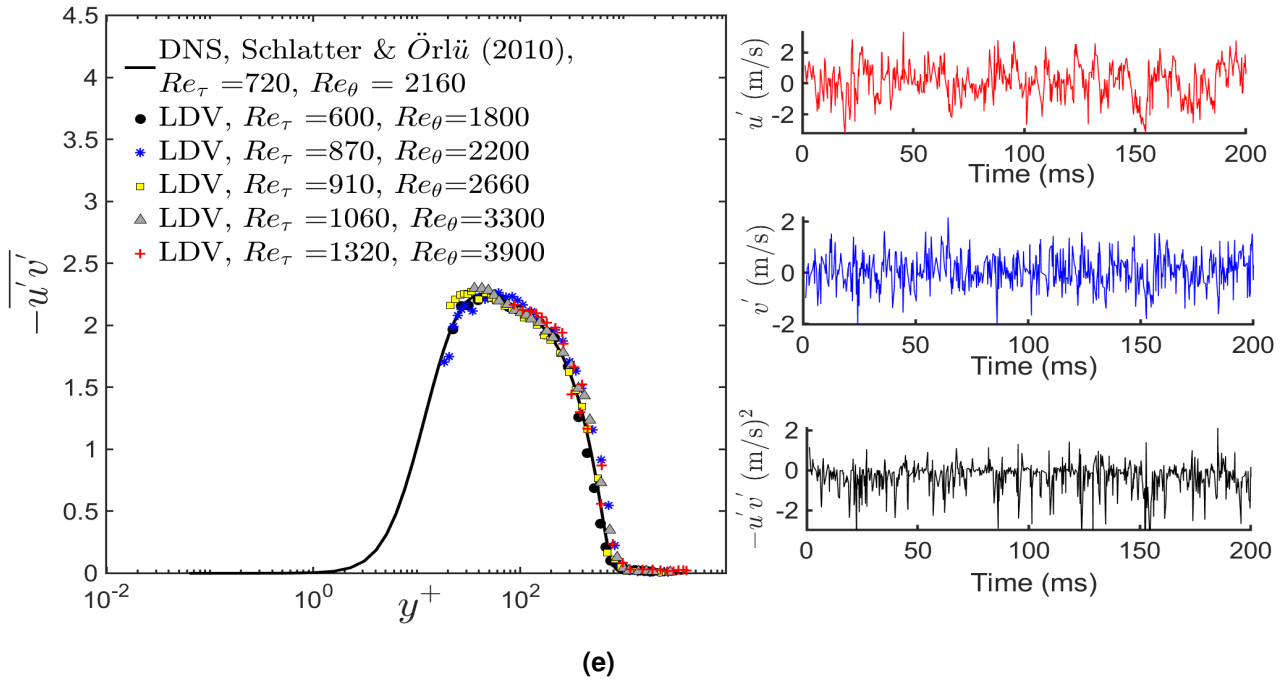
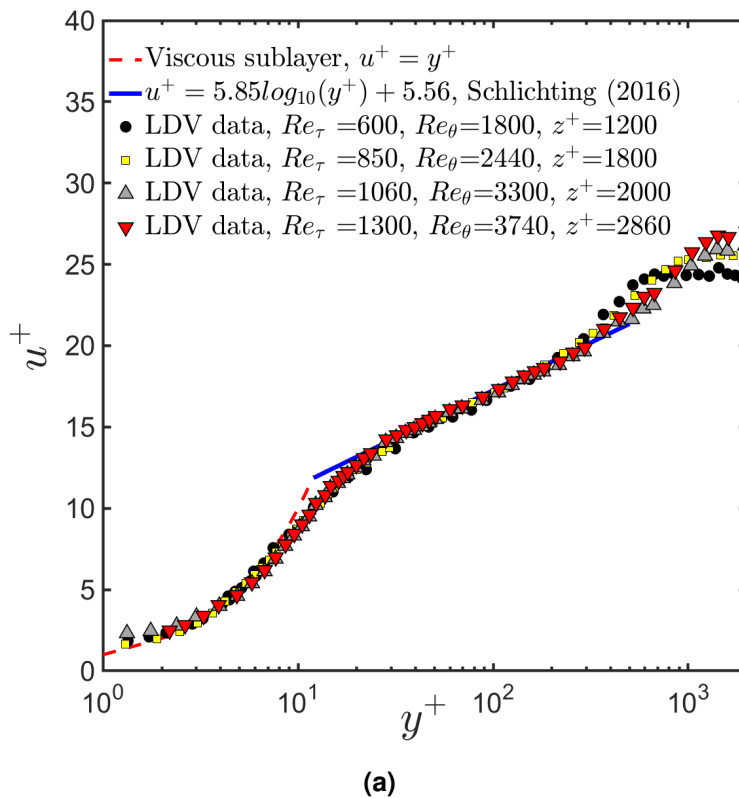
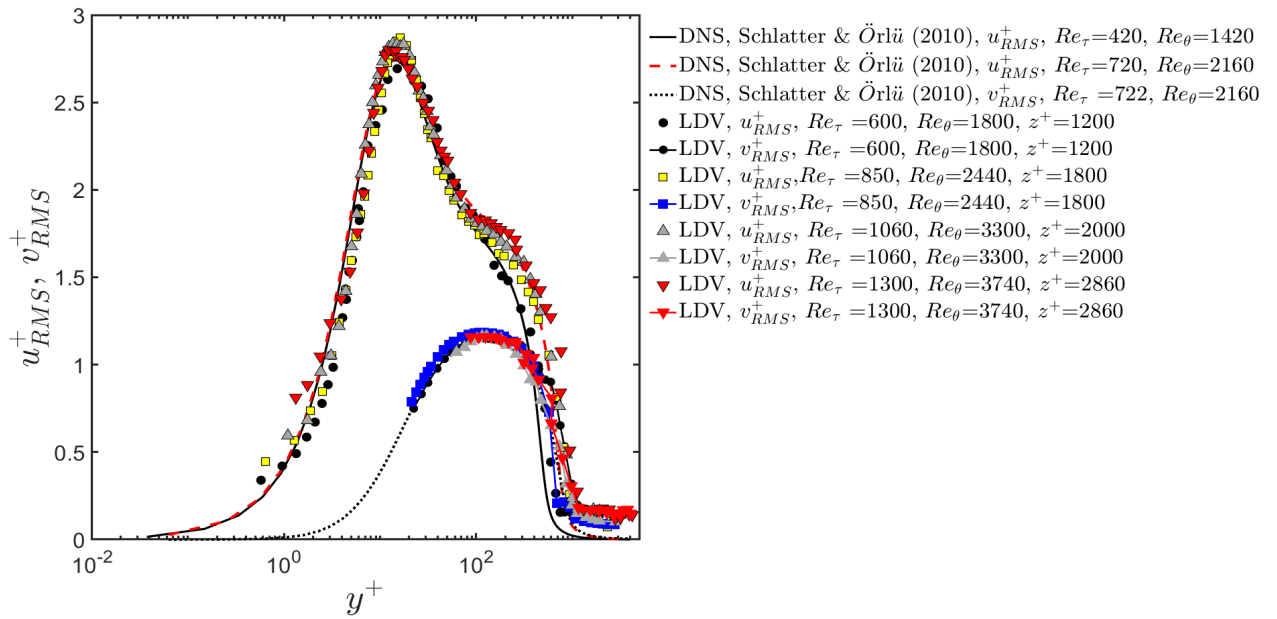
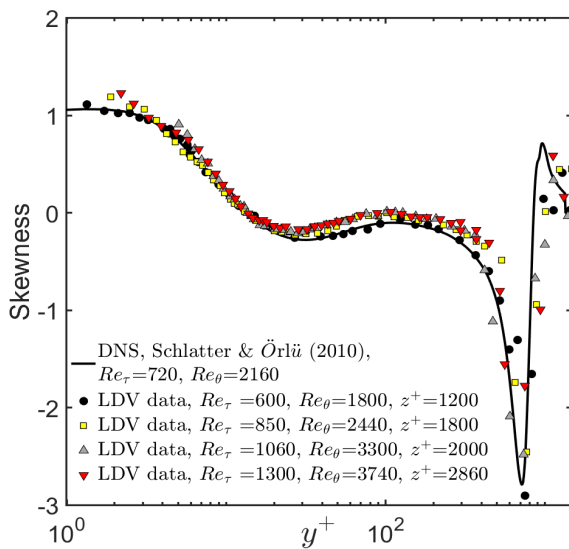


Figure 7.7 Turbulent boundary-layer canonical data measured by LDV at $z = 0$ for a Reynolds number range of $Re_\tau = 600$ to 1320 . (a) Mean streamwise velocity profiles, (b) turbulence intensity profiles of the both streamwise and spanwise velocities. Due to the surface reflection issues the spanwise direction velocity component measurement, started at $y^+ = 25$, (c) skewness profiles of the streamwise velocity, (d) kurtosis profiles of the streamwise velocity, and (e) Reynolds stress profiles, where insets show the fluctuating velocity components in streamwise, u' , and spanwise, v' , and the negative product of these components, $-u'v'$.

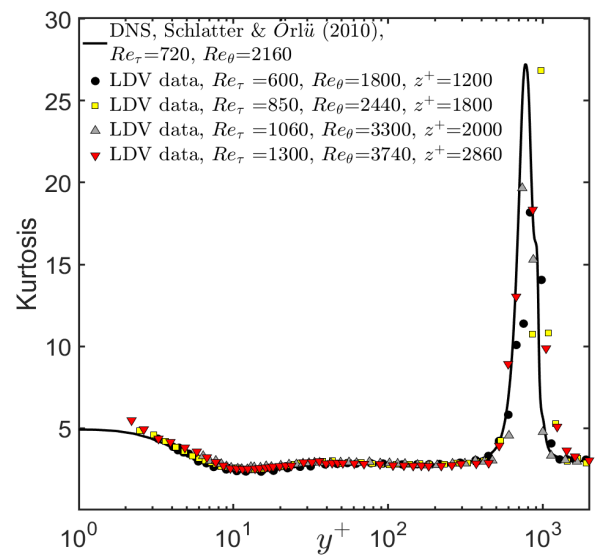




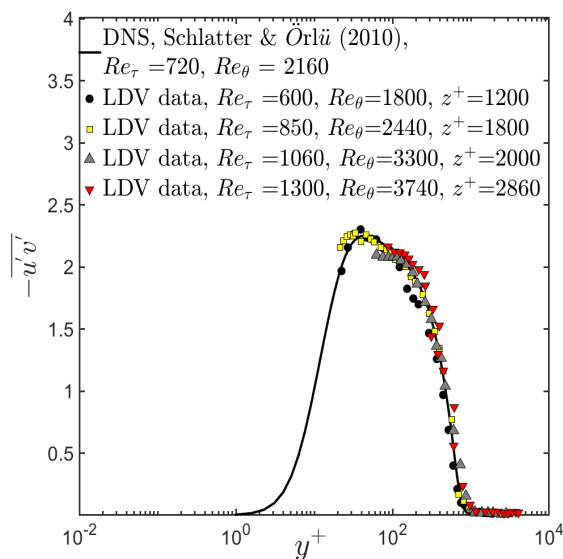
(b)



(c)



(d)



(e)

Figure 7.8 Turbulent boundary-layer canonical data measured by LDV at $z = 75\text{mm}$.

Turbulent boundary-layer measurements

performance of the devices. Here, up to 2×10^6 streamwise velocity data points were acquired with LDV from the within viscous sub-layer for each Reynolds number in the range of $Re_\tau = 600$ to 1320. For the wall-shear stress measurements, only the streamwise velocity component of the flow was captured by LDV, due to the surface reflection noise induced from the spanwise laser beam. At each experimental run, the data from the central MEMS sensor was captured using the external input port of the FSA3500 and a National Instrument DAQ card to ensure that the signal from the LDV and the MEMS sensor are time-stamped, while the data from the MEMS sensors on the spanwise locations were captured using the National Instrument DAQ card and a computer program written in LabVIEW. The voltage output signal from the MEMS sensors were post-processed and transferred into the wall-shear stress using the calibration curves, which are presented in Chapter 6.

The measured turbulent boundary-layer wall-shear stress parameters such as the mean wall-shear stress, $\overline{\tau_w}$, standard deviation, SD_{τ_w} , skewness, S_{τ_w} , and kurtosis, K_{τ_w} , are presented in Table 7.3, where the data captured by LDV and various MEMS sensors are compared. The LDV and MEMS sensing areas are normalised in wall units for the purpose of comparison and spatial resolution effects in the measurements. Here the width, length, and the area of the sensing elements can be normalised as $w^+ = W_e u_\tau / \nu$, $L^+ = L_e u_\tau / \nu$, $A^+ = W^+ \times L^+$, respectively. For $Re_\tau = 600$, MEMS DEV CC20 ($A^+ = 210.5$) was used in the central sensor plug ($z^+ = 0$), with the LDV laser beams focused at the top of its floating element at $y^+ = 3.5$. MEMS DEV SER27-1 ($A^+ = 107.5$) and DEV

Table 7.3 Turbulent flow wall-shear stress parameter measured by MEMS sensors and LDV.

	Device	z^+	y^+	$w^+ = w_e u_\tau / \nu$	$L^+ = L_e u_\tau / \nu$	$A^+ = w^+ L^+$	$\overline{\tau_w}$ (Pa)	SD_{τ_w}	S_{τ_w}	K_{τ_w}	Correlation
$Re_\tau = 600$	LDV	0	3.5	0.95	4.6	4.5	0.088	0.0392	1.14	5.07	-
	DEV CC20	0	-	14.5	14.5	210.5	0.085	0.0301	1.13	4.96	66%
	DEV SER27-1	1380	-	11.8	9.1	107.5	0.0839	0.0322	1.134	5	-
	DEV CC13	-1380	-	18.3	18.3	335	0.0835	0.0293	1.13	4.97	-
$Re_\tau = 910$	LDV	0	4	1.3	6.5	8.5	0.1247	0.0564	1.1425	5.24	-
	DEV SER27-1	0	-	16.6	12.8	211	0.1214	0.0457	1.1361	5.14	81%
	DEV SER26	1940	-	20.5	12.5	260	0.116	0.0421	1.1378	5.136	-
	DEV CC30	-1940	-	25.5	25.5	350	0.1147	0.0408	1.1212	5.02	-
$Re_\tau = 1060$	LDV	0	3.7	1.4	7	13.3	0.2142	0.0811	0.81	3.875	-
	DEV SER26	0	-	22.3	13.9	310	0.2083	0.0779	0.7557	3.79	76%
	DEV SER27-2	2100	-	18.1	13.9	252	0.2081	0.0769	0.80788	3.729	-
	DEV CC30	-2100	-	28	28	784	-	-	-	-	-
$Re_\tau = 1320$	LDV	0	4	1.9	9.5	17.1	0.399	0.1858	1.1465	5.224	-
	DEV SER27-2	0	-	24.5	18.8	460	0.3877	0.1552	1.1307	5.16	71%
	DEV SER27-1	2850	-	24.5	18.8	460	0.391	0.1544	1.1394	5.18	-
	DEV SER26	-2850	-	30.1	18.8	565	0.3934	0.154	1.1426	5.21	-

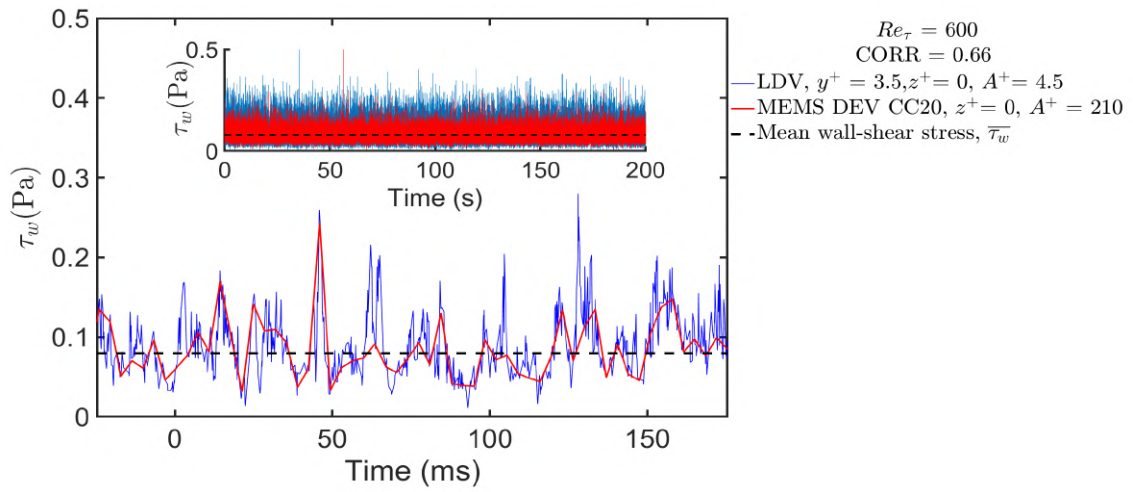
CC13 ($A^+ = 335$) were implemented on either side of it at $z^+ = 1380$ and $z^+ = -1380$, respectively. Here, the MEMS sensors slightly underestimated $\overline{\tau_w}$ by 3.4% for DEV CC20 and 5% for the devices on the spanwise locations, with respect to LDV measurement. The value of the wall-shear stress skewness, S_{τ_w} , measured by MEMS sensors are approximately 4 % less than the LDV measurements. The value of the wall-shear stress kurtosis measured by MEMS sensors is 2 % less than the values measured by LDV. For $Re_\tau = 910$, MEMS sensor number DEV SE27-1 ($A^+ = 211$) was used to measure the wall-shear stress at $z^+ = 0$, with the LDV focused above this sensor at $y^+ = 4$. DEV SER26 ($A^+ = 260$) and DEV CC30 ($A^+ = 350$) were implemented at $z^+ = 1940$ and $z^+ = -1940$ to measure the wall-shear stress parameters on across the span. The value of the mean wall-shear stress, $\overline{\tau_w}$ measured by the central MEMS is 2.6 % less than the LDV measurement. Moreover, the $\overline{\tau_w}$ values measured by the MEMS sensors in $z^+ = 1940$ and $z^+ = -1940$ are 6 % and 8 % smaller than the values obtained by the LDV at $z^+ = 0$, respectively. These values are 4 % and 5 % smaller than the central sensor measurement. MEMS sensors slightly underestimated the skewness and kurtosis values by 3.7 % and 1.9 %, respectively. At $Re_\tau = 1060$, device number DEV SER26 ($A^+ = 310$) was utilised at $z^+ = 0$ alongside with the LDV at $y^+ = 3.7$, to quantify the wall-shear stress. DEV SER27-2 ($A^+ = 252$) and DEV CC30 ($A^+ = 784$) were used for the measurement across the span. For the central MEMS sensor, the values of τ_w , SD_{τ_w} , S_{τ_w} , and K_{τ_w} are 2 %, 3.9 %, 6 %, and 2.1 % smaller compared to the values obtained by the LDV, respectively. After the measurement at this Reynolds number, it has been noticed that the Device number DEV CC30 failed to measure the fluctuating wall-shear stress values and hence, no values are reported for this device. For the final experiment at $Re_\tau = 1320$, two MEMS sensor replicas, DEV SER27-1 ($A^+ = 460$ and $z^+ = 2850$) and DEV SER27-2 ($A^+ = 460$ and $z^+ = 0$), are used alongside with DEV SER26 ($A^+ = 565$ and $z^+ = -2850$). The LDV laser beams were focused over the sensing element of DEV SER27-2 at $y^+ = 4$. It can be seen that the values of the mean wall-shear measured by DEV SER27-1 ($z^+ = 2850$) and DEV SER27-1 ($z^+ = 0$) are in excellent agreement, where the mean wall-shear stress value measured by DEV SER27-1 is only 0.85 % larger than DEV SER27-2.

From the statistical values presented in Table 7.3 it can be noticed that the values of the statistical parameters measured by the MEMS wall-shear stress sensors are

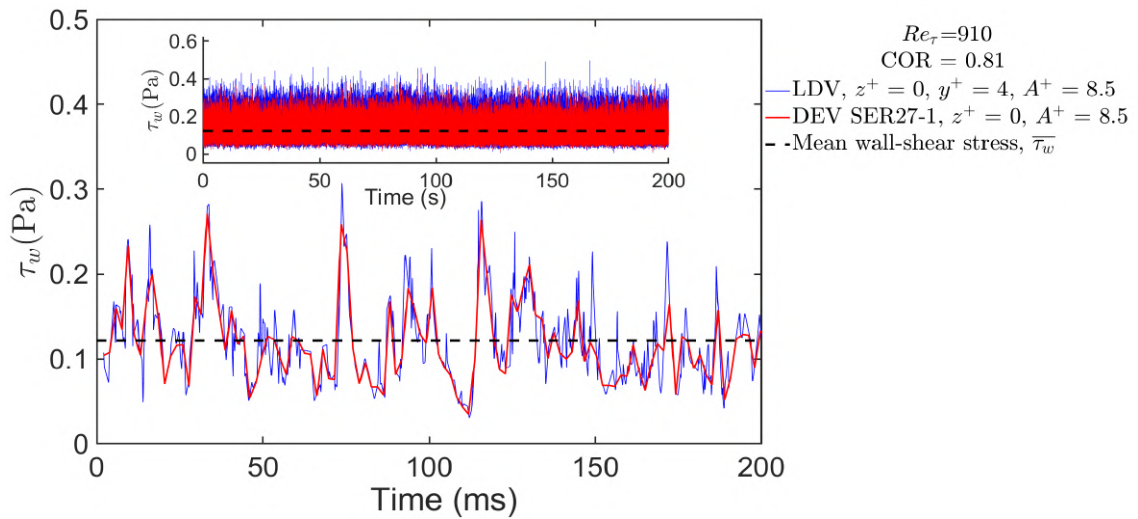
slightly underestimated compared to the LDV. This could be due to the fact that the LDV measurement is carried out at a wall-normal location above the wall ($y^+ \approx 4$). Another reason for the underestimation of the parameters can arise from the spatial attenuation, which is due to the difference in the sensing element sizes in the MEMS devices and the LDV. To elucidate the performance of the MEMS devices in capturing the wall-shear stress fluctuations, the instantaneous wall-shear stress time signals are shown in Figure 7.9. Figure 7.9a shows data for DEV CC20 and LDV ($y^+ = 4$) at $Re_\tau = 600$, Figure 7.9b illustrates signals at $Re_\tau = 910$ for DEV SER27-1 alongside with the LDV at $y^+ = 4$, Figure 7.9c demonstrates the signals at $Re_\tau = 1060$ for DEV SER26 alongside with the LDV at $y^+ = 3.7$, and Figure 7.9d shows signals at $Re_\tau = 1320$ for DEV SER27-2 alongside with the LDV at $y^+ = 4$. Plotting the time signals show, from an instantaneous point of view, that trend of the wall-shear stress signal measured by two independent measurements methods are similar. However, it can be seen that the number of the small scale fluctuations captured by MEMS are fewer compared to the LDV. To quantitatively determine the similarity the correlation between the wall-shear stress time signals can be defined as (Rabiner and Gold, 1975)

$$(\tau_{w,MEMS} \star \tau_{w,LDV})(\tau) \triangleq \int \tau_{w,MEMS}^*(\tau) \tau_{w,LDV}(\tau + t) dt \quad (7.9)$$

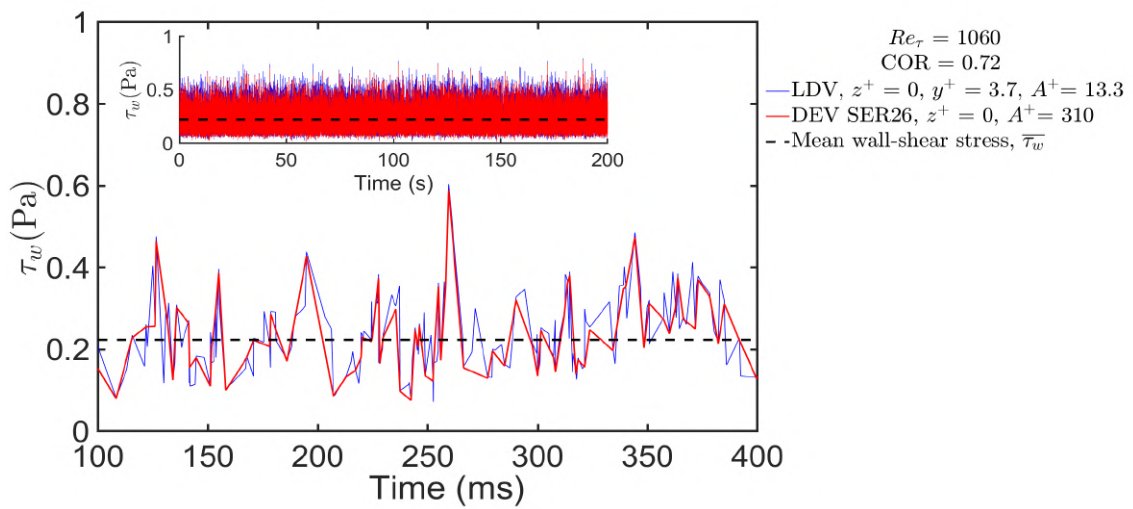
where $\tau_{w,MEMS}$ and $\tau_{w,LDV}$ are the wall-shear stress time signal measured by MEMS sensors and LDV, respectively, and $\tau_{w,MEMS}^*$ and τ are the complex conjugate and the lag, respectively. The value of the correlation between the DEV CC20 and the LDV at $Re_\tau = 600$ is 66%, which can be noticed in the presented time signal. This can be noticed in the corresponding time signal where the MEMS sensor captured the larger scale wall-shear stress fluctuations, while the smaller scale fluctuations that are presented in the LDV time signal, could not be captured by this device. The value of the correlation increases to 81 % for the measurement at $Re_\tau = 910$. L^+ value of 12.8 on DEV SER27-1 is 37.3 % smaller than L^+ value of 20.4 on DEV CC20. Similarly, W^+ value of 16.8 on DEV SER27-1 is 17.65% less than the corresponding value of 20.4 on DEV CC20. A comparison between the correlation values at $Re_\tau = 910$ and $Re_\tau = 1320$ demonstrates that the effect of spatial averaging in the wall-shear stress measurement increases with Reynolds number. Here, the correlation value reduces from 81% to 71 %, despite the



(a)



(b)



(c)

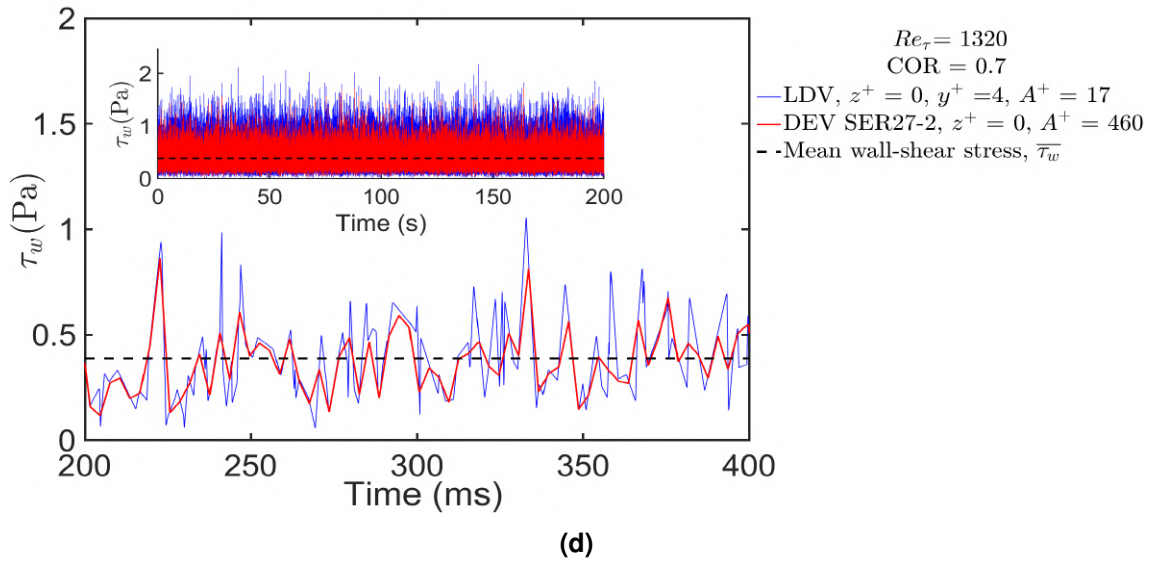


Figure 7.9 Wall-shear stress time signals captured by MEMS sensors and the LDV. (a) DEV CC20 and LDV τ_w time signals with a correlation of 66%, (b) DEV SER27-1 and LDV τ_w time signals with a correlation of 81%, (c) DEV SER26 and LDV τ_w time signals with a correlation of 72%, and (d) DEV SER27-2 and LDV τ_w time signals with a correlation of 70%.

fact that the sensors' geometries are similar, which indicates the increased effect of the spatial averaging on the MEMS sensor measurement as a result of an increase in the Reynolds number.

Figure 7.10 depicts the fluctuation magnitude of the wall-shear stress, $\tau_{w,RMS}^+ = \tau_{w,RMS}^l / \bar{\tau}_w$, as a function of Re_τ . Since MEMS sensor number DEV SER27 was used for measurement over the range of Re_τ , the value of $\tau_{w,RMS}^+$ is calculated for this device for the comparison against the LDV data. The value of $\tau_{w,RMS}^+$ for LDV measurement slightly increases from 0.445 at $Re_\tau = 600$ to 0.462 at $Re_\tau = 1320$. Nonetheless, for the MEMS sensor this value slowly increases from 0.373 to 0.407. Although the values of measured $\tau_{w,RMS}^+$ using the MEMS sensors are smaller than the LDV measurement (by up to 15%), the asymptotic $\tau_{w,RMS}^+$ value of ≈ 0.4 for the MEMS sensors and ≈ 0.44 for the LDV are in agreement with the value found in the experiments of Alfredsson et al. (1988) at $Re_\tau = 300$ and Moser et al. (1999).

The inset in Figure 7.10 demonstrate the effect of the wall-unit normalised sensors length, L^+ , and width, W^+ on the fluctuation magnitude of the wall-shear stress at $Re_\tau = 600$. It can be seen that the value of $\tau_{w,RMS}^+$ decreases as L^+ and W^+ increase. Interestingly, the trend here is in agreement with the previous investigation by Schlatter and Örlü (2010), Alfredsson et al. (1988), and Österlund (1999). To investigate the spatial attenuation of the sensors measurement due to the sensing element width, the

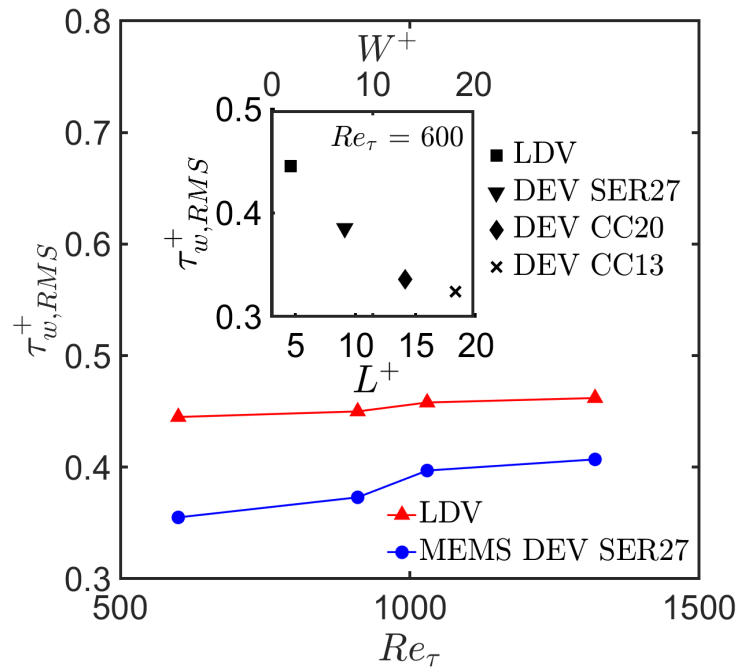


Figure 7.10 Fluctuation magnitude of the wall-shear stress, $\tau_{w,RMS}^+ = \tau_{w,RMS}^i / \overline{\tau_w}$, as a function of Re_τ . Red triangles show the data captured by LDV and blue circles represent the data captured by MEMS DEV SER27. Inset shows the effect of sensor sizes, L^+ and W^+ , on $\tau_{w,RMS}^+$ at $Re_\tau = 600$. Black square represent the LDV data, south pointing triangle show the MEMS SER27-1, diamond shows the data for MEMS CC20, and black cross represents the data for DEV CC13.

value of $\tau_{w,RMS}^+$ is obtained for DEV SER27-1 and DEV SER26, which have similar L^+ , at $Re = 1320$. The value of $\tau_{w,RMS}^+$ for DEV SER26 at $Re_\tau = 1320$ is equal to 0.393, which is 3.5% smaller than $\tau_{w,RMS}^+ = 0.407$ for DEV SER27-1, which could arise from spatial averaging effects due to the sensor width. Although the smaller value of $\tau_{w,RMS}^+$ measured by the MEMS sensor can be explained by the spatial resolution effects, it is not clear which dimension on the sensor's sensing element (L^+ or W^+) plays the main role in the sensors' spatial averaging.

Probability density functions (PDFs) of the fluctuating wall-shear stress, $B(\tau_w^i)$, acquired by MEMS sensors and the LDV at $Re_\tau = 600$ to 1320 are illustrated in Figure 7.11. Very good agreement can be observed across the two independent measurement methods, illustrating that the MEMS sensors are correctly capturing the wall-shear stress. It can be noticed that the PDFs obtained from the MEMS measurement are slightly underestimated compared to the LDV. The difference between the peak values in the PDFs between the MEMS and LDV is approximately 3.7% at $Re_\tau = 600$, which increases to 10% at $Re_\tau = 1320$. This is consistent with the trend that is observed in the fluctuation magnitude of the wall-shear stress, and can arise from the spatial

averaging effects in the MEMS devices. The distribution of the wall-shear stress data measured by all the devices are positively skewed. In addition to this, the fluctuations in the wall-shear stress are super-Gaussian, since $K_{\tau_w} > 3$, which means there is a large probability of extreme fluctuations in the wall-shear stress. Here, the values of K_{τ_w} are consistent with the previous researchers data (Alfredsson et al., 1988). This is also consistent with the physical behaviour of the fluid flow near the wall region, where positive velocity fluctuations, and hence forward velocity gradients will be more likely than the backward velocity gradients (Gubian et al., 2019). Normalising the wall-shear stress data sets by $\tau_{w,RMS}$ collapses the data at $Re_\tau = 600$ to 1320. The positive tail on the normalised wall-shear stress fluctuations indicate that MEMS sensors could capture large events in the flow alongside with the LDV, where the values of $\tau_w' / \tau_{w,RMS}$, extend beyond 7.5 for DEV SER26 and DEV SER27-2. The normalised PDFs of the fluctuating wall-shear stress additionally indicates that there is no negative wall-shear stress values, and hence no flow reversal events, are captured by the MEMS sensors, which can be justified by the fact that there is no wall-shear stress below $\tau_w' / \tau_{w,RMS} < -2$. This is not unexpected and it has been investigated by Örlü and Schlatter (2011), where by utilising DNS, it was shown that the contribution of the negative wall-shear stress values is less

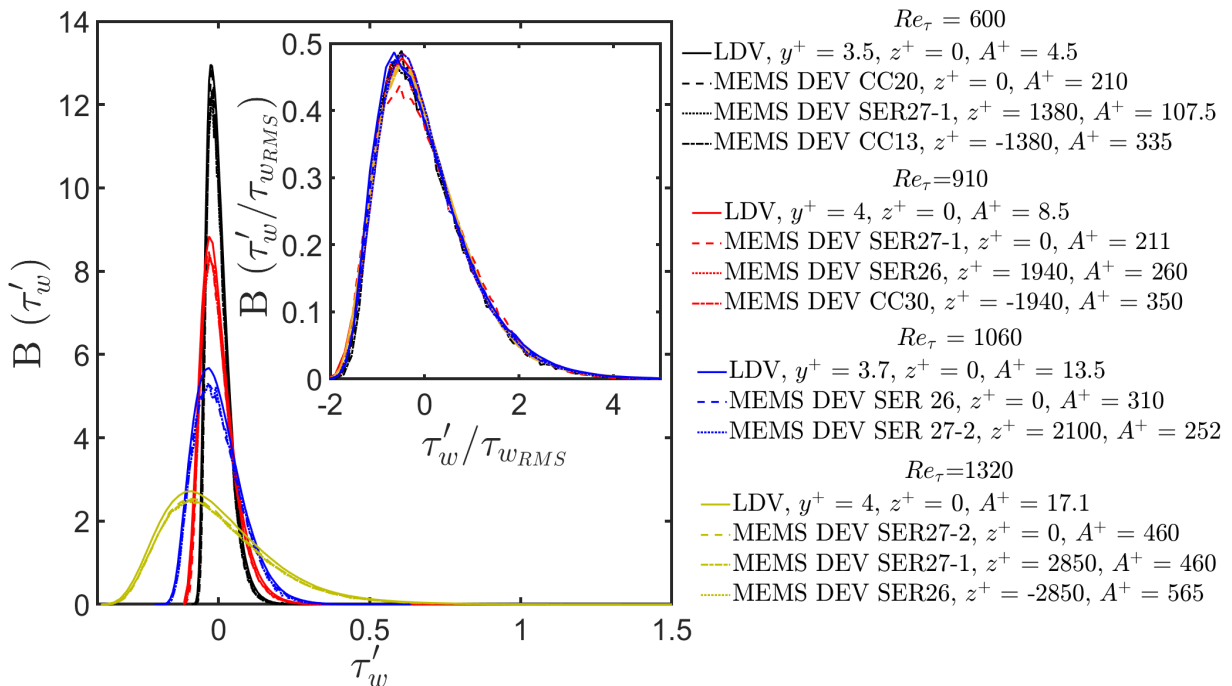


Figure 7.11 PDFs of fluctuating wall-shear stress measured by LDV and the MEMS sensors at $Re_\tau = 600$ (black lines), $Re_\tau = 910$ (red lines), $Re_\tau = 1060$ (blue lines), and $Re_\tau = 1320$ (orange lines). LDV data captured at the location of the central MEMS sensor for each Re_τ . The inset shows the normalised PDFs of the wall-shear stress fluctuations.

than 0.1% of the PDF. Since the nature of the MEMS sensors measurement allows the reversal flow events detection, a longer sampling period is required for the purpose of negative wall-shear stress detection. Moreover, it has been shown by Diaz-Daniel et al. (2017) that the probability of the flow reversal events increases with increasing Reynolds number. As a result of this, further flow sampling with MEMS wall-shear stress sensors is required at higher Reynolds numbers ($Re_\theta > 4000$) for a longer period of time for reversal flow detection.

7.3 Summary

The measurement of wall-shear stress using the MEMS sensors was discussed in this chapter. Turbulent boundary-layer measurement was carried out using the MEMS sensors, hot-wire, and LDV. The wall-shear stress measurement data from these independent measurement techniques over a range of $Re_\tau = 560$ to $Re_\tau = 1320$ have shown that the MEMS sensors can correctly quantify the wall-shear stress within the turbulent boundary-layer. MEMS wall-shear stress sensor can resolve the mean value of the wall-shear stress, $\overline{\tau_w}$, with high accuracy ($\approx 3\%$ difference in $\overline{\tau_w}$ values between MEMS sensors, hot-wire, and LDV). The accuracy of the MEMS sensors in the measurement of the fluctuating wall-shear stress is affected by the sensors' geometry. For both experimental runs, it has been found that the values of the $\tau_{w,RMS}^+$ measured by MEMS sensors are smaller than the values measured by the hot-wire and LDV. It has been discussed that this is linked to the different geometry of the sensing elements with various dimensions. Although $\tau_{w,RMS}^+$ is smaller for the MEMS sensors, the measured values are in agreement with the data from previous researchers. The highest correlation between the MEMS sensor and LDV wall-shear stress signal has been found to be 81% for MEMS DEV SER27-1 at $Re_\tau = 910$, which once more, shows the effect of the sensor dimensions on its measurement performance. The PDFs of τ_w' have shown very good agreement across the measurement techniques, which indicates that the MEMS sensors are able to correctly capture measure the wall-shear stress.

Chapter 8

Conclusion and Future Recommendations

8.1 Conclusion

Obtaining accurate, instantaneous measurements of wall-shear stress is notoriously challenging, which has significant fundamental and industrial importance. In this study, optical MEMS wall-shear stress sensors using the Moiré fringe pattern transduction have been developed for air flow measurements. Two types of MEMS sensors have been developed by utilising clamped-clamped and serpentine micro-springs. Analytical and FEA techniques were implemented for the mechanical modelling of the sensors' structure. In addition, the effect of geometrical parameters on the sensor performance, such as the mechanical sensitivity and the resonant frequency was investigated. It has been shown that the result from the analytical modelling and the FEA were in excellent agreement, which provides a reliable design procedure for the MEMS wall-shear stress sensors structure. It has been discussed that in order to detect the nanometer scale motion of the MEMS wall-shear stress sensors, movements of the Moiré fringe pattern, which amplifies the motion of the sensors by up to 90 times (DEV CC30), was tracked.

The design of the Moiré fringe pattern, which has been generated during the microfabrication process via the supposition of two sets of finely spaced sputtered gold gratings, has been presented, followed by a discussion on the sensors' displacement detection technique. It has been shown that the Moiré fringe pattern can be expressed by a

Conclusion and Future Recommendations

sinusoidal function. Any displacement in the sensor structure produces a transformation in the position of dark and light bands on the Moiré fringe pattern and consequently a phase shift in the corresponding sinusoidal function. As a result of this, the phase shift in the signal is directly related to the mechanical displacement of the sensor and eventually it can be utilised to quantify the wall-shear stress that is applied to the sensor. A novel rippling optoelectronics consist of an array of LEDs, an array of fibre optic cables, a pair of aspheric condenser lenses and a single photodiode, was developed to track the displacement of the Moiré fringe pattern. Experimental test-beds were developed as a proof of concept to ensure that the rippling optoelectronics can read the sensors displacement.

Microfabrication process was carried out to fabricate the MEMS wall-shear stress sensors using a four masks, bulk SOI process. The results of the inspection and metrology, using SEM and WLI, on the sensors indicated an excellent geometrical parameters agreement between the fabricated sensors and the designed values. Two sensor packaging were designed and developed to functionalise the MEMS sensors via bringing together the MEMS sensor dies and the required optoelectronics.

Sensors' calibration and their dynamic performance has been discussed in Chapter 6. The result of the sensor's calibration are presented in Table 6.1, where it has been shown that the mechanical sensitivity of the devices varied from 38 to 730 nm/Pa. Moreover, the experimentally verified dynamic range of the devices varies from 79 to 109.9 dB. Here the maximum value of the wall-shear stress was limited by the measurement facility limitations (i.e. manometer operation range), and hence, which indicates a potential for higher attainable values for the dynamic range of the devices. The values for other sensors' parameters such as the accuracy, repeatably and the minimum detectable wall-shear stress were also presented. In addition to sensors' calibration, the dynamic performance of the fabricated MEMS sensors were investigated, and it has been shown that resonant frequency of the fabricated devices cover a range of 1-8.4 kHz. The sensor's flat band, quality factors and time delays were also determined.

Finally, the fabricated devices were implemented in a wind tunnel for the turbulent boundary-layer flow measurement. Independent instantaneous wall-shear stress measurements were carried out in turbulent boundary-layer flows, utilising the developed MEMS sensors, hot-wire anemometry, and LDV to further explore the performance

of the developed sensors in turbulence measurement and investigate their ability to measure the wall-shear stress fluctuations. The results of the wall-shear stress measurement from these independent quantification techniques over a range of $Re_\tau = 560$ to 1320 have indicated that the MEMS sensors can correctly measure the wall-shear stress within the turbulent boundary-layer. The mean wall-shear stress values, $\overline{\tau_w}$, measured by the developed MEMS sensors have been demonstrated to be within 3% of the hot-wire and the LDV measurements. Considering that the accuracy error of the MEMS sensors was measured to be within a range of 1 to 2.36%, the 3% difference in the mean wall-shear stress value indicates the reliability of the MEMS sensors in $\overline{\tau_w}$ quantification. The values of the other statistical parameters indicated a 1 to 8% difference between the MEMS and the hot wire/LDV measurements. To further investigate the performance of the devices, time-stamped instantaneous wall-shear stress signals measured by the MEMS sensors and the LDV were presented for the first time. For MEMS DEV SER27-1 a minimum correlation of 81% with the LDV wall-shear stress time signal, has been observed, indicating the excellent promise of the MEMS sensors in capturing both mean and fluctuating values of the instantaneous wall-shear stress. The value of the correlation between the MEMS sensor signal and the LDV, however, was affected by several parameters. To capture the time-stamped wall-shear stress signals, the sampling frequency of the MEMS sensors were limited by the data rate of the LDV, which determined the system's sampling rate. Here, obtaining high LDV data rate (> 3000 kHz) values within the viscous sublayer is challenging due to the wall reflection effects and the low density of the seeding particles near the wall region. Considering a rippling frequency of 5-7 kHz of the MEMS sensors, some fluctuations can be filtered out from the MEMS sensors signal. In addition to this, the effect of the sensing element dimensions on the measurement has been presented, which showed a slight decrease in the magnitude of the wall-shear stress fluctuations, which requires further investigation.

8.2 Research contributions

The contribution of this research are as follow:

1. Successful development of optical MEMS wall-shear stress sensors by utilising two types of micro-springs.
2. Using serpentine micro-spring for 1D optical MEMS wall-shear stress sensors, which can boost the mechanical sensitivity, over an smaller area compared to the clamped-clamped micro-spring with the same mechanical sensitivity value. This can be used for MEMS wall-shear stress arrays, where a larger number of sensors can be placed over an area.
3. Utilising the rippling optoelectronics with a built in photodetector into the sensor package, which enhances the Moiré fringe pattern detection.
4. Design and development of novel sensor packaging for the rippling optoelectronics.
5. Instantaneous Wall-shear stress measurement within turbulent boundary-layer air flows using the optical MEMS wall-shear stress sensors alongside with hot-wire anemometry and LDV.
6. Wind tunnel testing of multiple wall-shear stress sensors to investigate the influence of the sensor size on the fluctuating wall-shear stress measurement.

8.3 Future Recommendations

The optical MEMS wall-shear stress sensors developed in this study shows excellent promise for the instantaneous wall-shear stress measurement within turbulent boundary-layer flows. However, additional design, development and experimental investigations are required to enhance the further develop them towards reliable turbulent flow measurement.

8.3.1 Sensor development

The size of the floating element on current sensors is limited by the Moiré fringe pattern area, as well as the resolution of the optical setup. To further reduce the size of the optical MEMS wall-shear stress sensors, it is recommended that a secondary optical

magnification technique be implemented to further amplify the Moiré fringe pattern displacement, providing the potential for smaller floating element sizes.

Using the serpentine micro-springs provides the opportunity to develop arrays of MEMS wall-shear stress sensors for the measurements over an area. Hence, it is recommended that a system of MEMS wall-shear stress arrays to be developed using this micro-spring configuration.

The sensors developed in this study were designed for the measurements in air flows. Additional design and development are also necessary for liquid measurements to take into the account the effects of the surface tension and higher fluid viscosity.

8.3.2 Microfabrication

Challenges in the microfabrication process resulted in relatively low number of successful devices. The first point of damage during the microfabrication was linked to the silicon undercutting that occurred during the DRIE of the sensor structure, which broke the silicon off the BOX layer during the photoresist. This undercutting effect can be reduced in the mask design process, by designing the gap sizes exist on the device to be identical. The second point of the damage occurred during the handle layer wet etching, where the surface tension effects damaged devices on removal from the KOH solution due to a thin membrane of oxide. Two solutions are recommended to mitigate this issue:

1. Using dry etching techniques such as XeF_2 and VHF to remove the handle and BOX layers on the SOI wafer and release the structures.
2. DRIE of the silicon to pattern the micro-structure (Step 11 in Figure 4.2) can be carried out after removing the handle and the BOX layer (Step 24 in Figure 4.2). Front to back alignment (FTBA) can be used to align the floating element with the Moiré fringe pattern, that is formed in the previous steps. For the the flow measurement in liquid flows, additional coating may be required (i.e. waterproof coating), which should be taken into account in the microfabrication process.

Using the recommend techniques can eliminate the undercutting and surface tension effects.

8.3.3 Sensor packaging and sensor control unit

One of the drawbacks of the optical MEMS sensors is the relatively large sensor packaging due to the size of the optical components. In this study, two generations of the sensor packages were designed and prototyped. Although the second generation sensor packaging was a substantial refinement compared to the first generation, supplementary improvement is suggested towards a smaller sensor packaging, via reducing the size of the optical components using machining techniques. Furthermore, the sensor packaging body can be manufactured using Aluminium/steel using machining techniques.

In addition to the sensor packaging body, the size of the sensor control unit can be reduced by using surface mounted electronic components. Further improvement is recommended in the sensor electronics to reduce the noise floor of the sensors.

8.3.4 Sensor characterisation

The calibration of the MEMS wall-shear stress sensors were carried out in a air flow for a wall-shear stress range of 0 to 5.32 Pa. The maximum achievable wall-shear stress in the calibration rig was limited by the operational range of the pressure transducer. In order to additionally investigate the performance of the sensors in higher wall-shear stress, a pressure transducer with a larger operational range can be used, which can be used to quantify the upper limit of the sensor dynamic range. The effect of the pressure gradient on the measurement of the wall-shear stress sensors also requires further experimental investigations.

The result of the MEMS sensor wind tunnel testing show excellent potential for these devices to be employed for the turbulent wall-shear stress measurements. However, additional experimental investigation is recommended to further explore the effect of the sensors geometry on its measurements. This can be implemented by using multiple replicas from an specific sensor type over a range of Reynolds numbers. In order to detect negative wall-shear stress values due to the rare flow reversal events, a long sampling period at higher Reynolds numbers ($Re_\theta > 4000$) is suggested. LDV measurements at $y^+ < 3$ was challenging due to the reflection of the sensor dies. Hence, it is recommended that an anti-reflective coating to be added to the surface of the sensor during the microfabriation process.

References

- Ackerman, J. D., Wong, L., Ethier, C. R., Allen, D. G. and Spelt, J. K. (1994), 'Preston-static tubes for the measurement of wall shear stress'.
- Adams, T. M. and Layton, R. A. (2014), *Introductory MEMS*, Springer.
- Agrawal, R., Whalley, R. D., Ng, H. C.-H., Dennis, D. J. and Poole, R. J. (2019), 'Minimizing recalibration using a non-linear regression technique for thermal anemometry', *Experiments in Fluids* **60**(7), 116.
- Alfredsson, P. H., Johansson, A. V., Haritonidis, J. H. and Eckelmann, H. (1988), 'The fluctuating wall-shear stress and the velocity field in the viscous sublayer', *The Physics of fluids* **31**(5), 1026–1033.
- Amidror, I. (2009), *The Theory of the Moiré Phenomenon: Volume I: Periodic Layers*, Vol. 38, Springer Science & Business Media.
- Ayaz, U., Ioppolo, T. and Ötügen, M. (2011), 'Wall shear stress sensor based on the optical resonances of dielectric microspheres', *Measurement science and technology* **22**(7), 075203.
- Bai, H., Li, W. J., Chow, W. and Zhou, Y. (2010), 'A carbon nanotube sensor for wall shear stress measurement', *Experiments in fluids* **48**(4), 679–691.
- Bailey, S. C., Kunkel, G. J., Hultmark, M., Vallikivi, M., Hill, J. P., Meyer, K. A., Tsay, C., Arnold, C. B. and Smits, A. J. (2010), 'Turbulence measurements using a nanoscale thermal anemometry probe', *Journal of Fluid Mechanics* **663**, 160.
- Bailly, C. and Comte-Bellot, G. (2015), *Turbulence*, Springer.
- Barlian, A. A. (2009), *Microfabricated piezoresistive shear stress sensors for underwater applications*, Stanford University.
- Barlian, A. A., Park, S.-J., Mukundan, V. and Pruitt, B. L. (2007), 'Design and characterization of microfabricated piezoresistive floating element-based shear stress sensors', *Sensors and Actuators A: Physical* **134**(1), 77–87.
- Barlian, A., Narain, R., Li, J., Quance, C., Ho, A., Mukundan, V. and Pruitt, B. (2006), 'Piezoresistive mems underwater shear stress sensors', in '19th IEEE International Conference on Micro Electro Mechanical Systems', IEEE, pp. 626–629.

References

- Barnard, C., Meloy, J. and Sheplak, M. (2016), An instrumentation grade wall shear stress sensing system, *in* '2016 IEEE SENSORS', IEEE, pp. 1–3.
- Barnard, C., Mills, D., Meloy, J. and Sheplak, M. (2016), Development of a hydraulically smooth wall shear stress sensor utilizing through silicon vias, *in* 'Solid State Sensors, Actuators, and Microsystems Workshop', pp. 234–237.
- Beer, F. P., Johnston Jr, E. R., DeWolf, J. T., DeWolf, J. T. and Oler, J. W. (2006), 'Mechanics of'.
- Bellhouse, B. J. and Schultz, D. L. (1968), 'The measurement of fluctuating skin friction in air with heated thin-film gauges', *Journal of Fluid Mechanics* **32**(4), 675–680.
- Borisenkov, Y., Gulitski, G., Kholmyansky, M., Krylov, S., Liberzon, A. and Tsinober, A. (2015), 'Micro-machined super-miniature hot-film multi-array probe for field experiments with sub-kolmogorov resolution', *Journal of Turbulence* **16**(6), 525–539.
- Breuer, K. (2000), MemS sensors for aerodynamic measurements-the good, the bad (and the ugly), *in* '38th Aerospace Sciences Meeting and Exhibit', p. 251.
- Breuer, K. S., Bayt, R. L. and Nayaar, A. (1999), 'Measurement of shear stress and temperature using memS fabricated sensors', *Proceedings of ASME MEMS; ASME: New York, NY, USA*.
- Brison, J. F., Charnay, G. and Comte-Bellot, G. (1979), 'Calculation of heat transfer between hot film and substrate on the basis of a two-dimensional model - Prediction of the dynamic response of typical probes', *International Journal of Heat and Mass Transfer* **22**, 111–119.
- Brücker, C., Bauer, D. and Chaves, H. (2007), 'Dynamic response of micro-pillar sensors measuring fluctuating wall-shear-stress', *Experiments in fluids* **42**(5), 737–749.
- Brücker, C., Spatz, J. and Schröder, W. (2005), 'Feasibility study of wall shear stress imaging using microstructured surfaces with flexible micropillars', *Experiments in fluids* **39**(2), 464–474.
- Bruun, H. H. (1996), 'Hot-wire anemometry: principles and signal analysis'.
- Buder, U., Petz, R., Kittel, M., Nitsche, W. and Obermeier, E. (2008), 'Aeromems polyimide based wall double hot-wire sensors for flow separation detection', *Sensors and Actuators A: Physical* **142**(1), 130–137.
- Bushnell, D. M. and Hefner, J. N. (1990), *Viscous drag reduction in boundary layers*, American Institute of Aeronautics and Astronautics.
- Castro, I. and Dianat, M. (1990), 'Pulsed wire velocity anemometry near walls', *Experiments in fluids* **8**(6), 343–352.

- Chandrasekharan, V., Sells, J., Meloy, J., Arnold, D. P. and Sheplak, M. (2011), 'A microscale differential capacitive direct wall-shear-stress sensor', *Journal of microelectromechanical systems* **20**(3), 622–635.
- Chandrasekharan, V., Sells, J., Meloy, J., Arnold, D. and Sheplak, M. (2009), A metal-on-silicon differential capacitive shear stress sensor, in 'TRANSDUCERS 2009-2009 International Solid-State Sensors, Actuators and Microsystems Conference', IEEE, pp. 1537–1540.
- Chen, J., Fan, Z., Zou, J., Engel, J. and Liu, C. (2003), 'Two-dimensional micromachined flow sensor array for fluid mechanics studies', *Journal of Aerospace engineering* **16**(2), 85–97.
- Chen, T.-A. (2012), *A micromachined floating element shear stress sensor using Moiré transduction for harsh environments*, University of Florida.
- Chen, T.-A., Mills, D., Chandrasekharan, V. and Sheplak, M. (2014), A miniaturized optical package for wall shear stress measurements in harsh environments, in 'Sensors for Extreme Harsh Environments', Vol. 9113, International Society for Optics and Photonics, p. 91130G.
- Chen, T.-A., Mills, D., Chandrasekharan, V., Zmuda, H. and Sheplak, M. (2010), Optical miniaturization of a mems-based floating element shear stress sensor with moiré amplification, in '48th AIAA Aerospace Sciences Meeting Including the New Horizons Forum and Aerospace Exposition', p. 498.
- Chew, Y. T., Khoo, B. C., Lim, C. P. and Teo, C. J. (1998), 'Dynamic response of a hot-wire anemometer. part II: A flush-mounted hot-wire and hot-film probes for wall shear stress measurements', *Measurement Science and Technology* **9**(5), 764–778.
- Coleman, H. W. and Steele, W. G. (2018), *Experimentation, validation, and uncertainty analysis for engineers*, John Wiley & Sons.
- Comte-Bellot, G. (1976), 'Hot-wire anemometry', *Annual Review of Fluid Mechanics* **8**(1), 209–231.
- Davidson, P. A. (2015), *Turbulence: an introduction for scientists and engineers*, Oxford university press.
- De Luca, A., Haneef, I., Coull, J. D., Ali, S. Z., Falco, C. and Udrea, F. (2015), 'High-sensitivity single thermopile soi cmos mems thermal wall shear stress sensor', *IEEE Sensors Journal* **15**(10), 5561–5568.
- Diaz-Daniel, C., Laizet, S. and Vassilicos, J. C. (2017), 'Wall shear stress fluctuations: Mixed scaling and their effects on velocity fluctuations in a turbulent boundary layer', *Physics of Fluids* **29**(5), 055102.

References

- Dijkstra, M., Van Baar, J., Wiegerink, R. J., Lammerink, T. S., De Boer, J. and Krijnen, G. J. (2005), 'Artificial sensory hairs based on the flow sensitive receptor hairs of crickets', *Journal of micromechanics and microengineering* **15**(7), S132.
- Ding, G.-H., Ma, B.-H., Deng, J.-J., Yuan, W.-Z. and Liu, K. (2018), 'Accurate measurements of wall shear stress on a plate with elliptic leading edge', *Sensors* **18**(8), 2682.
- Driver, D. (2003), 'Application of oil-film interferometry skin-friction measurement to large wind tunnels', *Experiments in Fluids* **34**(6), 717–725.
- Driver, D. M. (1998), 'Application of oil film interferometry skin-friction to large wind tunnels'.
- Dunn, P. F. and Davis, M. P. (2017), *Measurement and data analysis for engineering and science*, CRC press.
- Elsinga, G. and Westerweel, J. (2012), 'Tomographic-piv measurement of the flow around a zigzag boundary layer trip', *Experiments in fluids* **52**(4), 865–876.
- Elwenspoek, M. (1999), Thermal flow micro sensors, in 'CAS '99 Proceedings. 1999 International Semiconductor Conference (Cat. No.99TH8389)', Vol. 2, pp. 423–435 vol.2.
- Elwenspoek, M., Wiegerink, R. and Wiegerink, R. J. (2001), *Mechanical microsensors*, Springer Science & Business Media.
- Fan, Z., Chen, J., Zou, J., Bullen, D., Liu, C. and Delcomyn, F. (2002), 'Design and fabrication of artificial lateral line flow sensors', *Journal of micromechanics and microengineering* **12**(5), 655.
- Fedder, G. K. (1994), Simulation of microelectromechanical systems, PhD thesis, University of California, Berkeley.
- Fernholz, H., Janke, G., Schober, M., Wagner, P. and Warnack, D. (1996), 'New developments and applications of skin-friction measuring techniques', *Measurement Science and Technology* **7**(10), 1396.
- Fingerson, L. and Freymuth, P. (1977), *Thermal anemometers*, Taylor and Francis, Reading, Massachusetts.
- Fourchette, D., Modarress, D., Wilson, D., Koochesfahani, M. and Gharib, M. (2003), An optical mems-based shear stress sensor for high reynolds number applications, in '41st Aerospace Sciences Meeting and Exhibit', p. 742.
- Fraden, J. (2010), *Handbook of modern sensors*, Vol. 3, Springer.
- Gad-el Hak, M. (2005), *MEMS: introduction and fundamentals*, CRC press.

- Gerhart, P. M., Gerhart, A. L. and Hochstein, J. I. (2016), *Munson, Young and Okiishi's Fundamentals of Fluid Mechanics*, John Wiley & Sons.
- Ghouila-Houri, C., Gerbedoen, J.-C., Claudel, J., Gallas, Q., Garnier, E., Merlen, A., Viard, R., Talbi, A. and Pernod, P. (2016), 'Wall shear stress and flow direction thermal mems sensor for separation detection and flow control applications', *Procedia Engineering* **168**, 774–777.
- Ghouila-Houri, C., Talbi, A., Viard, R., Gallas, Q., Garnier, E., Molton, P., Delva, J., Merlen, A. and Pernod, P. (2020), 'Mems high temperature gradient sensor for skin friction measurements in highly turbulent flows', *IEEE Sensors Journal*.
- Gnanamanickam, E., Nottebrock, B., Große, S., Sullivan, J. and Schröder, W. (2013), 'Measurement of turbulent wall shear-stress using micro-pillars', *Measurement Science and Technology* **24**(12), 124002.
- Gnanamanickam, E. P. and Sullivan, J. P. (2012), 'Manufacture of high aspect ratio micro-pillar wall shear stress sensor arrays', *Journal of Micromechanics and Micro-engineering* **22**(12), 125015.
- Grosse, S., Nottebrock, B. and Schroeder, W. (2010), Measuring the two-dimensional, two-directional temporal wall-shear stress distribution with the micro-pillar shear-stress sensor mps³, in '48th AIAA Aerospace Sciences Meeting Including the New Horizons Forum and Aerospace Exposition', p. 495.
- Große, S. and Schröder, W. (2007), 'Mean wall-shear stress measurements using the micro-pillar shear-stress sensor mps³', *Measurement Science and Technology* **19**(1), 015403.
- Große, S., Soodt, T. and Schröder, W. (2008), 'Dynamic calibration technique for the micro-pillar shear-stress sensor mps³', *Measurement Science and Technology* **19**(10), 105201.
- Gubian, P.-A., Stoker, J., Medvescek, J., Mydlarski, L. and Baliga, B. R. (2019), 'Evolution of wall shear stress with reynolds number in fully developed turbulent channel flow experiments', *Physical Review Fluids* **4**(7), 074606.
- Gulitski, G., Kholmyansky, M., Kinzelbach, W., Lüthi, B., Tsinober, A. and Yorish, S. (2007a), 'Velocity and temperature derivatives in high-reynolds-number turbulent flows in the atmospheric surface layer. part 1. facilities, methods and some general results', *Journal of Fluid Mechanics* **589**, 57–81.
- Gulitski, G., Kholmyansky, M., Kinzelbach, W., Lüthi, B., Tsinober, A. and Yorish, S. (2007b), 'Velocity and temperature derivatives in high-reynolds-number turbulent flows in the atmospheric surface layer. part 2. accelerations and related matters', *Journal of Fluid Mechanics* **589**, 83–102.

References

- Haneef, I., Ali, S. Z., Udrea, F., Coull, J. D. and Hodson, H. P. (2007), High performance soi-cmos wall shear stress sensors, *in* 'SENSORS, 2007 IEEE', IEEE, pp. 1060–1064.
- Haritonidis, Joseph II. (1988), The Measurement of Wall Shear Stress, *in* MOHAMED GAD-EL-HAK, ed., 'Advances in fluid mechanics measurements', Vol. 45, Springer, Berlin, pp. 229–261.
- Higuchi, H. (1983), A miniature, directional surface-fence gage for three-dimensional turbulent boundary layer measurements, *in* '16th Fluid and Plasmadynamics Conference', p. 1722.
- Higuchi, H. (1985), 'A miniature, directional surface-fence gage', *AIAA journal* **23**(8), 1195–1196.
- Horowitz, S., Chen, T.-A., Chandrasekaran, V., Nishida, T., Cattafesta, L., Sheplak, M. and Tedjojuwono, K. (2004), A micromachined geometric moiré interferometric floating-element shear stress sensor, *in* '42nd AIAA Aerospace Sciences Meeting and Exhibit', p. 1042.
- Huang, J.-B., Ho, C.-M., Tung, S., Liu, C. and Tai, Y.-C. (1995), 'Micro thermal shear stress sensor with and without cavity underneath', *IEEE Instrumentation/Masurement Tech Conf IMTC'95*.
- Huang, J.-B., Tung, S., Ho, C.-M., Liu, C. and Tai, Y.-C. (1996), 'Improved micro thermal shear-stress sensor', *IEEE transactions on Instrumentation and Measurement* **45**(2), 570–574.
- Hughes, I. and Hase, T. (2010), *Measurements and their uncertainties: a practical guide to modern error analysis*, Oxford University Press.
- Hultmark, M., Vallikivi, M., Bailey, S. C. C. and Smits, A. (2012), 'Turbulent pipe flow at extreme reynolds numbers', *Physical review letters* **108**(9), 094501.
- Hutchins, N. and Choi, K.-S. (2002), 'Accurate measurements of local skin friction coefficient using hot-wire anemometry', *Progress in Aerospace Sciences* **38**(4-5), 421–446.
- Hutchins, N., Nickels, T. B., Marusic, I. and Chong, M. (2009), 'Hot-wire spatial resolution issues in wall-bounded turbulence', *Journal of Fluid Mechanics* **635**, 103.
- Hyman, D., Pan, T., Reshotko, E. and Mehregany, M. (1999), 'Microfabricated shear stress sensors, part 2: Testing and calibration', *AIAA journal* **37**(1), 73–78.
- Ioppolo, T., Ayaz, U., Otugen, V. and Sheverev, V. (2008), A micro-optical wall shear stress sensor concept based on whispering gallery mode resonators, *in* '46th AIAA Aerospace Sciences Meeting and Exhibit', p. 273.

- Ito, Y., Higuchi, T. and Takahashi, K. (2010), 'Submicroscale flow sensor employing suspended hot film with carbon nanotube fins', *Journal of Thermal Science and Technology* **5**(1), 51–60.
- Katrtsis, D., Kaiktsis, L., Chaniotis, A., Pantos, J., Efstathopoulos, E. P. and Marmarelis, V. (2007), 'Wall shear stress: theoretical considerations and methods of measurement', *Progress in cardiovascular diseases* **49**(5), 307–329.
- Khoo, B. C., Chew, Y. T., Lim, C. P. and Teo, C. J. (1998), 'Dynamic response of a hot-wire anemometer. part i: A marginally elevated hot-wire probe for near-wall velocity measurements', *Measurement Science and Technology* **9**(5), 751–763.
- Kline, S. J. (1953), 'Describing uncertainty in single sample experiments', *Mech. Engineering* **75**, 3–8.
- Kline, S. J., Reynolds, W. C., Schraub, F. and Runstadler, P. (1967), 'The structure of turbulent boundary layers', *Journal of Fluid Mechanics* **30**(4), 741–773.
- Kuo, J. T., Yu, L. and Meng, E. (2012), 'Micromachined thermal flow sensors—a review', *Micromachines* **3**(3), 550–573.
- Lenaers, P., Li, Q., Brethouwer, G., Schlatter, P. and Örlü, R. (2012), 'Rare backflow and extreme wall-normal velocity fluctuations in near-wall turbulence', *Physics of fluids* **24**(3), 035110.
- Li, J., Chen, J. and Liu, C. (2000), Micromachined biomimetic sensor using modular artificial hair cells, in 'Proceedings of Nanospace Conference'.
- Li, Y., Chandrasekharan, V., Bertolucci, B., Nishida, T., Cattafesta, L. and Sheplak, M. (2008), A mems shear stress sensor for turbulence measurements, in '46th AIAA Aerospace Sciences Meeting and Exhibit', p. 269.
- Li, Y., Papila, M., Nishida, T., Cattafesta, L. and Sheplak, M. (2006), Modeling and optimization of a side-implanted piezoresistive shear-stress sensor, in 'Smart Structures and Materials 2006: Sensors and Smart Structures Technologies for Civil, Mechanical, and Aerospace Systems', Vol. 6174, International Society for Optics and Photonics, p. 617409.
- Li, Y.-S. J., Haga, J. H. and Chien, S. (2005), 'Molecular basis of the effects of shear stress on vascular endothelial cells', *Journal of biomechanics* **38**(10), 1949–1971.
- Ligrani, P. and Bradshaw, P. (1987), 'Subminiature hot-wire sensors: development and use', *Journal of Physics E: Scientific Instruments* **20**(3), 323.
- Lin, Q., Jiang, F., Wang, X.-Q., Xu, Y., Han, Z., Tai, Y.-C., Lew, J. and Ho, C.-M. (2004), 'Experiments and simulations of mems thermal sensors for wall shear-stress measurements in aerodynamic control applications', *Journal of Micromechanics and Microengineering* **14**(12), 1640.

References

- Liu, C., Huang, J.-B., Zhu, Z., Jiang, F., Tung, S., Tai, Y.-C. and Ho, C.-M. (1999), 'A micromachined flow shear-stress sensor based on thermal transfer principles', *Journal of Microelectromechanical Systems* **8**(1), 90–99.
- Lobontiu, N. (2007), *Dynamics of microelectromechanical systems*, Vol. 17, Springer Science & Business Media.
- Löfdahl, L., Chernoray, V., Haasl, S., Stemme, G. and Sen, M. (2003), 'Characteristics of a hot-wire microsensor for time-dependent wall shear stress measurements', *Experiments in Fluids* **35**(3), 240–251.
- Löfdahl, L. and Gad-el Hak, M. (1999a), 'MEMS applications in turbulence and flow control', *Progress in Aerospace Sciences* **35**(2), 101–203.
- Löfdahl, L. and Gad-el Hak, M. (1999b), 'MEMS-based pressure and shear stress sensors for turbulent flows', *Measurement Science and Technology* **10**(8), 665–686.
- Lv, H., Jiang, C., Xiang, Z., Ma, B., Deng, J. and Yuan, W. (2013), 'Design of a micro floating element shear stress sensor', *Flow Measurement and Instrumentation* **30**, 66–74.
- Ma, B. H. and Ma, C. Y. (2016), 'A mems surface fence for wall shear stress measurement with high sensitivity', *Microsystem Technologies* **22**(2), 239–246.
- McCarthy, M., Frechette, L. G., Modi, V. and Tiliakos, N. (2003), Initial development of a mems wall shear stress sensor for propulsion applications, in 'Propulsion measurement sensor development workshop NASA marshall space flight center, Alabama'.
- McLaughlin, D. and Tiederman, W. (1973), 'Biasing correction for individual realization of laser anemometer measurements in turbulent flows', *The Physics of Fluids* **16**(12), 2082–2088.
- Meloy, J., Griffin, J., Cattafesta, L., Sells, J., Sheplak, M. and Chandrasekharan, V. (2011), Experimental verification of a mems based skin friction sensor for quantitative wall shear stress measurement, in '41st AIAA Fluid Dynamics Conference and Exhibit', p. 3995.
- Meloy, J., Sells, J., Chandrasekharan, V., Griffin, J., Cattafesta, L., Arnold, D. and Sheplak, M. (2012), Experimental verification of a capacitive shear stress sensor for low-speed wind tunnel applications, in 'Solid-State Sensor, Actuator, and Microsystems Workshop', pp. 303–306.
- Mills, D. A. (2014), A sapphire MEMS-based optical shear stress sensor for high-temperature applications, PhD thesis, University of Florida.
- Mills, D. A., Barnard, C. and Sheplak, M. (2017), Characterization of a hydraulically smooth wall shear stress sensor for low-speed wind tunnel applications, in '55th AIAA Aerospace Sciences Meeting', p. 0478.

- Mills, D. A., Blood, D. and Sheplak, M. (2016), Characterization of a sapphire optical wall shear stress sensor for high-temperature applications, *in* '54th AIAA Aerospace Sciences Meeting', p. 2016.
- Mills, D. A., Chen, T.-A. and Sheplak, M. (2015), Characterization of an optical moiré wall shear stress sensor for harsh environments, *in* '53rd AIAA Aerospace Sciences Meeting', p. 1917.
- Mills, D. A., Patterson, W. C., Keane, C. and Sheplak, M. (2018), Characterization of a fully-differential capacitive wall shear stress sensor for low-speed wind tunnels, *in* '2018 AIAA Aerospace Sciences Meeting', p. 0301.
- Mills, D. A., Patterson, W., Freidkes, B. and Sheplak, M. (2021), Temperature sensitivity reduction of a capacitive wall shear stress sensor system for low-speed wind tunnels, *in* 'AIAA Scitech 2021 Forum', p. 0022.
- Modarress, D., Fourquette, D., Taugwalder, F., Koochesfahani, M., Gharib, M. and Wilson, D. W. (2000), Diffractive optic fluid shear stress sensor, *in* 'Diffractive Optics and Micro-Optics Topical Meeting', p. 2.
- Monson, D. (1983), 'Instrument measures airflow friction without contact'.
- Moser, R. D., Kim, J. and Mansour, N. N. (1999), 'Direct numerical simulation of turbulent channel flow up to $Re_{\tau} = 590$ ', *Physics of fluids* **11**(4), 943–945.
- Naqwi, A. A. and Reynolds, W. C. (1987), Dual cylindrical wave laser-doppler method for measurement of skin friction in fluid flow., Technical report, STANFORD UNIV CA DEPT OF MECHANICAL ENGINEERING.
- Naughton, J., Robinson, J. and Durgesh, V. (2003), Oil-film interferometry measurement of skin friction-analysis summary and description of matlab program, *in* '20th International Congress on Instrumentation in Aerospace Simulation Facilities, 2003. ICIASF'03.', IEEE, pp. 169–178.
- Naughton, J. W. and Sheplak, M. (2002), 'Modern developments in shear-stress measurement', *Progress in Aerospace Sciences* **38**(6-7), 515–570.
- Ng, K.-Y., Shajii, J. and Schmidt, M. (1991), A liquid shear-stress sensor fabricated using wafer bonding technology, *in* 'TRANSDUCERS'91: 1991 International Conference on Solid-State Sensors and Actuators. Digest of Technical Papers', IEEE, pp. 931–934.
- Obi, S., Inoue, K., Furukawa, T. and Masuda, S. (1996), 'Experimental study on the statistics of wall shear stress in turbulent channel flows', *International journal of heat and fluid flow* **17**(3), 187–192.
- Örlü, R. and Schlatter, P. (2011), 'On the fluctuating wall-shear stress in zero pressure-gradient turbulent boundary layer flows', *Physics of fluids* **23**(2), 021704.

References

- Österlund, J. M. (1999), Experimental studies of zero pressure-gradient turbulent boundary layer flow, PhD thesis, Mekanik.
- Ou, Y., Qu, F., Wang, G., Nie, M., Li, Z., Ou, W. and Xie, C. (2016), 'A mems thermal shear stress sensor produced by a combination of substrate-free structures with anodic bonding technology', *Applied Physics Letters* **109**(2), 023512.
- Ozaki, Y., Ohyama, T., Yasuda, T. and Shimoyama, I. (2000), An air flow sensor modeled on wind receptor hairs of insects, in 'Proceedings IEEE Thirteenth Annual International Conference on Micro Electro Mechanical Systems (Cat. No. 00CH36308)', IEEE, pp. 531–536.
- Padmanabhan, A., Goldberg, H., Breuer, K. D. and Schmidt, M. A. (1996), 'A wafer-bonded floating-element shear stress microsensors with optical position sensing by photodiodes', *Journal of Microelectromechanical Systems* **5**(4), 307–315.
- Padmanabhan, A., Sheplak, M., Breuer, K. S. and Schmidt, M. A. (1997), Micromachined sensors for static and dynamic shear-stress measurements in aerodynamic flows, in 'Proceedings of International Solid State Sensors and Actuators Conference (Transducers '97)', Vol. 1, pp. 137–140 vol.1.
- Pan, T., Hyman, D., Mehregany, M., Reshotko, E. and Garverick, S. (1999), 'Microfabricated shear stress sensors, part 1: design and fabrication', *AIAA journal* **37**(1), 66–72.
- Patel, M. P., Reshotko, E. and Hyman, D. (2002), 'Microfabricated shear-stress sensors, part 3: Reducing calibration uncertainty', *AIAA journal* **40**(8), 1582–1588.
- Patel, V. (1965), 'Calibration of the preston tube and limitations on its use in pressure gradients', *Journal of Fluid Mechanics* **23**(1), 185–208.
- Perry, A. (1982), *Hot-wire Anemometry*, Oxford science publications, Clarendon Press.
URL: <https://books.google.co.uk/books?id=PJZRAAAAMAAJ>
- Preston, J. (1954), 'The determination of turbulent skin friction by means of pitot tubes', *The Aeronautical Journal* **58**(518), 109–121.
- Rabiner, L. R. and Gold, B. (1975), 'Theory and application of digital signal processing', *Englewood Cliffs: Prentice-Hall*.
- Romain, V., Abdelkrim, T., Philippe, P., Alain, M. and Vladimir, P. (2013), 'Miniaturised sensor comprising a heating element, and associated production method', *FR2977886 (A1)* pp. 01–18.
- Saleh, B. E. and Teich, M. C. (2019), *Fundamentals of photonics*, John Wiley & sons.
- Savelsberg, R., Schiffer, M., Obermeier, E. and Castro, I. P. (2012), 'Calibration and use of a mems surface fence for wall shear stress measurements in turbulent flows', *Experiments in fluids* **53**(2), 489–498.

- Schiffer, M., Obermeier, E., Grewe, F., Ebner, A. and Fernholz, H. (2006), Aeromems surface fence for wall shear stress measurements in turbulent flows, in '44th AIAA Aerospace Sciences Meeting and Exhibit', p. 645.
- Schlatter, P. and Örlü, R. (2010), 'Assessment of direct numerical simulation data of turbulent boundary layers', *Journal of Fluid Mechanics* **659**, 116–126.
- Schlichting, H. and Gersten, K. (2016), *Boundary-layer theory*, Springer.
- Schmidt, M. A. (1988), Microsensors for the measurement of shear forces in turbulent boundary layers, PhD thesis, Massachusetts Institute of Technology.
- Schmidt, M. A., Howe, R. T., Senturia, S. D. and Haritonidis, J. H. (1988), 'Design and calibration of a microfabricated floating-element shear-stress sensor', *IEEE Transactions on Electron Devices* **35**(6), 750–757.
- Schober, M., Obermeier, E., Pirskawetz, S. and Fernholz, H.-H. (2004), 'A mems skin-friction sensor for time resolved measurements in separated flows', *Experiments in fluids* **36**(4), 593–599.
- Sedra, A. S., Sedra, D. E. A. S., Smith, K. C. et al. (1998), *Microelectronic circuits*, New York: Oxford University Press.
- Sells, J., Chandrasekharan, V., Meloy, J., Sheplak, M., Zmuda, H. and Arnold, D. P. (2011), Microfabricated silicon-on-pyrex passive wireless wall shear stress sensor, in 'SENSORS, 2011 IEEE', IEEE, pp. 77–80.
- Sells, J., Chandrasekharan, V., Zmuda, H., Sheplak, M., Zmuda, H. and Arnold, D. P. (2010), Passive wireless direct shear stress measurement, in 'Solid-State Sensors, Actuators, and Microsystems Workshop Hilton Head Island, South Carolina', pp. 368–371.
- Settles, G. (1986), Recent skin friction techniques for compressible flows, in '4th joint fluid mechanics, plasma dynamics and lasers conference', p. 1099.
- Shajii, J., Ng, K.-Y. and Schmidt, M. A. (1992), 'A microfabricated floating-element shear stress sensor using wafer-bonding technology', *Journal of Microelectromechanical Systems* **1**(2), 89–94.
- Shanks, K., Senthilarasu, S. and Mallick, T. K. (2016), 'Optics for concentrating photovoltaics: Trends, limits and opportunities for materials and design', *Renewable and Sustainable Energy Reviews* **60**, 394–407.
- Sheplak, M., Cattafesta, L., Nishida, T. and McGinley, C. (2004), MemS shear stress sensors: Promise and progress, in '24th AIAA aerodynamic measurement technology and ground testing conference', p. 2606.

References

- Sheplak, M., Chandrasekaran, V., Cain, A., Nishida, T. and Cattafesta III, L. N. (2002), 'Characterization of a silicon-micromachined thermal shear-stress sensor', *AIAA journal* **40**(6), 1099–1104.
- Singiresu, S. R. et al. (1995), *Mechanical vibrations*, Addison Wesley Boston, MA.
- Sinha, N., Ma, J. and Yeow, J. T. (2006), 'Carbon nanotube-based sensors', *Journal of nanoscience and nanotechnology* **6**(3), 573–590.
- Spagnolo, G. S. and Ambrosini, D. (2000), 'Talbot effect application: measurement of distance with a fourier-transform method', *Measurement Science and Technology* **11**(1), 77.
- Squire, L. C. (1961), 'The motion of a thin oil sheet under the steady boundary layer on a body', *Journal of Fluid Mechanics* **11**(2), 161–179.
- Stanton, T. E., Marshall, D. and Bryant, C. N. (1920), 'On the conditions at the boundary of a fluid in turbulent motion', *Proceedings of the Royal Society of London. Series A, Containing Papers of a Mathematical and Physical Character* **97**(687), 413–434.
- Stevenson, J. and Jordan, J. (1989), 'Metrological gratings and moire fringe detection methods for displacement transducers', *IEE Proceedings A-Physical Science, Measurement and Instrumentation, Management and Education* **136**(5), 243–253.
- Sturzebecher, D., Anders, S. and Nitsche, W. (2001), 'The surface hot wire as a means of measuring mean and fluctuating wall shear stress', *Experiments in Fluids* **31**(3), 294–301.
- Sumer, B., Arnskov, M., Christiansen, N. and Jørgensen, F. (1993), 'Two-component hot-film probe for measurements of wall shear stress', *Experiments in Fluids* **15**(6), 380–384.
- Tanner, L. and Blows, L. (1976), 'A study of the motion of oil films on surfaces in air flow, with application to the measurement of skin friction', *Journal of Physics E: Scientific Instruments* **9**(3), 194.
- Tanner, L. H. (1977), 'A skin friction meter, using the viscosity balance principle, suitable for use with flat or curved metal surfaces (based on thickness measurement)', *Journal of Physics E: Scientific Instruments* **10**(3), 278–284.
- Tanner, L. H. and Kulkarni, V. G. (1976), 'The viscosity balance method of skin friction measurement: further developments including applications to three-dimensional flow', *Journal of Physics E: Scientific Instruments* **9**(12), 1114–1121.
- Tennekes, H. and Lumley, J. L. (2018), *A first course in turbulence*, MIT press.

- Tiliakos, N., Papadopoulos, G., Modi, V., O'Grady, A., McCarthy, M., Fréchet, L., Desbiens, J. and Larger, R. (2006), 'Mems shear stress sensor for hypersonic aero-propulsion test and evaluation', *2006 Annual ITEA Technology Review*.
- Tiliakos, N., Papadopoulos, G., O'Grady, A. M., Modi, V., Larger, R. and Fréchet, L. G. (2007), A mems-based shear stress sensor for high temperature applications, in 'Fluids Engineering Division Summer Meeting', Vol. 42894, pp. 1477–1478.
- Tseng, F.-G. and Lin, C.-J. (2003), 'Polymer mems-based fabry-perot shear stress sensor', *IEEE Sensors Journal* **3**(6), 812–817.
- Tung, S., Rokadia, H. and Li, W. J. (2007a), 'A micro shear stress sensor based on laterally aligned carbon nanotubes', *Sensors and Actuators A: Physical* **133**(2), 431–438.
- Tung, S., Rokadia, H. and Li, W. J. (2007b), 'A micro shear stress sensor based on laterally aligned carbon nanotubes', *Sensors and Actuators A: Physical* **133**(2), 431 – 438. Selected Papers from the 9th International Conference on Materials for Advanced Technologies.
- Turan, O., Azad, R. and Atamanchuk, T. (1987), 'Wall effect on the hot-wire signal without flow', *Journal of Physics E: Scientific Instruments* **20**(10), 1278.
- Van Oudheusden, B. (1992), 'Silicon thermal flow sensors', *Sensors and Actuators A: Physical* **30**(1-2), 5–26.
- Viard, R., Talbi, A., Merlen, A., Pernod, P., Frankiewicz, C., Gerbedoen, J. and Preobrazhensky, V. (2013), 'A robust thermal microstructure for mass flow rate measurement in steady and unsteady flows', *Journal of Micromechanics and Microengineering* **23**(6), 065016.
- von Papen, T., Buder, U., Ngo, H. D. and Obermeier, E. (2004), 'A second generation mems surface fence sensor for high resolution wall shear stress measurement', *Sensors and Actuators A: Physical* **113**(2), 151–155.
- Von Papen, T., Steffes, H., Ngo, H. and Obermeier, E. (2002), 'A micro surface fence probe for the application in flow reversal areas', *Sensors and Actuators A: Physical* **97**, 264–270.
- Weiss, J., EmmanuelJondeau, Giani, A., Charlot, B. and Combette, P. (2017b), 'Static and dynamic calibration of a mems calorimetric shear-stress sensor', *Sensors and Actuators A: Physical* **265**, 211 – 216.
- Weiss, J., Schwaab, Q., Boucetta, Y., Giani, A., Guigue, C., Combette, P. and Charlot, B. (2017), 'Simulation and testing of a mems calorimetric shear-stress sensor', *Sensors and Actuators A: Physical* **253**, 210 – 217.

References

- Whalley, R. D. (2011), Turbulent boundary-layer control with DBD plasma actuators using spanwise travelling-wave technique, PhD thesis, University of Nottingham.
- White, F. M. (2016), 'Fluid mechanics, 1999', *Mc Graw-Hill*.
- White, F. M. and Corfield, I. (2006), *Viscous fluid flow*, Vol. 3, McGraw-Hill New York.
- Winter, K. G. (1979), 'An outline of the techniques available for the measurement of skin friction in turbulent boundary layers', *Progress in Aerospace Sciences* **18**(C), 1–57.
- Wong, V. T. and Li, W. J. (2003), Bulk carbon nanotubes for micro anemometry, in 'Fluids Engineering Division Summer Meeting', Vol. 36975, pp. 1739–1744.
- Wu, X. and Moin, P. (2010), 'Transitional and turbulent boundary layer with heat transfer', *Physics of Fluids* **22**(8), 085105.
- Xiang, D., Yang, Y., Xu, Y. and Li, Y. (2010), Mems-based shear-stress sensor for skin-friction measurements, in '2010 IEEE Instrumentation & Measurement Technology Conference Proceedings', IEEE, pp. 656–661.
- Xu, Y., Jiang, F., Lin, Q., Clendenen, J., Tung, S. and Tai, Y.-C. (2002), Underwater shear-stress sensor, in 'Technical Digest. MEMS 2002 IEEE International Conference. Fifteenth IEEE International Conference on Micro Electro Mechanical Systems (Cat. No. 02CH37266)', IEEE, pp. 340–343.
- Xu, Y., Lin, Q., Lin, G., Katragadda, R. B., Jiang, F., Tung, S. and Tai, Y.-C. (2005), 'Micromachined thermal shear-stress sensor for underwater applications', *Journal of Microelectromechanical Systems* **14**(5), 1023–1030.
- Yokozeki, S., Kusaka, Y. and Patorski, K. (1976), 'Geometric parameters of moiré fringes', *Applied optics* **15**(9), 2223–2227.
- Zhao, J., Völlm, H., Feili, D., Panidis, T. and Seidel, H. (2012), 'Nano-scale hot wire sensors for turbulence measurement applications', *Procedia Engineering* **47**, 845–848.
- Zhao, Z., Shin, M., Gallman, J. M. and White, R. D. (2014), 'A microfabricated shear sensor array on a chip with pressure gradient calibration', *Sensors and Actuators A: Physical* **205**, 133–142.
- Zhe, J., Modi, V. and Farmer, K. R. (2005), 'A microfabricated wall shear-stress sensor with capacitive sensing', *Journal of Microelectromechanical Systems* **14**(1), 167–175.
- Ziliac, G. C. (1996), 'Further developments of the fringe-imaging skin friction technique'.
- Örlü, R. and Vinuesa, R. (2020), 'Instantaneous wall-shear-stress measurements: advances and application to near-wall extreme events', *Measurement Science and Technology* **31**(11), 112001.